Determinants of metal-specific transcriptional responses in bacteria

ANDREW JAMES PETER SCOTT

Determinants of metal-specific transcriptional responses in bacteria

Andrew James Peter Scott

Thesis submitted for the degree of Doctor of Philosophy

Department of Biosciences

Durham University

2018

Contents

List of Figures

List of Tables

Abstract

Metals are essential cofactors for life. However, their beneficial intrinsic chemical properties can be toxic if their cellular levels are not tightly regulated. In a bacterial cell, this control rests with a set of metal-sensing transcriptional regulators that respond to changes in intracellular metal availability to tune the expression of genes required for metal homeostasis. The correct metal ion, bound to its cognate sensor, acts allosterically to alter DNA-binding affinity leading to changes in promoter occupancy. The determinants for a metal-specific response are well understood. However, the problems posed by the mis-metalation of metallosensors exposed to excess non-cognate metal ions have only recently been considered. This study focuses on the response of a set of metalloregulators (from a single organism) to one metal to understand at a molecular level the risk for mis-metalation and, potentially, incorrect function.

The cellular complement of *Salmonella enterica* serovar Typhimurium metallosensors (MntR, Fur, RcnR, NikR, CueR, ZntR, and Zur) were purified, and their individual affinities for Ni(II), along with the effect of Ni(II) on DNA-binding, were determined using biophysical methods. The two cognate Ni(II)-sensors (NikR and RcnR) showed the tightest Ni(II) affinities. The remaining five sensors had weaker affinities that clustered within a narrow range below a threshold two orders of magnitude weaker than for RcnR. DNA-binding affinities suggest all the non-cognate sensors were capable of a Ni(II)-induced allosteric response *in vitro*. Simulations of cellular DNA-binding using Ni(II) and DNA affinities with estimates of protein copy number demonstrated that free Ni(II) must be buffered to low levels to ensure the fidelity of Ni(II)-specific transcriptional responses. Fur was identified as the non-cognate sensor most likely to be mis-metalated and mal-respond to Ni(II). The work suggests a general principle for maintaining metal-specific transcriptional responses by buffering individual metal ions within specific ranges.

Abbreviations

ABC	ATP-binding cassette
Ala	alanine
Arg	arginine
Asp	aspartate
Bfr	bacterioferritin
CDF	cation diffusion facilitator
Cys	cysteine
DTNB	5,5′-dithio-bis-(2-nitrobenzoic acid)
DTT	dithiothreitol
ECF	energy coupling factor
EDTA	ethylenediaminetetraacetic acid
EGTA	ethylene glycol-bis-(2-aminoethylether)-*N*-*N*-*N*′-*N*′-tetraacetic acid
FA	fluorescence anisotropy
FbaA	fructose-1,6-bisphosphate aldolase A
Ftn	bacterial ferritin
FZ3	FluoZin-3
Glx	glyoxalase
Gln	glutamine
Glu	glutamate
GuHCl	guanidine hydrochloride
Gly	glycine
HEPES	4-(2-hydroxyethyl)-1-piperazineethanesulfonic acid
ICP-MS	inductively coupled plasma mass spectrometry
IPTG	isopropyl-β-D-thiogalactoside
Kan	kanamycin
LB	Luria-Bertani broth
L-His/His	L-histidine
LMCT	ligand-to-metal charge transfer
Lys	lysine
MF2	mag-fura-2
MFP	membrane fusion protein
NiCoT	nickel and cobalt transporters
NRAMP	natural resistance-associated macrophage protein
NTA	nitrilotriacetic acid
OMF	outer membrane facing structure
P_0	sensor abundance determined under metal-limiting conditions
P_1	sensor abundance determined under metal-supplemented conditions
PAGE	polyacrylamide gel electrophoresis
PEG	polyethylene glycol
ppb	parts per billion
RND	resistance, nodulation, and division transporter
ROS	reactive oxygen species
SDS	sodium dodecyl sulphate
Ser	serine
SOD	superoxide dismutase
TBE	tris-borate-EDTA buffer
TCEP	tris(2-carboxyehtyl)phosphine hydrochloride

Thr	threonine
Trp	tryptophan
TSS	transformation and storage solution
Tyr	tyrosine
XAS	X-ray absorption spectroscopy

Statement of copyright

Acknowledgments

I would like to thank my supervisor, Peter Chivers, for assisting me with this project and providing me with the skills I required to carry out my research in the lab. I am grateful for all the advice you have given me (especially with how to approach writing this thesis) and for giving me the opportunity to work alongside you.

I would also like to thank my colleagues from the lab/office; Andrew Foster, Deenah Morton, Maria Martini, Marikka Beecroft, Kotryna Svedaite, Joy Nunn, Tessa Young, and Karrera Djoko. I have enjoyed sharing my time at university with you and appreciate the advice and knowledge you have provided me over the years. You have also kept me entertained during the months I spent writing my thesis – as well as during the long hours spent working with the anaerobic chamber! I must also thank my second supervisor, Nigel Robinson, for constructive and insightful discussions.

Durham University Triathlon Club has been a huge part of my life at Durham and I am thankful to all the members of the club from 2015-2018 for keeping me sane during my free time. I have some great memories from our adventures which I will not be forgetting any time soon. I will be looking forward to future "training camps" back in our Mediterranean home.

Special thanks to Dave & Rachael, Rory, Victoria, big Dave, and (of course) Sarah for ensuring I did not go homeless when writing up! Additional thanks to Lin and Katie for amusing me over the summer months in Durham.

Finally, I would like to thank my family, Dad, Mum, Chris, Gemma, Jacqui, Paul, and Lucy, for all the support during my time at Durham. Your interesting lives have always been a welcome distraction and I would not be where I am now without your continuing support. Hopefully I can repay you (supportively and financially) in the future.

Chapter 1: Introduction

1.1 Metals in biology

1.1.1 The importance of metals for life

Metal ions are essential for all life forms regardless of cellular size or complexity. Metals are required for a variety of structural and functional roles within a cell including protein stabilisation, enzyme active site catalysis (oxidation-reduction, hydrolytic, and acid-base chemistry), and electron transfer (Lippard and Berg, 1994, Da Silva and Williams, 2001, Reyes-Caballero et al., 2011). Different metals have different intrinsic properties, such as *d*-orbital valency, mass, atomic radii, polarisability, and charge (Da Silva and Williams, 2001, Dudev and Lim, 2014), which suit certain roles required by different proteins and enzymes. For example, Mn(II), which is a d^5 element, is considered "hard" in comparison to the "soft" d^{10} Cu(I), where "hard" is the term used to describe a small metal with a high charge and weakly polarisable, compared to a "soft" metal which is larger with a lower charge and strongly polarisable (Lippard and Berg, 1994, Reyes-Caballero et al., 2011).

The unique properties that make first row transition metal ions critical to an organism consequently correspond to processes that result in toxic effects for a cell. For example, *Escherichia coli* mutants that over accumulate iron grow poorly under aerobic conditions (Touati et al., 1995) because divalent iron (and copper) can produce hydroxyl radicals via the Fenton reaction (Fenton, 1894, Meneghini, 1997, Valko et al., 2005). This highly reactive species can lead to DNA damage, lipid peroxidation, and oxidative protein damage (Harber and Weiss, 1934, McCord and Day, 1978, Kehrer, 2000). Metal ions are also toxic due to adventitious binding involving proteins and other cellular components (see below).

Individual metal ion contents vary within cells, for example, in *E. coli* Zn and Fe are ~ 100 μM, Cu and Mn are ~ 10 μM, and Ni and Co are less than 10 μM (Finney and O'Halloran, 2003, Maret, 2010). In some cases, these levels are 100- to 1000-fold higher than those found outside the cell (Outten and O'Halloran, 2001). Metal demands also vary with metalloenzyme requirements under different growth conditions and in different cell types.

Metals present a chemical problem for cells arising from the Irving-Williams series (Irving and Williams, 1953). This work established a hierarchy of affinities of transition metals (Equation 1.1) for many different small organic ligands (e.g. free amino acids), as well as purified proteins, such as carbonic anhydrase (McCall and Fierke, 2004):

$$Mn^{2+} < Fe^{2+} < Co^{2+} < Ni^{2+} < Cu^{2+} > Zn^{2+} \quad (1.1)$$

For example, if the intracellular metal availability of first row divalent transition metals were the same, the occupancy of a metal binding site would reflect the Irving-Williams series and copper would bind preferentially to this population of sites at the exclusion of other metals. Note that Cu(I) also demonstrates high-affinity metal-binding for a given set of ligands, similar to Cu(II). Mis-metalation at a catalytic active site in an enzyme could lead to toxicity by competitive inhibition or an aberrant reaction mechanism. For example, mononuclear iron cluster enzymes threonine dehydrogenase and ribulose-5-phosphate 3-epimerase are inactivated by Zn(II) replacing Fe(II) at the catalytic site which can occur by two different mechanisms, either superoxide accumulation facilitating Fe(II) removal or Zn(II) overload in *E. coli* (Gu and Imlay, 2013). Furthermore, it is possible metal ions could bind to sites which would not normally accommodate a metal ion resulting in allosteric (non-competitive) inhibition of an enzyme.

Due to the risk of toxicity, a cell must control the intracellular concentration of metal ions through regulated synthesis of machinery that specifically controls the transport of metal ions into the cell, their sequestration and storage within the cell, and transport out of the cell under circumstances where excess metal begins to accumulate, to ensure sufficient supply to essential proteins while limiting the toxic consequences posed by them (see Section 1.2).

This thesis will explore the balance between specific and non-specific metal-binding within a functional class of proteins: the bacterial metalloregulators. These regulators are discussed later (Section 1.3), following an introduction to their relevance in bacteria.

1.1.2 Metalloproteins are abundant in cells

Metalloproteins are a major component of the total number of proteins. Estimates of metalloprotein abundance range from 25 to 47%, the variation of which is due to whether all metals are included or just transition elements (Rosenzweig, 2002, Andreini et al., 2008, Maret, 2010). There are a host of metal-dependent enzymes, including proteases, oxidoreductases, transferases, hydrolases, lyases, isomerases, and ligases (Waldron et al., 2009).

For example, superoxide dismutase (SOD) enzymes are metalloproteins which have evolved and remained in almost all forms of life, with the exception of a few anaerobic bacteria (McCord et al., 1971, Archibald and Fridovich, 1981, McCord and Fridovich, 1988, Miller, 2012). Once the atmosphere became aerobic, the production of toxic superoxide and consequential chain-reaction production of reactive oxygen species (ROS) meant it was

fundamental to develop cellular antioxidant defences such that at least three families of SODs evolved separately (Miller, 2012). SODs require a metal ion (or ions) for oxidation-reduction catalysis of superoxide to oxygen and hydrogen peroxide (Fridovich, 1989). The three families of SODs can contain Mn or Fe (some able to use Mn and Fe) (Archibald and Fridovich, 1981, Miller, 2012), Ni (Youn et al., 1996), or a CuZn complexed centre (Tainer et al., 1982).

Another example is vitamin B_{12} (cobalamin). Although not a protein itself, this cofactor is an essential nutrient for higher organisms (but not all plants) though is only produced by prokaryotes, requiring ~ 30 different enzymatic steps in the production of this extensively complex molecule (Warren et al., 2002). B_{12} is a member of the modified tetrapyrrole family, along with other molecules such as chlorophyll and haem, and is composed of a ring-contracted macrocyle which coordinates a central Co(II) atom (Hodgkin et al., 1955, Roth et al., 1996, Moore and Warren, 2012). The unique properties of the cobalt-carbon bonds provide the catalytic power associated with B_{12}-dependent enzymes including propanediol dehydratase, ethanolamine ammonia lyase, methionine synthetase, ribonucleotide reductases, among others involved in metabolic processes (Roth et al., 1996, Moore and Warren, 2012). B_{12} was originally discovered due to its ability to cure pernicious anaemia (Minot and Murphy, 1926).

1.2 The protein machinery of metal homeostasis

Metal homeostasis is achieved through the regulation of protein systems which facilitate metal import, storage, and efflux. The following section describes these protein systems for bacteria, although equivalent systems are required for all living organisms. A representation of the homeostatic mechanisms for one of the simplest systems in bacteria for an essential metal can be found in Figure 1.1.

1.2.1 Metal import

Metals cannot be synthesised or degraded (unlike organic nutrient molecules), therefore, they must be actively transported into the cell when required. Metal acquisition requires specific energy-dependent protein systems to achieve the intracellular concentrations described in Section 1.1.1. There are two mechanisms of transport; ATP-dependent (primary) and proton-motive-force-dependent (secondary). One of the largest super-families of transporters are the ATP-binding cassette (ABC) transporters, which are found in all

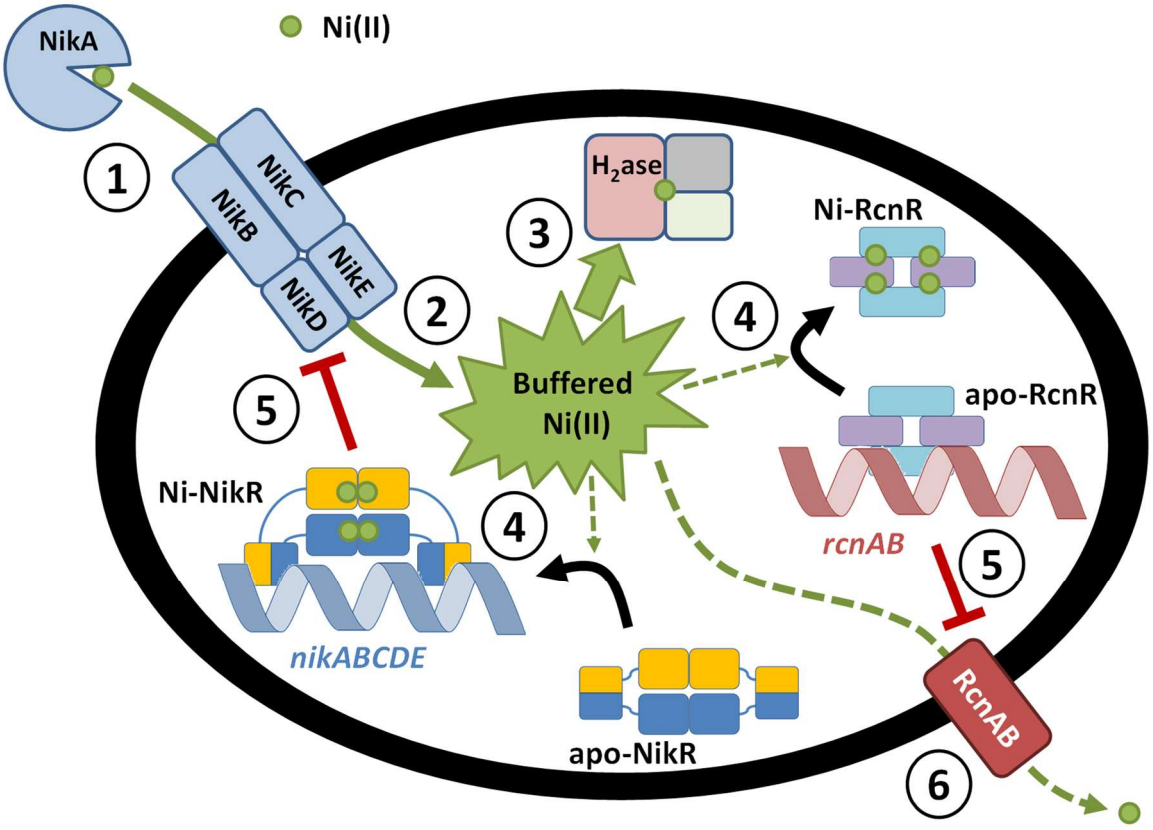

Figure 1.1 Ni(II) homeostasis in a bacterial cell (e.g. *E. coli* or *Salmonella*). (1) Periplasmic Ni(II) ions are selectively transported into the cytosol to supply the demand of the cell. (2) Inside the cell, Ni(II) is buffered by small molecule ligands. (3) Metallochaperones deliver the metal to the requiring metalloenzymes. (4) High buffered-Ni(II) concentrations are sensed by metalloregulators which result in altered gene expression. (5) Ni(II) importer synthesis is repressed and Ni(II) exporter synthesis is de-repressed. (6) Ni(II) is exported from the cell to prevent excess accumulation.

organisms (Higgins, 1992, Rice et al., 2014). This family, which is split into three subgroups (type I, type II, and energy-coupling factor (ECF) transporters), is required for the import of metals into the cell, including nickel (NikABCDE) (Navarro et al., 1993), cobalt (CbiMNQO) (Roth et al., 1993), iron (IrtAB) (Rodriguez and Smith, 2006), and zinc (ZnuABC) (Patzer and Hantke, 1998). These transporters tend to offer high selectivity and high affinity for their given metal (Lebrette et al., 2014). ABC transporters contain two transmembrane domains (e.g. NikB and NikC) and two nucleotide-binding domains (e.g. NikD and NikE) (Rice et al., 2014), though these can form as homodimers, as is the case with the products of the *znu* operon. These domains assemble to produce the membrane-spanning structure capable of substrate transport. Two types of ABC transporters (type I and type II) contain substrate binding proteins (e.g. NikA) which are located in the periplasm of Gram-negative bacteria and can associate with the transmembrane structure in order to couple ATP hydrolysis with substrate transport through the transmembrane domain (Rice et al., 2014).

Secondary metal transport can occur via the natural resistance-associated macrophage protein (NRAMP) metal ion transporters. NRAMP transporters couple energy stored in the proton gradient to accumulate metal ions intracellularly (Nevo and Nelson, 2006), with one example being the manganese importer, MntH (Makui et al., 2000). Another example of secondary transport is through metal permeases which can transport ions into the cytosol with high affinity, as is the case with the nickel permease, NixA (Mobley et al., 1995a). NixA is a member of the nickel and cobalt transporter (NiCoT) family and is predicted to be a monomer containing eight transmembrane helices in their structure (typical of this family) (Fulkerson and Mobley, 2000, Wolfram and Bauerfeind, 2002).

Gram-negative bacteria actively import metal ions from the extracellular space to the periplasm using TonB-dependent transporter complexes (Noinaj et al., 2010). This system is important for most metals and metal complexes in order to allow transport across the inner membrane, though similar extracellular transport could occur via non-specific porin proteins (Chivers et al., 2012). Some metals, iron in particular, are transported across bacterial membranes complexed to other molecules such as siderophores (Neilands, 1995). Siderophores are relatively low molecular weight ferric ion specific chelates (generally catechols or hydroxamates) and are excreted by bacteria under iron-starved conditions (Neilands, 1995). Siderophores form highly stable complexes with Fe(III) and can be brought into the cell once bound to an outer membrane receptor (e.g. FupA) via TonB-dependent mechanisms, linked to inner membrane iron transporters, such as FeoB (Neilands, 1995, Tsolis et al., 1996, Noinaj et al., 2010). Once inside the cell, Fe(III) is converted to

Fe(II) under the highly reducing conditions and loses its affinity for the siderophore molecules so that it is released to be utilised by the cell (Neilands, 1995).

1.2.2 Metal buffering and chaperone proteins

The need to ensure the absence of free (hydrated) metal ions is paramount, especially the most stable metals of the Irving-Williams series (Section 1.1.1), due to the toxic consequences associated with these species (Section 1.1.1). Although the cell can accumulate high intracellular concentrations of metals (Outten and O'Halloran, 2001), the majority is bound to the proteins that require them. The cell consists of a range of biomolecules such as small molecule ligands (e.g. amino acids and glutathione) and organic acids which buffer metal ions, as well as specialised proteins, called metallochaperones, all of which can help to decrease the concentration of hydrated metal ions (< 1 $cell^{-1}$ for Ni, Cu, and Zn) (Outten and O'Halloran, 2001, Changela et al., 2003, Foster et al., 2014a). In yeast, metallochaperones (indicated in brackets) have been identified for delivery of Cu(I) ions to enzymes such as the mitochondrial cytochrome oxidase (COX17) (Beers et al., 1997), the Golgi P_1-type ATPase (ATX1) (Lin et al., 1997, Pufahl et al., 1997), and cytoplasmic [CuZn] superoxide dismutase 1 (CCS) (Culotta et al., 1997, O'Halloran and Culotta, 2000). These small molecules and chaperones are likely to be crucial for ensuring correct metal transfer in all proteins and enzymes. Thus, specific interactions between metals and molecules occur before final delivery of the metal to its protein target. These specific interactions enhance the rate of metal exchange compared to simple diffusion of the extremely low concentration free metal ions.

1.2.3 Metal sequestration and storage in a cell

Storage proteins are important for iron metabolism and bacteria contain two types of ferritin-like molecules for storage of this metal; bacterial ferritins (Ftn) and bacterioferritins (Bfr) (Andrews, 2010, Rivera, 2017). These proteins utilise oxygen and hydrogen peroxide to oxidise Fe(II) to Fe(III) for compartmentalisation (Rivera, 2017). Ftns and Bfrs are 24 subunit complexes, with each subunit consisting of a four-helix bundle, that arrange into spherical hollow structures that can contain up to 4,500 iron atoms (Ford et al., 1984, Theil et al., 2006, Crichton and Declercq, 2010, Andrews, 2010). Crystal structures of *Pseudomonas aeruginosa* BfrB suggests the ferroxidase centres can arrange into two conformations; a “closed gate” conformation which allows for Fe(II) binding and an “open gate” conformation which is proposed to result after oxidation of Fe(II) to Fe(III), allowing the translocation of the metal to the interior core of the protein for storage (Weeratunga et al., 2010, Rivera, 2017). Protein-protein interactions are required for the mobilisation of

stored Fe(III), including proteins with electron transfer function (e.g. Bfd and Fpr) to assist in reduction of stored metal to Fe(II) (Weeratunga et al., 2009, Yao et al., 2012, Rivera, 2017). These proteins allow intracellular accumulation of iron for use when conditions demand significant iron availability (e.g. for processes such as respiration and DNA synthesis) or when growth changes to iron-limiting conditions. This method avoids the toxic consequences of free metal ion formation since the metal is sequestered away from functional proteins and enzymes in the cytosol.

1.2.4 Metal export

Accumulation of metal in the cytosol risks exceeding the specific binding capacity of the cell (protein and buffer), a potentially toxic event. Therefore, mechanisms to transport excess metal out of the cytosol are required for healthy growth. As with metal import, export is achieved in an energy-dependent manner, utilising the electrochemical potential gradient or ATP-driven processes. Efflux is mostly attributed to the three main families of transporter systems in bacteria; P-type ATPases, cation diffusion facilitator (CDF) transport, and resistance, nodulation and division (RND) transporters (Nies, 2003, Klein and Lewinson, 2011).

P-type ATPase efflux systems are specific for certain metals and have been shown to function when chaperone molecules deliver the correct metal to the membrane-embedded receptor (Tottey et al., 2002, González-Guerrero and Argüello, 2008, Klein and Lewinson, 2011). ATP hydrolysis is coupled with metal transport into the periplasm to decrease the concentration of a given metal in the cytosol. Examples of these proteins include CopA (copper) (Odermatt et al., 1993), ZntA (zinc) (Rensing et al., 1997), PfeT (iron) (Guan et al., 2015), and CadA (cadmium) (Nucifora et al., 1989).

CDF transporters in prokaryotes are generally six transmembrane domain structures that form homodimers, but can be much more complex in eukaryotes (Kolaj-Robin et al., 2015). These antiporter proteins couple proton translocation (into the cytosol) with metal transport into the periplasm (Nies and Silver, 1995, Kolaj-Robin et al., 2015) and are found in many different organisms including plants and animals (Nies, 2003). CDFs general confer specificity for metal ions, such as with MntE (manganese) (Rosch et al., 2009), NepA (nickel/cadmium) (Cubillas et al., 2013), and CepA (cobalt/cadmium) (Cubillas et al., 2013), though some can show a broader range of specificity, such as FieF and DmeF (Munkelt et al., 2004, Grass et al., 2005).

RND transporters are large protein complexes that consist of three main components; the RND structure which spans the inner membrane into the periplasm, the outer membrane

facing structure (OMF) which spans the outer membrane to connect the RND structure with the extracellular space, and the membrane fusion protein (MFP) which stabilises the RND and OMF structures together (Tseng et al., 1999, Nies, 2003, Kim et al., 2011). The RND structure is usually a trimer of 12 membrane-spanning helical protein subunits where the OMF is also generally a trimeric species containing a hollow tube to allow efflux of cations (or other substrates depending on the family) from the cytosol/periplasm directly into the extracellular space (Zgurskaya and Nikaido, 1999a, Zgurskaya and Nikaido, 1999b, Murakami et al., 2002, Nies, 2003). The three proteins are part of an operon (for genes termed *CBA*) which encode RND (A), MFP (B), and OMF (C), where some operons also include small chaperone proteins to deliver the metal to the transporter (e.g. CusF) (Franke et al., 2001, Franke et al., 2003, Nies, 2003). These transporters function as antiporters and utilise the proton-motive force to efflux specific metals (Nies, 1995), with examples including CzcCBA (cobalt, zinc, and cadmium) (Saier et al., 1994), CnrCBA (cobalt and nickel) (Saier et al., 1994), and CusCFBA (copper and silver) (Franke et al., 2001, Outten et al., 2001).

There are four additional families of efflux protein which have been characterised. These include the CHR family (chromate resistance), the NreB-like family (nickel resistance), CntR-like family (nickel resistance), and the RcnA-like family (Nies, 2003, Rodrigue et al., 2005). RcnA is required for resistance to both cobalt and nickel (Rodrigue et al., 2005), whereas another RcnA-like protein, MrdH, has been shown to confer resistance to nickel, zinc, and cadmium (Haritha et al., 2009).

1.3 Metal-sensing transcriptional regulators

1.3.1 Specialised proteins regulate metal transport and storage systems

The mechanisms for metal import, metal storage, and metal efflux (Sections 1.2.1, 1.2.2, 1.2.3, and 1.2.4) are required to balance supply with demand for a given essential metal ion. The bacterial cell contains metal-sensing transcriptional regulators (called metalloregulators, metallosensors, or sensors) which are proteins capable of regulating the genes associated with transport and storage for a specific metal ion (in some cases multiple but similar metal ions) (Giedroc and Arunkumar, 2007). There are seven major families of metalloregulators; ArsR/SmtB (San Francisco et al., 1990, Huckle et al., 1993), CopY (Odermatt and Solioz, 1995), CsoR/RcnR (Iwig et al., 2006, Liu et al., 2007), DtxR (Boyd et al., 1990), Fur (Ernst et al., 1978), MerR (Foster et al., 1979), and NikR (De Pina et al., 1999, Chivers and Sauer,

1999). These sensors have evolved for all essential transition metals, as well as non-essential (e.g. arsenic) and heavy metals (e.g. mercury) (Giedroc and Arunkumar, 2007). In most cases, they function by binding to a specific metal which allosterically activates or inhibits DNA-binding for their operator site, though some metal-bound regulators activate transcription by enhancing RNA polymerase binding. The metal-specific responses of these sensors results from intrinsic factors such as metal affinity and allostery, as well as extrinsic influences such as "access" to a particular metal (Foster et al., 2014a).

The current understanding is that metallosensors are detecting the concentration of metal ions within the intracellular polydisperse buffer (Section 1.2.2). The metal within this buffer is also accessible to chaperone proteins (Section 1.2.2) which provide competition with the sensors for metal. The set-point for which each sensor has adapted to respond (i.e. the concentration of metal that causes 50% of the transcriptional response) can be calculated through *in vitro* run-off transcription assay (or similar) experiments (Outten and O'Halloran, 2001) and by using *in vitro* affinity constants (both metal and DNA affinities) (Osman et al., 2017, Osman et al., 2018). Deviation from the buffered-metal set-points results in inhibition of importer synthesis or activation of exporter synthesis by the sensors as their metalation status changes.

1.3.2 Metal selectivity by metalloregulators

Selectivity of metal-binding by a metalloregulator cannot be attributed to affinity alone since proteins tend to bind metal ions in the order of the Irving-Williams series, as described in Section 1.1.1. A vital feature of metalloregulator function is an allosteric conformational change associated with metal-binding, generally to alter the affinity of the sensor for DNA to increase or decrease repression of gene synthesis depending on the mode of action for the sensor (i.e. co-repressor versus de-repressor, see Section 1.3.3). The geometry of metal-binding was shown to be highly important for driving these conformational changes, demonstrated by two sensors (SmtB and NmtR) from the same family of de-repressor proteins (ArsR/SmtB, see Section 1.3.1) that respond to different metal ions (Huckle et al., 1993, Cavet et al., 2002). SmtB is a Zn(II)-responsive regulator which coordinates this metal in a tetrahedral geometry (VanZile et al., 2000), whereas NmtR is Co(II)- and Ni(II)-responsive, coordinating both ions in an octahedral geometry (Cavet et al., 2002, Pennella et al., 2003). While NmtR can bind Zn(II) tighter than Co(II) and Ni(II) (Cavet et al., 2002), it was shown that, at equivalent concentrations, Co(II) was able to induce de-repression by NmtR whereas Zn(II) could not (Cavet et al., 2002). Zn(II) favours four coordinate geometries and it appears that this metal is bound to NmtR in a tetrahedral geometry

(Pennella et al., 2003) where this altered coordination environment is unable to induce the same conformational changes associated with octahedral binding by Co(II)/Ni(II) to drive NmtR off DNA (Cavet et al., 2002).

The types of ligands available in a metal-binding region could also be a determining factor for the coordination geometry and, therefore, eliciting the appropriate conformational changes in response to a metal binding. For example, soft metals prefer soft ligands, where the softness of a ligand follows the same trend in polarisability as metals (see Section 1.1.1); cysteine residues are most polarisable, histidine and methionine residues are less polarisable, and aspartate and glutamate residues are least polarisable (Lippard and Berg, 1994, Reyes-Caballero et al., 2011). The types of ligands in a particular site will also impact on the relative affinities of a sensor for different metal ions (Dudev and Lim, 2014).

1.3.3 The thermodynamic cycle of metalloregulation

Figure 1.2 represents a thermodynamic cycle which can be used to model metal- and DNA-binding by a metallosensor. Metal binding is possible for a sensor off DNA (K_1) or bound to DNA (K_2). Functional responses depend upon the ratio of K_3 (apo-sensor DNA affinity) and K_4 (holo-sensor DNA affinity), which can be calculated as a coupling free energy (ΔG_C) value (Section 2.9.4). In the case of co-repressor or de-repressor proteins, the DNA-bound forms of the sensors prevent transcription of the regulated genes, whereas the off-DNA forms allow it. Co-repressor proteins have a negative ΔG_C whereas de-repressor proteins have a positive ΔG_C. On the other hand, activator proteins initiate transcription when bound to DNA, but fail to do so when off DNA. MerR-like proteins are a family of activating sensors which only activate transcription when bound to both metal and DNA (discussed further in Section 1.3.10). Metals which generate a small magnitude ΔG_C will not affect the promoter occupancy by a sensor but could titrate active protein. Through measuring at least three of the equilibrium constants (K_1, K_2, K_3, and K_4) in Figure 1.2, the set-point of a sensor can be determined using this thermodynamic cycle (Osman et al., 2017, Osman et al., 2018).

1.3.4 Mis-metalation of metalloregulators

As described earlier (Section 1.1.1), adventitious metal-binding is associated with toxicity in a cell. Metalloregulators therefore pose a target for adventitious binding by excess non-cognate metal ions. It is unknown how extensive this binding could be in a cell and how widespread the possibility for mal-responses by regulators could be. A recent study has investigated the effect of cognate and non-cognate sensors on transcriptional activity during short-term exposure to both Co(II) and Zn(II) (Osman et al., 2017). This indicated that non-

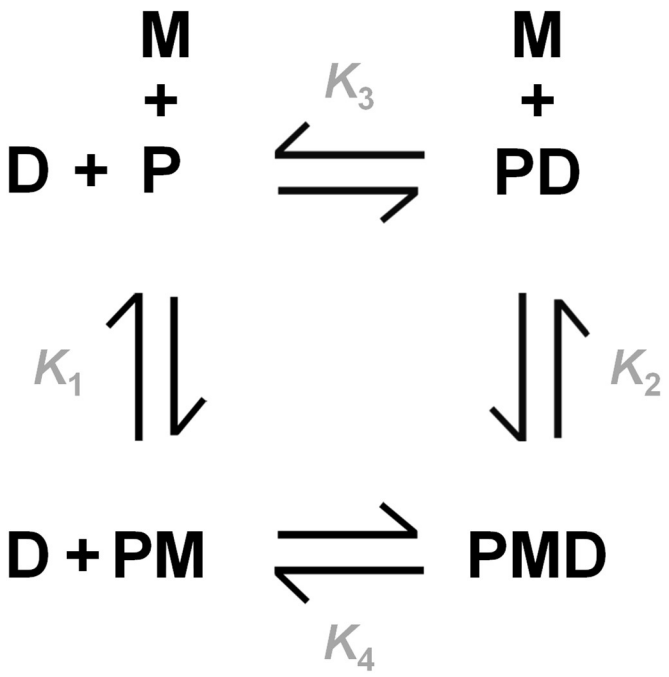

Figure 1.2 Thermodynamic cycle for metal-sensing transcriptional regulators. The metal- and DNA-binding equilibria are indicated with corresponding equilibrium constants (for dissociation). Metal (*M*) can bind to protein (*P*) with equilibrium constant K_1 to form a protein-metal complex (*PM*). *PM* can bind to DNA (*D*) with equilibrium constant K_4 to form a protein-metal-DNA complex (*PMD*). Additionally, *P* can bind to *D* with equilibrium constant K_3 to form a protein-DNA complex (*PD*). *PD* can bind *M* with equilibrium constant K_2 to form *PMD* through an alternative pathway.

specific responses occur during the initial stages of "metal shock" and can be predictable based on the thermodynamic properties of each sensor (Section 1.3.3) (Osman et al., 2017). This suggests an alternative toxic effect of exposure to metal whereby mal-responses could cause dysregulation of additional metals inside the cell. However, the specificity of metal-dependent transcriptional responses has not been conducted for a complete cellular set of metalloregulators with respect to a single metal ion. By using a single metal, it should be possible to view general trends by a set of sensors and could be used for making cellular predictions (e.g. which sensors are most susceptible to mal-responses) as well as general predictions for other metal ions.

1.3.5 The *Salmonella* set of metallosensors

Salmonella enterica serovar Typhimurium (*Salmonella* or *Sty*) is an enteric bacterium which causes gastroenteritis in humans. The critical process of regulating internal essential metal concentrations in *Salmonella* is governed through seven metallosensors from five of the protein families (Section 1.3.1); MntR (Mn), Fur (Fe), RcnR (Co/Ni), NikR (Ni), CueR (Cu), ZntR (Zn), and Zur (Zn) (Ikeda et al., 2005, Osman et al., 2010, Osman et al., 2017, Osman et al., 2018). *Salmonella* has been used as the model organism for experiments in this thesis. The following sections provide detail on the structure and function of *Salmonella* sensor homologues.

1.3.6 MntR structure and function

MntR is a manganese-sensing transcriptional regulator within the DtxR family (Que and Helmann, 2000). DtxR family regulators are responsive to manganese or iron and other members include the founding protein, DtxR (Fe), as well as IdeR (Fe), and AntR (Mn) (Sen et al., 2006, Golynskiy et al., 2006, Merchant and Spatafora, 2014). MntR was considered a co-repressor protein which downregulates transcription of manganese importers, such as *mntA* and *mntH*, as well as *mntS* which encodes a short protein proposed to be a manganese chaperone (Que and Helmann, 2000, Patzer and Hantke, 2001, Kehres et al., 2002a, Waters et al., 2011). However, the metal-bound protein has also been shown to activate expression of manganese exporter proteins including *mntP* and *mntE* (Waters et al., 2011). *Salmonella* MntR has been studied for manganese binding, as well as effects on transcription for genes such as *sitA* (importer) and *mntS* (Kehres et al., 2000, Kehres et al., 2002a, Kehres et al., 2002b, Ikeda et al., 2005, Osman et al., 2018).

Bacillus subtilis MntR responds *in vivo* to two inherently different metals; Mn(II) and Cd(II) (Que and Helmann, 2000). Cd(II) delivery into bacterial cells has been demonstrated via

manganese-transporters (Que and Helmann, 2000). The crystal structure for *B. subtilis* MntR has been resolved, shown in Figure 1.3, and demonstrates a dinuclear metal site in the presence of both Mn(II) and Cd(II) (Kliegman et al., 2006). Two binding sites per monomer were initially identified (site A and site B), however, further analysis of the data revealed the metal ion from site B can bind in an alternative orientation (termed site C) (Kliegman et al., 2006), thus there are three possible metalated forms of MntR; A-loaded, AB-loaded, and AC-loaded protein. Mn(II) ions loaded into site A and site B sit 3.3 Å apart whereas those in site A and site C sit 4.4 Å apart, though the coordinating ligands are mostly the same (except for a solvent molecule in AB and an additional backbone oxygen in AC) but differ in side chain conformations, where two glutamate residues (Glu99 and Glu102) bridge the two sites in both cases (see Figure 1.3c) (Kliegman et al., 2006). The two binding sites are located at the interface of the N-terminal DNA-binding domain and the C-terminal dimerisation domain of each MntR monomer (Kliegman et al., 2006). Mn(II) binds to the A-site in a hepta-coordinate geometry, and the C-site in a hexa-coordinate geometry (McGuire et al., 2013), where the AC-loaded MntR is considered physiologically relevant. Cd(II) binds in a similar orientation, however, the structure bound to Zn(II) only consists of one metal ion located in the A-site (Kliegman et al., 2006). The smaller Zn(II) ion does not favour a high coordination number and binds with a tetrahedral geometry which displaces the bridging residues (Glu99 and Glu102) so that the second site will not form (Kliegman et al., 2006). Site A has since been described as a "selectivity filter" in order to distinguish between metal ions and preventing full mis-metalated activation of the co-repressor, governed by occupancy of the C-site too (Kliegman et al., 2006, McGuire et al., 2013).

The affinity of *B. subtilis* MntR for the first row transition metals has been determined which, as expected, follows the order of the Irving-Williams series (Golynskiy et al., 2006). Though, as mentioned with Zn(II), the coordination is not necessarily predictable since each metal will have different properties associated with it. Moreover, only Mn(II) (and Cd(II)) elicit tight DNA binding (to the *mntH* promoter) by the protein, with Co(II), Fe(II), Ni(II), Zn(II), and Cu(II) increasing the DNA affinity compared to apo-MntR, but not to the extent of Mn(II)-MntR (Lieser et al., 2003, Golynskiy et al., 2005). These metals stabilise the dimerisation domain without drastically altering the structure (Golynskiy et al., 2005), however, Mn(II)-binding does result in a "caliper-like" motion of the DNA-binding domains, fixing them in a conformation that has a tight affinity for the specific recognition sequence of nucleotides (different for each promoter) (Kliegman et al., 2006).

In vitro studies using *B. subtilis* MntR show that while Mn(II) and Cd(II) are required to cause the necessary allosteric changes for tight DNA association of MntR, an intermediate

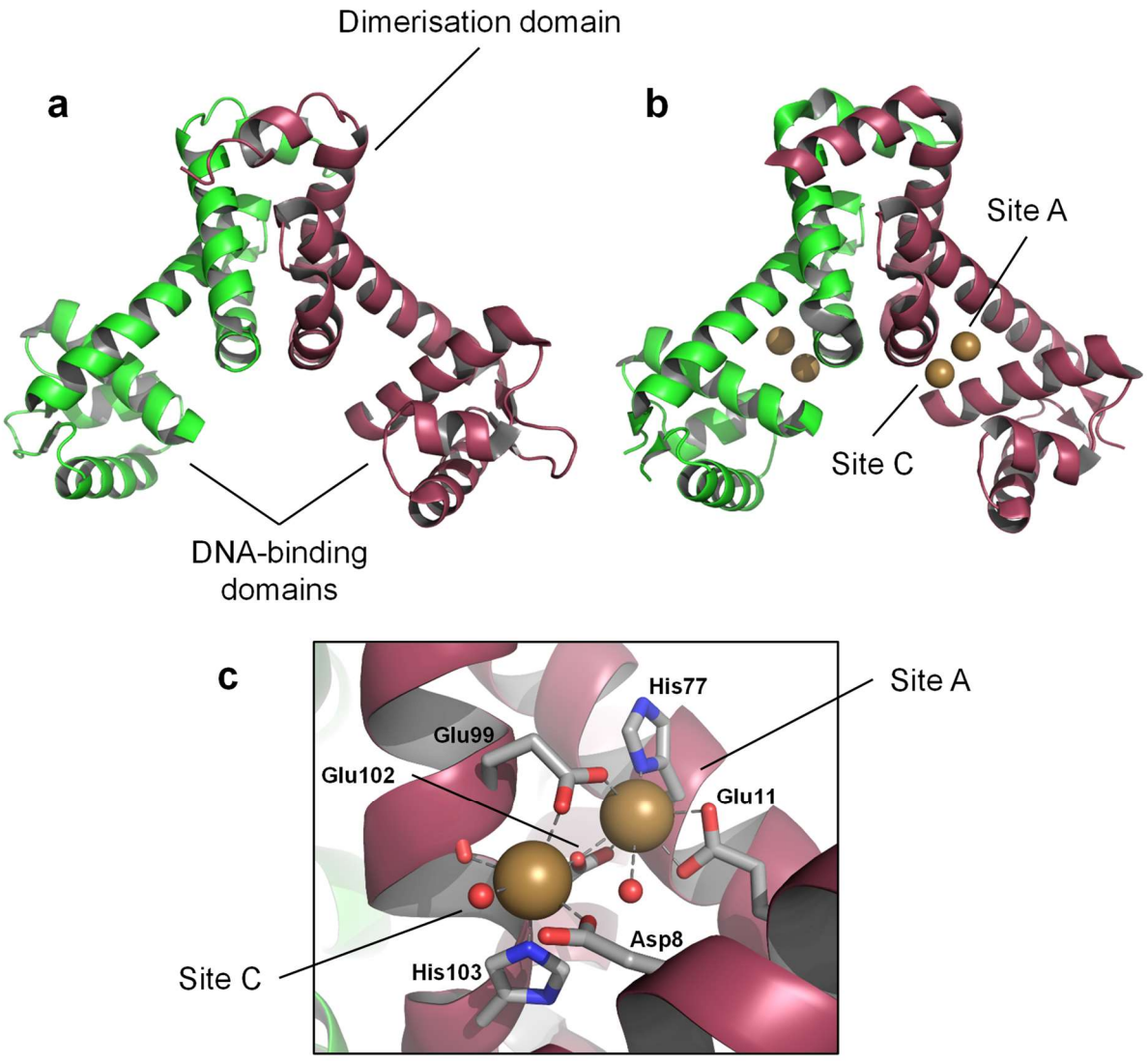

Figure 1.3 Structure of *B. subtilis* MntR. (a) The apo-MntR dimer with each subunit indicated by a different colour (PDB file: 2HYG). **(b)** The Mn(II)-bound protein with metal ions indicated as bronze spheres (PDB file: 2F5D). **(c)** The dinuclear metal-binding site indicating Mn(II) ions coordinated with hepta-coordinate and octahedral geometries for the A- and C-sites, respectfully, by the protein ligands Glu11 (bidentate), His77, Glu99 (bidentate), Glu102, and a solvent molecule for the A-site or Asp8, Glu99, Glu99 backbone oxygen, Glu102, His103, and a solvent molecule for the C-site, where solvent molecules are indicated as red spheres.

response can be achieved with Fe(II) and Co(II) (Golynskiy et al., 2005). DNA-binding studies with the *mntH* promoter suggest Ni(II)-MntR binds two orders of magnitude weaker than Mn(II)-MntR (as does Zn(II)-MntR) (Lieser et al., 2003). However, subsequent studies revealed a Ni(II)-MntR DNA affinity for the *mntA* promoter region to be four-fold tighter than that for *mntH* (Golynskiy et al., 2005), whereas the affinity of Mn(II)-MntR remained relatively similar, which raises the question as to why the Ni(II)-bound protein could interact differently with these two sequences (note that the two DNA fragments used for *mntA* and *mntH* were different lengths).

1.3.7 Fur and Zur structure and function

Fur, the founding member of the Fur-family of regulators (Ernst et al., 1978), is considered a global regulator, controlling iron homeostasis, oxidative and acid responses, virulence, and redox mechanisms in bacteria (Ernst et al., 1978, Hantke, 1981, Bagg and Neilands, 1985, Escolar et al., 1999). Other regulators in this family include Mur (Mn), Nur (Ni), and Zur (Zn), among other non-metal sensors (e.g. PerR) (Fillat, 2014). *Salmonella* encode homologues for both Fur and Zur (Ernst et al., 1978, Campoy et al., 2002). Zur controls the expression of genes related to zinc uptake (*znuABC*), ribosomal proteins (*L31p* and *L36p*), and periplasmic zinc trafficking proteins (*zinT*) (Patzer and Hantke, 1998, Panina et al., 2003). *Sty*Fur has been well-studied and recent work has characterised *Sty*Zur (Campoy et al., 2002, Osman et al., 2015, Osman et al., 2017, Osman et al., 2018). Most recently Zur was shown to be at risk of mis-metalation by Co(II) (Osman et al., 2017).

Crystal structures of Fur were initially elusive but have now been resolved from multiple bacterial species (Pohl et al., 2003, Pecqueur et al., 2006, Sheikh and Taylor, 2009, Dian et al., 2011, Butcher et al., 2012, Deng et al., 2015, Pérard et al., 2018), all with varying numbers of metal binding sites (generally two or three), but each dimeric structure shows the same overall V-shaped protein, shown in Figure 1.4. Some of the Fur proteins have been found to contain structural Zn(II) ions (experiments have determined that the *Salmonella* protein contains a structural Zn site (Osman et al., 2018)) which may be necessary for the protein to dimerise (Dian et al., 2011), though the protein has been shown to dimerise in the absence of this structural zinc (Butcher et al., 2012). The structural site is coordinated by at least two cysteine residues, in some cases four (as for *Salmonella*), in a tetrahedral geometry within each monomer (Figure 1.4d) (Althaus et al., 1999, Gonzalez de Peredo et al., 1999, Vitale et al., 2009, Dian et al., 2011). The structural zinc site is found in the C-terminal dimerisation domain of the protein and can help with stabilisation (Dian et al., 2011). In addition to the dimerisation domain, the protein also contains an N-terminal, winged-helix,

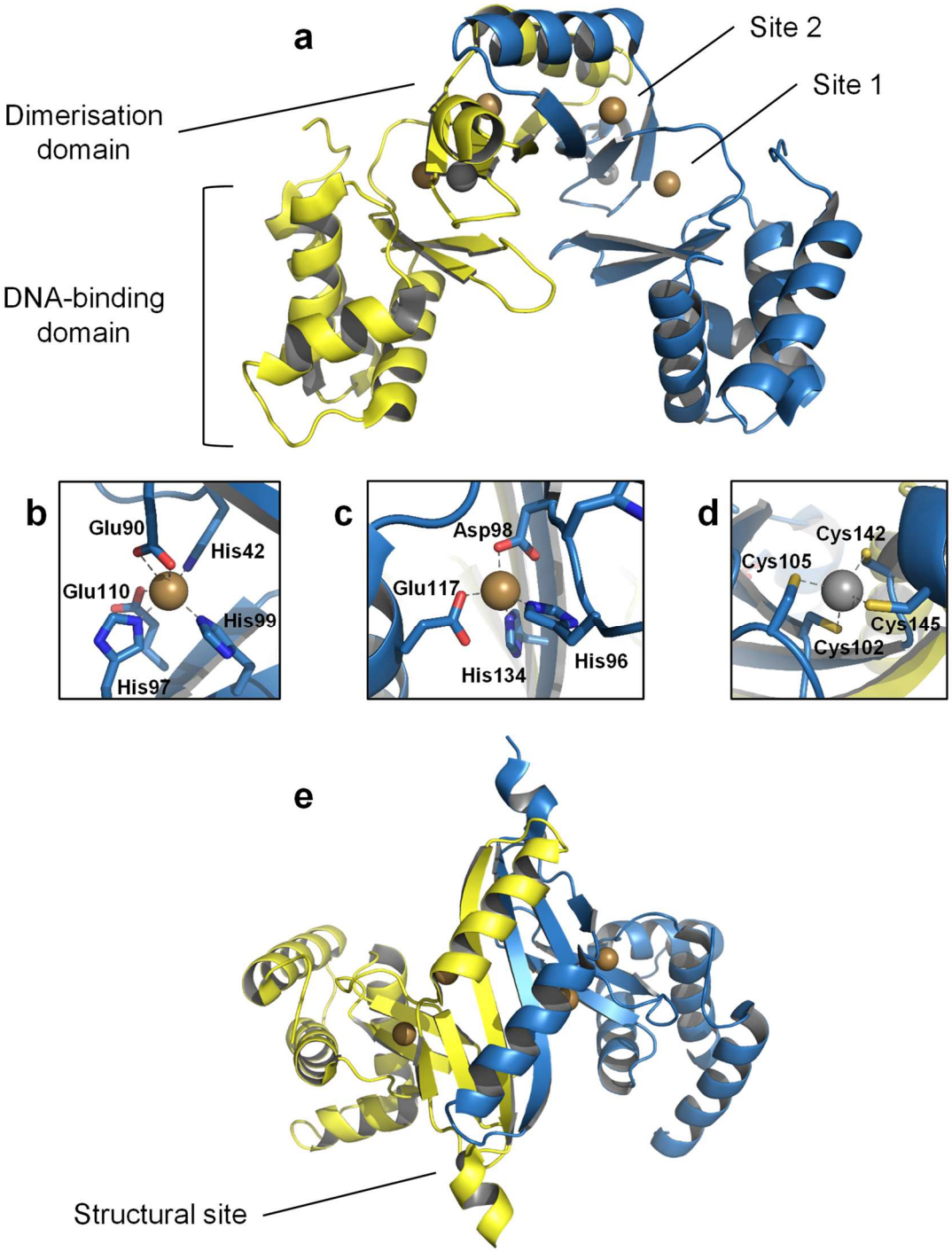

Figure 1.4 Structure of *H. pylori* Fur. (a) The Zn(II)-bound dimeric protein with the two-regulatory metal-sites (site 1 and site 2) and the structural site filled (PDB file: 2XIG). Each subunit is indicated by a different colour, the regulatory metal ions are indicated as bronze spheres and the structural metal ions are indicated as grey spheres. **(b)** Regulatory site 1 with the Zn(II) ion coordinated by His42, His97, His99, Glu90 (bidentate), and Glu110 in an octahedral geometry. Note: this site is tetrahedral on the other chain (His42, Glu90, His97, and His99). **(c)** Regulatory site 2 with the Zn(II) ion coordinated by His96, Asp98, Glu117, and His134 in a tetrahedral geometry. **(d)** The structural Zn(II)-site with the metal coordinated by Cys102, Cys105, Cys142, and Cys145 in a tetrahedral geometry. **(e)** Shows the structure in (a) from above, looking down on the dimerisation domains.

DNA-binding domain with a flexible loop to hinge the two domains together (see Figure 1.4a) (Pohl et al., 2003). The majority of holo-Fur structures are loaded with Zn(II) where it is indicated that each monomer subunit contains two exchangeable metal sites (each termed differently within the literature). The first site (site 1) is located at the interface of the DNA-binding domain and the dimerisation domain, incorporating conserved residues (His, Glu, and Asp generally) from both domains, and has been shown to bind metals in different geometries, though Mn(II) bound in the *Magnetospirillum gryphiswaldense* structure shows a hexa-coordinate geometry (Deng et al., 2015), similar to the recently determined Fe(II)-bound *Francisella tularensis* tetrameric structure (Pérard et al., 2018). The second site (site 2) is located almost entirely within the dimerisation domain (also consisting of His, Glu, and Asp residues generally), though does appear to be coordinated by one ligand form the DNA-binding domain in the *M. gryphiswaldense* structure with Mn(II) (Deng et al., 2015). Both sites incorporate residues from the hinge loop. Zn(II) has been found to bind site 1 and site 2 in both tetrahedral and distorted octahedral geometry (Pohl et al., 2003, Dian et al., 2011) and suggests neither site has a particular preference for non-cognate metal binding, though an octahedral geometry is expected for Fe(II) binding in both cases. The metal affinities of Fur have been determined for some divalent first row transition metals and shows that Zn(II) can bind the protein much tighter than Mn(II) and Fe(II) (Mills and Marletta, 2005).

Escherichia coli Fur has been reported to directly regulate over 90 genes (Hantke, 2001) and plays a role (directly or indirectly) in the expression of up to 190 genes (Abed et al., 2007). Initially considered to be just a co-repressor protein, Fur has been shown to co-activate gene expression (not always directly e.g. RyhB (Balbontín et al., 2016)), as well as repressing expression as apo-Fur (acting as a de-repressor protein) (Hall and Foster, 1996, Seo et al., 2014), where these binding events could be determined by the specific nucleotide sequence at each promoter (Delany et al., 2003). Unlike MntR, multiple divalent transition metals (including Mn(II), Fe(II), Co(II), Ni(II), and Zn(II)) have been shown to activate Fur for DNA-binding *in vitro* (de Lorenzo et al., 1987, Bagg and Neilands, 1987, Dian et al., 2011).

Crystal structures for holo-Fur follow the trend showing two DNA-binding domains per dimer with a similar fold but are asymmetrical where metal in site 1 stabilises the DNA-binding domains in a configuration that could interact with two consecutive major grooves of DNA (Pohl et al., 2003, Pecqueur et al., 2006, Ahmad et al., 2009, Dian et al., 2011). Interestingly, one apo-Fur structure shows that without metal the DNA-binding domain is orientated 180° compared to that in the holo-Fur structures, as well as noticeable changes in the loop region between the two domains, indicating that metal binding is associated with organising the DNA-binding domains and fixing the flexible loop to accommodate this

(Butcher et al., 2012). The structure for DNA-bound *M. gryphiswaldense* Mn(II)-Fur, shown in Figure 1.5, demonstrates that although the DNA-binding domains appear locked in an active DNA-binding conformation, when bound to DNA the distance between them is further reduced to better fit consecutive major grooves (Deng et al., 2015). As well as major groove contacts, Fur has also been shown to interact with minor grooves to improve detection of the specific sequence of nucleotides at a given site (Deng et al., 2015). Two Fur dimers were shown to be bound to the *fur-box* sequence (Figure 1.5b) and demonstrate cross-dimer protein-protein contacts (mostly in the major groove) which are likely the reason for reports of cooperative DNA-binding by this protein (Baichoo and Helmann, 2002, Lavrrar and McIntosh, 2003, Deng et al., 2015).

Mutational studies indicate that site 1 is required for DNA-binding of Fur and that site 2 improves DNA affinity but does not appear to be essential for binding (possibly playing a tuning role) (Deng et al., 2015). Mobility shift assays have estimated the DNA affinities for Fur bound to different divalent transition metals where Mn(II), Fe(II), and Co(II) suggested the tightest interaction at ~ 20 nM (though Ni(II)-Fur was not conducted) (Mills and Marletta, 2005).

The structure of Zur (the other Fur-family metallosensor in *Salmonella*) homologues have been solved by X-ray crystallography (Lucarelli et al., 2007, Shin et al., 2011, Gilston et al., 2014) which demonstrate the same overall structure as Fur, shown in Figure 1.6. The structures from *Mycobacterium tuberculosis* and *Streptomyces coelicolor* indicate there are three distinct zinc binding sites per Zur monomer; one at the interface (hinge region) of the DNA-binding domain and dimerisation domain, with the other two located in the dimerisation domain (Lucarelli et al., 2007, Shin et al., 2011), similar to the organisation of metal sites in Fur. Characterisation of the *E. coli* Zur protein (93% sequence identity with *Salmonella*) also indicated there are three metal-binding sites per monomer, however, the crystal structure of the protein in complex with DNA indicates the presence of only two sites (though there was disorder in the C-terminal domain of the protein which could have missed an additional ion bound) (Gilston et al., 2014). Zur has been shown to contain one structural zinc site per monomer (experimentally demonstrated for *Salmonella* Zur (Osman et al., 2015)) which appears to be coordinated by four cysteine residues (Cys93, Cys96, Cys143, and Cys146 for the *E. coli* protein, which are conserved in *Salmonella*) in a tetrahedral geometry within the dimerisation domain, required for stable dimer formation (see Figure 1.6e) (Lucarelli et al., 2007, Shin et al., 2011). Mutational analysis has demonstrated the zinc site in the hinge region (site 1) is very important for Zn(II)-induced promoter binding, whereas the final zinc site in the dimerisation domain (site 2) plays a less significant role

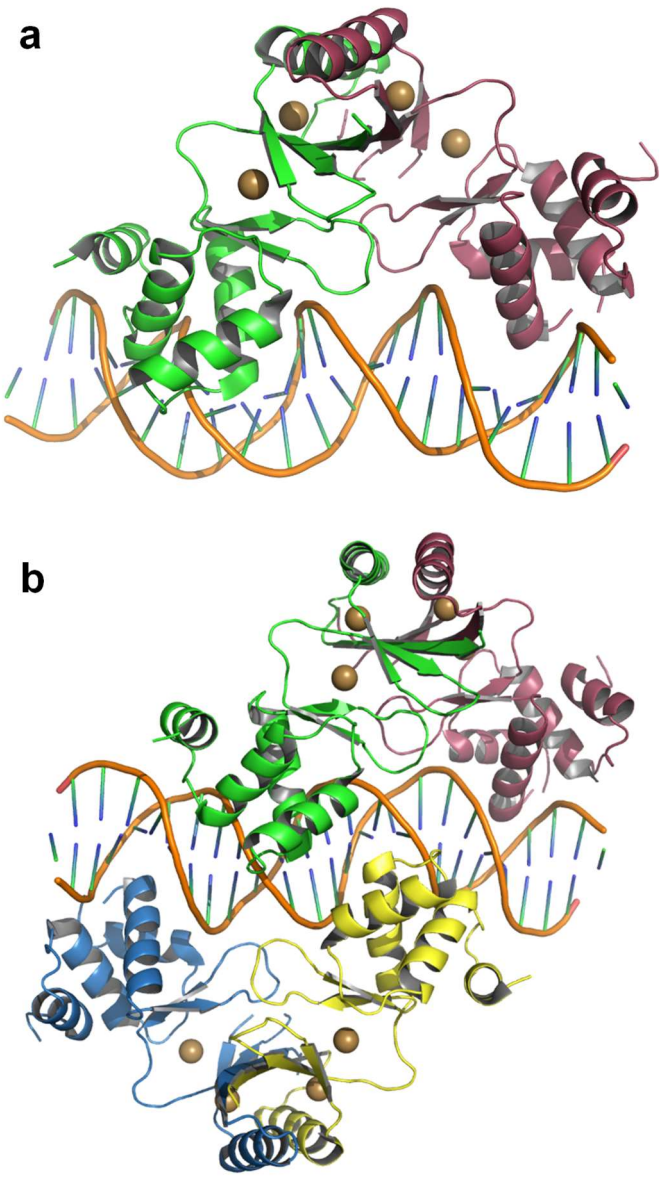

Figure 1.5 Structure of *M. gryphiswaldense* Fur bound to DNA. (a) The structure for one Mn(II)-bound Fur dimer bound to *P. aeruginosa fur-box* sequence. **(b)** Two Fur dimers bound to the same sequence of DNA as in (a) (PDB file: 4RB1). Individual subunits are indicated by different colours and Mn(II) ions are indicated as bronze spheres in the structure (note: *Mg*Fur does not contain a structural Zn(II)-site).

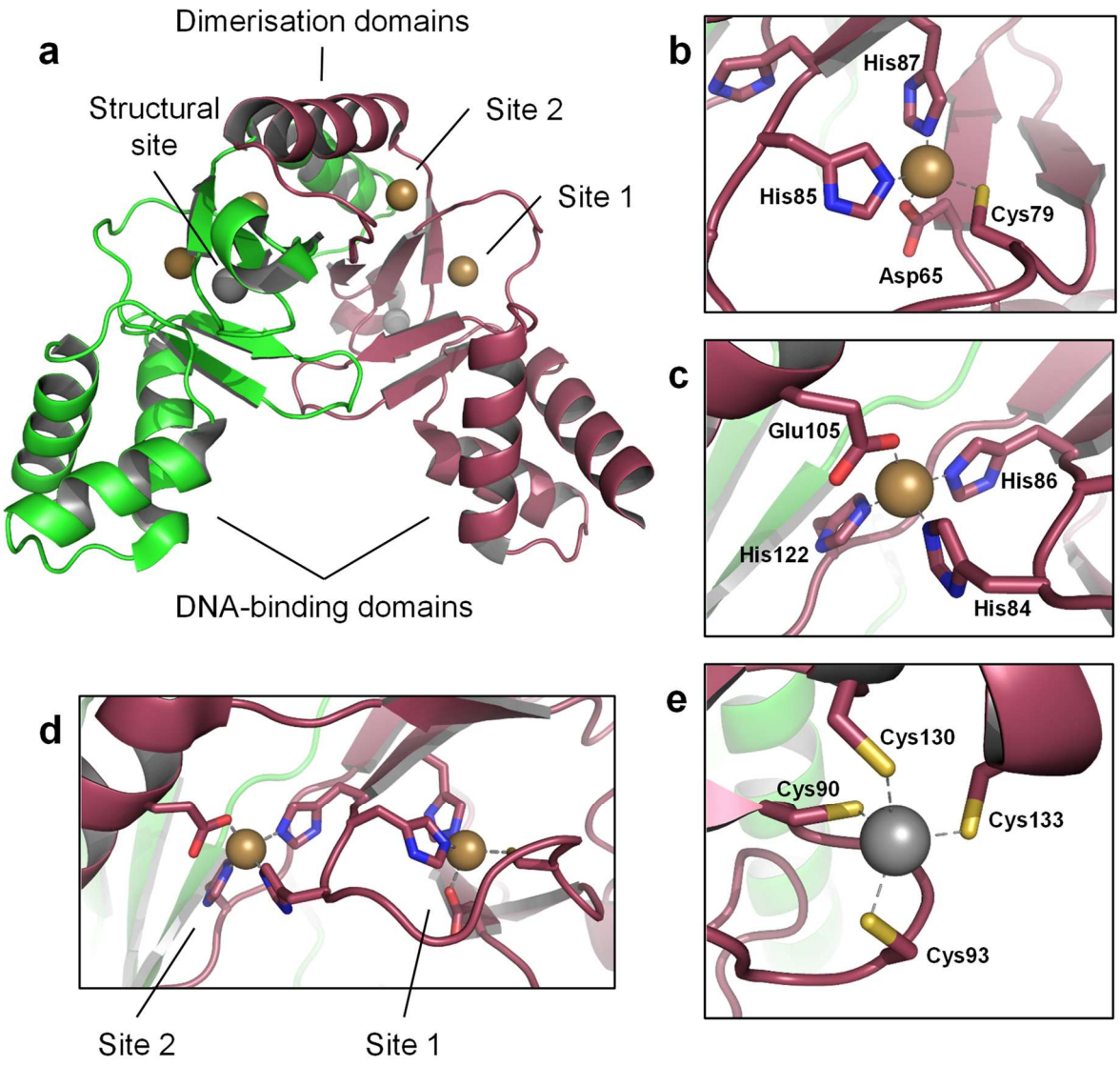

Figure 1.6 Structure of *S. coelicolor* Zur. (a) The Zn(II)-bound dimeric protein, including the two regulatory sites (site 1 and site 2) and the structural site, with each subunit indicated by a different colour (PDB file: 3MWM). Regulatory Zn(II) ions are indicated as bronze spheres and structural Zn(II) ions are indicated as grey spheres. **(b)** Regulatory site 1 with the Zn(II) coordinated by Asp65, Cys79, His85, and His87 in a tetrahedral geometry. **(c)** Regulatory site 2 with the Zn(II) coordinated by His84, His86, Glu105, and His122 in a tetrahedral geometry. **(d)** Both regulatory sites, indicating their positions relative to each other. **(e)** The structural site with the Zn(II) coordinated by Cys90, Cys93, Cys130, and Cys133 in a tetrahedral geometry.

though may be important for tuning the DNA-binding response (Shin et al., 2011), as with Fur. Regulatory site 1 contains Zn(II) coordinated in a tetrahedral geometry with two residues from the DNA-binding domain (Asp62 and Cys76) and two from the dimerisation domain (His81 and His83) in the *M. tuberculosis* structure (Lucarelli et al., 2007). The residues from the *E. coli* structure differ so that only one from the DNA-binding domain (His77) coordinates the zinc with three from the dimerisation domain (Cys88, His96, and Glu111), though the types of ligands are the same for both (Gilston et al., 2014). The second regulatory site (site 2) has been shown to recruit three histidine and one glutamate residues to coordinate a zinc ion in a tetrahedral geometry from the *M. tuberculosis* and *S. coelicolor* structures (see Figure 1.6c) (Lucarelli et al., 2007, Shin et al., 2011).

Crystal structures generally indicate site 1 stabilises a closed conformation of the protein so the two DNA-binding domains are fixed in a position where the winged helix-turn-helix motifs can interact with two consecutive major grooves (Gilston et al., 2014). Like Fur, Zn(II)-Zur has been shown to bind cooperatively to gene targets where two dimers are found on opposite sides of the DNA, explaining the unexpectedly large protected region of DNA for a protein of its size (Patzer and Hantke, 1998, Gilston et al., 2014). Each dimer makes contacts with both the major and minor grooves of DNA and the two central bases in the promoter sequence appear important for a tight Zur-DNA complex since they are distorted to increase the major groove width coupled with undertwisting of the DNA (Gilston et al., 2014). The cooperativity is driven by protein-protein contacts where two salt-bridges are formed between opposite dimers through a tyrosine and arginine residue (Tyr45 and Arg65 in *E. coli*) (Gilston et al., 2014).

1.3.8 RcnR structure and function

RcnR is a founding member of the CsoR/RcnR family of metalloregulators, along with the Cu(I)-responsive CsoR protein (Iwig et al., 2006, Liu et al., 2007). Other members of this family include the Ni(II)-responsive InrS protein (Foster et al., 2012) and the non-metal formaldehyde-sensor FrmR (Herring and Blattner, 2004, Osman et al., 2015). RcnR has been shown to control expression of the Co(II) and Ni(II) exporter, RcnA (Iwig et al., 2006) (Section 1.2.4), a periplasmic protein, RcnB (Blériot et al., 2011), as well as self-regulating its own expression (Iwig and Chivers, 2009). *Salmonella* RcnR has been studied previously, mostly focusing on the Co(II)-specific responses of this protein (Osman et al., 2015, Osman et al., 2016, Osman et al., 2017, Osman et al., 2018).

RcnR structure/function studies have focused largely on the *E. coli* protein. This protein is a de-repressor consisting of a novel four-helical bundle DNA-binding mechanism which has

two target sites, between the divergently transcribed *rcnAB* (note that *Salmonella* does not contain *rcnB*) and *rcnR* genes, that it can bind in the absence of its cognate metals (Iwig et al., 2006, Iwig and Chivers, 2009). While RcnR has been shown to bind a range of transition metals *in vitro* (Higgins et al., 2012), only Co(II) and Ni(II) elicit an allosteric response *in vivo*, allowing for gene synthesis (Iwig et al., 2008). A crystal structure of any form of RcnR has not been reported. But, from structures of other family members, such as CsoR (Liu et al., 2007, Sakamoto et al., 2010, Dwarakanath et al., 2012, Chang et al., 2014), several things can be inferred. The structure of *Streptomyces lividans* apo-CsoR shows the protein contains three α-helices (α1-α3) (Dwarakanath et al., 2012) though, in the *Geobacillus thermodenitrificans* Cu(I)-CsoR structure, four α-helices are described where α2 is split into α2a and α2b due to a kinked region in the helix, likely a result of altered conformation to accommodate metal-binding (Chang et al., 2014). The main structural unit of CsoR is formed by interaction of helices α1 and α2 from two monomeric subunits to form a dimer (Chang et al., 2014). The structure is further oligomerised into a tetramer (dimer of dimers), as previously suggested for RcnR (Iwig et al., 2008), where α3 helices mediate contacts between the dimers (Chang et al., 2014). The structure of *G. thermodenitrificans* CsoR is shown in Figure 1.7.

The metal-binding region of CsoR is shown to involve residues from two monomer subunits (within the α2 and α2′ helices) and is located at the periphery of the structure (Liu et al., 2007, Chang et al., 2014). XAS studies have determined the best fits for transition metal binding to RcnR and suggests both Co(II) and Ni(II) bind to RcnR with octahedral geometry (Iwig et al., 2008), which differs to the square planar Ni(II) sites in both NikR (Section 1.3.9) and InrS (Foster et al., 2012). The metal binding site of RcnR would appear to be at the interface of two monomeric subunits, as seen with CsoR (see Figure 1.7) (Liu et al., 2007), however, determining the absolute metal-binding ligands for Ni(II)-RcnR has proved troublesome. Recent studies have suggested a model including the N-terminal amine (Ser2 is the N-terminal residue in *E. coli* and *Salmonella* after cleavage of Met1 (Iwig et al., 2008)), Glu63, and His64 from one monomer and Cys35 from another as coordinating ligands and in order to generate a hexa-coordinate geometry, recruits Glu63 as a bidentate ligand and a carbonyl oxygen from the N-terminal serine residue (from the *E. coli* protein) (Iwig et al., 2008, Higgins et al., 2012, Carr et al., 2017, Huang et al., 2018). Recruiting the N-terminus of RcnR appears important for metal-binding specificity since it is required in the Co(II)- and Ni(II)-bound forms of the protein (Carr et al., 2017). RcnR was shown to coordinate non-cognate Zn(II) with either four or five ligands that did not include the N-terminus and required solvent molecules to make up the proposed geometries (Carr et al., 2017), where

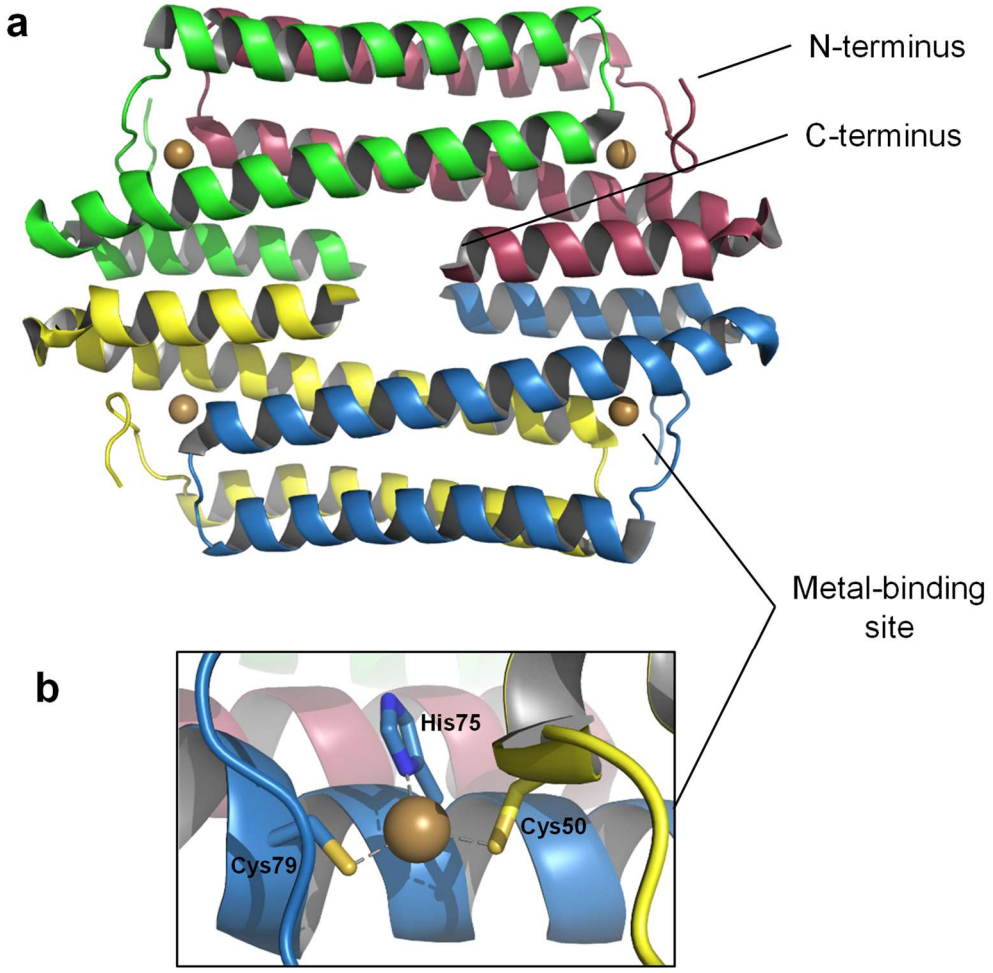

Figure 1.7 Structure of *G. thermodenitrificans* CsoR. (a) The copper-bound tetramer of CsoR with each subunit indicated by a different colour and metal ions indicated by bronze spheres (PDB file: 4M1P). **(b)** The trigonal Cu(I)-binding site, coordinated by Cys50′, His75 and Cys79 from two subunits.

this alternative ligand recruitment (and geometry) likely results in a structure that does not confer the appropriate conformational changes to drive allostery (see Section 1.3.2).

E. coli RcnR has been shown to bind to a TACT-G_6-N-AGTA promoter sequence possibly through minor groove contacts (Iwig and Chivers, 2009). The G-tract appears to stabilise A-form DNA which is important for high affinity binding by RcnR (Iwig and Chivers, 2009). Additionally, it was demonstrated that RcnR can wrap DNA which increases its DNA affinity ~ 4-fold when using a > 150 base pair oligonucleotide compared to < 80 base pairs sequence (Iwig and Chivers, 2009). The contacts between RcnR and DNA to achieve wrapping appear to be non-specific, unlike the TACT-G_6-N-AGTA promoter sequence (Iwig and Chivers, 2009).

No structure has been determined for CsoR/RcnR family proteins bound to DNA to suggest a mechanism for DNA-binding. Both the α1 and α2 helices of RcnR contain many positively charged residues (e.g. arginine and lysine) with some highly conserved across the family (Huang et al., 2018). Mutation to these residues, including Arg14 and Lys17 from *E. coli* RcnR, demonstrates apo-protein DNA affinity is significantly weaker *in vivo* compared to wild-type RcnR (Huang et al., 2018). Equally, an arginine residue (Arg65) which fills the "hole" in the donut-shaped *G. thermodenitrificans* CsoR protein has been shown to decrease the DNA-affinity for the apo-protein, as well as other charged residues which could form salt-bridges to stabilise the DNA-bound conformation (Chang et al., 2014). It appears clear that metal-binding must disrupt these residues from interacting with the duplex in order to weaken the DNA-affinity of CsoR/RcnR and these conformational changes could be driven by the kinking of the α2 helix demonstrated in the Cu(I)-CsoR structure (Chang et al., 2014). The crystal structure of *E. coli* FrmR shows the tetramer with one face signal-free and the other face signal-triggered, highlighting key conformational differences within the same protein (Denby et al., 2016). It demonstrates formation of a hydrogen-bond network in response to signal-binding transmits conformational twisting of helices such that the patches of positively charged residues implicated in DNA-binding are moved further apart (~ 10 Å), where models predict convincing DNA interactions would be lost in this conformation (Denby et al., 2016). Interestingly, studies with both CsoR and RcnR have indicated that the apo-protein is more dynamic compared to metal-bound protein which incurs a greater level of structural rigidity (Chang et al., 2014, Huang et al., 2018).

1.3.9 NikR structure and function

NikR, which is the only known member of this protein family, was discovered in *E. coli* and regulates nickel import commonly during anaerobic growth when nickel is required for

hydrogenase but also under conditions which require urease in other bacteria (Section 1.4.1) (De Pina et al., 1999, Chivers and Sauer, 1999). Ni(II) is imported into the cell via NikABCDE (Section 1.2.1) where *nikABCDE* expression is activated by FNR (Wu et al., 1989, de Pina et al., 1995), a global regulator of oxygen utilisation (Kiley and Beinert, 1998), and repressed by NikR (Chivers and Sauer, 1999, Chivers and Sauer, 2000). NikR also controls the expression of NixA (Contreras et al., 2003), which is important for providing nickel during urease maturation in *H. pylori* (Bauerfeind et al., 1996). *Salmonella* NikR was discovered by homology to *E. coli* NikR and has been characterised for Ni(II)-binding stoichiometry, Ni(II)-affinity, and DNA-affinity for *nixA*, as well as *in vivo* DNA studies for both *nikA* and *nixA* (Osman et al., 2018).

NikR has been intensively studied experimentally, structurally, and computationally. This protein is a co-repressor which has a tight affinity for DNA when bound to Ni(II) (Chivers and Sauer, 2000). The protein forms stable tetramers in solution (Chivers and Sauer, 2002) where each monomeric subunit contains two domains; an N-terminal DNA-binding domain and a C-terminal metal-binding domain, connected by a flexible linker, shown in Figure 1.8 (Chivers and Sauer, 1999, Schreiter et al., 2003). The DNA-binding domain contains a ribbon-helix-helix motif which interacts with DNA, unique to metalloregulatory proteins (Chivers and Sauer, 1999). A dimer is required to generate a ribbon-helix-helix motif and two dimers combine to form the tetramer (dimer of dimers), stabilised by contacts between the metal-binding domains (Schreiter et al., 2003). Each metal-binding domain contains a ferredoxin-like fold (βαββαβ), structurally homologous to ACT-like domains (Grant, 2006), and the tetramer is stabilised by an eight-stranded antiparallel β-sandwich structure (Schreiter et al., 2003). Ni(II) binds to *E. coli* NikR with high affinity (high femtomolar to low picomolar range (Chivers and Sauer, 2002, Wang et al., 2004)) in a metal site at the interface of the two dimer C-terminal domains (Schreiter et al., 2003). This site is made of His87, His89, and Cys95 from the β3- and β4-strands of one subunit and His76′ from helix α3 of the other, which coordinate Ni(II) in a four-coordinate square planar geometry (Figure 1.8c) (Schreiter et al., 2003). The two C-terminal domains required to form the high-affinity Ni(II) site are not from the two subunits which dimerise to create the ribbon-helix-helix domain, but instead from subunits across the dimer-dimer interface. An interesting hydrogen-bond network has been identified between the two subunits that make up one pair of Ni(II) sites which could allow cross-talk with Ni(II)-binding, or stabilise the structure for DNA-binding (Schreiter et al., 2003). Metal-binding increases the stability of the α3 helix in the crystal structure (compared to apo-NikR) which could be important for DNA-binding (Schreiter et al., 2003). Each monomer has one high-affinity Ni(II)-binding site (four per

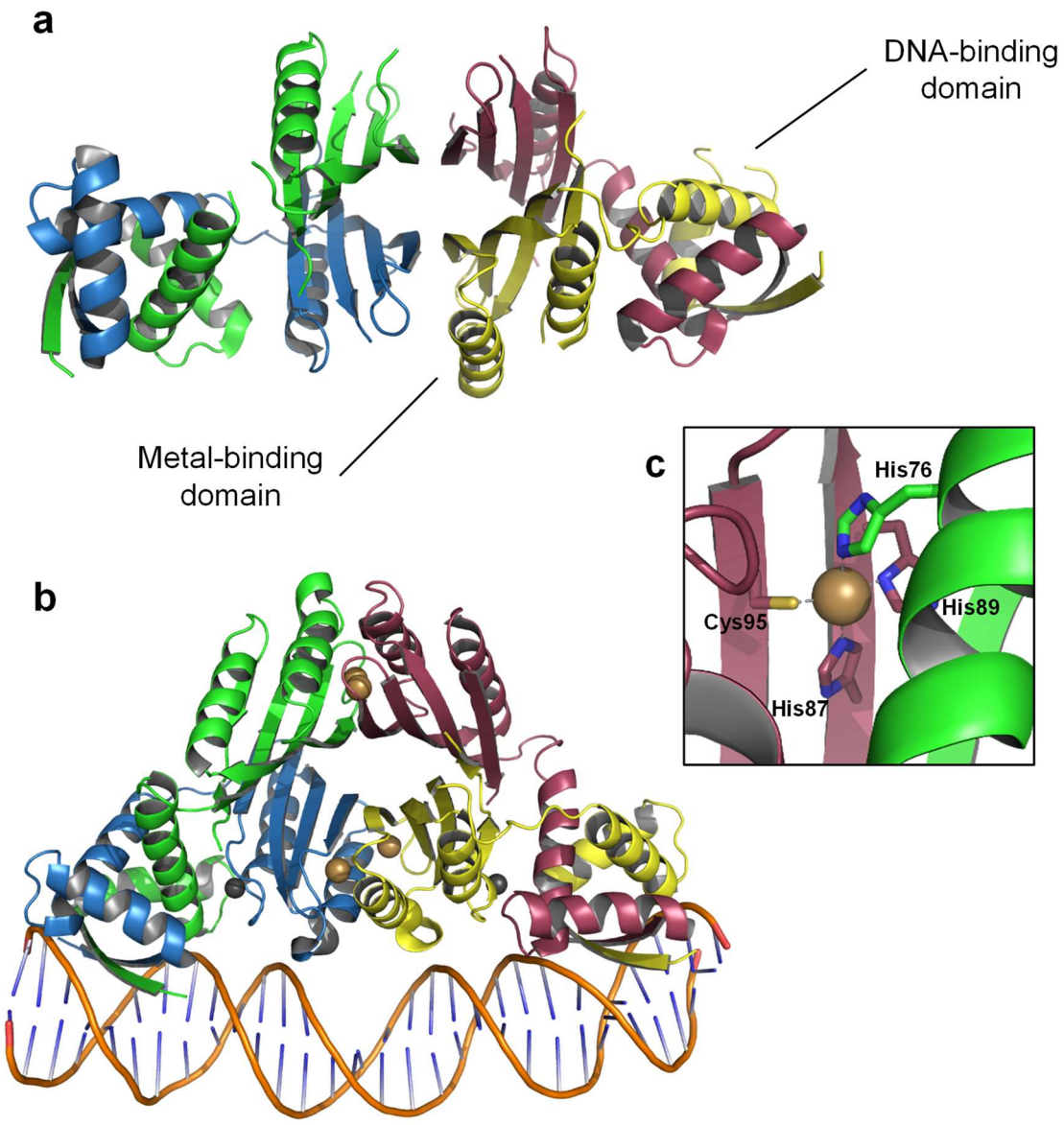

Figure 1.8 Structure of *E. coli* NikR. (a) The apo-NikR tetramer with each subunit indicated by a different colour (PDB file: 1Q5V). **(b)** Holo-NikR bound to the *nik* promoter with Ni(II) ions indicated as bronze spheres and K(I) ions indicated as black spheres (PDB file: 2HZV). **(c)** The square-planar high-affinity Ni(II)-binding site from the C-terminal metal-binding domain of NikR, indicating the coordinating ligands His76′, His87, His89, and Cys95.

tetramer) where the protein requires the metal to generate a measurable DNA-affinity, calculated to be in the low nanomolar range (Bloom and Zamble, 2004). Ni(II)-binding to the high-affinity site has been shown to increase the stability of the protein against chemical and thermal denaturation (Chivers and Sauer, 2002, Wang et al., 2004), as well as proteolytic cleavage (Dias and Zamble, 2005).

The presence of a second, low-affinity Ni(II) site has been proposed since addition of excess Ni(II) increases the affinity of NikR for its promoter to 15-20 pM (Chivers and Sauer, 2000, Bloom and Zamble, 2004). The Ni(II)-affinity of this site has been estimated as ~ 30 nM (Bloom and Zamble, 2004) and its purpose could be to completely shut down expression of NikR target genes when Ni(II) concentrations become too high. Due to precipitation issues with loading NikR in excess of 1:1 Ni(II) ions per monomer, the exact location and coordination environment of the low-affinity site has not been fully determined. Studies show that the Ni(II) is likely coordinated in an octahedral geometry with two histidine and four N/O ligands (Leitch et al., 2007), with one study suggesting the histidine residues could be His48 and His110 (Wang et al., 2010a). The physiological relevance of this site has been evaluated in this study (Chapter 5).

NikR has been shown to bind other transition metals *in vitro*, including Co(II), Zn(II), Cu(II), and Cd(II) (Bloom and Zamble, 2004, Wang et al., 2004), however, only Ni(II) has been shown to induce regulation of gene synthesis *in vivo* (Leitch et al., 2007). Co(II) and Zn(II) have been shown to bind NikR in different geometries with different ligands and neither results in the same stabilised structure as Ni(II)-NikR against denaturation, or shows the same α-helical content, indicating the α3 helix remains distorted and not stabilised (Wang et al., 2004, Leitch et al., 2007, Phillips et al., 2008). Cu(II) though does increase stability of the protein, almost to the same extent as Ni(II), and structures show that Cu(II) binds in the same site, with the same ligands, in the same geometry as Ni(II) (Phillips et al., 2008). Crucially, Cu(II) concentrations in the cell are expected to be non-existent due to the reduced environment such that Cu(I) is expected to be the primary form of this metal intracellularly (Davis and O'Halloran, 2008). Cu(I) typically binds sensors with lower coordination numbers and therefore is unlikely to form a square planar geometry (Changela et al., 2003, Liu et al., 2007, Rubino and Franz, 2012, Chang et al., 2014). Indeed, XAS data suggests Cu(I) binds to NikR with tri-coordinate geometry (Leitch et al., 2007).

NikR represses transcription of *nikABCDE* by binding to the 28 base pair palindromic operator sequence that is 5′-GTATGA-N_{16}-TCATAC-3′ (Chivers and Sauer, 2000, Schreiter et al., 2006). The two half sites are separated by 16 base pairs which means that the two ribbon-helix-helix domains per tetramer can interact with the major groove of DNA two

turns apart (Chivers and Sauer, 2000, Schreiter et al., 2006). The exact mechanism by which metal induces binding to DNA has not been fully elucidated. The structure of DNA-bound holo-NikR has been resolved which identifies three types of interactions for stabilisation on DNA; specific contacts between the ribbon-helix-helix domain and the major groove, non-specific contacts between the DNA-binding domain and the phosphate backbone, and non-specific contacts between the metal-binding domain and the phosphate backbone (Figure 1.8b) (Schreiter et al., 2006). The DNA-binding domains are oriented in a cis-conformation (both pointing down to the DNA) which requires unwinding of helix α2 in order to maintain this structure (Schreiter et al., 2006). Additionally, there is a potassium binding site at the interface of the DNA-binding domain and the metal-binding domain which recruits Glu30 and Asp34 (conserved residues) along with carbonyl backbone oxygens that could lock the structure in the DNA-bound conformation (Schreiter et al., 2006). Mutations demonstrate this K-site is required for DNA-binding by NikR (Wang et al., 2010b). Both apo- and holo-NikR structures in the absence of DNA do not represent the DNA-binding domains in the cis-arrangement required for DNA-binding which suggests metal-binding does not pre-organise a high-affinity DNA conformation (Schreiter et al., 2003). Mutating two of the residues involved in non-specific contacts with DNA from the metal-binding domain (Lys64 and Arg65) significantly reduces the ability of Ni(II)-NikR to bind to its operator site (Krecisz et al., 2012) demonstrating the importance of these non-specific contacts. Therefore, the proposed mechanism for DNA binding is that non-specific contacts between the metal-binding domain and DNA allow the protein to localise itself to the duplex where it can travel one-dimensionally occasionally dropping its DNA-binding domains (as suggested through molecular dynamics simulations (Bradley et al., 2008, Cui and Merz, 2008)) to sample the specific sequence of nucleotides and once this interaction occurs at the correct operator, the movement is retarded allowing the second DNA-binding domain to contact the alternative half-site where both can be stabilised with potassium ions (Phillips et al., 2008, Wang et al., 2010b).

The NikR proteins from *Salmonella* and *E. coli* (K-12) differ by only two amino acids (99% identity) near the linker region between the two domains: Ser38 in *E. coli* which is Gly38 in *Salmonella* and Gln47 in *E. coli* which is Glu47 in *Salmonella*. In *Salmonella*, the operator site for *nixA* contains a similar palindromic sequence to *nikA* except for one nucleotide difference in one of the half sites for NikR binding (5′-GTGTGA-N_{16}-TCATAC-3′) (Osman et al., 2018).

1.3.10 CueR and ZntR structure and function

CueR and ZntR are members of the MerR family of regulators which function as activators of gene expression (Brocklehurst et al., 1999, Outten et al., 2000). *E. coli* CueR controls the expression of genes associated with copper homeostasis, including *copA* (part of an efflux system) and *cueO* (an oxidase which catalyses the conversion of Cu(I) to the less toxic Cu(II)) (Outten et al., 2000, Outten et al., 2001). ZntR, which is a Zn(II)-sensing regulator, also controls the expression of an efflux protein (ZntA) (Xiong and Jayaswal, 1998, Brocklehurst et al., 1999). The founding member of this family, MerR, was discovered due to its ability to confer resistance to mercury in bacteria (O'Halloran and Walsh, 1987). Other members of this family include GolS (Checa et al., 2007), NimR (Kidd et al., 2011), and CadR (Lee et al., 2001). Both *Salmonella* CueR and ZntR have been studied *in vivo* and *in vitro* (Osman et al., 2010, Osman et al., 2015, Osman et al., 2017, Osman et al., 2018).

CueR exists as a dimer where each monomer contains an N-terminal DNA-binding domain, a dimerisation domain, and a C-terminal metal-binding domain, shown in Figure 1.9 (Changela et al., 2003). Cu(I), Ag(I), and Au(I) can all bind to CueR and are coordinated linearly between two conserved cysteine residues – one located at the C-terminal end of the dimerisation helix and the second at the N-terminal end of a short helix found at the C-terminus of each monomer (Changela et al., 2003). A short loop region connects the two helices containing the metal-binding cysteine residues which appears to be ordered with metal bound (Changela et al., 2003). Two Cu(I) ions can bind to one dimer of CueR and this metal-bound form of the protein activates transcription (Philips et al., 2015).

Gene expression of *copA* and *cueO* is activated *in vivo* and *in vitro* by CueR bound to Cu(I), Ag(I), and Au(I), but not by the divalent ions Zn(II) and Hg(II) (Outten et al., 2000, Changela et al., 2003). CueR is bound to DNA in the apo-form which represses gene expression (Philips et al., 2015). Specific conformational changes associated with the activating metal ions allow RNA polymerase to bind to the promoter and express the genes (Philips et al., 2015). Apo-CueR sits on DNA with the N-terminal domains interacting with the major grooves and causes minor distortion of the duplex (Philips et al., 2015). The conformational changes associated with activated CueR arise from stabilisation of the metal-binding loop which alter the positions of residues in the hinge between the DNA-binding domain and the dimerisation helix which further transfers through a hydrogen-bond network (Philips et al., 2015). The C-terminal helix is also stabilised further in a hydrophobic cavity which all leads to a decrease in the distance between the dimerisation helices (i.e. the two N-terminal DNA-binding domains move closer) in a “scissor” movement (Philips et al., 2015). The rigid DNA-binding domains’ movements force additional kinking and undertwisting of the DNA

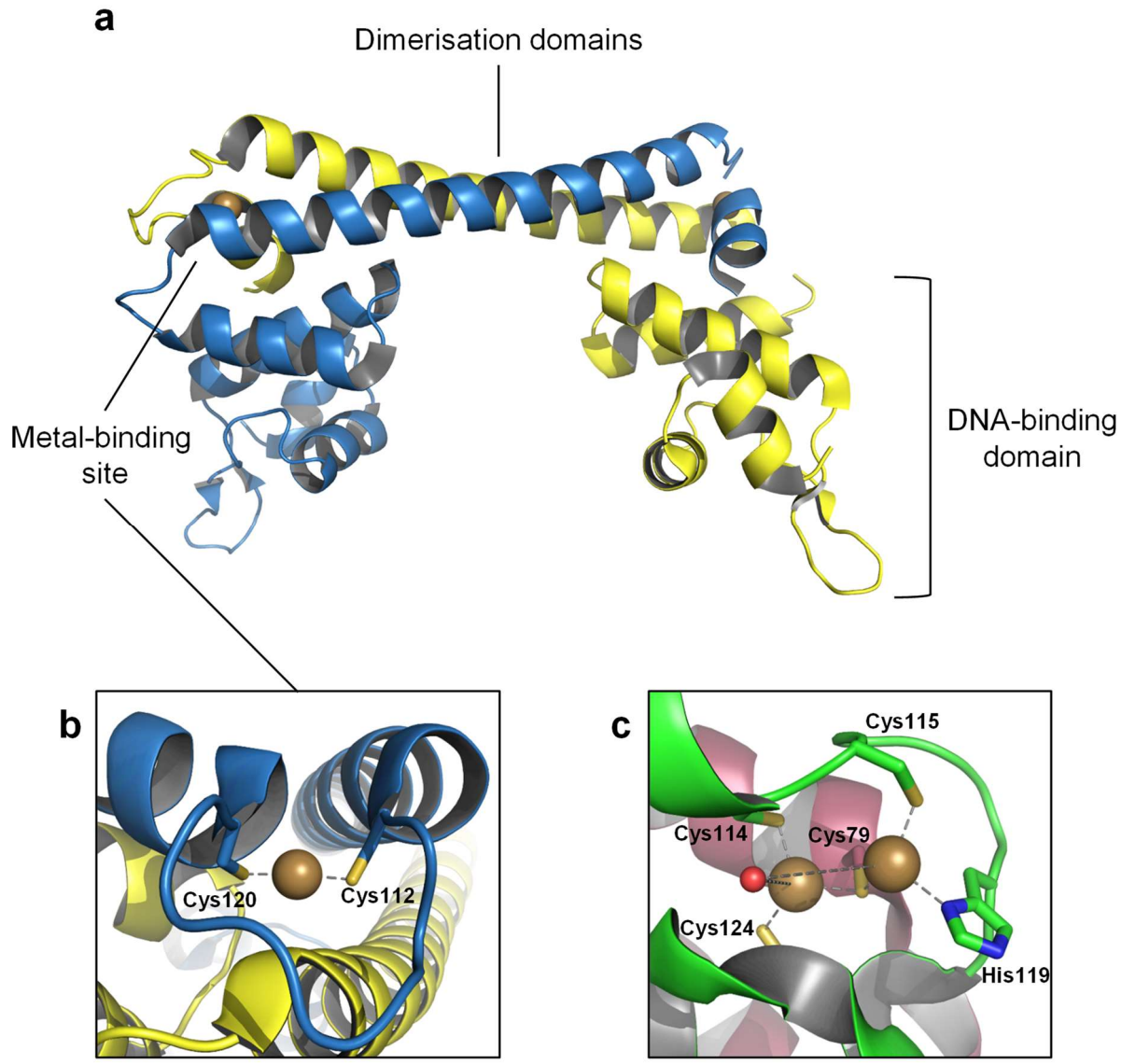

Figure 1.9 Structure of *E. coli* CueR and ZntR. (a) Cu(I)-bound dimeric CueR with each subunit indicated by a different colour and metal ions indicated as bronze spheres (PDB file: 1Q05). **(b)** The Cu(I)-binding site of CueR with the metal ion coordinated in a linear geometry by Cys112 and Cys120. **(c)** The Zn(II)-binding site of ZntR which is filled as a dinuclear site with Zn(II) ions and indicates the metal binding ligands Cys79′, Cys114, Cys115, His119, and Cys124 as well as a sulphate or phosphate group (red sphere) coordinating both metals in tetrahedral geometries (PDB file: 1Q09).

(Philips et al., 2015). The -10 and -35 promoter elements, which are unusually spaced in MerR regulator promoters (O'Halloran et al., 1989), are brought together in the correct phase to allow for effective RNA polymerase association, shown in Figure 1.10 (Philips et al., 2015).

Structurally, ZntR is the same as CueR, however, the residues in the metal-binding domain differ so that the protein can accommodate a divalent metal ion which prefers a higher coordination number (Changela et al., 2003). Interestingly, each metal-binding domain has been crystalised containing two Zn(II) ions (i.e. a dinuclear site; Figure 1.9c) (Changela et al., 2003), however, this is not consistent with all *in vitro* data (can favour a stoichiometry of one metal per monomer) (Osman et al., 2015). The two Zn(II) ions are coordinated in a tetrahedral geometry by cysteine and histidine residues (Changela et al., 2003), consistent with mutational studies (Khan et al., 2002). One of the coordinating cysteine residues (Cys79) is located at the N-terminus of the dimerisation helix from the opposite monomer (this is a non-coordinating serine residue (Ser77) in CueR which is believed to help in the selectivity of the metal-binding site for monovalent ions) (Changela et al., 2003, Ibáñez et al., 2015). Zn(II)-ZntR activates gene expression in the same mechanism as described for CueR. *In vivo* data suggests ZntR cannot be activated by other metals such as Co, Ni, or Cu (Brocklehurst et al., 1999).

ZntR and Zur (Section 1.3.7) regulate the intracellular buffered zinc concentration where *in vitro* studies show Zur responds to lower cellular concentrations of zinc, resulting in decreased import of Zn(II) (among other responses), before ZntR can be activated to increase efflux of the ion, suggesting these proteins work in series to control intracellular zinc (Outten and O'Halloran, 2001).

1.4 Nickel and its role in bacteria

1.4.1 Nickel is required for the function of multiple proteins and enzymes

Nickel homeostasis by bacteria provides a good model system due to being generally well-studied, simple, and it represents a tight binding Irving-Williams series metal (Section 1.1.1). Additionally, nickel-bound proteins can produce spectroscopic features which enable monitoring of these species during *in vitro* experiments. A simplified model for nickel requirement and regulation has been shown in Figure 1.1.

Nickel is found naturally in the environment at concentrations ranging from nanomolar to low micromolar (Macomber and Hausinger, 2011). It is essential for growth of

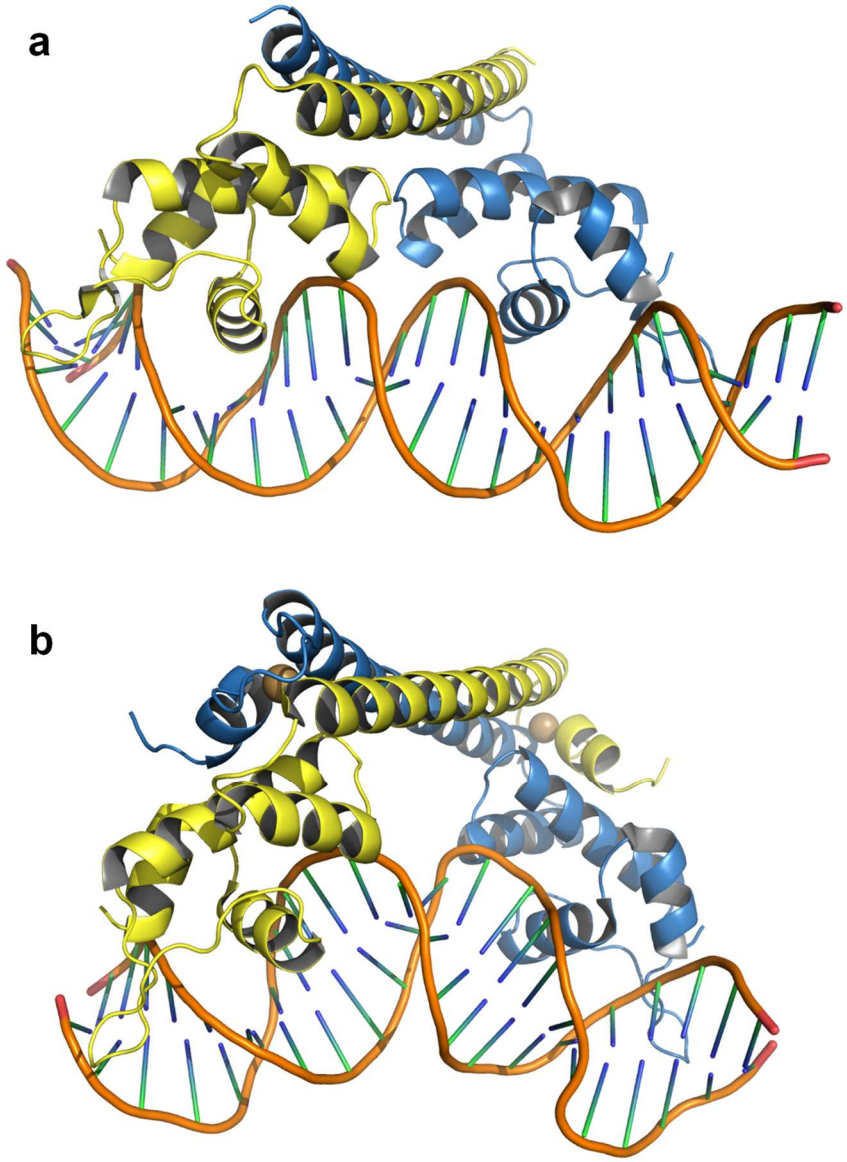

Figure 1.10 Structure of *E. coli* CueR bound to DNA. (a) The dimeric apo-protein bound to *copA* promoter where the metal-binding domains were unstructured in the crystal (PDB file: 4WLS). **(b)** The Ag(I)-bound protein on the same DNA sequence where the metal ions are indicated as bronze spheres (PDB file: 4WLW).

microorganisms such that, like other essential transition metals, it is concentrated within the cell (Finney and O'Halloran, 2003). Nickel import in bacteria is largely down to the ABC-type transporter NikABCDE and NiCoT family member NixA (Section 1.2.1). This metal is required at the centre of enzymes including [NiFe]-hydrogenase, urease, Ni-SOD, and glyoxalase (Glx), among others (Mulrooney and Hausinger, 2003, Boer et al., 2014). Excess nickel can be exported by the Ni(II)- (and Co(II)-) specific exporter protein RcnA (Section 1.2.4).

Hydrogenases, which catalyse the reversible oxidation of hydrogen, are required during anaerobic respiration in order to minimise the build-up of reduced species by reducing protons to hydrogen molecules, as well as serving other roles in a cell (Vignais et al., 2001, Mulrooney and Hausinger, 2003). Both nickel and iron are required at the centre of the [NiFe]-hydrogenase enzyme where insertion of the nickel is assisted by a selection of metallochaperone proteins, including HypA, HypB, and SlyD, among others, in *E. coli* (Blokesch and Böck, 2002, Reissmann et al., 2003, Zhang et al., 2005, Leach et al., 2007, Chung and Zamble, 2011, Douglas et al., 2013).

Urease catalyses the hydrolysis of urea to ammonia and carbamate which is an essential mechanism for survival of bacteria which colonise the stomach, such as *Helicobacter pylori* since the ammonia is able to neutralise the acidic environment surrounding this bacterium (Mobley et al., 1995b). In other environments the ammonia can be used as a nitrogen source for the growth of bacteria. Urease, which is composed of multiple subunits that generally organise into trimers in bacteria, contains a dinuclear nickel active site (Jabri et al., 1995, Benini et al., 1999, Ha et al., 2001). Again, a complement of metallochaperones are required to form the metallocenter in urease, including UreD, UreE, UreF, and UreG (Lee et al., 1993, Soriano and Hausinger, 1999).

SODs are essential for aerobic cellular survival, as described in Section 1.1.2. Ni-SOD is shown to be a hexameric protein (Wuerges et al., 2002) which binds one nickel per subunit (Youn et al., 1996, Choudhury et al., 1999), however, the mechanism of loading the enzyme with nickel remains unknown.

The two-component glyoxalase system (which consists of Glx I and Glx II) is necessary to protect the cell from methylglyoxal which can react with DNA or proteins forming adducts (Phillips and Thornalley, 1993, Inoue and Kimura, 1995, Thornalley, 1998). *E. coli* Glx I is a nickel containing enzyme and catalyses the isomerisation of hemithiolacetal (the product of methylglyoxal and glutathione) where the product (*S*-D-lactoylglutathione) becomes the substrate for Glx II which hydrolyses it to lactate and reforms glutathione (Thornalley, 1998,

Clugston et al., 1998, Mulrooney and Hausinger, 2003). Homodimeric Glx I contains two nickel active sites at the dimer interface (He et al., 2000), though, as with Ni-SOD, the nickel insertion mechanism is unknown.

1.4.2 Nickel toxicity in bacteria

All transition metal ions are toxic in a cell through processes such as the displacement of cognate metals within metalloproteins or allosterically inhibiting enzymes (discussed in Section 1.1.1), as well as through generating ROS which can damage DNA, proteins, and lipids (Meneghini, 1997, Valko et al., 2005). This is true for nickel which can inhibit iron- and α-ketoglutarate-dependent dioxygenases (such as TauD) likely by replacing the iron in the active site (Kalliri et al., 2005), as well as inhibiting non-metal-containing enzymes (e.g. *N*-carbamoyl D-amino acid amidohydrolase) possibly through binding to catalytic residues (Cys/Glu/Lys) (Louwrier and Knowles, 1996, Nakai et al., 2000, Wang et al., 2001).

E. coli fructose-1,6-bisphosphate aldolase A (FbaA), a Zn-dependent enzyme, is essential for growth on glucose (Böck and Neidhardt, 1966). FbaA contains two zinc-binding sites; one responsible for stabilising the catalytic intermediate species and a second, at a structurally distinct site, that has no established function (Hall et al., 1999). *E. coli* growth on glucose is inhibited in the presence of excess nickel which correlates with nickel binding to the second zinc site of FbaA and allosterically inactivating the enzyme and consequently glycolysis (Macomber et al., 2011).

While copper and iron are most commonly associated with ROS generation (Valko et al., 2005), exposure to high concentrations of nickel has been shown to induce ROS and mechanisms which protect the cell from ROS both *in vitro* (Kasprzak and Hernandez, 1989, Kawanishi et al., 1989, Lloyd and Phillips, 1999) and *in vivo* (Healy et al., 1955, Randhawa et al., 2001, Van Nostrand et al., 2008), although bacterial cells appear more resilient to nickel-induced damage than mammalian cells (Kasprzak et al., 2003).

1.5 Aims of the project

The metal-specificity of a transcriptional response *in vivo* has been attributed to the metallosensor which achieves the best affinity, allostery, or access for the particular metal ion in question (although effective allosteric changes by a sensor in response to the given metal are essential in all cases) (Foster et al., 2014a). Most *in vivo* data collected to investigate this has been conducted in studies which progress for several hours. Over this time scale, it is possible the cell can adapt its intracellular environment as well as begin homeostatic procedures to control the internal metal concentrations such that the polydisperse buffer is able to restrict the access by non-cognate sensors for the wrong metal. The recent research investigating the effect of short-term "metal shock" on metalloregulators (Section 1.3.4) suggests mal-responses are a physiological consequence and therefore have the potential to increase the toxicity associated with a single metal pressure. The mal-responsive effects have not been determined for a full set of cellular metalloregulators in response to a single metal ion, and therefore the aims of this study were as follows:

1. Characterise the full set of metalloregulators from *Salmonella* for Ni(II)-binding and determine the Ni(II)-specific thermodynamic properties of each, including Ni(II)-affinities and DNA-affinities.

2. Use the Ni(II)-specific thermodynamic values for the *Salmonella* sensors to model DNA occupancy (and therefore infer the effect on transcription) in response to Ni(II) to predict the mal-responsive cellular consequences.

3. Investigate the contribution of a small molecule component of the polydisperse buffer (specifically L-histidine) to ensure the correct metalation and response by sensors with their cognate metals.

Chapter 2: Materials and Methods

2.1 Strains, media, and plasmids

2.1.1 Bacterial strains and plasmids

Genes encoding *Salmonella enterica* serovar Typhimurium SL1344 metal sensor proteins (*mntR*, *fur*, *rcnR*, *nikR*, *cueR*, *zntR*, and *zur*) were cloned into pET-29a (*kan*^{r}) for protein overexpression (a generous gift from Dr. Deenah Morton, Durham University) (Osman et al., 2013, Osman et al., 2015, Osman et al., 2017, Osman et al., 2018).

E. coli BL21 (DE3) (genotype: F^- *ompT hsdS* (r_B^- m_B^-) *dcm gal* λ(DE3)) was used for overexpression of recombinant proteins (Studier and Moffatt, 1986).

2.1.2 Bacterial growth media

Cells were cultured on either solid or liquid Luria-Bertani (LB) medium (10 g tryptone, 5 g yeast extract, and 5 g sodium chloride L^{-1}) (Bertani, 1951). Solid medium was generated on plates with addition of 1.5% agar (weight/volume; Melford) prior to autoclaving. All media was made up in ultra-pure Milli-Q water (18.2 MΩ·cm) before sterilisation by autoclaving. Liquid cell cultures were grown at 37°C with 180 rpm rotational shaking (Stuart orbital incubator SI600), unless stated otherwise. Kanamycin (kan; Melford) at 50 μg mL^{-1} was used for selection of transformed *E. coli* on solid medium.

2.2 Chemicals, reagents, and buffers

2.2.1 Chemicals, reagents, and plasticware

Except where noted, all chemicals and reagents were from Sigma-Aldrich Life Science (Sigma). All buffers and stocks used Milli-Q water as the solvent unless indicated. Plasticware was from Starlab except ICP-MS tubes which were from Sarstedt.

2.2.2 Prepared stock solutions

5,5'-dithio-bis-(2-nitrobenzoic acid) (DTNB). A 3 mM DTNB stock was made by dissolving solid into 10 mM 4-(2-hydroxyethyl)-1-piperazineethanesulfonic acid (HEPES; Melford) pH 7.5, 50 mM KCl. Fresh stocks were made as necessary based on the half-life of DTNB in buffer solution (Riddles et al., 1983).

Dithiothreitol (DTT). Solid DTT (Melford; stored at 4°C) was either added directly to buffer solutions or dissolved in Milli-Q water (1 M stock). Buffers containing DTT were made fresh as required due to the relatively quick oxidation of DTT in aerobic solutions ($t_{1/2}$ ~ hours).

Ethylenediaminetetraacetic acid (EDTA). A 0.5 M EDTA (Fluka) stock was made by dissolving the solid free acid in Milli-Q water. The solution pH was increased to 8.0 by addition of NaOH, which is also necessary to dissolve the solid EDTA. After adjusting the pH, the solution was made up to the correct volume by adding Milli-Q water. The stock was stored on the bench.

Ethylene glycol-bis-(2-aminoethylether)-N-N-N'-N'-tetraacetic acid (EGTA). A 0.1 M EGTA stock was made by dissolving solid in Milli-Q water. Aliquots of 1 M NaOH were added to obtain pH 7.5. After adjusting the pH, the solution was made up to the final volume by adding Milli-Q water in a volumetric flask. The stock was stored on the bench.

L-histidine (L-His or His). A 0.2 M stock of L-His (Acros Organics) was made by dissolving solid in a small volume of Milli-Q water. 10 mM HEPES pH 7.5 (final volume concentration) was added followed by titration of KOH from a 1 M or 4 M stock to a pH of 7.5. The volume was corrected using Milli-Q water and the stock was then aliquoted into 1.5 mL microfuge tubes and frozen at -20°C to avoid oxidation during long term storage. Individual tubes were thawed and used for 3-5 days or refrozen within hours of use.

Nickel chloride ($NiCl_2$). A ~ 0.2 M Ni(II) stock was made by dissolving the solid into Milli-Q water in a 15 mL conical polypropylene tube. This stock was analysed by ICP-MS (Section 2.5.2) to determine an accurate Ni concentration. The stock was diluted to 10 mM and 1 mM final concentrations in plastic 15 mL conical polypropylene tubes, and these were also analysed by ICP-MS to determine accurate Ni concentrations. These stocks were used for all experiments involving Ni(II).

Tris(2-carboxyehtyl)phosphine hydrochloride (TCEP). A 0.5 M TCEP stock was made by dissolving the solid (Melford; stored at 4°C) into a small volume of Milli-Q water. 10 mM HEPES pH 7.5 (final volume concentration) was diluted into the solution before correcting the pH to 7.5 by titrating with 1 M NaOH. The total volume was then corrected with addition of Milli-Q water. The TCEP solution was aliquoted into 1.5 mL microfuge tubes and stored at -20°C. TCEP was used as a reducing agent and was added to buffers immediately before use.

Zinc chloride ($ZnCl_2$) and zinc sulphate ($ZnSO_4$). These stocks (0.1 M) were made up as described for $NiCl_2$ but accurate concentrations were not determined because the solutions were only used during protein overexpression and purification of Fur and Zur.

2.2.3 Buffers

The buffers described below were used for the purification (and experimentation) of the *Salmonella* sensors. Metal- and DNA-binding affinity measurements were performed in two different buffers (Buffer E and Buffer N, respectively) so that all measured parameters could be compared across all seven sensors.

Buffer A – 100 mM sodium phosphate pH 8.0, 500 mM NaCl, 10 mM imidazole

Buffer B – 100 mM sodium phosphate pH 8.0, 500 mM NaCl, 35 mM imidazole

Buffer C – 100 mM sodium phosphate pH 8.0, 100 mM NaCl, 250 mM imidazole

Buffer D – 10 mM HEPES pH 7.5, 100 mM NaCl, 2 mM TCEP

Buffer D-500 – 10 mM HEPES pH 7.5, 500 mM NaCl, 2 mM TCEP

Buffer E – 10 mM HEPES pH 7.5, 400 mM KCl, 100 mM NaCl

Buffer F – 10 mM HEPES pH 7.0, 300 mM NaCl, 10 mM EDTA, 10 mM DTT

Buffer G – 10 mM HEPES pH 7.0, 800 mM NaCl, 10 mM EDTA, 10 mM DTT

Buffer H – 10 mM HEPES pH 7.0, 100 mM NaCl, 10 mM EDTA, 10 mM DTT

Buffer H-200 – 10 mM HEPES pH 7.0, 200 mM NaCl, 10 mM EDTA, 10 mM DTT

Buffer J – 10 mM HEPES pH 7.0, 240 mM KCl, 60 mM NaCl

Buffer K – 10 mM HEPES pH 7.0, 800 mM KCl, 200 mM NaCl

Buffer L – 20 mM sodium phosphate pH 7.4, 300 mM NaCl, 10 mM imidazole

Buffer L-5 – 20 mM sodium phosphate pH 7.4, 300 mM NaCl, 5 mM imidazole

Buffer L-100 – 20 mM sodium phosphate pH 7.4, 300 mM NaCl, 100 mM imidazole

Buffer L-300 – 20 mM sodium phosphate pH 7.4, 300 mM NaCl, 300 mM imidazole

Buffer M – 10 mM HEPES pH 7.5, 300 mM NaCl, 5 mM EDTA

Buffer N – 10 mM HEPES pH 7.5, 240 mM KCl, 60 mM NaCl

Buffer P – 10 mM HEPES pH 7.5, 800 mM KCl, 200 mM NaCl

Buffer Q – 10 mM HEPES pH 7.5, 100 mM NaCl, 1 mM EDTA, 5 mM DTT

Buffer Q-300 – 10 mM HEPES pH 7.5, 300 mM NaCl, 1 mM EDTA, 5 mM DTT

Buffer R – 10 mM HEPES pH 7.0, 50 mM NaCl, 1 mM EDTA, 5 mM DTT

Buffer R-5 – 10 mM HEPES pH 7.0, 5 mM NaCl, 1 mM EDTA, 5 mM DTT

Buffer S – 10 mM HEPES pH 7.0, 4 mM KCl, 1 mM NaCl

Buffer T – 20mM HEPES pH 7.0, 240 mM KCl, 60 mM NaCl

2.2.4 Preparation of metal-free buffers

Chelex-100 was used to remove trace transition metals from buffer stocks used for protein purification and analysis. Chelex-100 (~ 50 g, where 1 g Chelex-100 is ~ 1 mL volume) was added to a glass column and washed through with 3-4 column volumes of Milli-Q water. The column was then washed with a sequence of solutions as follows: 1 column volume of 1 M HCl, then 3-4 column volumes of Milli-Q water, then 1 column volume of 1 M NaOH, then 3-4 column volumes of Milli-Q water. The column was then washed with 1-2 column volumes of a high concentration buffer (0.2-0.5 M) in the pH range for the metal-free buffers (e.g. HEPES pH 7.5). The volume of buffer to be treated was at least 500 mL (generally 1 L). The first 150-200 mL of this buffer was washed through the column to remove the high concentration buffer stock and equilibrate with the desired concentration. The remainder of the buffer was collected either in 50 mL polypropylene tubes or acid-washed glassware (previously soaked in 5% nitric acid for at least 12 h to remove bound trace metals before washing with Milli-Q water). The pH for each fraction of Chelex-treated buffer was measured to ensure it was not altered in the process. Small discrepancies in pH could be corrected using clean NaOH or HCl ensuring care was taken not to contaminate the buffers with metal. Fractions were discarded if the pH was significantly different ($> \pm 0.5$ pH units from pre-treated stock). Reducing agents were added to buffers after Chelex-treatment.

2.3 Protein overexpression

2.3.1 Competent cells

Chemically competent cells (Chung et al., 1989) were transformed with the appropriate plasmid. Transformation and storage solution (TSS) was prepared using 10% (w/v) polyethylene glycol (PEG 8000), 5% (v/v) dimethyl sulfoxide, 30 mM $MgCl_2$, dissolved in

LB media (Section 2.1.2) and corrected to pH 6.5. The solution was then filter sterilised and stored at 4°C for up to two months.

A 2 mL culture of *E. coli* BL21 (DE3) in LB media was grown at 37°C with shaking until OD_{600} 0.4-0.6. Cells were then transferred to ice (> 10 min) to stop growth. 1 mL of chilled cells was pipetted into a 1.5 mL microfuge tube and pelleted using a Heraeus Fresco 17 microcentrifuge (Thermo Scientific) at 8,000 rpm for 5 min (4°C). The supernatant was discarded and the cell pellet was re-suspended by pipetting with 80 µL TSS per mL of original culture. TSS competent cells were either used immediately or stored at -80°C for future use.

2.3.2 Transformations

Plasmids expressing *Salmonella* sensors (1-2 µL of ~ 25-35 ng μL^{-1} stock) were added to a 1.5 mL microfuge tube on ice. 70 µL of TSS competent cells were then added to the plasmid and mixed, keeping on ice. The cells were then transferred to a 42°C dry block for 90 s, then immediately returned to ice. 900 µL of LB media was then added to the cells followed by shaking at 180 rpm (37°C for ≥ 30 min). 50-200 µL of transformed cells were spread onto an LB kan plate and incubated at 37°C (14-16 h). Single colonies were used directly to grow large scale cultures for overexpression of protein (Section 2.3.3). Glycerol stocks were prepared from each plasmid in BL21 (DE3) using a 2 mL overnight culture (LB, 37°C, 14-16 h) where 1 mL of dense cell culture was mixed with 1 mL 50% glycerol in a cryogenic vial before being stored at -80°C. Re-streaking from freezer stocks was also used to generate fresh colonies for protein overexpression.

2.3.3 Protein overexpression

Several single colonies from an LB plate (either fresh transformants or re-streaked from frozen stocks) were picked and added to 50 mL LB kan media and incubated at 37°C with shaking until OD_{600} ~ 0.8. This starter culture was divided into multiple conical flasks containing 500 mL of media (2-4 L total volume) and grown under the same conditions until OD_{600} 0.8-1.0 (New Brunswick Excella E25), when isopropyl-β-D-thiogalactoside (IPTG; Melford), dissolved in Milli-Q water, was added (final concentration 0.5 to 1 mM) to induce protein expression. Cultures were grown for at least 2 h (generally 3-4 h) before harvesting. For *Sty*Fur and *Sty*Zur overexpression, cell cultures were supplemented with 50 µM $ZnSO_4$ (final concentration) to ensure occupancy of the Zn-structural site in these proteins (Section 1.3.7). After growth, cells were pelleted by centrifugation (Beckman Coulter Avanti J-20 XP) at 4,000 rpm for 25-30 min (4°C). The supernatant was removed and the pellet was re-

suspended with 8 mL buffer per L of culture. The buffer used for each protein is described in the relevant purification protocol. Re-suspended cells were transferred to 50 mL conical polypropylene tubes (typically 1-2 L of cells per tube) and stored at -80°C (note: RcnR was not stored for more than 3 days before purifying the protein).

2.3.4 Cell lysis and clarification

Frozen cell pellets containing overexpressed proteins were thawed by placing the tube in a beaker of cold water. Thawed cells were transferred to ice and lysed by sonication (5 × 1 min cycles, 3 s pulses with 1 s rest at 45-55% power; Bandelin Sonoplus sonicator). 50 mM phenylmethane sulfonyl fluoride solution (dissolved in 100% ethanol) was pipetted (~ 200 µL) into the sample between each cycle to a final concentration of 1 mM. Cells were mixed between each 1 min cycle to ensure homogeneity. The lysate was clarified by centrifugation at 15,000 rpm for 25-30 min (4°C). The supernatant was collected for purification, whereas the pellet was discarded.

2.4 Protein purification

All proteins were purified using chromatographic procedures that exploit their native physicochemical properties. Each protein required an individual protocol and these are described below. SDS-PAGE analysis (Section 2.5.1) was carried out after completion of individual chromatography steps for each protein.

2.4.1 Purification of *Sty*NikR

Purification of *Sty*NikR followed an established procedure (Osman et al., 2018). Buffer A was used to re-suspend cell pellets after collection from large scale cell culture (Section 2.3.3) and to equilibrate the first column (Ni-NTA). After cell lysis and clarification, nickel was added to the cell lysate in order to prevent NikR removing the metal from the Ni-NTA resin (Chivers and Sauer, 2000). A 10 mL solution of 1 part Buffer C and 100 parts Buffer A with $NiCl_2$ was added to the lysate to achieve 100 µM Ni(II) as a final concentration. The lysate was inverted gently to ensure mixing of the nickel. Minor precipitation was sometimes observed but this did not affect the protein yield. The purification step used 3 mL of Ni-NTA agarose resin (Thermo Scientific) added to a glass column and equilibrated with 15 column volumes of Buffer A. Cell lysate was then loaded onto the resin and, with the stopcock closed, mixed to allow binding to the resin. After resin settled in the column, the stopcock was opened to obtain a flow rate of ~ 1 mL min^{-1}, collecting the flow-through as a single

fraction in a single polypropylene tube. The resin was then washed with 15 column volumes of Buffer A and the flow-through collected as a single fraction. The resin was then washed with 10 column volumes of Buffer B, collecting a single fraction. Finally, the protein was eluted with 8 mL of Buffer C, collecting a single fraction. The eluate was then diluted with 2 volumes of Buffer D in preparation for ion-exchange chromatography. A 5 mL HiTrap Q HP anion exchange column (GE Healthcare) was equilibrated with 5 column volumes of Buffer D (1 mL min^{-1}) using a peristaltic pump (Rainin Dynamax Peristaltic Pump). The diluted Ni-NTA eluate was then loaded onto the column, collecting the flow-through as a single fraction. The column was then washed with 5 column volumes of Buffer D. The protein was then eluted using Buffer D-500 as 4.5 mL, 5.5 mL, and 3 × 5 mL collected fractions. The protein typically eluted in fraction 2, visible because of the brown colour of Ni(II)-NikR. After elution, EDTA (10 mM final) and L-histidine (500 μM final) were added to fraction 2 to generate metal-free NikR (37°C for 12-16 h). The resulting solution was applied to a HiLoad 26/600 Superdex 75 pg column equilibrated in Chelex-treated Buffer D + 1 mM TCEP to remove any trace metals (Section 2.2.4) and EDTA, which can interfere with later steps (Chumanov and Burgess, 2011). The eluate was collected in 5 mL fractions (2.5 mL min^{-1}) and NikR-containing fractions (typically 3 fractions) were pooled and loaded onto a 1 mL HiTrap Q HP column (GE Healthcare) equilibrated with 10 column volumes of Chelex-treated Buffer D for transfer to an anaerobic glove box (Belle Technology). Once in the glove box, the column was washed, using a syringe, with 10 column volumes of Chelex-treated Buffer D without TCEP. The protein was eluted with Buffer E as 0.9 mL, 1.1 mL, 3 × 1 mL collected fractions. NikR eluted in the second fraction and protein content and thiol reactivity (NikR contains two cysteine residues) were determined as described in Section 2.5.3 before storage. If the NikR stock concentration exceeded 1.5 mM it was diluted to < 1 mM with Buffer E to avoid precipitation over time. NikR stocks were stored at room temperature because precipitation was noticeable at 4°C. Lower concentration (< 500 μM) NikR stocks were less susceptible to precipitation at 4°C.

2.4.2 Purification of *Sty*RcnR

Purification of *Sty*RcnR followed an established procedure (Osman et al., 2015). Cell pellets (Section 2.3.3) were re-suspended in Buffer F. After cell lysis and clarification (Section 2.3.4), the lysate was loaded onto a 5 mL HiTrap Heparin HP affinity column (GE Healthcare) previously equilibrated with 5 column volumes of Buffer F (1 mL min^{-1} with a peristaltic pump), collecting the flow-through as one fraction. The column was then washed with 5 column volumes of Buffer F. The protein was eluted from the column with Buffer G as 4.5 mL, 5.5 mL, and 3 × 5 mL collected fractions. The majority of RcnR eluted in fraction

2. RcnR was further purified by running size exclusion chromatography (HiLoad 26/600 Superdex 75 pg) equilibrated with 1 column volume of Buffer F. Fraction 2 from the Heparin column was then loaded onto the column (2.5 mL min^{-1}), collecting 5 mL fractions. The cleanest fractions containing RcnR were pooled and diluted with 2 volumes of 10 mM HEPES pH 7.0, 10 mM DTT. The protein was then loaded onto a 5 mL HiTrap SP HP cation exchange column (GE Healthcare), equilibrated with 5 column volumes of Buffer H (1 mL min^{-1}). The flow-through was collected as one fraction. The column was then washed with 5 column volumes of Buffer H-200, collecting the flow-through as one fraction. The protein was then eluted with Buffer F as 4.5 mL, 5.5 mL, and 3 × 5 mL collected fractions. RcnR typically eluted in fraction 2 and was loaded onto a 1 mL HiTrap Heparin HP affinity column (GE Healthcare), previously equilibrated with 10 column volumes of Buffer F. The column with bound protein was moved into the anaerobic glove box. The column was then washed, using a syringe, with 10 column volumes of Buffer J and the protein was eluted with Chelex-treated Buffer K as 0.9 mL, 1.1 mL, and 3 × 1 mL collected fractions. RcnR eluted primarily in fraction 2 and the stock concentration was quantified and tested for thiol reactivity (RcnR contains one cysteine residue) as described in Section 2.5.3 before storage at 4°C. Stocks were used for experiments within 2-3 weeks of purifying.

2.4.3 Purification of *Sty*MntR

Purification of *Sty*MntR followed an established procedure (Osman et al., 2018). Cell pellets (Section 2.3.3) were re-suspended in Buffer L. After cell lysis and clarification (Section 2.3.4), the lysate was loaded onto a 5 mL HiTrap HisTrap HP affinity column (GE Healthcare) previously equilibrated with 5 column volumes of Buffer L (1 mL min^{-1} with a peristaltic pump), collecting the flow-through as one fraction. The column was then washed with 5 column volumes of Buffer L, collecting the flow-through as one fraction. The protein was then eluted with 5 mL Buffer L-100 followed by 4 × 5 mL Buffer L-300, all collected as 5 mL fractions. The majority of MntR was eluted in fraction 2. MntR was further purified by running size exclusion chromatography (HiLoad 26/600 Superdex 75 pg) equilibrated with 1 column volume of Buffer M. Fraction 2 from the HisTrap column was then loaded onto the column (2.5 mL min^{-1}), collecting 5 mL fractions. The cleanest fractions containing MntR were pooled and loaded onto a 1 mL HiTrap Heparin HP affinity column, equilibrated with 10 column volumes of Buffer M. The column was then washed with 10 column volumes of Chelex-treated Buffer N before eluting the protein with Chelex-treated Buffer P as 0.9 mL, 1.1 mL, and 3 × 1 mL collected fractions. MntR eluted primarily in fraction 2 and the protein concentration was quantified (Section 2.5.4) before storage at 4°C. MntR does not contain any cysteine residues so the protein was not transferred to the anaerobic glove box.

2.4.4 Purification of *Sty*Fur

Purification of *Sty*Fur followed an established procedure (Osman et al., 2018). Cell pellets (Section 2.3.3) were re-suspended in Buffer L + 1 mM TCEP. After cell lysis and clarification (Section 2.3.4), the lysate was loaded onto a 5 mL HiTrap HisTrap FF affinity column (GE Healthcare), previously equilibrated with 5 column volumes of Buffer L + TCEP (2.5 mL min^{-1} with a peristaltic pump), collecting the flow-through as one fraction. The column was then washed with 5 column volumes of Buffer L + TCEP, collecting the flow-through as one fraction. The protein was then eluted with 5 mL of Buffer L-100 + 1 mM TCEP followed by 7 × 5 mL Buffer L-300 + 1 mM TCEP, collecting 5 mL fractions. Three of fractions 3-8 that contain the most Fur were pooled and diluted with 2 volumes of 10 mM HEPES pH 7.0, 1 mM TCEP. The combined fractions were loaded onto a 5 mL HiTrap Q HP anion exchange column equilibrated with 5 column volumes of Buffer D at pH 7.0 (1 mL min^{-1}). The column was then washed with 5 column volumes of Buffer D, collecting the flow-through as one fraction. Fur was eluted with Buffer K + 1 mM TCEP as 4.5 mL, 5.5 mL, and 3 × 5 mL collected fractions. Fur eluted primarily in fraction 2 and an estimate for the concentration of the protein was calculated using A_{280} (with the extinction coefficient found in Section 2.5.4). Note: the Fur concentration was an overestimate due to non-zinc metal-specific spectral features which increase the absorbance at A_{280}. Two equivalents of $ZnCl_2$ were added to the fraction to populate the Zn-structural site. $ZnCl_2$ was added using a concentrated stock (~ 100 mM) with multiple small volume additions (~ 10 µL) coupled with gentle mixing. After ~ 1 h with the $ZnCl_2$ (20°C), 7.5 mM EDTA was added to the fraction which was then left to equilibrate overnight (4°C). Fur was further purified by running size exclusion chromatography (HiLoad 26/600 Superdex 75 pg) equilibrated with 1 column volume of Chelex-treated Buffer D + 1 mM TCEP. The Zn(II)- and EDTA-treated Fur was loaded onto the column (2.5 mL min^{-1}), collecting 5 mL fractions. The cleanest fractions containing Fur were pooled and loaded onto a 1 mL HiTrap Q HP anion exchange column equilibrated with 10 column volumes of Chelex-treated Buffer D + 1 mM TCEP. The column with bound protein was moved into the anaerobic glove box. The column was then washed, using a syringe, with 10 column volumes of Chelex-treated Buffer J and the protein was eluted with Chelex-treated Buffer P as 0.9 mL, 1.1 mL, and 3 × 1 mL collected fractions. Fur eluted primarily in fraction 2 and the stock concentration was quantified and tested for thiol reactivity (Fur contains four cysteine residues) as described in Section 2.5.3 before storage at 4°C. The sample was also analysed by ICP-MS (Section 2.5.2) to determine the Zn occupancy of structural sites.

2.4.5 Purification of *Sty*CueR

Purification of *Sty*CueR followed an established procedure (Osman et al., 2013). Cell pellets (Section 2.3.3) were re-suspended in Buffer Q. After cell lysis and clarification (Section 2.3.4), the lysate was loaded onto a 5 mL HiTrap Heparin HP affinity column, previously equilibrated with 5 column volumes of Buffer Q (1 mL min^{-1} with a peristaltic pump), collecting the flow-through as one fraction. The column was then washed with 5 column volumes of Buffer Q, collecting the flow-through as one fraction. The protein was then eluted with Buffer Q-300 as 4.5 mL and 5 × 5 mL collected fractions. CueR was typically eluted in fraction 3 or 4. The cleanest fraction was further purified by running size exclusion chromatography (HiLoad 26/600 Superdex 75 pg) equilibrated with 1 column volume of Buffer Q-300. The chosen CueR fraction from the Heparin column was loaded onto the column (2.5 mL min^{-1}), collecting 5 mL fractions. The cleanest fractions containing CueR were pooled and diluted with 2 volumes of 10 mM HEPES pH 7.5, 5 mM DTT. The protein was then loaded onto a 1 mL HiTrap Heparin HP affinity column, equilibrated with 10 column volumes of Buffer Q. The column with bound protein was moved into the anaerobic glove box. The column was then washed, using a syringe, with 10 column volumes of Chelex-treated Buffer D without TCEP and the protein was eluted with Chelex-treated Buffer E as 0.9 mL, 1.1 mL, and 3 × 1 mL collected fractions. CueR eluted primarily in fraction 2 and the stock concentration was quantified and tested for thiol reactivity (CueR contains five cysteine residues) as described in Section 2.5.3 before storage at 4°C.

2.4.6 Purification of *Sty*ZntR

Purification of *Sty*ZntR followed an established procedure (Osman et al., 2015). Cell pellets (Section 2.3.3) were re-suspended in Buffer L-5. After cell lysis and clarification (Section 2.3.4), the lysate was loaded onto a 5 mL HiTrap HisTrap FF affinity column, previously equilibrated with 5 column volumes of Buffer L-5 (2.5 mL min^{-1} with a peristaltic pump), collecting the flow-through as one fraction. The column was then washed with 5 column volumes of Buffer L-5, collecting the flow-through as one fraction. The protein was then eluted with Buffer L-100 as 4.5 mL, 5.5 mL, and 3 × 5 mL collected fractions. ZntR was primarily eluted in fraction 2. ZntR was further purified by running size exclusion chromatography (HiLoad 26/600 Superdex 75 pg) equilibrated with 1 column volume of Buffer R. Fraction 2 from the HisTrap column was loaded onto the column (2.5 mL min^{-1}), collecting 5 mL fractions. The cleanest fractions containing ZntR were pooled and diluted with 9 volumes of 10 mM HEPES pH 7.0, 5 mM DTT. The protein was then loaded onto a 1 mL HiTrap Heparin HP affinity column, equilibrated with 10 column volumes of Buffer

R-5. The column with bound protein was moved into the anaerobic glove box. The column was then washed, using a syringe, with 10 column volumes of Chelex-treated Buffer S and the protein was eluted with Chelex-treated Buffer E as 0.9 mL, 1.1 mL, and 3 × 1 mL collected fractions. ZntR eluted primarily in fraction 2 and the stock concentration was quantified and tested for thiol reactivity (ZntR contains four cysteines residues) as described in Section 2.5.3 before storage at room temperature (due to precipitation at 4°C).

2.4.7 Purification of *Sty*Zur

Purification of *Sty*Zur followed an established procedure (Osman et al., 2015). Cell pellets (Section 2.3.3) were re-suspended in Buffer L-5. After cell lysis and clarification (Section 2.3.4), the lysate was loaded onto a 5 mL HiTrap HisTrap FF affinity column, previously equilibrated with 5 column volumes of Buffer L-5 (2.5 mL min^{-1} with a peristaltic pump), collecting the flow-through as one fraction. The column was then washed with 5 column volumes of Buffer L-5, collecting the flow-through as one fraction. The protein was then eluted with Buffer L-100 as 4.5 mL, 5.5 mL, and 3 × 5 mL collected fractions. Zur was primarily eluted in fraction 2. Zur was further purified by running size exclusion chromatography (HiLoad 26/600 Superdex 75 pg) equilibrated with Buffer R. Fraction 2 from the HisTrap column was loaded onto the column (2.5 mL min^{-1}), collecting 5 mL fractions. The cleanest fractions containing Zur were pooled and diluted with 2 volumes of 10 mM HEPES pH 7.0, 5 mM DTT. The protein was then loaded onto a 1 mL HiTrap Heparin HP affinity column, equilibrated with 10 column volumes of Buffer Q. The column with bound protein was moved into the anaerobic glove box. The column was then washed, using a syringe, with 10 column volumes of Chelex-treated Buffer D without TCEP and the protein was eluted with Chelex-treated Buffer E as 0.9 mL, 1.1 mL, and 3 × 1 mL collected fractions. Zur eluted primarily in fraction 2 and the stock concentration was quantified and tested for thiol reactivity (Zur contains nine cysteine residues) as described in Section 2.5.3 before storage at 4°C. The sample was also analysed by ICP-MS (Section 2.5.2) to determine the Zn occupancy of structural sites.

2.5 Analysis of purified proteins

2.5.1 Assessment of protein purity (SDS-PAGE)

The protein content of fractions following each purification step for each *Salmonella* sensor was assessed by 15% sodium dodecyl sulphate polyacrylamide gel electrophoresis (SDS-PAGE) (Laemmli, 1970). Protein samples were produced by diluting with water and addition

of 6x loading buffer (Ausubel, 2002). Samples were denatured at 95°C for 5 min. Then 15-20 µL of sample was loaded and the gel was run at 200 V for 45-60 min. Separation was halted once the loading dye reached the bottom of the gel. The gel was recovered and stained with Instant Blue (Expedeon) and imaged (Bio-Rad XR+ Gel Documentation System). Gel images showing the representative final purity of protein are presented in Chapter 3.

2.5.2 Metal content determination (ICP-MS)

Metal content of $NiCl_2$ stocks and protein fractions were determined using inductively coupled plasma mass spectrometry (ICP-MS) in conjunction with a standard curve. Samples for the standard curve were produced by diluting a multi-metal stock (Mn, Fe, Co, Ni, Cu, and Zn) into 2.5% nitric acid (with Milli-Q water (v/v); Merck) to obtain a series of samples with metal concentrations generally between 1 and 500 parts per billion (ppb), though the exact range depended on the expected concentrations for different samples. The standard curve also included an internal standard (10 ppb Ag alone, or 10 ppb each of Ag, In, and Be) and matrix-matched buffer. The matrix-matched buffer corresponded to the sample buffer without sample to control for any contributions from the buffer that might affect measurements. Experimental samples were a 1:10 dilution of the original sample in 2.5% nitric acid and also included the internal standard. All samples were prepared in 8 mL polypropylene tubes and carefully vortexed (~ 5 s) before analysis. Protein-containing samples were analysed shortly after preparation to avoid complications due to precipitation. Other samples could be stored at 4°C before analysis within 24 h. All plasticware was used directly from the original packaging to avoid metal contamination (e.g. by autoclaving).

2.5.3 Quantification of free protein thiols (DTNB)

Free thiol content was assayed by standard methods using DTNB (Ellman, 1959, Collier, 1973). Protein samples were diluted (with Buffer E) so that the total concentration of cysteine residues present was between 5 and 20 µM. DTNB stock (Section 2.2.2) was added to the sample to a final concentration of 50-100 µM. The sample was mixed by pipetting and left at 25°C for ~ 1 h. Scans were carried out in UV transparent plastic cuvettes (Eppendorf). Only protein stocks with > 90% thiol reactivity were used for experiments, but free thiol values were typically present at 95% of the expected value.

2.5.4 Protein quantification (UV/visible spectroscopy)

Protein concentration was determined using the intrinsic UV absorbance of each sensor and established extinction coefficients. The estimated extinction coefficient ($\varepsilon_{280\ nm}$) for NikR was 4,398 M^{-1} cm^{-1} (generated by comparison with the denatured extinction coefficient (ε_{276}

$_{nm}$) of 4,440 M^{-1} cm^{-1} (Chivers and Sauer, 2002)). The experimentally determined extinction coefficients ($\varepsilon_{280\ nm}$) for the other sensors were: *Sty*RcnR 2,422.4 M^{-1} cm^{-1}; *Sty*MntR 7,940 M^{-1} cm^{-1}; *Sty*Fur 6,672.5 M^{-1} cm^{-1}; *Sty*CueR 5,136 M^{-1} cm^{-1}; *Sty*ZntR 11,505 M^{-1} cm^{-1}; and *Sty*Zur 4,823 M^{-1} cm^{-1} (Osman et al., 2015, Osman et al., 2018).

2.5.5 Protein quantification (Bradford assay)

Protein concentration determination of some experimental samples (e.g. co-migration studies) were determined by Bradford assay (Bradford, 1976). Coomassie plus Bradford assay reagent (Thermo Scientific) was mixed with known concentrations of protein (50:50 v/v sample to reagent) to generate a standard curve ($A_{595\ nm}$) and determine the concentration range of protein over which the curve is linear. Samples were incubated for 5 min at 20°C. Protein concentrations were estimated using the corresponding standard curve, diluting where necessary to fall within the linear range of the assay.

2.6 Anaerobic sample handling

Proteins containing cysteine residues (all except *Sty*MntR) required the presence of reducing agents (TCEP or DTT) during purification under ambient conditions. They were transferred into an anaerobic glove box (described in Section 2.4 for each protein) and washed with N_2-purged buffers to remove the reductant before elution in the relevant N_2-purged, reductant-free buffer. O_2-free, N_2-purged buffers were achieved by flowing N_2 (g) through buffer (≥ 2 h) within an attached anaerobic compartment before storage in the anaerobic glove box. O_2 levels inside the glove box were kept < 9 ppb and typically between 2-3 ppb. Unless specified, experiments with purified protein (except MntR) were carried out after transfer to the anaerobic glove box. Gas-tight quartz cuvettes (Hellma) were used to maintain samples anaerobically when outside the glove box.

2.7 Metal stoichiometry determination

The nickel stoichiometry of *Salmonella* sensors was determined using complementary methods as described below. Unless specified, all experiments were carried out with protein samples diluted into Buffer E.

2.7.1 UV/visible spectroscopy

Each *Salmonella* sensor was diluted (final concentrations between 10 and 30 μM) and titrated with $NiCl_2$ stocks (Section 2.2.2) under anaerobic conditions (where applicable, see Section 2.6). UV/visible spectra (λ35 UV/vis spectrophotometer; PerkinElmer) were measured after each Ni(II) addition (3 min equilibration, 25°C). Sensors with Ni(II)-dependent spectral features (NikR, RcnR, CueR, ZntR, and Zur) were titrated until no further spectral changes were observed (Chapter 3). Ni(II) stoichiometry was estimated from the Ni(II):sensor ratio at the point of saturation.

2.7.2 Fluorescence spectroscopy

Tyrosine fluorescence was used to determine the Ni(II) stoichiometry of *Sty*Fur. The protein was diluted under anaerobic conditions (Section 2.6). Intrinsic fluorescence emission (λ_{ex} = 276 nm; λ_{em} = 290-340 nm at 25°C) was collected on a Cary Eclipse fluorescence spectrophotometer (Agilent Technologies; scan rate = 120 nm min^{-1}; data interval = 1 nm; averaging time = 0.5 s) after each $NiCl_2$ addition to determine the stoichiometry, as was done by UV/visible spectroscopy (Section 2.7.1).

2.7.3 Co-migration through size exclusion column

Co-migration studies were carried out in the anaerobic chamber for all protein except *Sty*MntR. Desalting columns (PD-10, 2.5 mL Sephadex G-25 resin; GE Healthcare) were used to separate metal-bound protein and free metal. A fresh column was used for each sensor and equilibrated with 10 column volumes of Chelex-treated Buffer E, except NikR which used Buffer E, pH 8.0 (Section 3.2.1). Sensor proteins (15-20 μM in 500 μL) were incubated with excess Ni(II) (1.25, 1.5, 2.5, 2.5, 2.5, and 7 equivalents per monomer for NikR, RcnR, MntR, Fur, CueR, and Zur, respectively) and then loaded onto the PD-10 column. Buffer E was added to the column in 500 μL additions (≥ 10 column volumes in total) and a corresponding volume of flow-through was collected in microfuge tubes. Each fraction was analysed for protein concentration, either by $A_{280\ nm}$ (MntR, Fur, and Zur) or Bradford assay (NikR, RcnR, and CueR). A small volume (1:100) of 0.5 M EDTA was added to remove Ni(II) bound to protein when the $A_{280\ nm}$ feature was obscured by Ni(II)-dependent spectral features (e.g. ZntR and Zur). ICP-MS analysis for each fraction was performed to determine metal concentrations (Section 2.5.2). The ratio of Ni(II) to protein was determined by averaging the two collected fractions which contained the highest concentration of protein.

To determine the stoichiometry including weaker Ni(II) sites (K_d > ~ 10^{-7} M), the same experiment was performed for MntR, Fur, CueR, and Zur, but with 5 μM $NiCl_2$ added to Buffer E for both column equilibration and protein elution. This experiment was also conducted for ZntR (20 μM in 500 μL) where the protein sample was loaded with 2.5 equivalents of Ni(II) per monomer initially (fractions scanned by $A_{280\ nm}$). The addition of Ni(II) to Buffer E required a baseline correction for each sensor which was done by averaging the Ni concentration of the first 3-4 fractions collected that do not contain protein and subtracting this value from the remaining fractions.

2.8 Determination of Ni(II)-affinity

2.8.1 Competition with EGTA (NikR, RcnR, Fur, and CueR)

EGTA (K_{Ni} 5.15 × 10^{-11} M, pH 7.5, calculated using Schwarzenbach's α-coefficient (Martell and Smith, 1974, Xiao and Wedd, 2010)) competition experiments for NikR, RcnR, and CueR used a serial dilution of Ni(II) across 10-13 samples (800 μL). Buffer E containing Ni(II) and EGTA (where Ni(II) < EGTA; exact concentrations are described in the text; Sections 3.2.2, 3.3.2, and 3.6.3) was serially diluted (0.6-fold) into Buffer E containing EGTA only (where [EGTA] was equivalent to that from the Ni(II)/EGTA buffer). Proteins, from purified stocks, were diluted equally into each tube. The final concentrations of Ni(II) and EGTA accounted for this dilution. Samples were equilibrated for > 16 h at 25°C before transferring to a gas-tight quartz cuvette and collecting the UV/visible spectrum (Section 2.7.1). The Ni(II)-sensor concentration in each sample was determined from a Ni(II)-dependent spectral feature (see Sections 3.2.2, 3.3.2, and 3.6.3). Ni(II) was titrated into one sample of each protein in excess of the EGTA concentration to determine the maximum absorbance expected for each Ni(II)-sensor complex in the absence of competition (note: NikR precipitates under such conditions).

EGTA competition experiments for Ni(II) with Fur (Section 3.5.2) were performed in a two-way gas-tight quartz cuvette with 3 min equilibration time (25°C) after successive Ni(II) additions to a single sample. Ni(II) binding to Fur was monitored by tyrosine fluorescence emission (λ_{em} = 302 nm, see Section 2.7.2).

2.8.2 Competition with bicine (CueR, ZntR, and Zur)

Bicine (K_{Ni} 1.07 × 10^{-7} M, pH 7.5, calculated using Schwarzenbach's α-coefficient (Xiao and Wedd, 2010, Dojindo, 2013)) competition experiments for CueR, ZntR, and Zur used

serial dilution of Ni(II) across 10-13 samples (800 µL). Buffer E containing 90 µM Ni(II) and 100 µM bicine was serially diluted (0.6-fold) into Buffer E + 100 µM bicine. Proteins, from purified stocks, were diluted equally into each tube. The final concentrations of Ni(II) and bicine accounted for this dilution. Samples were equilibrated for > 16 h at 25°C before transferring to a gas-tight quartz cuvette and collecting the UV/visible spectrum (Section 2.7.1). The Ni(II)-sensor concentration in each sample was determined from a Ni(II)-dependent spectral feature (see Sections 3.6.3, 3.7.3, and 3.8.3). Ni(II) was titrated into one sample of each protein in excess of the bicine concentration to determine the maximum absorbance expected for each Ni(II)-sensor complex in the absence of competition.

2.8.3 Competition with FluoZin-3 (RcnR, MntR, Fur, CueR, ZntR, and Zur)

FluoZin-3 (Thermo-Fisher Scientific; K_{Ni} 2.85 × 10^{-9} M (Zhao et al., 2009)) competition experiments for RcnR, CueR, ZntR, and Zur with Ni(II) used separate samples (15-22 samples, 200 µL in 1.5 mL microfuge tubes) in Buffer E to which different amounts of $NiCl_2$ were added with protein and competitor concentration constant. Samples were equilibrated for > 1.5 h (usually 3-4 h) at 25°C in the anaerobic glove box. For measurements, samples were removed from the glove box in batches of 5 with their microfuge tube lids kept closed to limit oxygen contamination. Samples were added to a quartz fluorescence cuvette (Starna) and allowed to equilibrate at 25°C for 3 min. Fluorescence emission spectra were collected in triplicate to determine Ni(II)-FluoZin-3 concentration (λ_{ex} = 494 nm, λ_{em} = 500-550 nm, with max at 520 nm; scan rate = 120 nm min^{-1}; data interval = 1 nm; averaging time = 0.5 s) and then averaged. The concentrations of protein and competitor in the experiment were assumed based on the dilution from a master stock with known concentration since the concentrations were too low to quantify by absorbance.

Ni(II) titrations of MntR and Fur in competition with FluoZin-3 were performed as a conventional titration of Ni(II) to protein and competitor. Buffer E containing protein and FluoZin-3 was added to a two-way gas-tight quartz cuvette (800 µL and 1 mL total volumes for MntR and Fur, respectively). After each Ni(II) addition, the sample was allowed to equilibrate at 25°C (> 5 min) before scanning. The equilibration time was frequently much longer than 5 min (up to 1 h), with the longer times required when FluoZin-3 was competing against tighter protein sites. This is likely due to the rapid binding of nickel by FluoZin-3 (< 1 s (Zhao et al., 2009)) followed by slow competition of the protein to remove it from the competitor. After equilibrium had been reached, the sample was scanned three times and then averaged.

2.8.4 Competition with mag-fura-2 (MntR, ZntR, and Zur)

Mag-fura-2 (Thermo-Fisher Scientific; K_{Ni} 2.44 × 10^{-8} M (experimentally determined, see Section 7.1)) competition experiments for Zur with Ni(II) used separate samples (10-17 samples, 200 µL in 1.5 mL microfuge tubes) in Buffer E to which different amounts of $NiCl_2$ were added with protein and competitor concentration constant. Samples were equilibrated for 3-4 h at 25°C in the anaerobic glove box. For measurements, samples were removed from the glove box in batches of 5 with their microfuge tube lids kept closed to limit oxygen contamination. Samples were added to a quartz fluorescence cuvette and allowed to equilibrate at 25°C for 3 min. Fluorescence emission spectra were collected in triplicate to determine Ni(II)-mag-fura-2 concentration (λ_{ex} = 366 nm, λ_{em} = 450-550 nm, with max at 510 nm; scan rate = 200 nm min^{-1}; data interval = 0.667 nm; averaging time = 0.2 s) and then averaged. The concentrations of protein and competitor in the experiment were assumed based on the dilution from a master stock with known concentration since the concentrations were too low to quantify by absorbance.

The Ni(II) titration of ZntR in competition with mag-fura-2 was performed as a conventional titration of Ni(II) to protein and competitor. Buffer E containing protein and mag-fura-2 was added to a two-way gas-tight quartz cuvette (1 mL total volume). After each Ni addition, the sample was allowed to equilibrate at 25°C (5 min) before scanning. The sample was scanned three times and then averaged.

The Ni(II) titration of MntR in competition with mag-fura-2 followed the same procedure as ZntR except the sample was scanned after each Ni(II) addition by UV/visible spectroscopy (following mag-fura-2 absorbance at 366 nm) after equilibrating at 25°C (5 min).

2.9 DNA-binding experiments

2.9.1 Preparation of fluorescently-labelled DNA duplexes

Single-stranded oligonucleotides (Table 2.1) were purchased from Sigma. Forward (F) strands were 5′ labelled with hexachlorofluorescein (HEX). Oligonucleotides were re-suspended in Milli-Q water (final concentration ~ 100 µM). Concentrations were determined in triplicate using 1 in 10 dilutions (into Milli-Q water), scanned using a NanoDrop 1000

Table 2.1 Oligonucleotide pairs (F and R) used for the determination of DNA affinities by FA.

No.	Oligonucleotide name	Nucleotide sequence	Source
1	*nixA*-Pro_F	HEX-5′-AGGTGTGACGTTTTAATCAAATGATCATACAT-3′	Osman et al., 2018
2	*nixA*-Pro_R	5′-ATGTATGATCATTTGATTAAAACGTCACACCT-3′	Osman et al., 2018
3	*nikA*-Pro_F-unlabelled	5′-GCGTATGATGTTTTTAAAAGATCGTCATACTT-3′	This study
4	*nikA*-Pro_R	5′-AAGTATGACGATCTTTTAAAAACATCATACGC-3′	This study
5	*rcnRA*-Pro_F	HEX-5′-TACTCCCCCCCAGTATAGAATACTACCCCCCAGTA-3′	Osman et al., 2016
6	*rcnRA*-Pro_R	5′-TACTGGGGGGTAGTATTCTATACTGGGGGGGAGTA-3′	Osman et al., 2016
7	*mntS*-Pro_F	HEX-5′-CTATAAAACATAGCCTGTGCTATATCTGTATG-3′	Osman et al., 2018
8	*mntS*-Pro_R	5′-CATACAGATATAGCACAGGCTATGTTTTATAG-3′	Osman et al., 2018
9	*fur-box*_F	HEX-5′-GGGGATAATGATAATCATTATCGGG-3′	Osman et al., 2018
10	*fur-box*_R	5′-CCCGATAATGATTATCATTATCCCC-3′	Osman et al., 2018
11	*copA*-Pro_F	HEX-5′-CTTGACCTTAACCTTGCTGGAAGGTTTAACCTT-3′	Osman et al., 2018
12	*copA*-Pro_R	5′-AAGGTTAAACCTTCCAGCAAGGTTAAGGTCAAG-3′	Osman et al., 2018
13	*zntA*-Pro_F	HEX-5′-AATAGCGCTTGACTCTGGAGTCGACTCCAGAGTGTATCCTCCGG-3′	Osman et al., 2018
14	*zntA*-Pro_R	5′-CCGGAGGATACACTCTGGAGTCGACTCCAGAGTCAAGCGCTATT-3′	Osman et al., 2018
15	*znuA*-Pro_F	HEX-5′-TAGAATGTTATAATATCACATTTCACACATTCA-3′	Osman et al., 2017
16	*znuA*-Pro_R	5′-TGAATGTGTGAAATGTGATATTATAACATTCTA-3′	Osman et al., 2017

spectrophotometer (Thermo Scientific). Duplex annealing was achieved by adding F-strands and reverse (R) strands (10 μM final concentrations) to a microfuge tube containing 25 μL Chelex-treated Buffer T where Milli-Q water was added to achieve a total volume of 50 μL (final buffer condition: 10 mM HEPES pH 7.0, 120 mM KCl, 30 mM NaCl). Control samples containing either F- or R-strand oligonucleotides were set up in parallel, with Milli-Q water added to compensate for the volume of the omitted oligonucleotide. Samples were heated at 95°C for 10 min in a TC-3000 thermocycler (Techne) then the temperature was allowed to decrease to 20°C overnight (14-16 h). Annealed duplexes were stored at -20°C, wrapped in aluminium foil to protect from ambient light.

2.9.2 Native gel analysis of duplex formation

Annealed duplexes were analysed by native gel electrophoresis using hand-poured gels (12% acrylamide in 1x Tris-Borate-EDTA (TBE) buffer). Reactions and control samples were prepared for analysis by diluting into 1x annealing buffer (Section 2.9.1) and 6x DNA loading dye (Thermo Scientific). The gel was run for ~ 90 min at 90 V then placed in 1x TBE buffer containing 0.5 μg mL^{-1} of ethidium bromide for 30 min before viewing under a UV-lamp and photographed (Bio-Rad XR+ Gel Documentation System). Samples which indicated visible single-strand oligonucleotide bands were discarded.

2.9.3 *Salmonella* sensor DNA titrations (fluorescence anisotropy)

The DNA affinities of each *Salmonella* sensor for its operator, or a representative operator, were determined by fluorescence anisotropy (FA). Apo or metal-loaded sensors (in Buffer E) were titrated against a fixed concentration of the relevant operator duplex in 1 mL of Chelex-treated Buffer N using a two-way gas-tight quartz cuvette. After each addition of protein, the sample was allowed to equilibrate for 3 min at 25°C then scanned (λ_{ex} 530 nm, λ_{em} 570 nm) using a modified Cary Eclipse fluorescence spectrophotometer (Agilent Technologies). Each data point collected was an average of triplicate values where the modified program runs three replicate scans (averaging time = 15 s, Ex. slit = 5 nm, Em. slit = 5 nm) to generate one such value. The ratio of vertically and horizontally polarised emitted light was determined at each protein concentration to produce an observed anisotropy value (r_{obs}; see Equation 2.1).

$$r_{obs} = \frac{I_{\parallel} - I_{\perp}}{I_{\parallel} - 2I_{\perp}} \tag{2.1}$$

The change in anisotropy (Δr_{obs}) over the titration was used to monitor the fraction of DNA bound. The buffer for metal-free proteins also contained 1 mM EDTA to prevent trace metal

contaminations from affecting the experiment. To generate Ni(II)-sensor samples, 0.95 and 1.05 equivalents of Ni(II) were added to NikR and RcnR, respectively, to determine the holo-protein DNA affinities. RcnR was given at least 30 min (25°C) equilibration time with Ni(II) whereas NikR was left overnight (14-16 h, 25°C) to equilibrate due to initial aggregation (also the reason behind sub-saturating the protein with metal). MntR, Fur, CueR, ZntR, and Zur were loaded with Ni(II) as described in the text (Chapter 4) and were allowed to equilibrate at 25°C for > 30 min (> 2 h for Zur). For ZntR, 5 μM Ni(II) was also added to the buffer in order to populate weaker Ni(II) sites within the protein.

2.9.4 Calculation of the coupling free energy (ΔG_C) for DNA-binding

The coupling free energy for a reaction can be described by the following equation:

$$\Delta G_C = -RT \ln K_C \tag{2.2}$$

where R is the gas constant (~ 8.314 J mol^{-1} K^{-1}), T is the temperature in Kelvin (298.15 K at room temperature), and K_C is the ratio of the equilibrium (dissociation) constants that describe the DNA-affinities for the metal-free (K_3) and the metal-bound (K_4) sensor (see Equation 2.3).

$$K_C = \frac{K_3}{K_4} \tag{2.3}$$

ΔG_C represents the free energy difference associated with the change in DNA affinity as a result of metal binding and provides a consistent method for comparing this change in affinity instead of considering the absolute affinity values for different sensors (Giedroc and Arunkumar, 2007, Guerra and Giedroc, 2012). The values considered here have units of kcal mol^{-1} (1 J ≈ 2.39 × 10^{-4} kcal).

ΔG_C values were calculated for each individual data set for K_3 and K_4 (not the overall combined affinity values, see Section 2.10.2). For sensors with > 1:1 protein:DNA, the affinity for the first binding event (i.e. K_{4a}) was used in the calculation. The final ΔG_C value was the average from the replicate data sets for each sensor, and the standard deviation is reported.

2.10 Data fitting and simulations

Metal and DNA titration data for each sensor were analysed using DynaFit (Kuzmic, 1996) to generate best fits for experimental data using nonlinear least-squares regression. Binding models describing the equilibria present in a titration are generated using the DynaFit scripting protocol (see Sections 7.2-7.6) and allowed for simultaneous fitting of all data sets collected as well as determination of confidence intervals for the parameter(s) of interest. DynaFit was also used to simulate data to determine the experimental limits of the assay and to model the effect of physiological competitors on sensor DNA occupancy.

2.10.1 Determination of sensor Ni(II) affinity (K_1)

Ni(II) titration data sets for one sensor-competitor pair were fit simultaneously in the same script (Section 7.2). Stepwise affinities were determined for each site within the oligomeric protein where Ni(II)-binding was modelled sequentially using statistical factors for loading to identical sites (Section 2.10.3). The Ni(II) stoichiometry is discussed in the main text and determines the number of sequential events.

For all calculated stepwise affinity values, the 95% confidence interval was determined using Monte-Carlo simulations as part of the DynaFit script. A wide interval indicated a less well-defined K value, likely due to the limits of an assay (e.g. differences between competitor and protein Ni(II) affinity). In parallel, simulations of 10-fold tighter and 10-fold weaker K values were performed for each titration to graphically demonstrate the limit of each competition experiment.

2.10.2 Determination of sensor DNA affinities (K_3 and K_4)

DNA titration data sets were fit simultaneously in the same script for each protein to determine K_3 (Section 7.3). A modified script was required to simultaneously fit K_4 values (Section 7.4), taking into account the average K_1 metal affinities (Section 2.10.4) for the number of sites of interest for each sensor (determined by the Ni(II) ratio added to the protein). This allows for the presence of apo-sensor in the case of weak Ni(II)-binding proteins. Each data set (for K_3 and K_4) was also fit individually to calculate ΔG_C (Section 2.9.4). Stepwise affinities (and associated statistical factors, see Section 2.10.3) were required when multiple binding events were observed per DNA duplex (RcnR, Fur, CueR, and Zur). 95% confidence intervals were determined as described in Section 2.10.1.

2.10.3 Statistical coefficients for modelling identical stepwise binding events

Statistical coefficients are required for determining the stepwise affinities for equivalent binding sites in a multimeric system. These coefficients account for the available sites remaining in the multimer as sites are filled with successive binding events. The coefficients are easily calculated from the ratios of the rate constants for each binding event (where $K_d = k_d/k_a$). Shown below is the derivation of the coefficients for a molecule with four equivalent binding sites (e.g. K_1 for NikR), with K_{d1} representing the dissociation constant for the first binding event. In this case, the rate constant for Ni(II)-binding (k_a) is multiplied by 4 because there are 4 sites that can bind Ni(II) compared to the final binding event (K_{d4}) where only one site remains for Ni(II)-binding:

$$K_{d1} = \frac{k_d}{4k_a} \; ; \; K_{d2} = \frac{2k_d}{3k_a} \; ; \; K_{d3} = \frac{3k_d}{2k_a} \; ; \; K_{d4} = \frac{4k_d}{k_a}$$

K_{d2}, K_{d3}, and K_{d4} can be rewritten as a function of K_{d1}, linked by a statistical coefficient (a, b, and c, respectively):

$$K_{d2} = \frac{2k_d}{3k_a} = a\left(\frac{k_d}{4k_a}\right), \qquad \therefore \; a = \frac{8}{3} \tag{2.4}$$

$$K_{d3} = \frac{3k_d}{2k_a} = b\left(\frac{k_d}{4k_a}\right), \qquad \therefore \; b = 6 \tag{2.5}$$

$$K_{d4} = \frac{4k_d}{k_a} = c\left(\frac{k_d}{4k_a}\right), \qquad \therefore \; c = 16 \tag{2.6}$$

The statistical coefficient ($x = 4$) for the simpler case of two equivalent binding events was determined using the same approach as above.

2.10.4 Determination of average affinity constants (K_1, K_3, and K_4)

Stepwise affinity values (K_1, K_3, and K_4), accounting for appropriate statistical coefficients (Section 2.10.3), for equivalent binding events (or for two binding events with different affinities) were converted to an average affinity (units of M) by calculating the n^{th} root of the β-value (where n is the total number of binding events described by the β-value, e.g. $\beta_4 = K_{1a}K_{1b}K_{1c}K_{1d}$; units of M^4).

When the number of binding events with different affinities (i.e. not related by statistical coefficients) was greater than two (only applicable for K_1), the average affinity was determined by modelling Ni(II) binding (using stepwise affinities) to a protein concentration of 1×10^{-16} M (i.e. a concentration below the tightest affinity Ni(II) site). The concentration

of Ni(II) at which the selected protein sites were 50% metal bound was determined from the model curve, equating to the average affinity value.

An average K_1 was determined for the number of sites of interest when determining sub-stoichiometric and fully loaded K_4 values (Section 2.10.2) using the methods described above.

2.10.5 Calculation of cellular sensor and DNA concentrations

Sensor abundances (oligomers per cell) were determined elsewhere under metal limiting conditions (P_0) and in growth media supplemented with cognate metal (P_1) (Osman et al., 2017, Osman et al., 2018). The number of DNA targets for each sensor has also been determined elsewhere (Osman et al., 2018). These values were converted to concentration using Avogadro's constant (6.02×10^{23} mol^{-1}) and a cellular volume of 1×10^{-15} L.

2.10.6 Simulation of sensor Ni(II)-occupancy

The Ni(II)-bound occupancy of each *Salmonella* sensor was simulated (Section 7.5) at physiological concentrations using the stepwise K_1 affinities coupled with the cellular concentration (Section 2.10.5). To determine the fraction of Ni(II) bound to allosterically active sites, additional sites were removed from the simulation but the allosteric site affinities remained the same (including appropriate statistical coefficients calculated for the protein as a whole). When L-histidine was included as a physiological competitor, the simulation used Ni(II)-affinities (pH 7.5) of 6.40×10^{-7} M (K_{d1}) and 8.85×10^{-6} M (K_{d2}) (Zhang et al., 2000).

2.10.7 Simulation of fractional DNA occupancy by sensors

DNA occupancy by a sensor can be determined using average affinity constants (Section 2.10.4) through a recently described mathematical model (Model 1) (Osman et al., 2018). In this model, Ni(II) availability is defined as a buffered concentration where metal transfer occurs through associative ligand exchange and equilibria are included which link promoter occupancy to the change in sensor abundance from P_0 to P_1 as a linear relationship.

Additionally, DNA occupancy can be modelled using DynaFit (Section 7.6) for each sensor with appropriate concentrations and average affinity constants (Model 2). In this case, protein concentrations were fixed to a single value but the model could include L-histidine as a buffer molecule (Section 2.10.6). This model described the total concentration of Ni(II) added to the system where L-histidine is used to replicate the intracellular buffer.

Occupancy of DNA by NikR, RcnR, MntR, Fur, and Zur is modelled for both apo- and holo-protein forms bound to DNA (i.e. *PD* and *PMD* species from Figure 1.2). For CueR and

ZntR, only holo-protein bound to DNA is modelled as occupying the promoter (i.e. *PMD* only from Figure 1.2).

DNA occupancy can be estimated by K_1 affinity alone using the following equation:

$$Occupancy = \frac{[Ni].K_1}{1 + [Ni].K_1} \tag{2.7}$$

Chapter 3: Determination of Ni(II) affinities of the *Salmonella* sensors

3.1 Introduction

3.1.1 Background information and outcomes

Metallosensors bind transition metals with affinities in order of the Irving-Williams series (Section 1.1.1). *Salmonella* encodes seven sensors (MntR, Fur, RcnR, NikR, CueR, ZntR, and Zur), with the prediction that each sensor has the tightest affinity for its cognate metal across the set of sensors. Furthermore, this means that the available (or buffered) level of each metal is only in the range of the cognate sensor's affinity, generating specific transcriptional responses to changes in buffered cognate metal in the cytosol. Hence, MntR will have the tightest affinity for Mn(II), even though it will bind most other metals more tightly. But, because the other sensors have a tighter affinity for their cognate metals, the buffered levels of these metals will not affect MntR, thus it is not predicted to be widely mis-metalated and therefore remains able to sense changes in available Mn(II). However, this raises questions about the ranges of affinities of sensors for non-cognate metals and the consequences if the intracellular buffered level of a particular metal becomes too high, even for a short period. Some insight has been provided by a recent study showing Zn(II) and Co(II) sensing is poised on the edge of infidelity (Osman et al., 2017).

Here, using Ni(II) as the model metal, stepwise K_1 values (Section 1.3.3) have been determined for the set of seven *Salmonella* sensors as the first step to investigate more extensively the capacity for mis-metalation and mal-responses of sensors in a bacterial cytosol. Only one homologue of the non-cognate sensors (*B. subtilis* MntR) has previously been studied for Ni(II) binding (Golynskiy et al., 2006), making it difficult to predict what range of K_1 values would be observed. Ni(II) affinities were measured for native, untagged proteins under the same buffer condition, using different competitor molecules. The two cognate Ni(II) sensors, *Sty*NikR and *Sty*RcnR, were found to have the tightest affinities for Ni(II), analogous to the Zur/ZntR sensors for Zn(II) (Outten and O'Halloran, 2001, Osman et al., 2017). Surprisingly, the Ni(II) affinities of the other five sensors clustered within a fairly narrow range, with *Sty*Fur possessing the next tightest Ni(II) affinity after RcnR. The results suggested an evolved affinity threshold that separates specific and non-specific Ni(II)-binding proteins in the *Salmonella* cytosol. These stepwise affinity values were used to determine average K_1 values for each sensor, which is later used to determine promoter

occupancy (Chapter 5), in conjunction with K_3 and K_4 (Chapter 4), as a function of Ni(II) availability.

3.1.2 Overview of the experimental approach

To determine Ni(II)-affinities, each sensor was purified using established protocols (Section 2.4; Figure 3.1). Experiments with purified sensors were carried out under O_2-free conditions (except MntR, see Section 2.6) to eliminate the deleterious effects of cysteine oxidation on Ni(II) binding (see Section 3.3.3). Protein with < 90% cysteine reactivity after transfer to the anaerobic chamber was not used for determination of Ni(II)-binding parameters. Ni(II)-binding stoichiometry of the purified sensors was assessed by changes in the UV/visible spectrum of the protein upon Ni(II) addition for five of the seven sensors, the intrinsic fluorescence of one (Fur), and by co-migration of Ni(II) and protein through a size exclusion column for all seven sensors. Competition assays are a well-established method for determining metal-protein affinities when these values are sub-micromolar (Pennella et al., 2006) and were used to determine K_1 values for the sensors since these affinities are typically too tight to be determined by direct titration. Ni(II)-binding was detected using spectroscopic signals (UV/visible or fluorescence) from either the Ni(II)-sensor or a Ni(II)-competitor complex. Several competitors that spanned a range of Ni(II) affinities (10^{-14} to 10^{-6} M; Figure 3.2) were used to corroborate Ni(II)-affinity values for each sensor. Monte-Carlo simulations were used to determine the 95% confidence interval for each value (Section 2.10.1). Model curves using 10-fold tighter and 10-fold weaker affinity values were used to identify the limits of the assay under the given experimental condition. Ni(II)-affinities are reported first for the cognate sensors (NikR and RcnR), then for the non-cognate sensors in order of their cognate metal across the first transition row (i.e. from Mn to Zn).

3.2 NikR

3.2.1 The Ni(II)-specific characteristics of *Salmonella* NikR are similar to the *E. coli* protein

The intrinsic absorbance of *Sty*NikR arises from three tyrosines (residues 25, 58, and 60). Ni(II)-binding resulted in spectroscopic features at 243 nm, 262 nm, and 302 nm (Figure 3.3a), characteristic of ligand-to-metal charge transfers (LMCTs) arising from the Ni(II)-Cys95 thiolate interaction. The broad, low-intensity feature at ~ 463 nm is associated with *d-d* transitions that are characteristic of a planar geometry (Wang et al., 2004). These features were identical to those previously reported for *E. coli* NikR (Chivers and Sauer, 2002). The

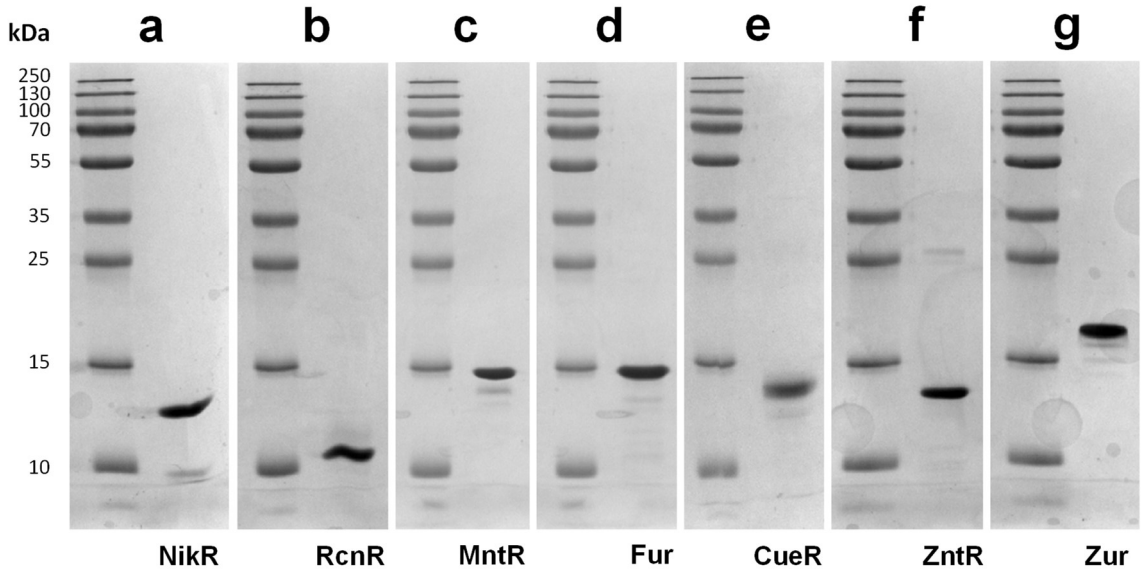

Figure 3.1 Representative SDS-PAGE analysis of *Salmonella* sensor purification. Each panel represents a gel with molecular weight ladder in the left-hand lane and the *Salmonella* sensor in the right-hand land. **(a)** NikR, **(b)** RcnR, **(c)** MntR, **(d)** Fur, **(e)** CueR, **(f)** ZntR, and **(g)** Zur.

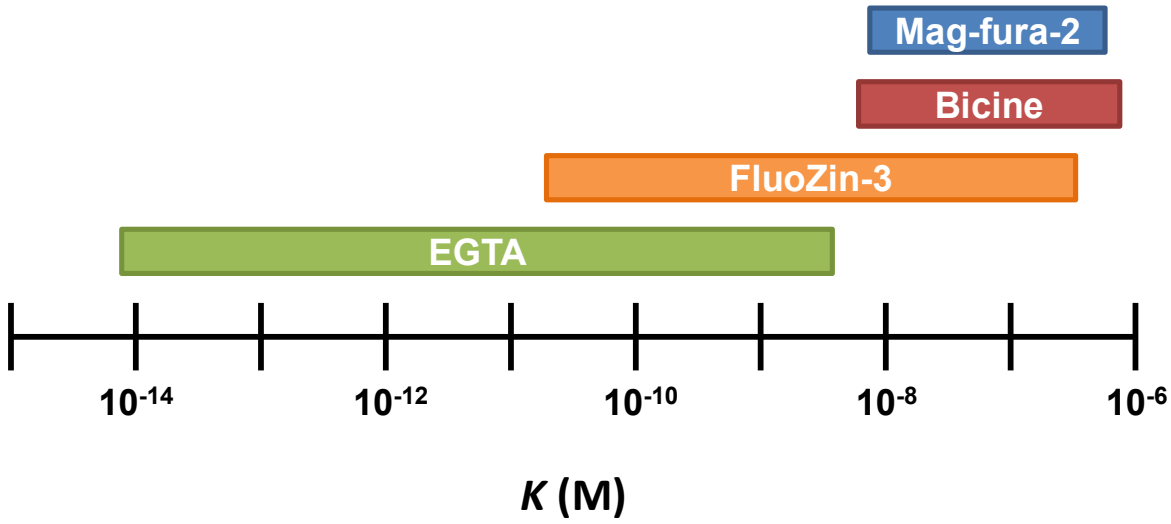

Figure 3.2 Effective Ni(II) affinity ranges for Ni(II)-competitor probes used to determine sensor K_1 values. Ranges are determined based on experimental conditions (competitor and protein concentration) using the observed results in combination with the 10-fold tighter and 10-fold weaker limits. Simulations could be used to predict effective ranges under different competitor or protein concentrations and optimise an assay for accurate determination of affinity. For example, increasing competitor concentration would extend the lower limit of its effective range to a tighter *K* value. Simulations could also be used to design experiments to predict the validity of a fitting model.

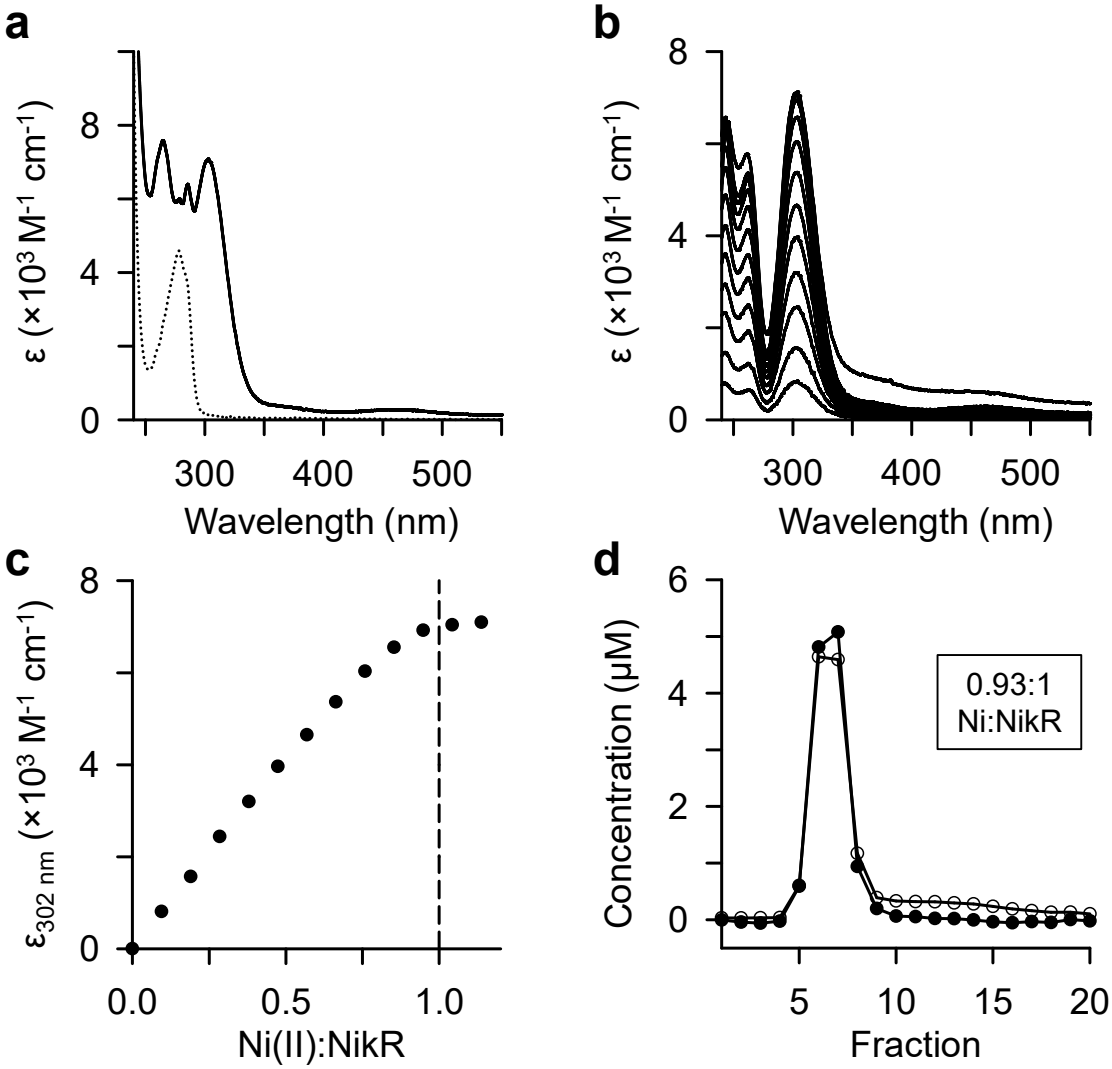

Figure 3.3 Determination of the Ni(II) binding stoichiometry of *Sty*NikR. (a) UV/visible spectra for Ni(II)-NikR (solid line) and apo-NikR (dotted line), both with 10.6 μM NikR monomer. **(b)** Difference spectra for stepwise Ni(II) addition to 10.6 μM NikR. **(c)** Stoichiometry of Ni(II) binding to NikR determined from (b) following increase in $\varepsilon_{302\ nm}$. The dashed line indicates 1:1 binding of Ni(II) to the NikR monomer, or 4:1 Ni:NikR$_4$. **(d)** Co-elution of Ni(II) and NikR through size exclusion chromatography (20 μM NikR monomer with 25 μM Ni(II) applied to the column). NikR concentration (●) determined by Bradford assay and Ni(II) concentration (○) determined by ICP-MS. All above data were collected in buffer E, pH 8.0.

Ni(II)-dependent peaks increased linearly with Ni(II) binding up to 1:1 stoichiometry (Figure 3.3b-c), i.e. four Ni(II) per NikR tetramer. Extinction coefficients for each feature were calculated (Table 3.1). In contrast to the other sensors, the stoichiometric addition experiments were performed in buffer E, pH 8.0 instead of 7.5 because both *E. coli* and *Salmonella* NikR have the tendency to aggregate as Ni(II) concentrations approach 1:1 stoichiometry at neutral pH (Chivers and Sauer, 2000). The increased pH allowed the absorbance at 302 nm to plateau after 1:1 stoichiometry (Figure 3.3c), although there was evidence of slight aggregation in the final Ni(II) addition (Figure 3.3b).

The stoichiometry of Ni(II)-binding was also determined by monitoring the co-migration of Ni(II) and NikR through a PD-10 size exclusion column. The G-25 resin is a desalting matrix and proteins elute in the void volume of this column. Therefore, any small molecules eluting with the protein are most likely to be tightly bound (no dissociation within the ~ 5 min run time) and stoichiometry can be determined within the protein containing fractions. The Ni(II) content of NikR fractions was determined to be 0.93:1 Ni(II):NikR monomer (Figure 3.3d), close to the expected 1:1 ratio.

3.2.2 NikR binds Ni(II) with femtomolar affinity

The Ni(II) affinity of *Sty*NikR was determined by competition with the metal chelator EGTA (Chivers and Sauer, 2002) monitoring the abundance of Ni(II)-NikR using $A_{302\ nm}$. The Ni(II)-EGTA complex does not have any distinct spectroscopic features – an increase in absorbance in the UV-range (< 280 nm) is too broad to use to determine the concentration of Ni(II)-EGTA present at any point but also does not interfere with the 302 nm feature. Three different NikR monomer concentrations were used in competition with EGTA (Figure 3.4a). All three titrations were fit simultaneously (Section 2.10.1) to a model of four equivalent sites per tetramer (Section 7.2). The data fit to a stepwise affinity ($K_{1a\text{-}d}$) of 7.38×10^{-14} M (Table 3.2). Simulated curves for 10-fold tighter and weaker stepwise affinity were plotted against the 12.6 μM data set, and demonstrated that the titrations fell within the upper and lower limits of the assay (Figure 3.4b).

A hydrogen bond network connects two sites within the NikR tetramer (Section 1.3.9). The absolute affinities for each site in the pair could be marginally different if cross-talk is achieved and may account for the slight deviation compared to the overall fit for data collected at 9.0 μM and 16.0 μM protein. Attempting to fit two pairs of sites with slightly different affinities did not appear to solve the deviation (data not shown).

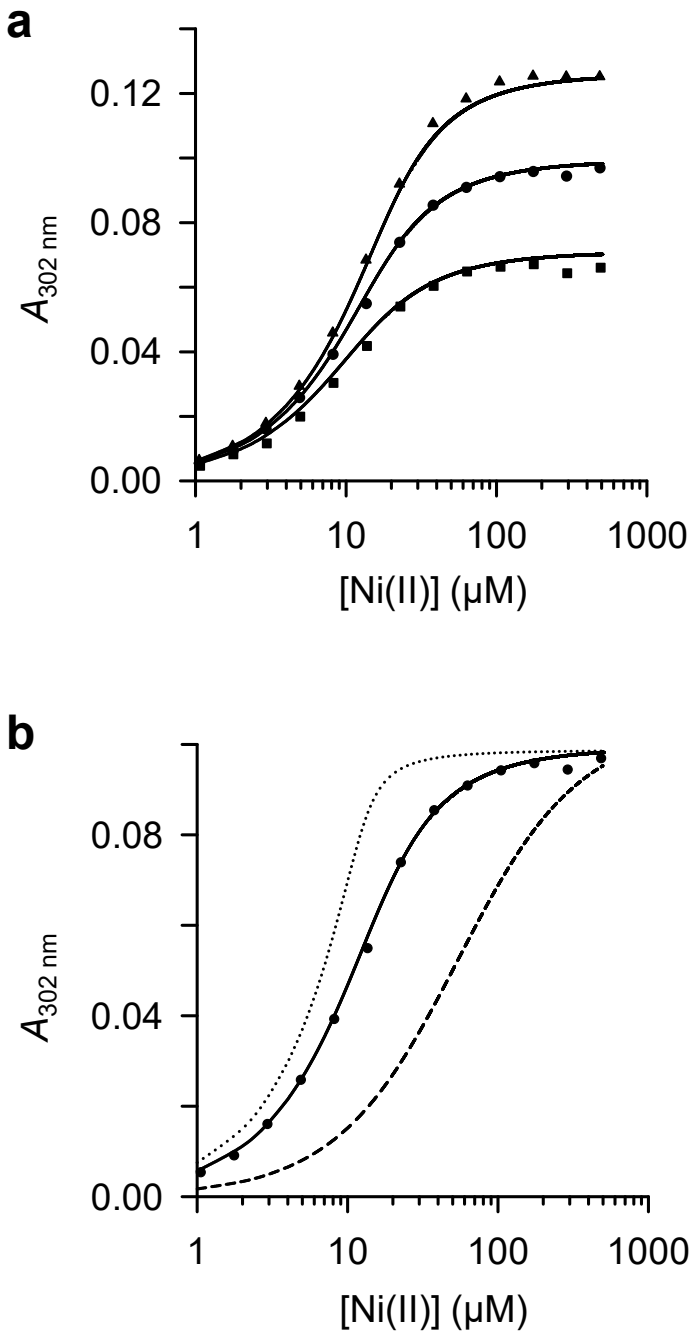

Figure 3.4 Determination of *Sty*NikR Ni(II) affinity by competition with EGTA. (a) Ni(II) titration to three NikR monomer concentrations; 16.0 μM (▲) and 776 μM EGTA; 12.6 μM (●) and 780 μM EGTA; 9.0 μM (■) and 786 μM EGTA. The plotted data correspond to the $A_{302\ nm}$ feature of Ni(II)-NikR. Solid lines indicate best simultaneous fit to all three data sets. The K_1 values and 95% confidence interval from the fit are listed in Table 3.2. **(b)** Modelled fits for 12.6 μM NikR titration using $K_{1a\text{-}d}$ 10-fold tighter (dotted line) or 10-fold weaker (dashed line) to show the limits of the assay.

3.3 RcnR

3.3.1 *Salmonella* RcnR binds Ni(II) similarly to the *E. coli* protein

The intrinsic absorbance of *Sty*RcnR arises from a single tyrosine (residue 88). Ni(II)-binding results in UV/visible spectral features of low intensity (Figure 3.5a-b) compared to several of the other *Salmonella* sensors. Structure-function studies of *E. coli* RcnR showed that Cys35 directly coordinates the Ni(II) and in the Cys35Ala variant the spectral features are significantly reduced even though the protein is still functionally Ni(II) responsive (Iwig et al., 2008). The difference spectra for the stoichiometric Ni(II) titration to *Sty*RcnR (Figure 3.5b) revealed spectral features at 280 nm and 286 nm, with a shoulder at 326 nm, similar to *E. coli* RcnR (Iwig et al., 2008). Extinction coefficients have been calculated for these features (Table 3.1). These peaks increased linearly up to 1:1 Ni(II) to RcnR monomer (Figure 3.5c), or four Ni(II) per RcnR tetramer, as shown for the *E. coli* protein (Iwig et al., 2008). The Ni(II):RcnR stoichiometry determined by co-migration through a size exclusion column was 0.94:1 (Figure 3.5d).

3.3.2 RcnR has a Ni(II) affinity four orders of magnitude tighter than previously estimated

The Ni(II) affinity of RcnR was determined by competition assay. Initial experiments suggested the Ni(II) affinity of *Sty*RcnR was tighter than the previously published value for *Ec*RcnR ($2.5 \pm 0.4 \times 10^{-8}$ M (Iwig et al., 2008)). Therefore, the Ni(II) affinity was determined using competitors with progressively tighter Ni(II) affinities, including EGTA. Following the Ni(II)-RcnR feature at 326 nm, four titration data sets were fit in competition with EGTA (Figure 3.6a) to a four-equivalent sites model for *Sty*RcnR with an affinity ($K_{1a\text{-}d}$) of 1.18×10^{-12} M (Table 3.2). This value was within the limits of the assay (Figure 3.6b), noting that for most protein concentrations, the data points at the two highest Ni(II) concentrations did not follow the obvious trend set by early data points, and a large jump in absorbance occurred when Ni(II) exceeded the concentration of EGTA. These data points were omitted from the final fit when determining the Ni(II) affinity of RcnR.

3.3.3 Corroborating the *Sty*RcnR Ni(II)-binding model

Initially, the Ni(II) affinity was measured using the weaker FluoZin-3 competitor. Ni(II)-binding to FluoZin-3 was followed by an increase in fluorescence (Section 2.8.3) and it was immediately clear that RcnR could outcompete FluoZin-3 for Ni(II) (Figure 3.7a), as indicated by the lack of Ni(II)-FluoZin-3 fluorescence up to a concentration approximately three-quarters that of RcnR, consistent with RcnR being largely saturated with Ni(II) before

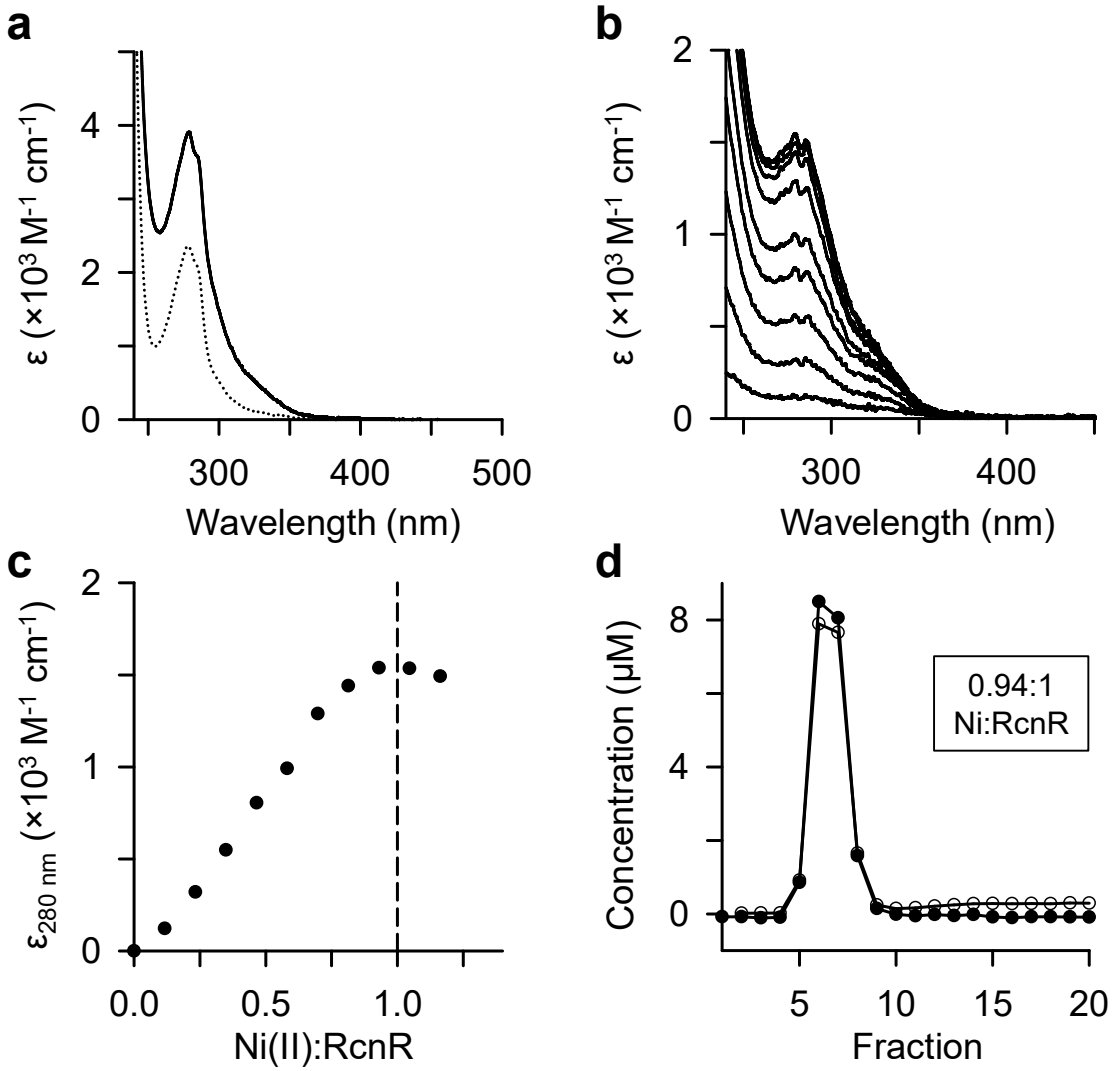

Figure 3.5 Determination of the Ni(II) binding stoichiometry of *Sty*RcnR. **(a)** UV/visible spectra for Ni(II)-RcnR (solid line) and apo-RcnR (dotted line), both with 17.2 μM RcnR monomer. **(b)** Difference spectra for stepwise Ni(II) addition to 17.2 μM RcnR. **(c)** Stoichiometry of Ni(II) binding to RcnR determined from (b) following increase in $\varepsilon_{280\ nm}$. The dashed line indicates 1:1 binding of Ni(II) to the RcnR monomer, or 4:1 Ni:$RcnR_4$. **(d)** Co-elution of Ni(II) and RcnR through size exclusion chromatography (20 μM RcnR monomer with 30 μM Ni(II) applied to the column). RcnR concentration (●) determined by Bradford assay and Ni(II) concentration (○) determined by ICP-MS.

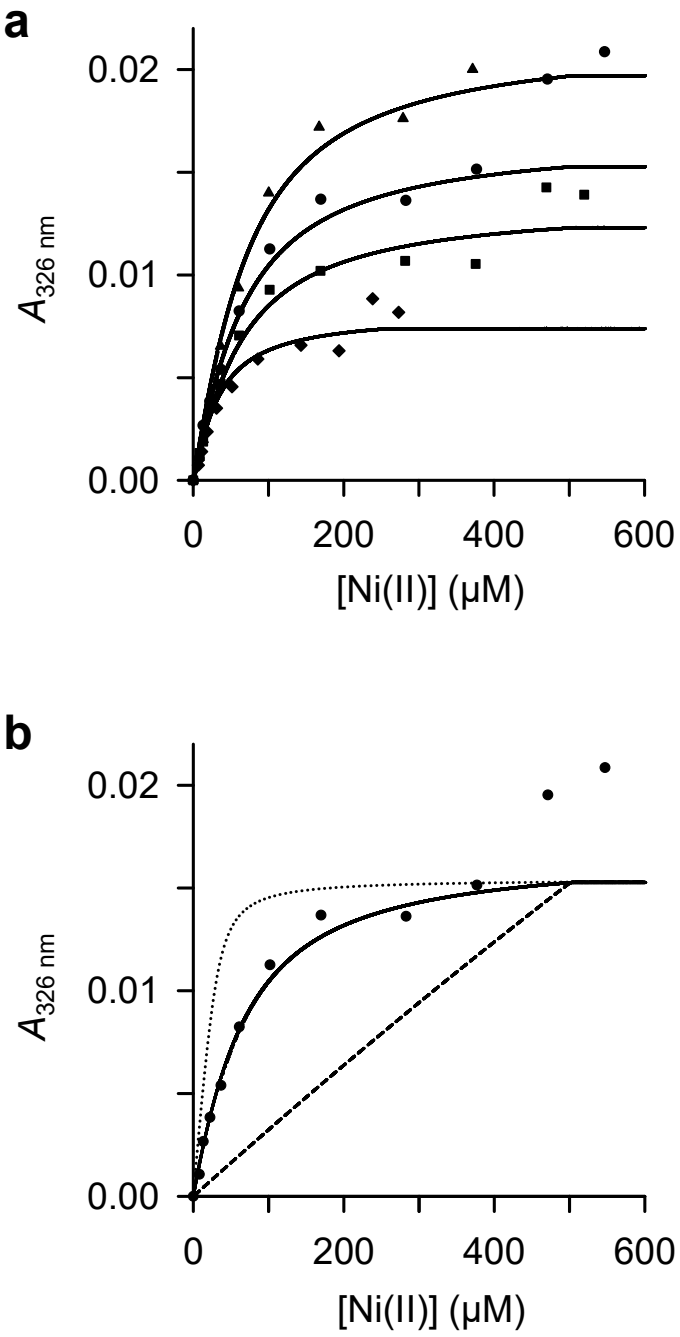

Figure 3.6 Determination of *Sty*RcnR Ni(II) affinity by competition with EGTA. (a) Ni(II) titration to four RcnR monomer concentrations; 40.4 μM (▲) and 464 μM EGTA; 31.5 μM (●) and 471 μM EGTA; 25.3 μM (■) and 479 μM EGTA; 15.3 μM (♦) and 243 μM EGTA. The plotted data correspond to the $A_{326\ nm}$ feature of Ni(II)-RcnR. Solid lines indicate best simultaneous fit to all three data sets. The K_1 values and 95% confidence interval from the fit are listed in Table 3.2. **(b)** Modelled fits for 31 μM RcnR titration using $K_{1a\text{-}d}$ 10-fold tighter (dotted line) or 10-fold weaker (dashed line) to show the limits of the assay.

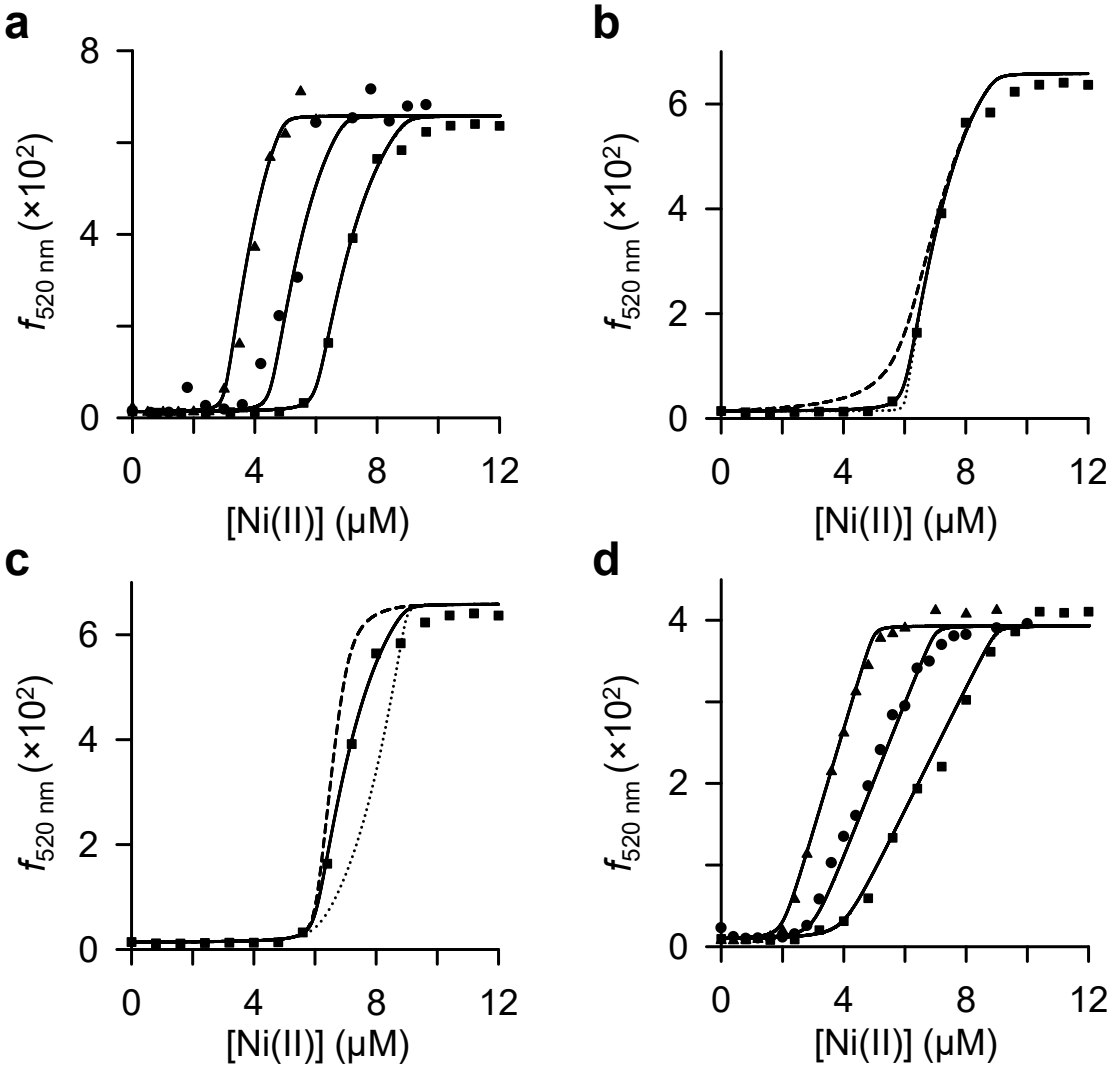

Figure 3.7 Determination of *Sty*RcnR Ni(II) affinity by competition with FluoZin-3. (a) Ni(II) titration to three RcnR monomer concentrations, 4 μM (▲), 6 μM (■), and 8 μM (●), in competition with 1 μM FluoZin-3. The plotted data correspond to FluoZin-3 emission ($f_{520\ nm}$). Solid lines indicate best simultaneous fit to all three data sets. The data was fit as $K_{1a\text{-}c}$ 2.00×10^{-12} M and K_{1d} 9.70×10^{-9} M (RcnR 94% reduced). **(b)** Modelled fits for 8 μM RcnR titration using $K_{1a\text{-}c}$ 10-fold tighter (dotted line) or 10-fold weaker (dashed line) to show the limits of the assay. **(c)** Same as (b) expect with limits for K_{1d}. **(d)** Ni(II) titration to RcnR with undetermined thiol reactivity. Conditions otherwise the same as in (a). The data was fit as $K_{1a\text{-}b}$ 7.00×10^{-12} M and $K_{1c\text{-}d}$ 1.48×10^{-9} M.

FluoZin-3 bound the metal. These data were simultaneously fit to a different four sites model and generated values of $K_{1a\text{-}c}$ 2.00×10^{-12} M and K_{1d} 9.70×10^{-9} M. The $K_{1a\text{-}c}$ value was at the lower limit of the assay (Figure 3.7b), while the K_{1d} value falls within the range of this competitor (Figure 3.7c) and was not too dissimilar from the *Ec*RcnR value (see Section 3.3.2).

During the course of the work with *Sty*RcnR, different protein preparations were used, which revealed variations in the Ni(II)-affinities determined and provided insight into the discrepancy between the affinity determined in Section 3.3.2 for *Sty*RcnR and that previously reported for *Ec*RcnR. For example, an earlier preparation of *Sty*RcnR showed a weaker affinity in competition with FluoZin-3 (Figure 3.7d). This experiment used the same protein concentrations as in Figure 3.7a but the increase in FluoZin-3 fluorescence at lower Ni(II) concentration indicated less competition with RcnR and a different model. The affinities determined here were $K_{1a\text{-}b}$ 7.00×10^{-12} M and $K_{1c\text{-}d}$ 1.48×10^{-9} M where again the tighter-binding events were at the lower limit but the weaker-binding events could be fit and were comparable to the *Ec*RcnR value. A likely explanation for this discrepancy was thiol oxidation (Cys35), which would either reduce the active population of protein (if a Cys-S-S-Cys inter-subunit disulphide bond formed) or reduce the affinity if Cys35 was oxidised to -S-OH or higher. Initial preparations had not been rigorously analysed for cysteine oxidation and protein purified from cell pellets stored at -80°C for weeks to months generated the variable affinity values, suggesting oxidation was a potential cause. All subsequent preparations were purified soon after growth and only when > 90% of thiols were active was the protein stock considered useful for experimentation. Such samples remained stable to oxidation when stored anaerobically. The *Ec*RcnR protein was handled aerobically in the presence of reducing agent (TCEP), though this was removed for affinity measurements. Due to the presumed effect of oxidation on *Sty*RcnR Ni(II) binding observed in this work, it seems most likely that the Ni(II)-affinity determined for *Ec*RcnR reflected use of partially oxidised protein.

The varying RcnR models from different protein preparations can be compared to highlight the disparity between them. These models with their determined affinities (EGTA affinity calculated in Section 3.3.2, initially estimated affinity from FluoZin-3 data, and reported affinity for *Ec*RcnR) are shown in Figure 3.8a with data from the FluoZin-3 "$K_{1a\text{-}c} + K_{1d}$" model. Similarly, Figure 3.8b shows that using the "$K_{1a\text{-}c} + K_{1d}$" model, from the FluoZin-3 experiment, can fit the *Sty*RcnR EGTA with relatively good agreement. The data fits well because the total response was not fixed and varied to fit the majority of the data points with good agreement but it was clear that the end points were different where the fit was

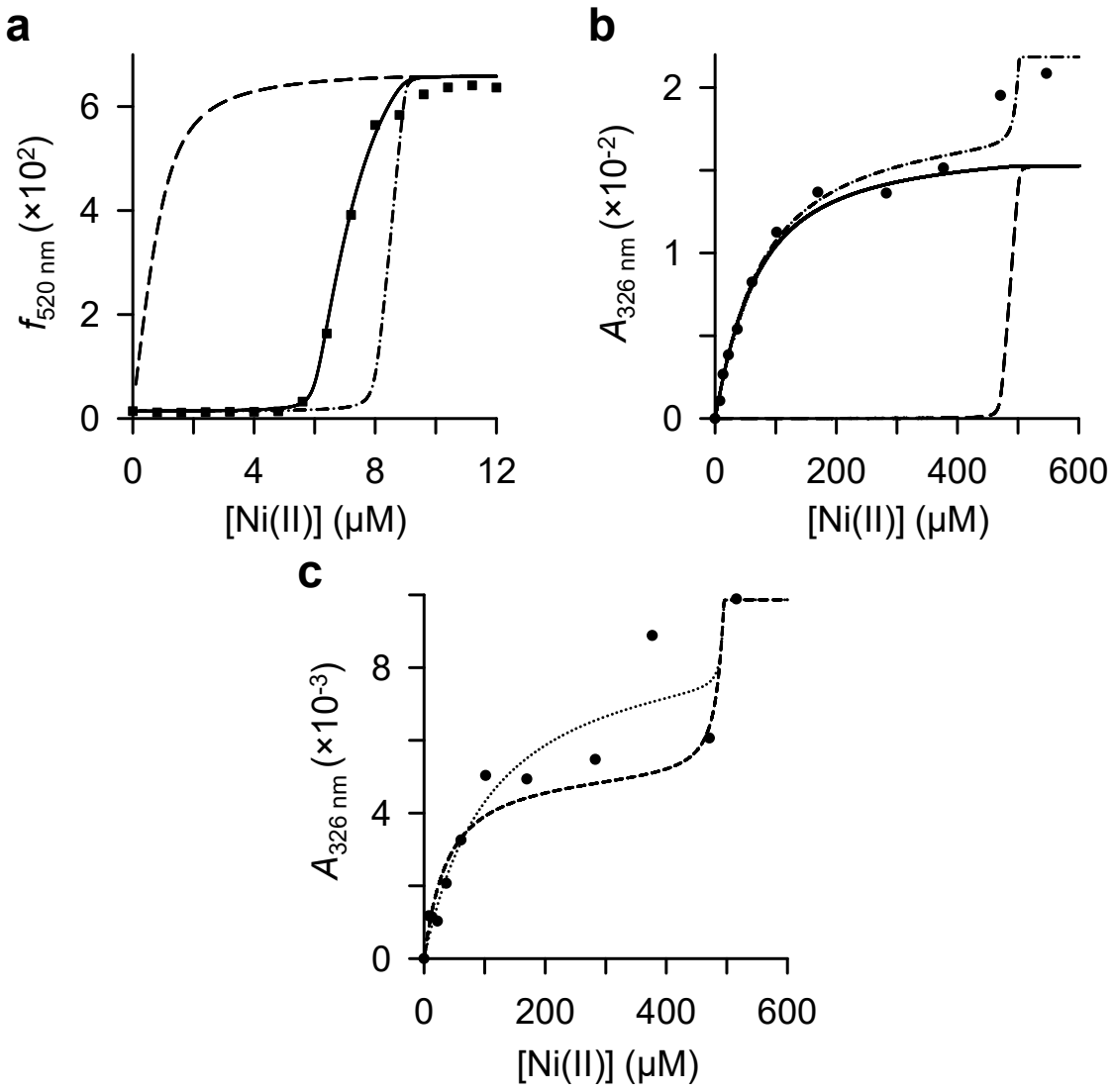

Figure 3.8 Simulations to compare *Sty*RcnR affinity values determined from competition with FluoZin-3 and EGTA. (a) Ni(II) titration to RcnR and FluoZin-3 (from Figure 3.7b) showing a single data set and the fit (solid line). Also simulated are the expected curves based on the EGTA affinity/model from Figure 3.6a (dash-dot-dash line) and for the previously published affinity of 2.50×10^{-8} M (dashed line). **(b)** Ni(II) titration to RcnR and EGTA showing a single data set (Figure 3.6a) and the fit (solid line). Also simulated is the $K_{1a\text{-}c} + K_{1d}$ model seen with FluoZin-3 (Figure 3.7b) with the same affinities (dash-dot-dash line). The final simulation is that for the previously published affinity at 2.50×10^{-8} M (dashed line). **(c)** Ni(II) titration to RcnR (undetermined thiol reactivity) and EGTA showing that the data fitted to neither the $K_{1a\text{-}b} + K_{1c\text{-}d}$ model (dashed line) or $K_{1a\text{-}c} + K_{1d}$ model (dotted line), as implied from two FluoZin-3 experiments with different RcnR preps. The simulations in (c) were run with a response fixed to the final end point of the titration.

overestimating the final response from Ni(II)-RcnR. Furthermore, an early Ni(II) titration data set for RcnR (undetermined thiol reactivity) and EGTA with a fixed response does not fit to either of the "$K_{1a\text{-}b} + K_{1c\text{-}d}$" or "$K_{1a\text{-}c} + K_{1d}$" models suggested from the FluoZin-3 data (Figure 3.8c). This indicated a fixed ratio of high-affinity to low-affinity sites (either 2:2 or 3:1 from the two models) does not exist, suggesting an external variable (likely oxidation) contributed to the different affinities.

3.4 MntR

3.4.1 The MntR dimer can bind four Ni(II) ions

The intrinsic absorbance of *Sty*MntR arises from two residues (Tyr41 and Trp89). Addition of Ni(II) did not produce metal-dependent spectral features (Figure 3.9a), though there was a slight reduction in the absorbance of the protein in the 250-300 nm range (2% decrease at 280 nm). The lack of intense Ni(II)-dependent spectral features was consistent with the absence of cysteine residues in *Sty*MntR, eliminating the possibility of features due to thiolate LMCT bands. It remains possible that Ni(II)-binding could result in low-intensity spectral features which would be apparent at greater protein concentrations (also applicable for *Sty*Fur, see Section 3.5.1). The aromatic residue absorbance change could be due to Ni(II)-binding either altering the local environment surrounding the Tyr residue or causing a larger scale conformational change (i.e. via a network of intramolecular interactions) with longer range effects on the Trp residue. To determine whether MntR could indeed bind Ni(II), metal and protein were mixed and their co-migration through a size exclusion column was examined (Figure 3.9b). This experiment showed that Ni(II) bound to MntR with a 1.14:1 Ni(II) to MntR monomer stoichiometry. To test if this stoichiometry reflected dissociation of a more weakly bound Ni(II) from a 2:1 complex (MntR binds two Mn(II) per monomer), the co-migration study was repeated using running buffer that contained 5 μM $NiCl_2$ to allow population of additional weaker Ni(II) sites (Figure 3.9c). Under this condition, the ratio of Ni(II):MntR monomer was found to be 1.91:1 (effectively 2:1), indicating that MntR has two Ni(II) sites per monomer, or four per dimer, which can bind to Ni(II) with sub-micromolar affinity, but with a difference in affinity between the first and second sites of each monomer.

3.4.2 Ni(II) binds to MntR with negative cooperativity

The Ni(II) affinities of the binding sites within the MntR dimer were determined by competition assay. The lack of a Ni(II)-dependent UV/visible feature of MntR required the

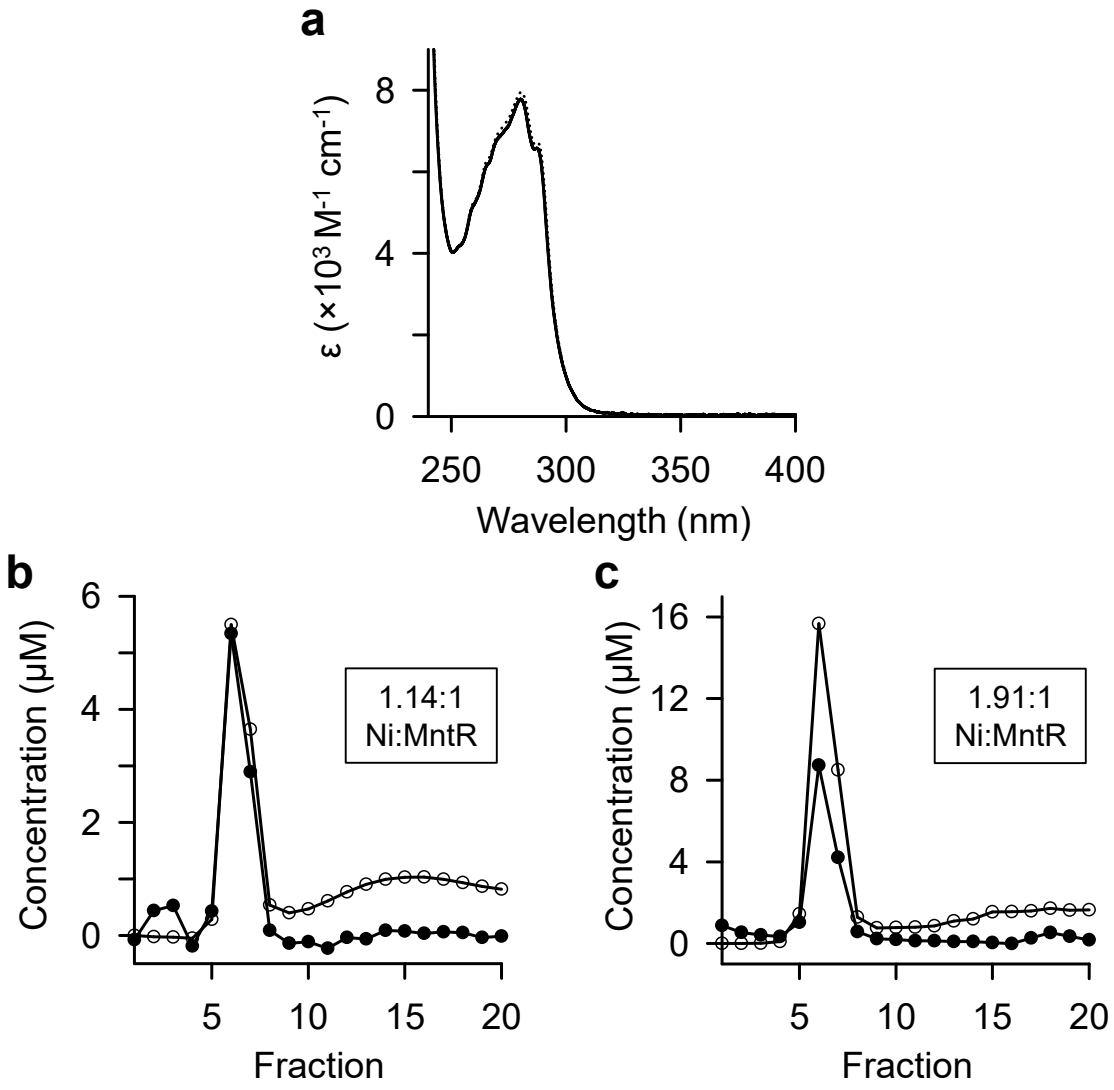

Figure 3.9 Determination of the Ni(II) binding stoichiometry of *Sty*MntR. (a) UV/visible spectra for Ni(II)-MntR (solid line) and apo-MntR (dotted line), both with 20.9 μM MntR monomer. **(b)** Co-elution of Ni(II) and MntR through size exclusion chromatography (15 μM MntR monomer with 40 μM Ni(II) applied to the column). MntR concentration (●) determined by $A_{280\ nm}$ and Ni(II) concentration (○) determined by ICP-MS. **(c)** Same as (b) except 15 μM MntR monomer loaded with 32 μM Ni(II) and a running buffer containing 5 μM $NiCl_2$.

use of a competitor with spectroscopic changes upon Ni(II)-binding. Ni(II) was titrated to three concentrations of MntR monomer in competition with FluoZin-3 (Figure 3.10a). The simplest model was expected to be $K_{1a} = K_{1b}$ and $K_{1c} = K_{1d}$ (based on the co-migration studies), however, this model was not a good fit. Instead the data was fit as K_{1a}, K_{1b}, and $K_{1c\text{-}d}$, where $K_{1a} \neq K_{1b}$ (allowing for cooperativity), and generated the affinities of K_{1a} 1.70×10^{-10} M, K_{1b} 2.26×10^{-8} M, and $K_{1c\text{-}d}$ 1.30×10^{-7} M (Table 3.2). The limits for these affinity values suggested that K_{1a} could be an underestimation as the data points were tending towards the lower limit (Figure 3.10b). Without access to a tighter competitor with a spectroscopic change upon Ni(II) binding, it was not possible to further probe the first Ni(II) binding site. K_{1b} was well defined (Figure 3.10c) but $K_{1c\text{-}d}$ was at the upper limit of the assay (Figure 3.10d), indicating these weaker sites would be better determined using a less competitive Ni(II) chelator. The data indicated significant negative cooperativity (100-fold change) between the first two Ni(II)-binding events (K_{1a} and K_{1b}) with this protein.

Mag-fura-2, was used to further investigate the weaker $K_{1c\text{-}d}$ sites in the MntR dimer. The Ni(II) affinity of mag-fura-2 is an order of magnitude weaker than that of FluoZin-3 (see Sections 2.8.3 and 2.8.4). Ni(II) was titrated to three concentrations of MntR monomer and mag-fura-2, following $A_{366\,nm}$ of the chelator (Figure 3.11a), and fit to the same model as for FluoZin-3 which generated affinities of K_{1a} 4.60×10^{-10} M, K_{1b} 1.68×10^{-8} M, and $K_{1c\text{-}d}$ 2.68×10^{-7} M (Table 3.2). The value for K_{1a} was again at the lower-limit of the assay (Figure 3.11b), as expected due to the weaker affinity of mag-fura-2 compared to FluoZin-3. The K_{1b} data were within the limits of the assay (Figure 3.11c). The limits for $K_{1c\text{-}d}$ suggested this value could be weaker still (Figure 3.11d). The 95% confidence interval for the $K_{1c\text{-}d}$ affinity from the mag-fura-2 titration was narrower than for FluoZin-3, suggesting a better fit value (Table 3.2).

3.5 Fur

3.5.1 Ni(II) binding to Fur results in different spectral features compared to Fe(II)

The intrinsic absorbance of *Sty*Fur arises from four tyrosines (residues 40, 56, 128, and 130). *Sty*Fur is active as a dimer and contains a spectroscopically silent structural zinc-site coordinated by four cysteine residues (Section 1.3.7) within each monomer (two Zn per dimer). These atoms are kinetically trapped and are not known to undergo substitution with other metals. Therefore, metal-free or apo-Fur refers here to the protein with Zn in the structural sites (also for Zur, see Section 3.8.1). When analysed for thiol reactivity, *Sty*Fur

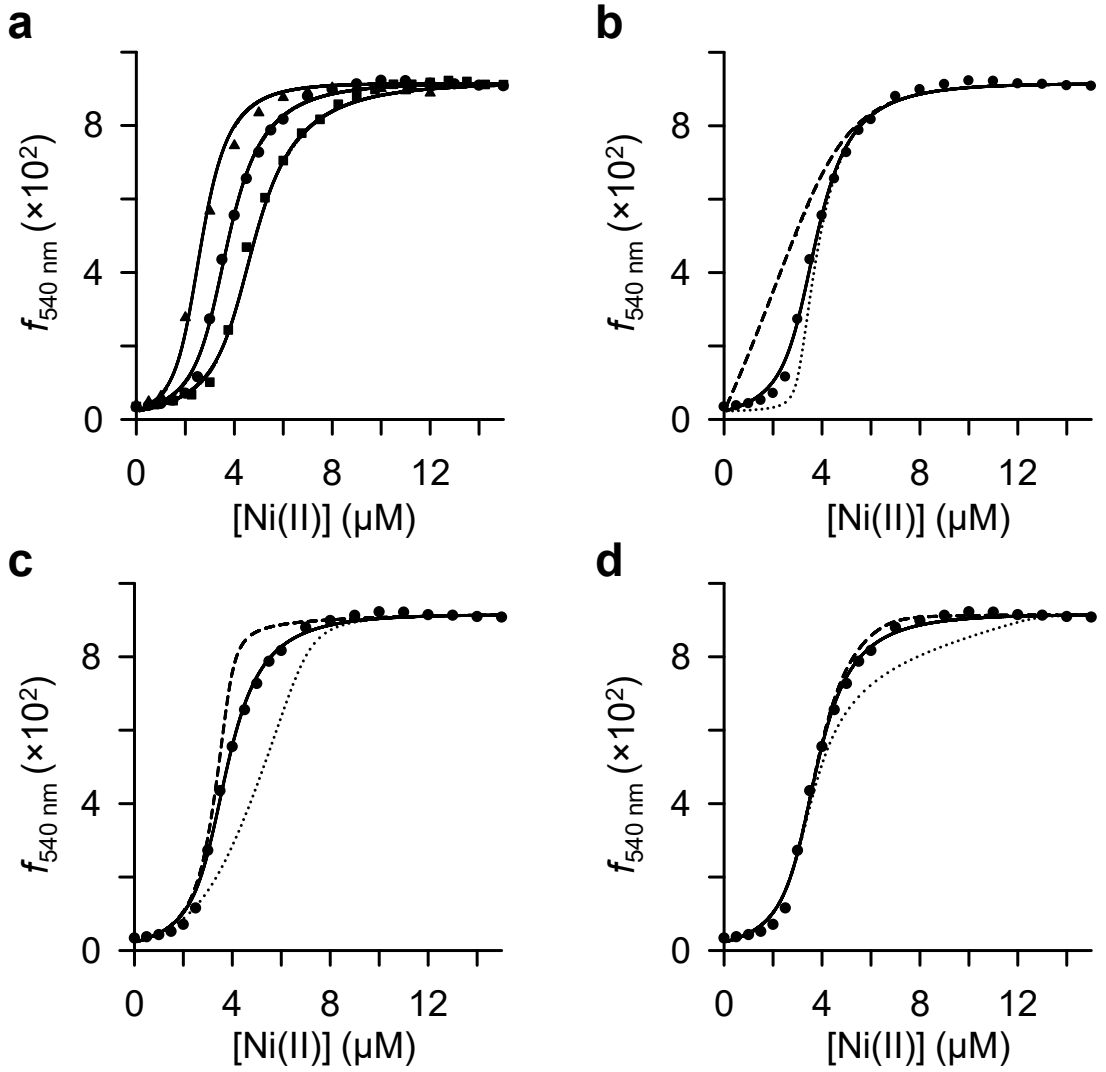

Figure 3.10 Determination of *Sty*MntR Ni(II) affinity by competition with FluoZin-3. (a) Ni(II) titration to three MntR monomer concentrations, 4 μM (▲), 6 μM (●), and 8 μM (■),in competition with 1 μM FluoZin-3. The plotted data correspond to FluoZin-3 emission ($f_{540\ nm}$). Solid lines indicate best simultaneous fit to all three data sets. The K_1 values and 95% confidence interval from the fit are listed in Table 3.2. **(b)** Modelled fits for 6 μM MntR titration using K_{1a} 10-fold tighter (dotted line) or 10-fold weaker (dashed line) to show the limits of the assay. **(c)** Same as (b) except with limits for K_{1b}. **(d)** Same as (b) except with limits for $K_{1c\text{-}d}$.

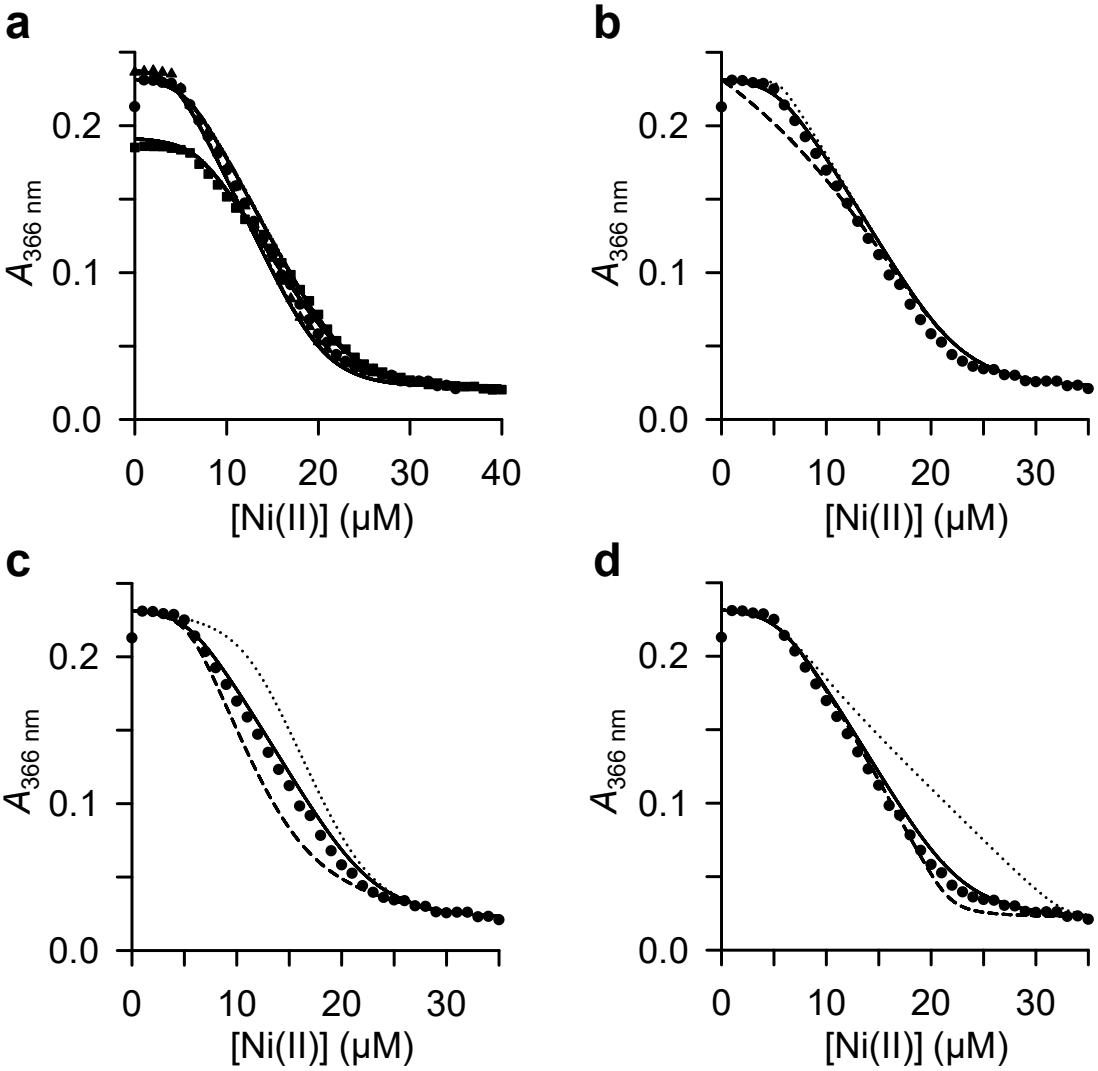

Figure 3.11 Determination of *Sty*MntR Ni(II) affinity by competition with mag-fura-2. (a) Ni(II) titration to three MntR monomer concentrations; 13.4 μM (■) and 8.4 μM mag-fura-2; 11.2 μM (●) and 10.4 μM mag-fura-2; 8.8 μM (▲) and 10.7 μM mag-fura-2. The plotted data correspond to mag-fura-2 absorbance ($A_{366\ nm}$). Solid lines indicate best simultaneous fit to all three data sets. The K_1 values and 95% confidence interval from the fit are listed in Table 3.2. **(b)** Modelled fits for 11.2 μM MntR titration using K_{1a} 10-fold tighter (dotted line) or 10-fold weaker (dashed line) to show the limits of the assay. **(c)** Same as (b) except with limits for K_{1b}. **(d)** Same as (b) except with limits for $K_{1c\text{-}d}$.

does not show the expected Cys content until after > 48 h of incubation, due to the structural Zn (this contrasts with *Sty*Zur, in which the homologous residues react within 2 h). Addition of Ni(II) did not produce metal-dependent UV/visible spectral features (Figure 3.12a), although a small change at 276 nm was observed (< 1% decrease). This was consistent with absence of any free cysteine residues to coordinate Ni(II) and through which LMCTs would be observed. In contrast, Ni(II) binding to Fur quenches the intrinsic tyrosine fluorescence (Figure 3.12b) and this spectroscopic change was used to determine the stoichiometry of Ni(II)-binding (Figure 3.12c). Fluorescence quenching plateaued at a Ni(II):Fur monomer ratio of 1:1.

Co-migration studies were carried out with Ni(II) and Fur to independently measure the stoichiometry, and revealed a Ni(II):Fur monomer ratio of 1.83:1 (Figure 3.12d). The addition of 5 μM $NiCl_2$ to the running buffer increased that value to 2.28:1 Ni(II):Fur monomer ratio (Figure 3.12e), again approximately 2:1. The simplest conclusion from these experiments was that Fur can bind four Ni(II) per dimer where only one pair of Ni(II) sites caused a fluorescence change, in contrast to Fe(II) binding (2:1 stoichiometry) (Osman et al., 2018). Therefore, the spectroscopically silent Ni(II) binding site could be at a spatially different site compared to Fe(II)-Fur or binds at the same site but does not result in the same allosteric conformation, thus limiting changes in the tyrosine environment.

3.5.2 Fur dimer has two tight-binding sites and two weaker-binding sites for Ni(II)

The Ni(II) affinity of Fur was first probed by competition assay, titrating Ni(II) to three different concentrations of Fur monomer in competition with FluoZin-3 (Figure 3.13a). Ni(II) added to approximately 1:1 Ni(II):Fur monomer did not cause a fluorescence change and indicated that the protein was binding the metal, outcompeting FluoZin-3. After this, there appeared to be good competition in the range of FluoZin-3. Therefore, the data was fit to a model where $K_{1a} = K_{1b}$ and $K_{1c} = K_{1d}$ which generated affinities of $K_{1a\text{-}b}$ 8.00×10^{-12} M and $K_{1c\text{-}d}$ 9.60×10^{-10} M (Table 3.2). $K_{1a\text{-}b}$ was at the lower limit of the assay, too tight to fit a reliable value (Figure 3.13b), but $K_{1c\text{-}d}$ was within the limits (Figure 3.13c).

The tighter Fur Ni(II) site caused quenching of tyrosine fluorescence and so an affinity could be measured using EGTA. Ni(II) was titrated to three concentrations of EGTA in competition with Fur monomer (Figure 3.14a). Each titration had slightly different starting fluorescence intensities which suggested slight variations in the concentration of Fur. The Fur concentrations were too low to quantify by $A_{280\text{ nm}}$ so each concentration was estimated during the fitting of the data and allowed to vary within 10% of the expected concentration. The second binding sites ($K_{1c\text{-}d}$) were necessarily included in the model to fit the data (using

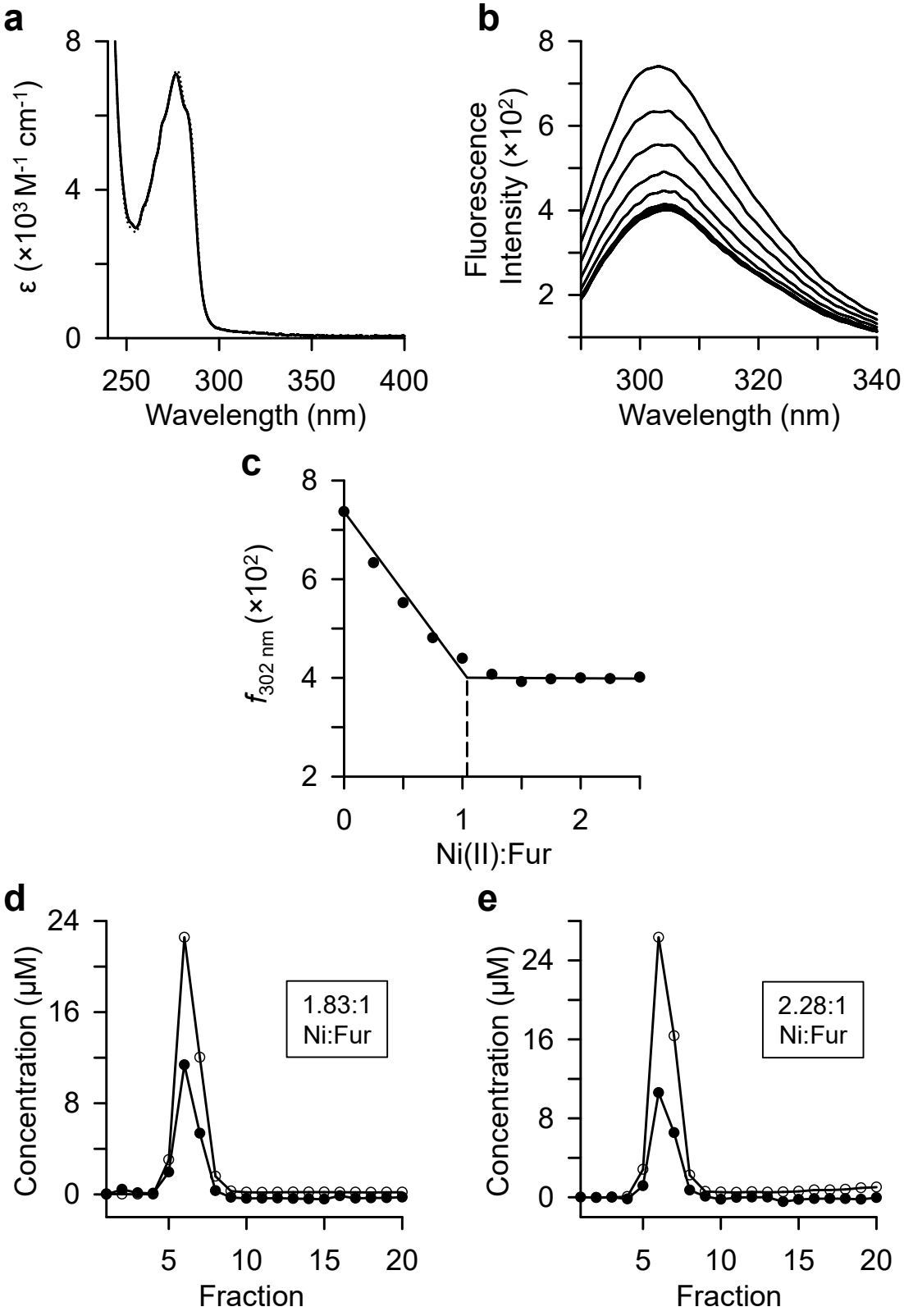

Figure 3.12 Determination of the Ni(II) binding stoichiometry of *Sty*Fur. (a) UV/visible spectra for Ni(II)-Fur (solid line) and apo-Fur (dotted line), both with 25.6 μM Fur monomer. **(b)** Fluorescence emission spectra for stepwise Ni(II) addition to 4 μM Fur monomer (λ_{ex} 276 nm). **(c)** Stoichiometry of Ni(II) binding to Fur determined from (b) following change in $f_{302\ nm}$ emission. **(d)** Co-elution of Ni(II) and Fur through size exclusion chromatography (20 μM Fur monomer with 50 μM Ni(II) applied to the column). Fur concentration (●) determined by $A_{280\ nm}$ and Ni(II) concentration (○) determined by ICP-MS. **(e)** Same as (d) except a running buffer containing 5 μM $NiCl_2$.

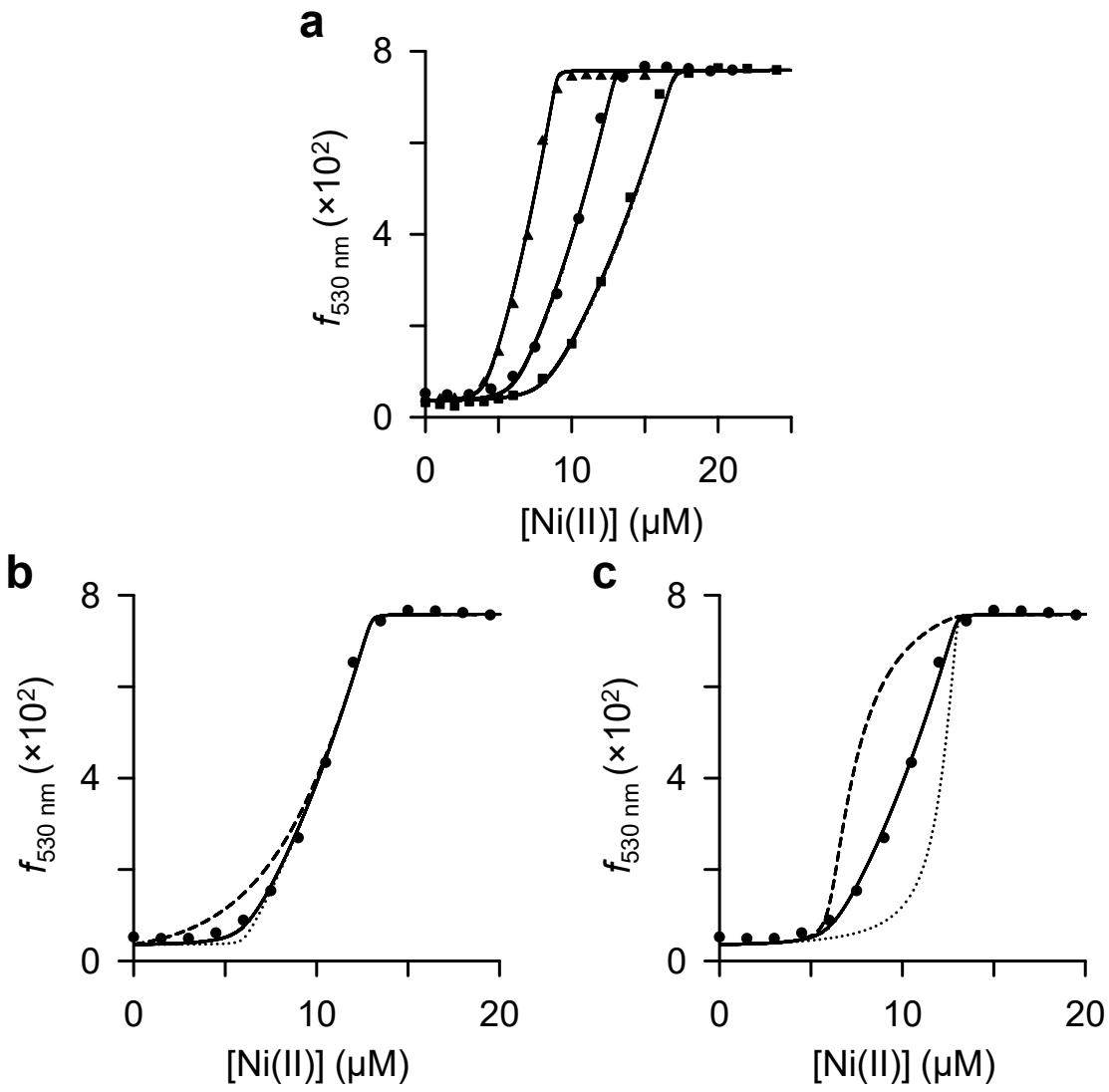

Figure 3.13 Determination of *Sty*Fur Ni(II) affinity by competition with FluoZin-3. (a) Ni(II) titration to three Fur monomer concentrations, 4 μM (▲), 6 μM (●), and 8 μM (■), in competition with 1 μM FluoZin-3. The plotted data correspond to FluoZin-3 emission ($f_{530\ nm}$). Solid lines indicate best simultaneous fit to all three data sets. The K_1 values and 95% confidence interval from the fit are listed in Table 3.2. **(b)** Modelled fits for 6 μM Fur titration using $K_{1a\text{-}b}$ 10-fold tighter (dotted line) or 10-fold weaker (dashed line) to show the limits of the assay. **(c)** Same as (b) except with limits for $K_{1c\text{-}d}$.

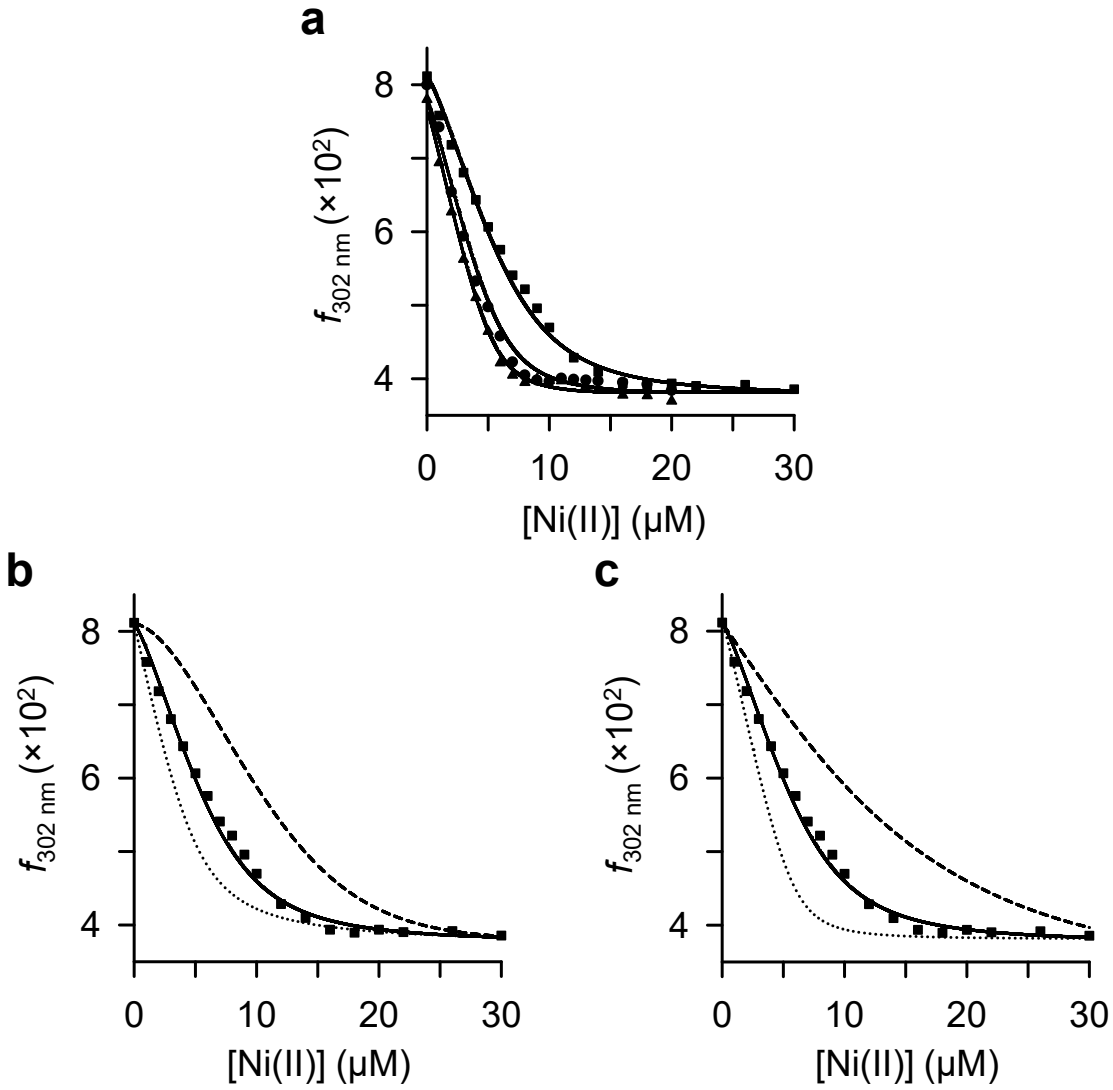

Figure 3.14 Determination of *Sty*Fur Ni(II) affinity by competition with EGTA. (a) Ni(II) titration to 4 μM Fur monomer in competition with three EGTA concentrations, 10 μM (▲), 15 μM (●), and 30 μM (■). The plotted data correspond to Fur emission ($f_{302\ nm}$). Solid lines indicate best simultaneous fit to all three data sets. The K_1 values and 95% confidence interval from the fit are listed in Table 3.2, where $K_{1c\text{-}d}$ values were fixed to those determined from Figure 3.13a. **(b)** Modelled fits for 30 μM EGTA titration using K_{1a} 10-fold tighter (dotted line) or 10-fold weaker (dashed line) to show the limits of the assay. **(c)** Same as (b) except with limits for K_{1b}.

the Ni(II) affinity calculated with FluoZin-3), acting as silent competitors with no fluorescence response. The model which best fit the data allowed K_{1a} and K_{1b} to vary (thus allowing for cooperativity) and determined affinities of K_{1a} 1.19 × 10^{-11} M and K_{1b} 2.52 × 10^{-12} M (Table 3.2), with the limits shown in Figure 3.14b-c.

3.6 CueR

3.6.1 CueR binds Ni(II) with intense spectral features

The intrinsic absorbance of *Sty*CueR arises from three tyrosines (residues 20, 36, and 39). The addition of Ni(II) produced intense absorbance features at 247 nm, 297 nm, 303 nm, 340 nm, and 410 nm (Figure 3.15a). Calculated extinction coefficients are reported in Table 3.1. CueR contains five cysteines (residues 63, 112, 120, 129, and 130) where Cys112 and Cys120 coordinate Cu(I) in the *E. coli* protein (Changela et al., 2003), and Cys129 and Cys130 are not visible in the structure but are located close to the Cu(I) binding site. Stepwise additions of Ni(II) to CueR caused the appearance of Ni(II)-dependent spectral features (Figure 3.15b) in both a linear (Figure 3.15c) and nonlinear manner (Figure 3.16) with saturation at 1.5 Ni(II) per CueR monomer (three Ni(II) per CueR dimer), where Cys129 and Cys130 could form an additional Ni(II) site since they appear to play a role in the binding of other metals (Stoyanov and Brown, 2003). The linear portions of these traces were manually fit with straight lines generating breaks at visible inflexion points. These lines suggested successive binding events produce different signal changes (e.g. breaks at 0.5:1 and 1:1 Ni(II):CueR monomer). The different features suggested binding events with different Ni(II) geometries, or that the original Ni(II)-site geometry changed with successive binding events. For example, the weak feature at 410 nm (Figure 3.16d) is indicative of planar geometry but only increases significantly between 0.5 to 1.5 equivalents of Ni(II), suggesting a different geometry was formed during binding of the first 0.5 equivalents. A detailed structural understanding of how Ni(II) binds to CueR was not pursued as it was not required to understand the thermodynamic effect of Ni(II) on CueR activity. However, the curvature could be a result of competition between different affinity sites, i.e. one feature could be linear until a weaker site becomes more competitive (due to effectively reducing the concentration of tighter sites as they fill). Therefore, Ni(II) will be shared between the alternative sites and no longer stoichiometrically loaded to the tight site (discussed further in Section 3.7.1).

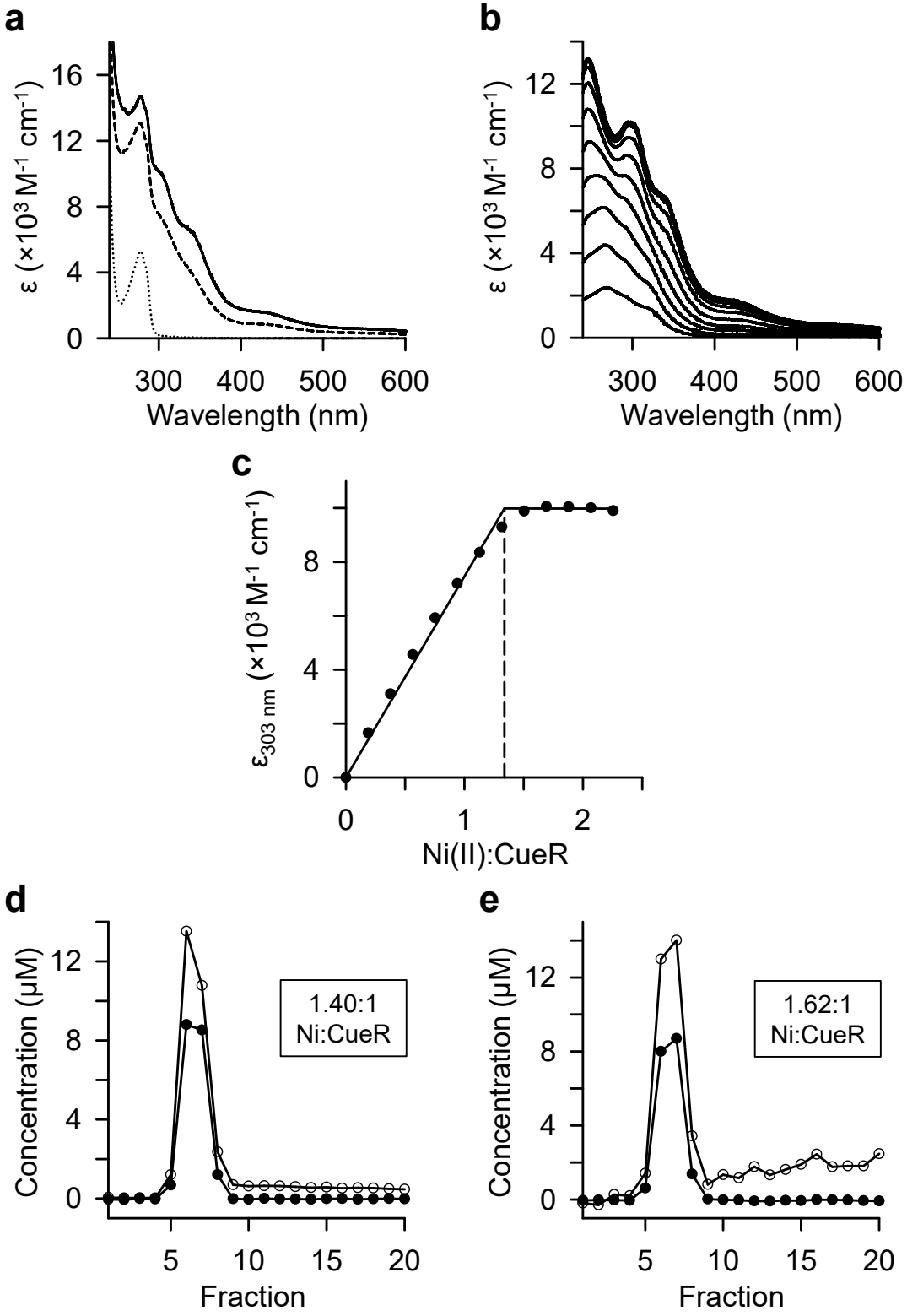

Figure 3.15 Determination of the Ni(II) binding stoichiometry of *Sty*CueR. (a) UV/visible spectra for 1.5:1 Ni(II)-CueR (solid line), 1:1 Ni(II)-CueR (dashed line), and apo-CueR (dotted line), all with 10.6 μM CueR monomer. **(b)** Difference spectra for stepwise Ni(II) addition to 10.6 μM CueR. **(c)** Stoichiometry of Ni(II) binding to CueR determined from (b) following increase in $\varepsilon_{303\ nm}$. The dashed line indicates 1.5:1 binding of Ni(II) to the CueR monomer, or 3:1 Ni:$CueR_2$. **(d)** Co-elution of Ni(II) and CueR through size exclusion chromatography (20 μM CueR monomer with 50 μM Ni(II) applied to the column). CueR concentration (●) determined by Bradford assay and Ni(II) concentration (○) determined by ICP-MS. **(e)** Same as (d) except a running buffer containing 5 μM $NiCl_2$.

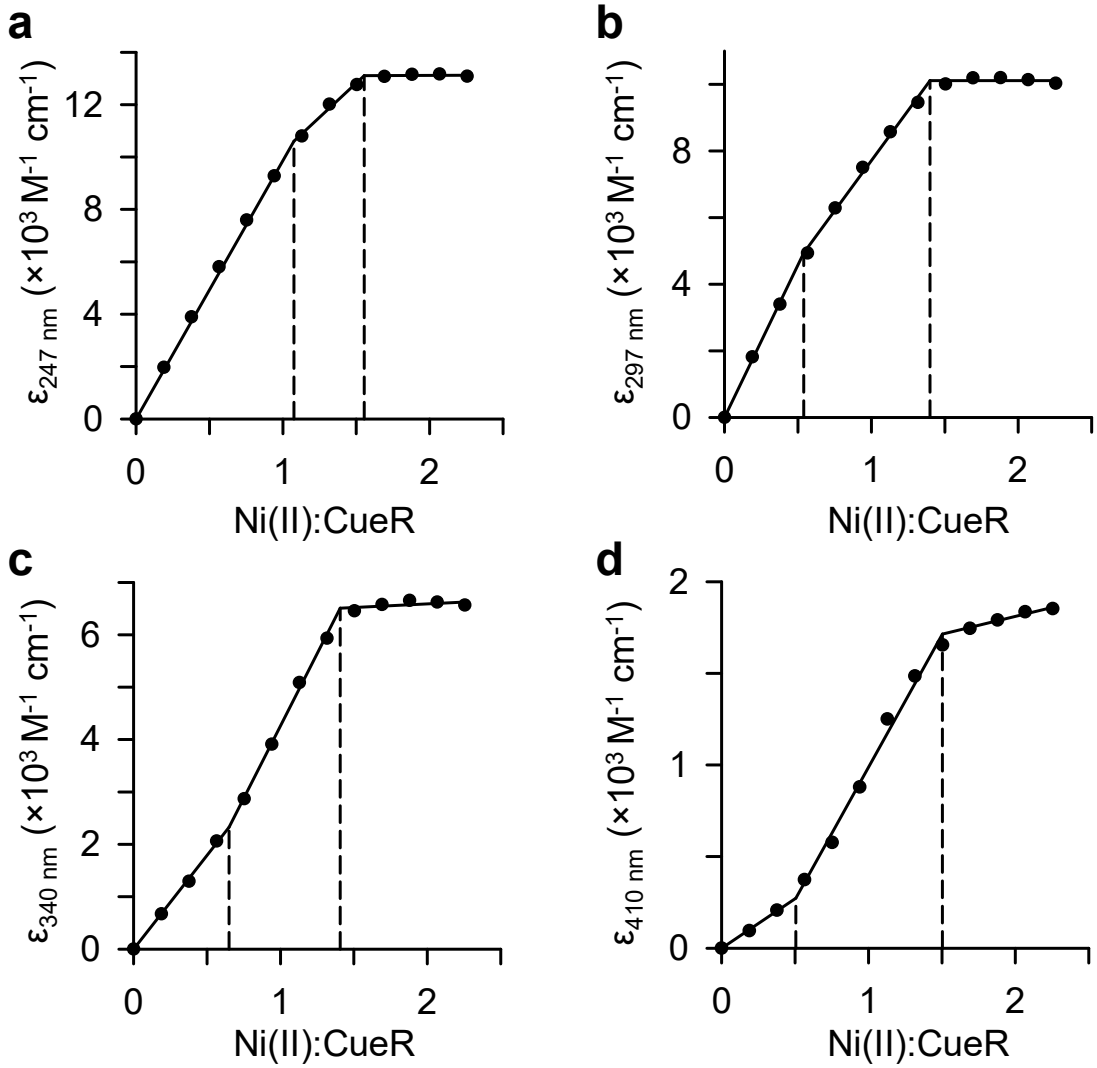

Figure 3.16 *Sty*CueR exhibits nonlinear absorbance changes during stepwise Ni(II) addition. (a), **(b)**, **(c)**, and **(d)** Stoichiometry of Ni(II) binding to CueR (10.6 μM monomer) determined from Figure 3.15b following increase in $\varepsilon_{247\ nm}$, $\varepsilon_{297\ nm}$, $\varepsilon_{340\ nm}$, and $\varepsilon_{410\ nm}$, respectively. The dashed lines represent observed inflexion points.

3.6.2 CueR co-migrates with three Ni(II) ions per dimer

The Ni(II):CueR stoichiometry was determined independently by size exclusion chromatography (Figure 3.15d). The observed value of 1.40:1 Ni(II) to CueR monomer closely matched the value from the UV/visible stoichiometry addition experiment (Section 3.6.1). To test for weaker sites, 5 μM $NiCl_2$ was added to the running buffer (Figure 3.15e) and a similar value was obtained (1.62:1 Ni(II) to CueR monomer). *E. coli* CueR can bind up to three Cu(I) ions per monomer, though only one binds with a high affinity (Chen et al., 2003), indicating an abundant metal binding capacity in this protein. It appears likely that each CueR monomer binds one Ni(II) in or around the Cu(I) binding site because of the intense thiolate LMCT absorbance features. There are additional ligands near the Cu(I)-binding site (His76 and Asp79, conserved between *E. coli* and *Salmonella*) which could orientate to coordinate a Ni(II) ion that requires a higher coordination number than Cu(I). Equally, a coordination environment might recruit non-protein ligands (e.g. water or chloride ions). Alternatively, the additional Ni(II) could be bound at the interface of the two monomers where the *E. coli* structure indicates that two histidine residues (one from each monomer) are positioned centrally on the dimerisation helix which could coordinate a Ni(II) ion, though likely requiring additional ligands. However, the DNA-bound structure of CueR indicates these residues are in a compact position with surrounding hydrophobic residues (Philips et al., 2015) where a Ni(II) ion may negatively impact DNA binding. A further possibility is that two Ni(II) ions bind a CueR dimer relatively favourably but binding of the third causes an allosteric change that drastically reduces the affinity of the equivalent site for the fourth Ni(II) ion.

3.6.3 CueR has a picomolar affinity for Ni(II)

The Ni(II) affinity of CueR was investigated by competition with FluoZin-3, titrating Ni(II) to three CueR monomer concentrations in competition with FluoZin-3 (Figure 3.17a). The data was fit simultaneously using a model that incorporated the observed 3:2 stoichiometry to produce a pair of sites with equivalent affinities $K_{1a\text{-}b}$ 1.57×10^{-10} M and a third site K_{1c} 9.70×10^{-9} M (Table 3.2). Both values were within the limits of the assay (Figure 3.17b-c).

Additional Ni(II) titrations were carried out with different competitors to corroborate the affinities determined using FluoZin-3. Bicine is a spectroscopically silent chelator with a weaker Ni(II) affinity than FluoZin-3 (Section 2.8.2), and was suitable for probing the K_{1c} site of CueR. The experiment used the Ni(II)-dependent CueR absorbance feature at 303 nm to monitor Ni(II)-CueR formation. This wavelength was selected for its linear response to Ni(II) loading (Figure 3.15c). The single set of data for bicine (Figure 3.18a) was fit using

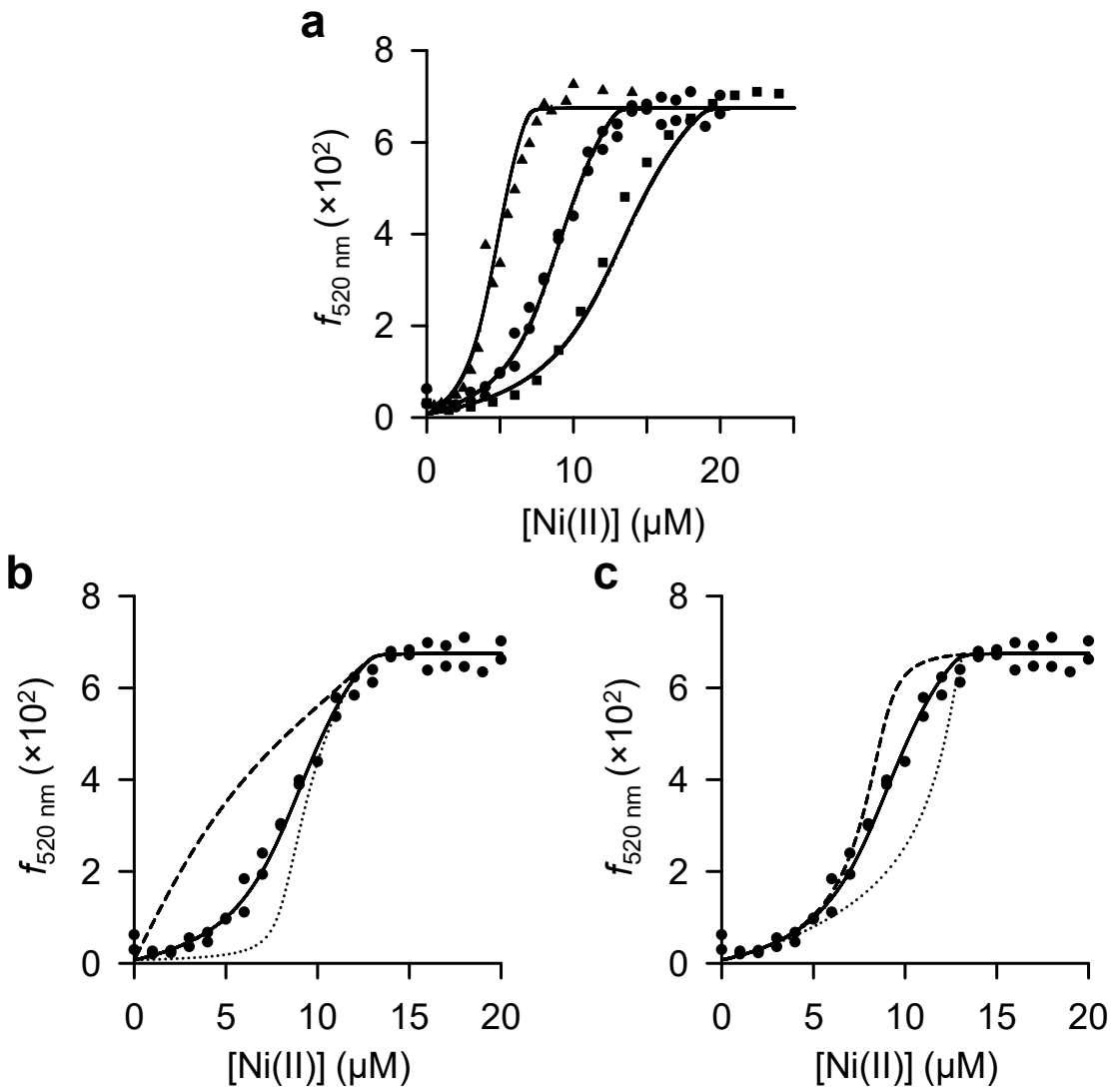

Figure 3.17 Determination of *Sty*CueR Ni(II) affinity by competition with FluoZin-3. (a) Ni(II) titration to three CueR monomer concentrations, 4 μM (▲), 8 μM (●), and 12 μM (■), in competition with 1 μM FluoZin-3. The plotted data correspond to FluoZin-3 emission ($f_{520\ nm}$). Solid lines indicate best simultaneous fit to all three data sets. The K_1 values and 95% confidence interval from the fit are listed in Table 3.2. **(b)** Modelled fits for 8 μM CueR titration using $K_{1a\text{-}b}$ 10-fold tighter (dotted line) or 10-fold weaker (dashed line) to show the limits of the assay. **(c)** Same as (b) except with limits for K_{1c}.

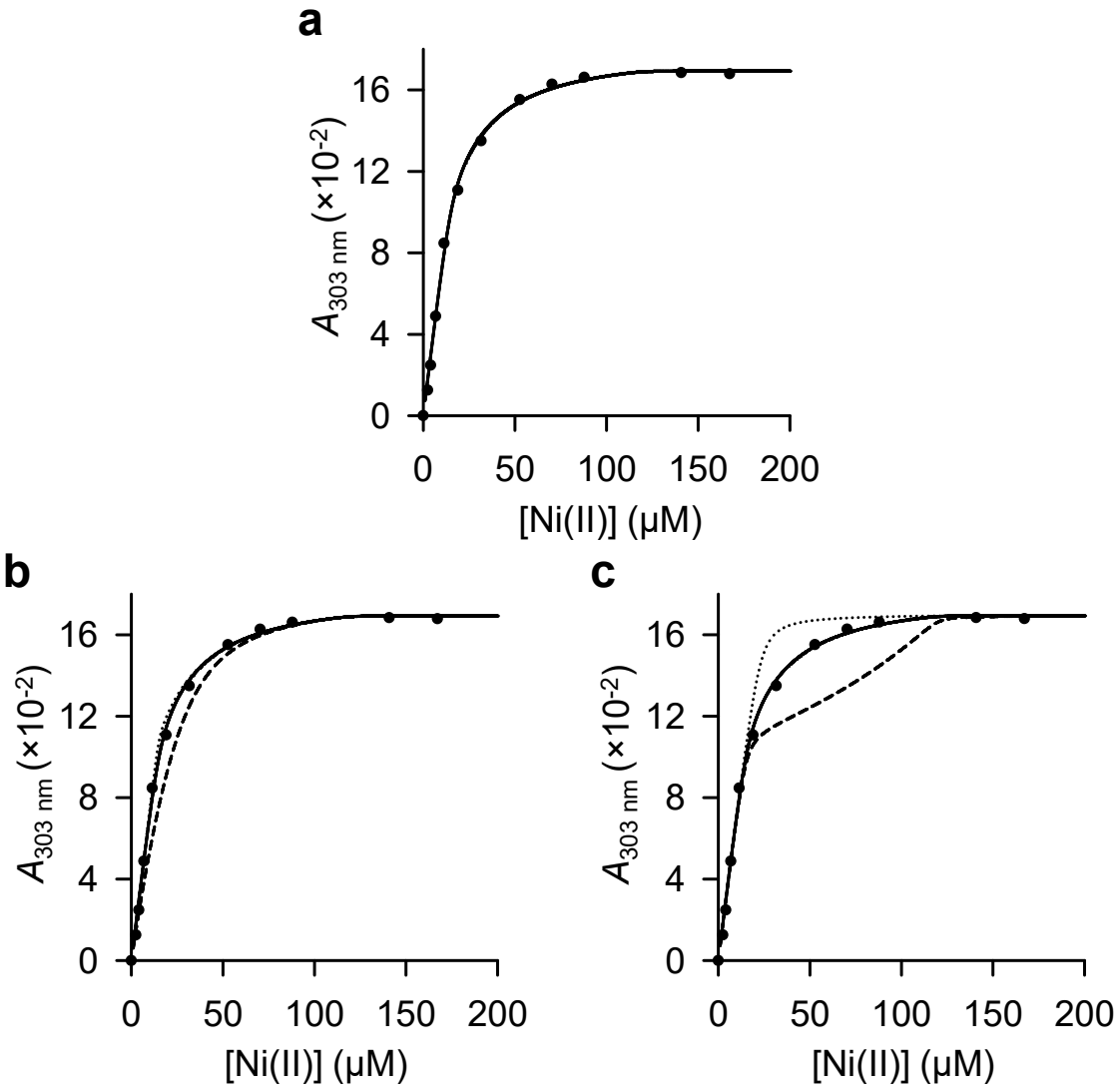

Figure 3.18 Determination of *Sty*CueR Ni(II) affinity by competition with bicine. (a) Ni(II) titration to 15.4 μM CueR monomer and 97.6 μM bicine. The plotted data correspond to the $A_{303\ nm}$ feature of Ni(II)-CueR. The solid line indicates best fit to the data set. The K_1 values and 95% confidence interval from the fit are listed in Table 3.2. **(b)** Modelled fits for this data using $K_{1a\text{-}b}$ 10-fold tighter (dotted line) or 10-fold weaker (dashed line) to show the limits of the assay. **(c)** Same as (b) except with limits for K_{1c}.

the same model as above and generated affinities of $K_{1a\text{-}b}$ 1.95×10^{-10} M and K_{1c} 1.85×10^{-8} M (Table 3.2). The limits for the assay indicated that $K_{1a\text{-}b}$ was a lower limit value because it overlaid the 10-fold tighter curve (Figure 3.18b). This outcome is consistent with the FluoZin-3 competition since bicine is a weak competitor for the $K_{1a\text{-}b}$ sites. K_{1c} was within the limits (Figure 3.18c) and the affinity closely matched that from the FluoZin-3 data (1.9-fold weaker).

The Ni(II) titration was also performed using EGTA as a competitor to corroborate the $K_{1a\text{-}b}$ affinity value. Ni(II) binding to CueR was monitored by $A_{303\ nm}$ for a single set of data (Figure 3.19a). The same model as above was used to fit the data and the resulting affinities were $K_{1a\text{-}b}$ 1.82×10^{-10} M and K_{1c} 2.24×10^{-9} M (Table 3.2). The 10-fold limits for the assay clearly indicated that $K_{1a\text{-}b}$ was within the limits of the assay (Figure 3.19b), whereas K_{1c} was at the 10-fold weaker limit (Figure 3.19c). The model was adjusted to allow the EGTA concentration to vary and resulted in a value 20% lower than the expected concentration. The reason for this difference was not pursued because of the multiple data sets that supported a consistent $K_{1a\text{-}b}$ affinity.

3.7 ZntR

3.7.1 Ni(II) binding to ZntR results in multiple intense spectral features

The intrinsic absorbance of *Sty*ZntR arises from seven tyrosines (residues 2, 20, 21, 40, 53, 123, and 141). As with CueR, Ni(II)-binding produced intense absorbance features (Figure 3.20a) that saturated beyond a stoichiometry of 1:1 Ni(II) to ZntR monomer. Absorbance maxima were identified at 245 nm, 262 nm, 297 nm, 319 nm, 333 nm, and 410 nm, and extinction coefficients have been calculated (Table 3.1). The intense absorbance features likely resulted from LMCTs between Ni(II) and cysteine residues (ZntR contains four cysteines; residues 79, 114, 115, and 124) and all are assumed to be involved in coordinating the cognate Zn(II) ions in the *E. coli* ZntR structure (79′ from one monomer and 114, 115, and 124 from the other with His119 as a fifth ligand) (Changela et al., 2003). The dinuclear Zn(II) site in the *E. coli* ZntR structure is not consistent with all experimental data for this protein (Section 1.3.10) and therefore the site is probably tetrahedral (Cys_4 coordination). Nonetheless, numerous potential ligands for Ni(II) coordination are available around the Zn(II) binding site. Stepwise Ni(II) additions to ZntR (Figure 3.20b) revealed that the Ni(II)-dependent features had different behaviours (Figure 3.21). Interestingly, when the ratio of Ni(II) to ZntR was > 1:1, the spectrum between 260-290 nm decreased in absorbance after

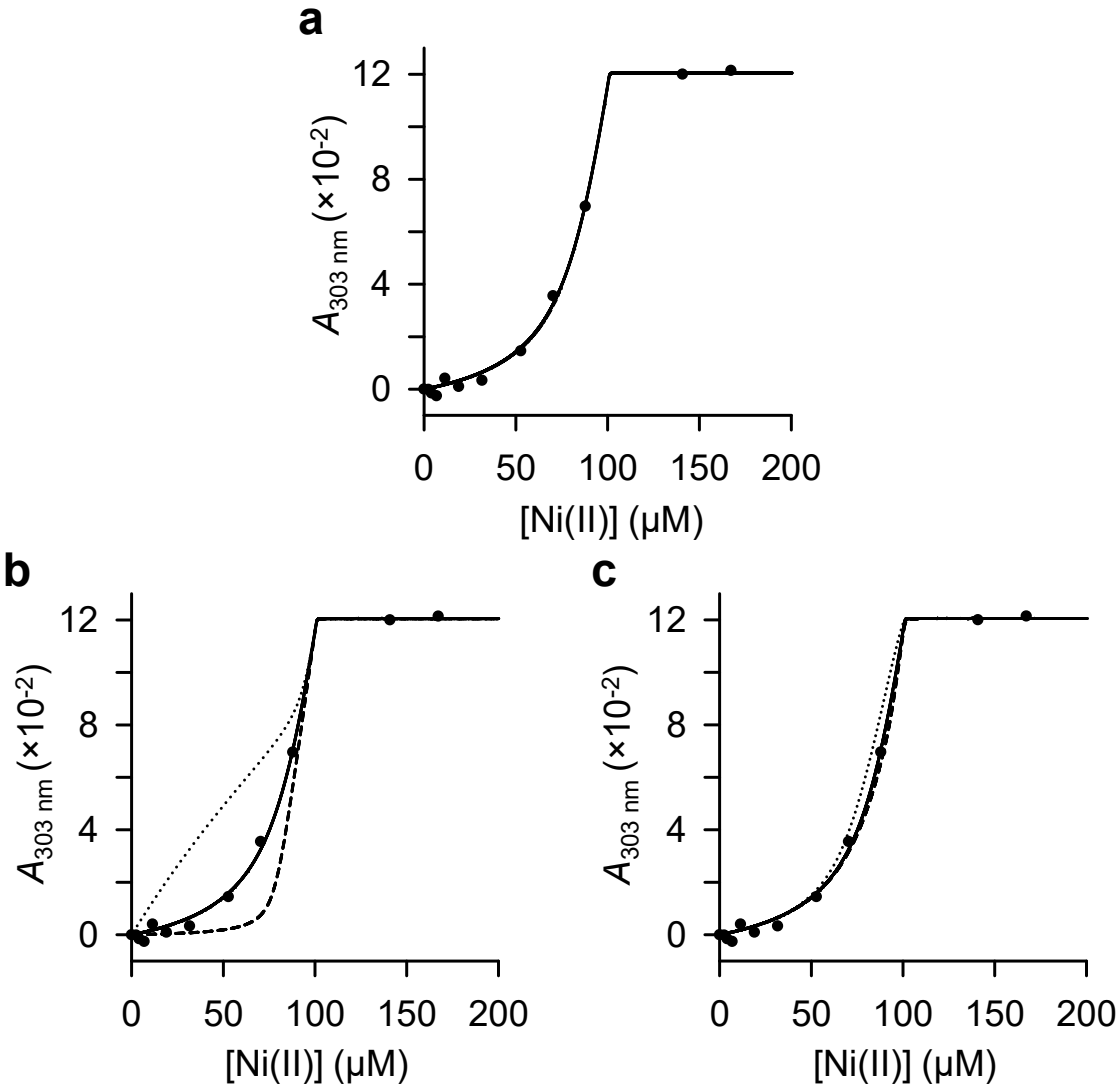

Figure 3.19 Determination of *Sty*CueR Ni(II) affinity by competition with EGTA. (a) Ni(II) titration to 16.0 μM CueR monomer and 97.6 μM EGTA (see Section 3.6.3). The plotted data correspond to the $A_{303\ nm}$ feature of Ni(II)-CueR. The solid line indicates best fit to the data set. The K_1 values and 95% confidence interval from the fit are listed in Table 3.2. **(b)** Modelled fits for this data using $K_{1a\text{-}b}$ 10-fold tighter (dotted line) or 10-fold weaker (dashed line) to show the limits of the assay. **(c)** Same as (b) except with limits for K_{1c}.

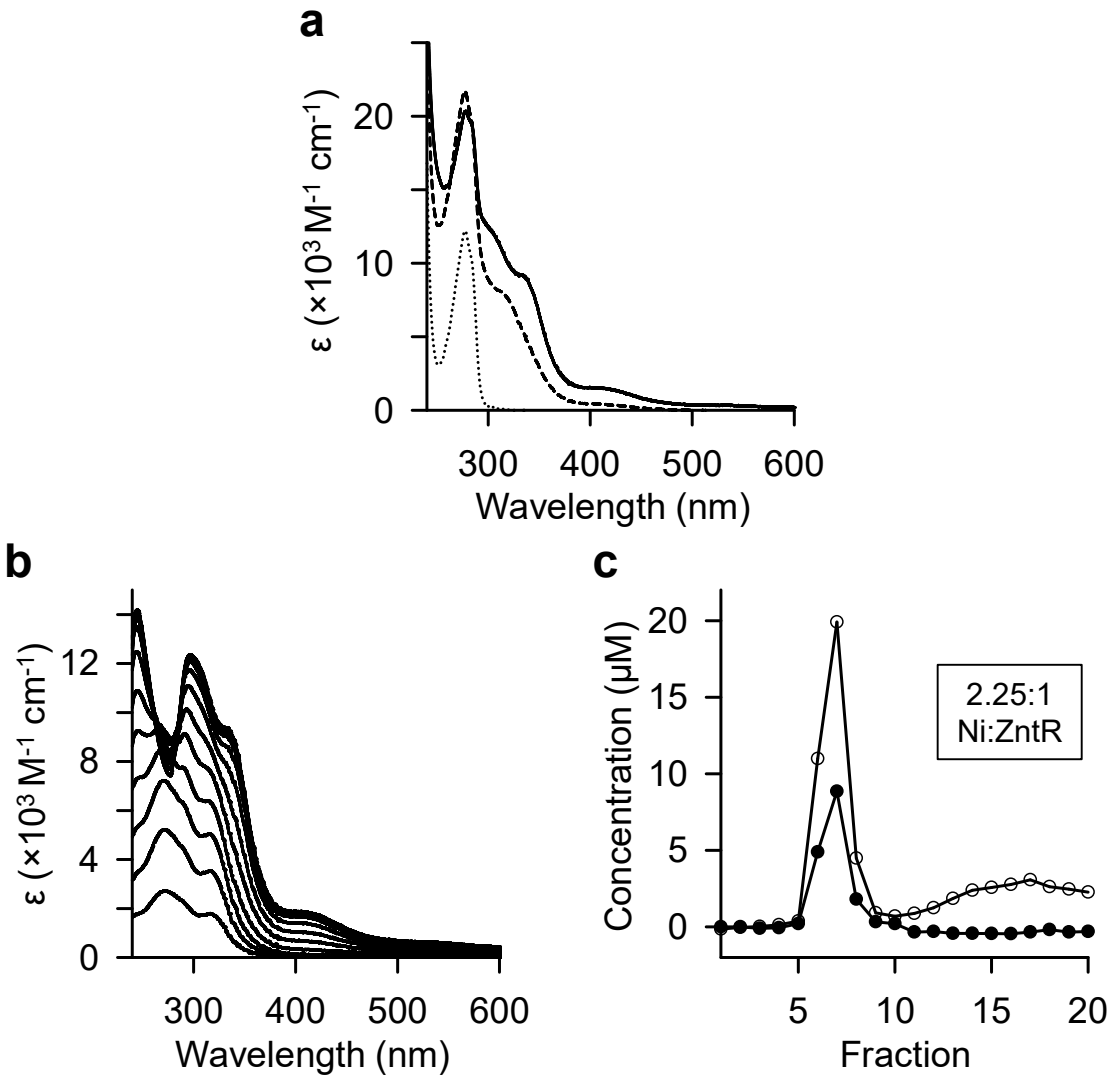

Figure 3.20 Determination of the Ni(II) binding stoichiometry of *Sty*ZntR. (a) UV/visible spectra for 2:1 Ni(II)-ZntR (solid line), 1:1 Ni(II)-ZntR (dashed line), and apo-ZntR (dotted line), all with 10.3 μM ZntR monomer. **(b)** Difference spectra for stepwise Ni(II) addition to 10.3 μM ZntR. **(c)** Co-elution of Ni(II) and ZntR through size exclusion chromatography with a running buffer containing 5 μM $NiCl_2$ (20 μM ZntR monomer with 60 μM Ni(II) applied to the column). ZntR concentration (●) determined by $A_{280\ nm}$ and Ni(II) concentration (○) determined by ICP-MS.

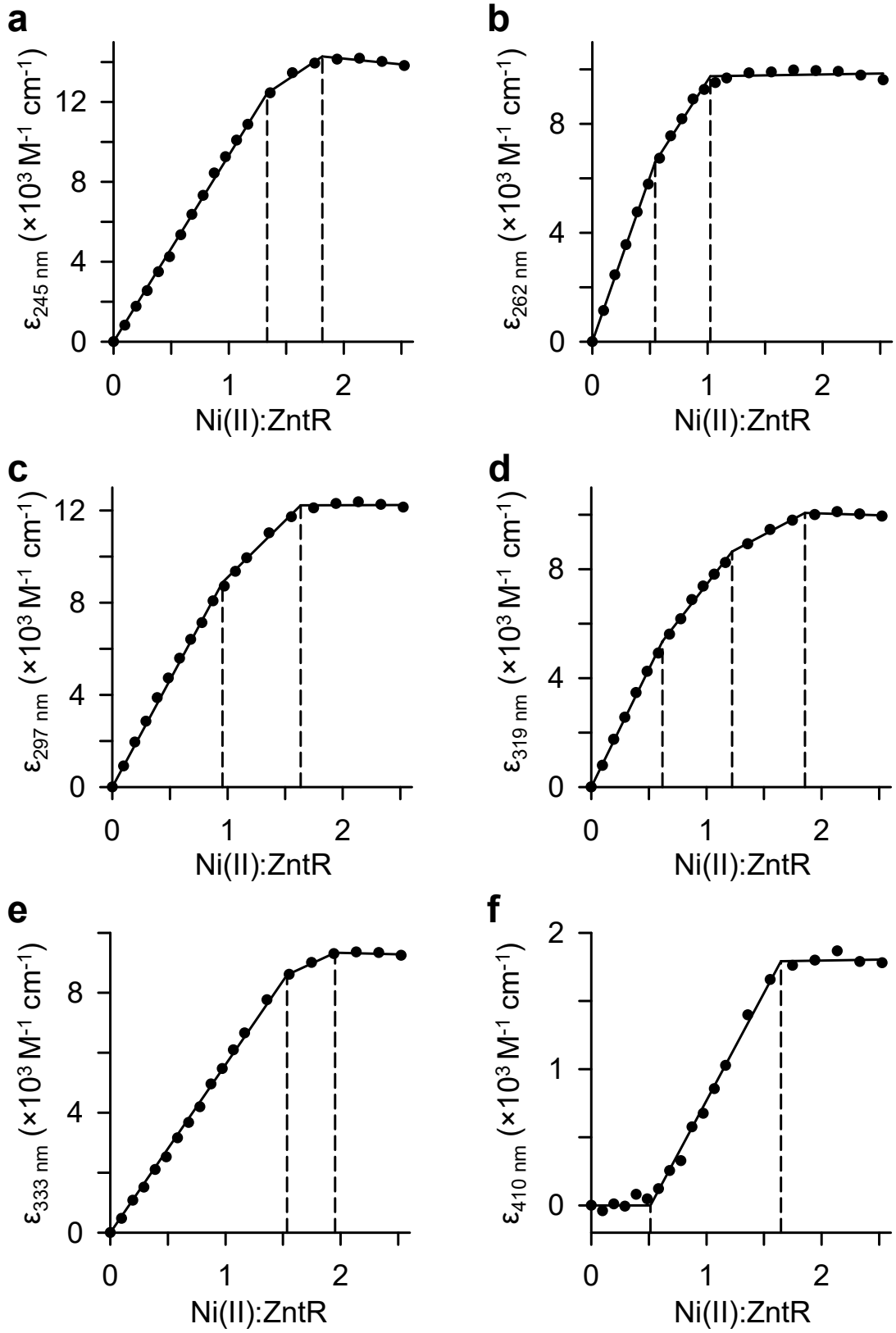

Figure 3.21 *Sty*ZntR exhibits nonlinear absorbance changes during stepwise Ni(II) addition. **(a)**, **(b)**, **(c)**, **(d)**, **(e)**, and **(f)** Stoichiometry of Ni(II) binding to ZntR (10.3 μM monomer) determined from Figure 3.20b following increase in $\varepsilon_{245\ nm}$, $\varepsilon_{262\ nm}$, $\varepsilon_{297\ nm}$, $\varepsilon_{319\ nm}$, $\varepsilon_{333\ nm}$, and $\varepsilon_{410\ nm}$, respectively. The dashed lines represent observed inflexion points.

initially increasing in that range. This could be explained if Ni(II) binding beyond 1:1 stoichiometry affected the environment of one or more tyrosine residues (Tyr123 is adjacent to the Zn(II) site) causing a decrease in absorbance intensity. Notably, deprotonation of a tyrosine shifts A_{max} from 276 nm to 295 nm (Crammer and Neuberger, 1943). Other features appeared more pronounced after 1:1 stoichiometry, such as the peak at 333 nm which formed from the shoulder in the peak at 319 nm (most obvious in Figure 3.20a). Figure 3.21 follows each of the absorbance features, mentioned above, which revealed mostly nonlinear responses (similar to CueR in Section 3.6.1). Straight lines have been manually fit to the titration data indicating obvious inflexion points. The final inflexion usually resulted in a plateau that suggested a 2:1 stoichiometry of Ni(II) to ZntR monomer. Attempting to use these features to interpret Ni(II) binding to ZntR, as done with CueR, was more challenging since the features show more curvature in comparison. Nevertheless, like CueR, ZntR has a low intensity absorbance feature at 410 nm, indicative of a planar Ni(II) geometry, that appeared after 0.5:1 Ni(II) equivalents had been added. The feature increased until a 1.5:1 ratio was achieved and plateaued. $A_{333\ nm}$ was the most linear feature which began showing slight curvature after 1.5:1 Ni(II):ZntR monomer. As mentioned in Section 3.6.1, the nonlinear responses could be the result of competition between different sites which have different spectral features owing to a different set of coordinating ligands. These different sites could effectively be acting as a silent competitor preventing full stoichiometric addition to one site at a time. This internal competition was simulated and similarly curved traces are observed when modelling one site with a linear response compared to a competitive site which does not produce a response (Figure 3.22).

3.7.2 ZntR can bind four Ni(II) ions per dimer

The co-migration of Ni(II) with ZntR through size exclusion chromatography was carried out to provide an independent determination of stoichiometry. Ni(II) was loaded to the protein and run through a size exclusion column using buffer containing 5 μM $NiCl_2$. The data (Figure 3.20c) revealed a Ni(II):ZntR monomer ratio of 2.25:1 (2:1 to the nearest whole number) or four Ni(II) ions per dimer. The *E. coli* ZntR crystal structure suggests ZntR has the capability to facilitate the 4:1 Ni(II):ZntR dimer stoichiometry observed here. Alternatively, two histidine residues (His76 and His77) are found at the N-terminal end of the dimerisation helix, which contains the Zn(II) ligand Cys79 that could coordinate additional Ni(II) ions along with nearby aspartate/glutamate residues (Asp73 and Glu75) or possibly with water molecules. If this were the case, then dramatic consequences regarding DNA affinity would be expected. Given the additional number of histidine residues around

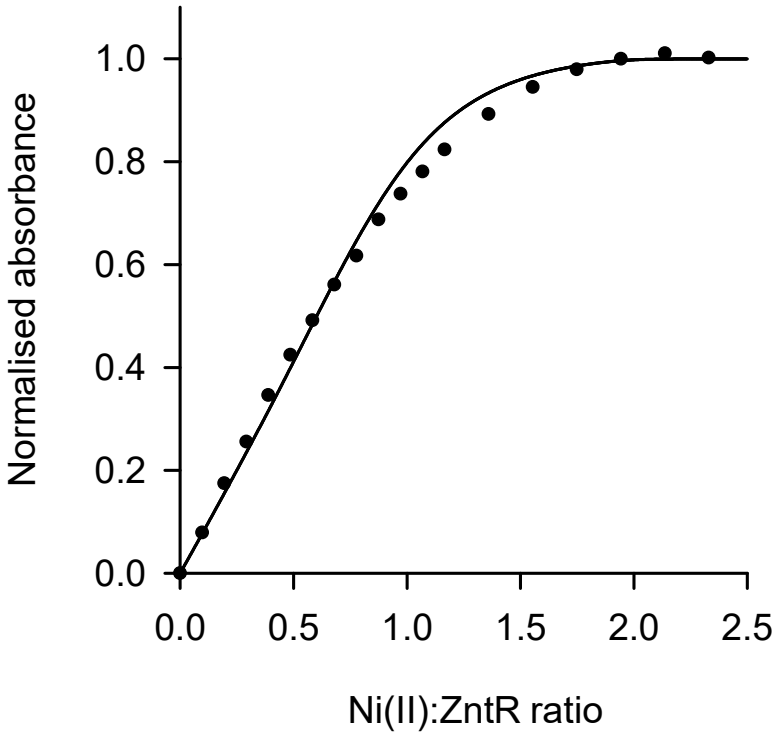

Figure 3.22 Simulation of stoichiometric Ni(II) binding to ZntR with a spectroscopically silent site. The simulation model assumed that normalised absorbance ($A_{319\ nm}$) originated from the first pair of Ni(II) binding sites in the dimer and the second pair of Ni(II) sites are spectroscopically silent (as in Fur and MntR). The Ni(II) affinities used to generate the simulated data (solid line) were taken from Table 5.1.

the metal-binding loop in ZntR compared to CueR, it was unsurprising that the number of Ni(II) ions bound to ZntR was greater than the structurally homologous CueR.

3.7.3 Ni(II) binds to ZntR with negative cooperativity

The Ni(II) affinity of ZntR was investigated by titration of the metal to three ZntR monomer concentrations in competition with FluoZin-3 (Figure 3.23a). The data was fit simultaneously to a model where $K_{1a} \neq K_{1b}$ (allowing for cooperativity) and $K_{1c} = K_{1d}$. This model determined affinity values of K_{1a} 1.40×10^{-10} M, K_{1b} 1.62×10^{-9} M, and $K_{1c\text{-}d}$ 9.90×10^{-9} M (Table 3.2). The limits for each determined affinity (Figure 3.23b-d) indicated that all K_1 values were within the limits of the assay. The simple model $K_{1a\text{-}b} + K_{1c\text{-}d}$ did not fit well for early data points. The chosen model indicated negative cooperativity (10-fold) between K_{1a} and K_{1b}.

Additional Ni(II) titrations were carried out with different competitors to corroborate the affinities determined using FluoZin-3. The Ni(II) affinity of ZntR was measured using mag-fura-2 (Figure 3.24a), fitting the single set of data to the same model as above and generating affinities as K_{1a} 8.00×10^{-10} M, K_{1b} 3.76×10^{-9} M, and $K_{1c\text{-}d}$ 6.65×10^{-8} M (Table 3.2). The calculated limits indicated that K_{1a} was approaching the 10-fold tighter limit (Figure 3.24b), though the 95% confidence interval range was still narrow. In contrast, K_{1b} (Figure 3.24c) and $K_{1c\text{-}d}$ (Figure 3.24d) were within the limits of the assay. The K_{1a}, K_{1b}, and $K_{1c\text{-}d}$ affinities here are approximately 6-fold, 2-fold, and 7-fold weaker, respectively, compared to the values measured with FluoZin-3, indicating good consistency.

The Ni(II) titration was also performed using bicine as a competitor. Ni(II) binding to ZntR followed the Ni(II)-dependent feature at 333 nm for a single set of data (Figure 3.25a). The same model was used with resulting affinity values as K_{1a} 8.30×10^{-9} M, K_{1b} 8.20×10^{-10} M, and $K_{1c\text{-}d}$ 4.63×10^{-9} M (Table 3.2). The limits indicated that both K_{1a} (Figure 3.25b) and K_{1b} (Figure 3.25c) were at the lower limit, whereas $K_{1c\text{-}d}$ was within the limits of the assay (Figure 3.25d). $K_{1c\text{-}d}$ here fit ~ 2-fold tighter than with FluoZin-3, also indicating good consistency.

3.8 Zur

3.8.1 Zur can bind six Ni(II) ions per dimer

The intrinsic absorbance of *Sty*Zur arises from three tyrosines (residues 45, 64, and 85). Like other members of the Fur-family, Zur contains a kinetically trapped, structural Zn site

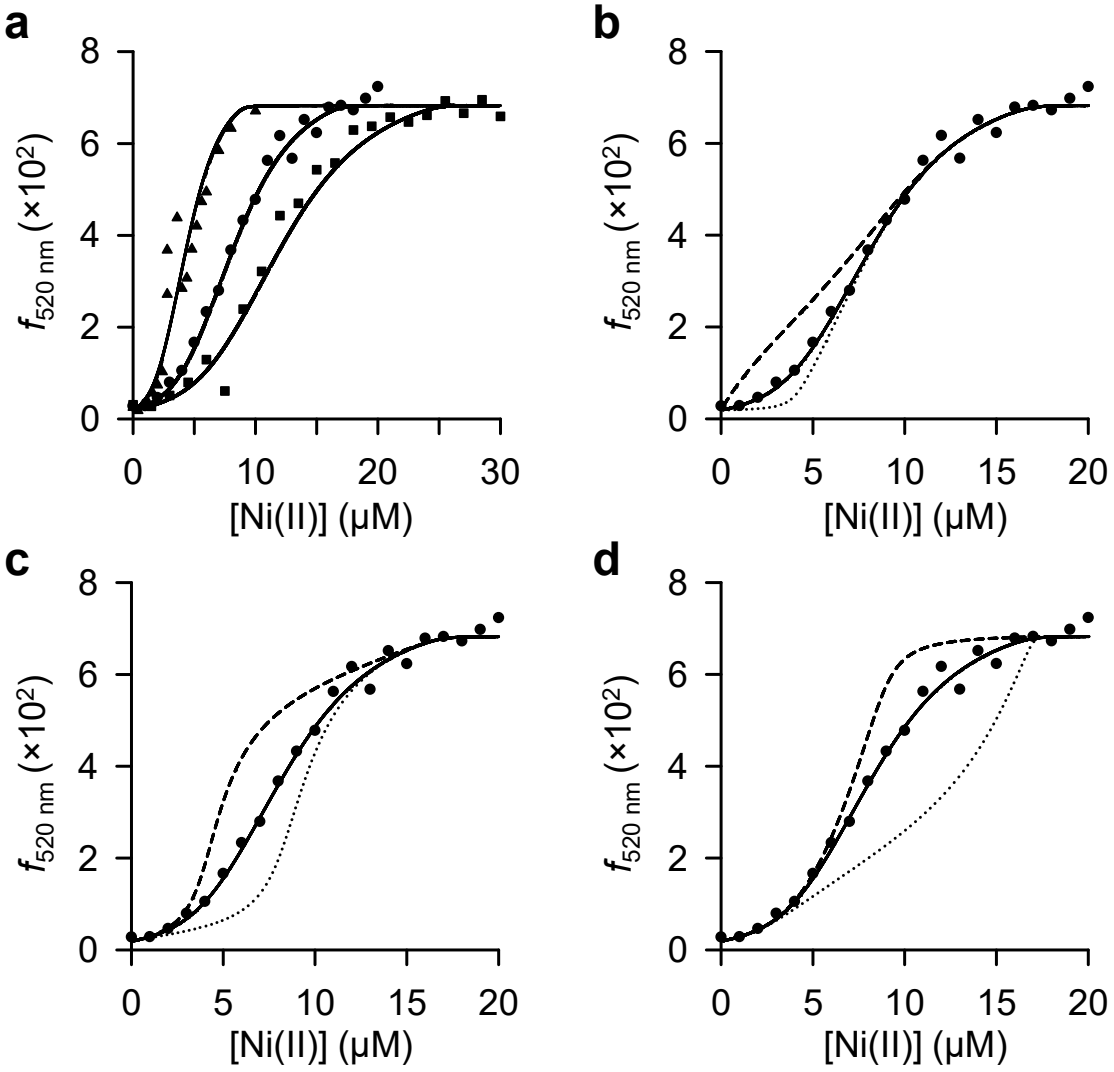

Figure 3.23 Determination of *Sty*ZntR Ni(II) affinity by competition with FluoZin-3. (a) Ni(II) titration to three ZntR monomer concentrations, 4 μM (▲), 8 μM (●), and 12 μM (■), in competition with 1 μM FluoZin-3. The plotted data correspond to FluoZin-3 emission ($f_{520\,nm}$). Solid lines indicate best simultaneous fit to all three data sets. The K_1 values and 95% confidence interval from the fit are listed in Table 3.2. **(b)** Modelled fits for 8 μM ZntR titration using K_{1a} 10-fold tighter (dotted line) or 10-fold weaker (dashed line) to show the limits of the assay. **(c)** Same as (b) except with limits for K_{1b}. **(d)** Same as (b) except with limits for $K_{1c\text{-}d}$.

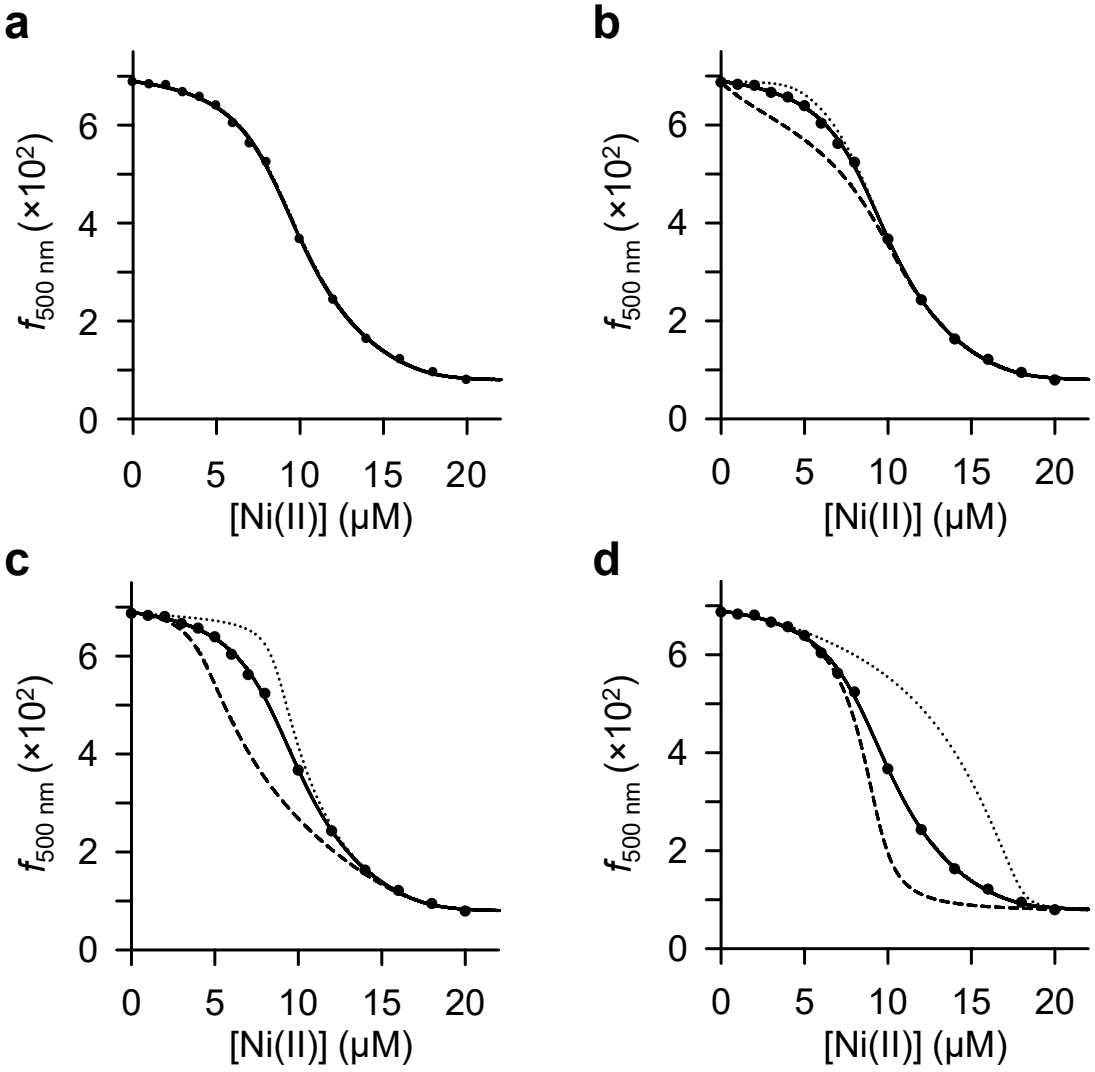

Figure 3.24 Determination of *Sty*ZntR Ni(II) affinity by competition with mag-fura-2. (a) Ni(II) titration to 8.4 μM ZntR monomer and 1.3 μM mag-fura-2. The plotted data correspond to mag-fura-2 emission ($f_{500\,nm}$). The solid line indicates best fit to the data set. The K_1 values and 95% confidence interval from the fit are listed in Table 3.2. **(b)** Modelled fits for this data using $K_{1a\text{-}b}$ 10-fold tighter (dotted line) or 10-fold weaker (dashed line) to show the limits of the assay. **(c)** Same as (b) except with limits for K_{1b}. **(d)** Same as (b) except with limits for $K_{1c\text{-}d}$.

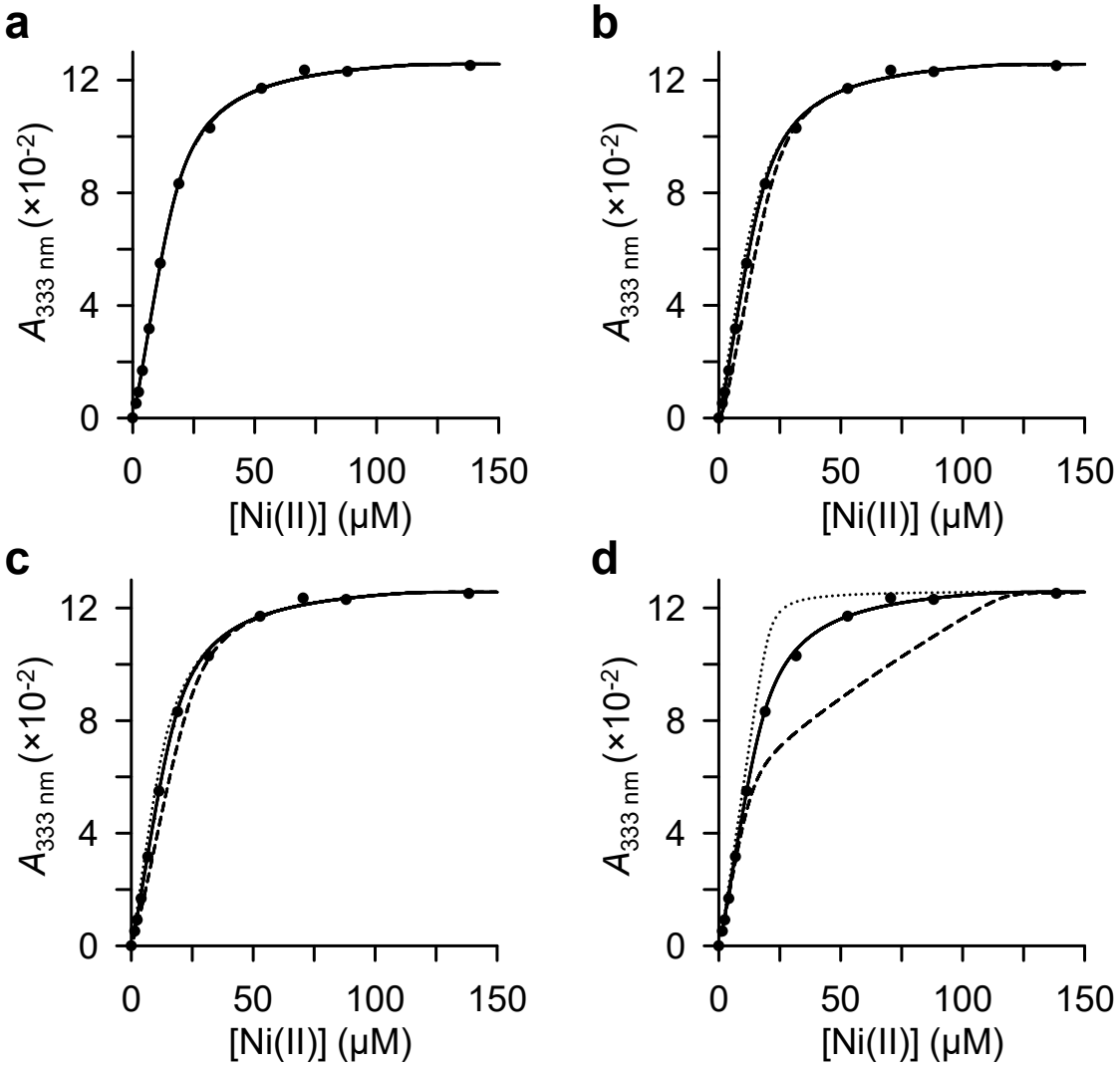

Figure 3.25 Determination of *Sty*ZntR Ni(II) affinity by competition with bicine. (a) Ni(II) titration to 9.8 μM ZntR monomer and 98 μM bicine. The plotted data correspond to the $A_{333\ nm}$ feature of Ni(II)-ZntR. The solid line indicates best fit to the data set. The K_1 values and 95% confidence interval from the fit are listed in Table 3.2. **(b)** Modelled fits for this data using $K_{1a\text{-}b}$ 10-fold tighter (dotted line) or 10-fold weaker (dashed line) to show the limits of the assay. **(c)** Same as (b) except with limits for K_{1b}. **(d)** Same as (b) except with limits for $K_{1c\text{-}d}$.

comprised of four cysteines (residues 103, 106, 143, and 146 in the *E. coli* protein) within each monomer subunit (Gilston et al., 2014). As with *Sty*Fur, these Zn(II) sites are spectrally silent. Stepwise addition of Ni(II) to Zur revealed intense Ni(II)-dependent absorbance features (Figure 3.26a). The difference spectra (Figure 3.26b) revealed a very intense feature at 264 nm, with a shoulder at 290 nm, and a less intense feature at 340 nm. Extinction coefficients have been determined for these features (Table 3.1). The feature at 264 nm (Figure 3.26c) showed a plateau starting at 3:1 Ni(II) per Zur monomer (or six Ni(II) per dimer). The intense absorbance features are likely a result of strong LMCTs with cysteine residues in the protein. *Sty*Zur contains five more cysteine residues in addition to the four coordinating the structural Zn. One of these residues (Cys88) coordinates Zn(II) in the regulatory site, as seen from the *E. coli* structure (Section 1.3.7). The number of thiolate ligands cannot be estimated from the absorbance intensity alone but the magnitude of the Ni(II)-dependent feature at 264 nm suggested the recruitment of more than one thiolate group. It is possible that the sites are very similar based on the generation of absorbance features at just three wavelengths (compared to CueR and ZntR).

The Ni(II):Zur stoichiometry was independently determined by co-migration through a size exclusion column. Ni(II) was added to Zur and left to equilibrate for 2-3 hours before loading onto the column (the importance of the longer equilibration time is discussed in Section 3.8.2). Analysis of the eluted fractions (Figure 3.26d) revealed a 2.08:1 Ni(II) to Zur monomer stoichiometry (four Ni(II) ions per dimer). As this ratio was lower than expected from the UV/visible experiment, co-migration was repeated with 5 μM $NiCl_2$ added to the buffer (Figure 3.26e). The resulting ratio (2.92:1) was in excellent agreement with the UV/visible stoichiometry experiment. This data suggested that one possible pair of sites in the dimer was much weaker than two other pairs of sites. In both experiments, the Zn(II):Zur ratio in the protein containing fractions was 1:1, indicating that Ni(II) had not displaced Zn(II) from the structural site, or that if a Zn(II) ion was displaced, it was able to bind to another site within the protein.

3.8.2 Ni(II) appears to undergo ligand exchange when initially bound to Zur

A key observation upon Ni(II) addition to Zur was the change in spectral features over time. Initially, $A_{340\ nm}$ was much more pronounced but this feature decreased in intensity over the first 60 min, coincident with an increase in $A_{264\ nm}$ intensity (Figure 3.27), slowly reaching a plateau after ~ 2 h. This suggested that a slow exchange between protein conformations were required to see the full 264 nm feature. Alternatively, the Ni(II) ion could bind to the protein in a kinetically favourable site but over time, or as protein structure changes with further

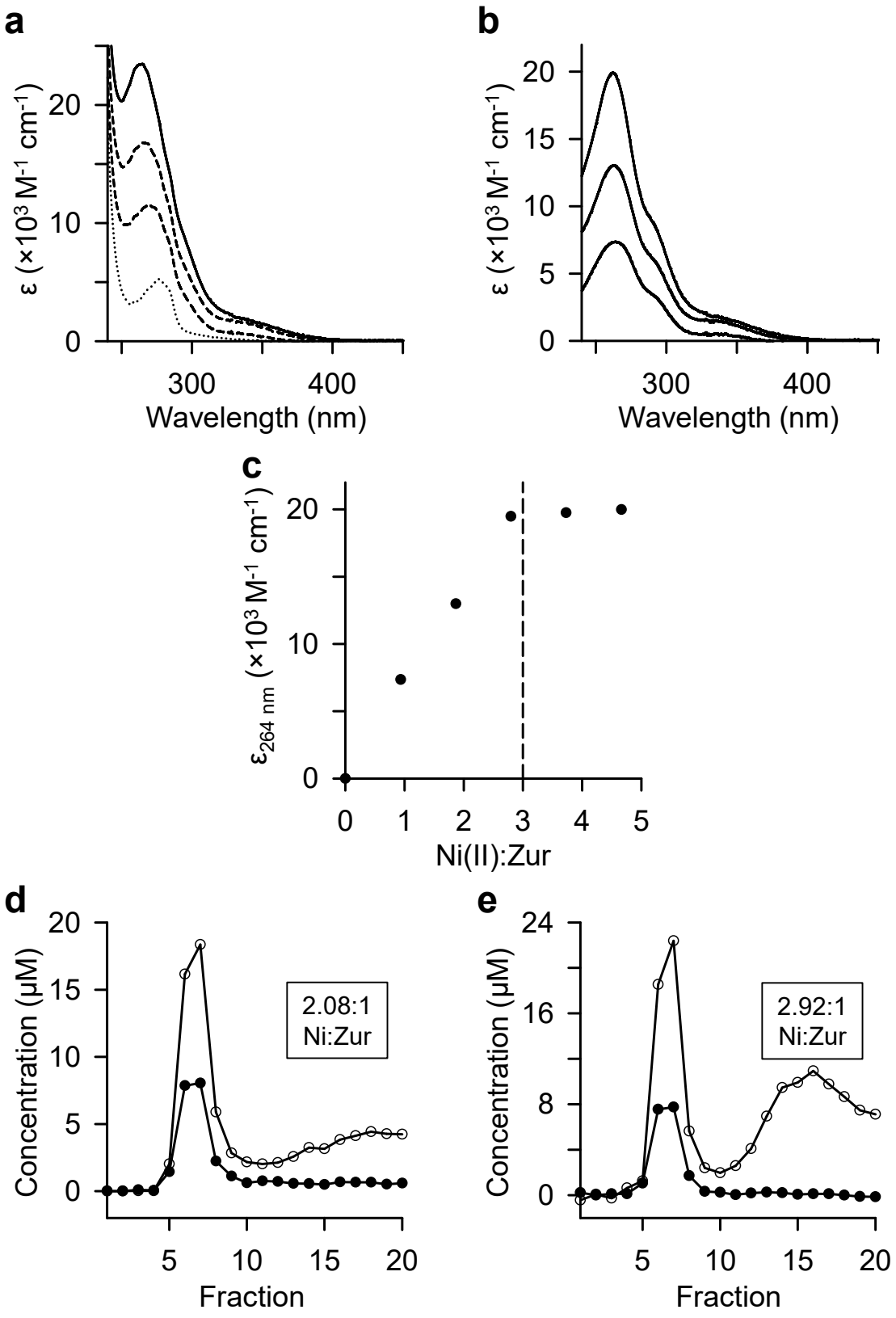

Figure 3.26 Determination of the Ni(II) binding stoichiometry of *Sty*Zur. (a) UV/visible spectra for 3:1 Ni(II)-Zur (solid line), 2:1 and 1:1 Ni(II)-Zur (both dashed line), and apo-Zur (dotted line), all with 10.7 μM Zur monomer. **(b)** Difference spectra for stepwise Ni(II) addition to 10.7 μM Zur. **(c)** Stoichiometry of Ni(II) binding to Zur determined from (b) following increase in $\varepsilon_{264\ nm}$. **(d)** Co-elution of Ni(II) and Zur through size exclusion chromatography (20 μM Zur monomer with 140 μM Ni(II) applied to the column). Zur concentration (●) determined by $A_{280\ nm}$ and Ni(II) concentration (○) determined by ICP-MS. **(e)** Same as (d) except a running buffer containing 5 μM $NiCl_2$.

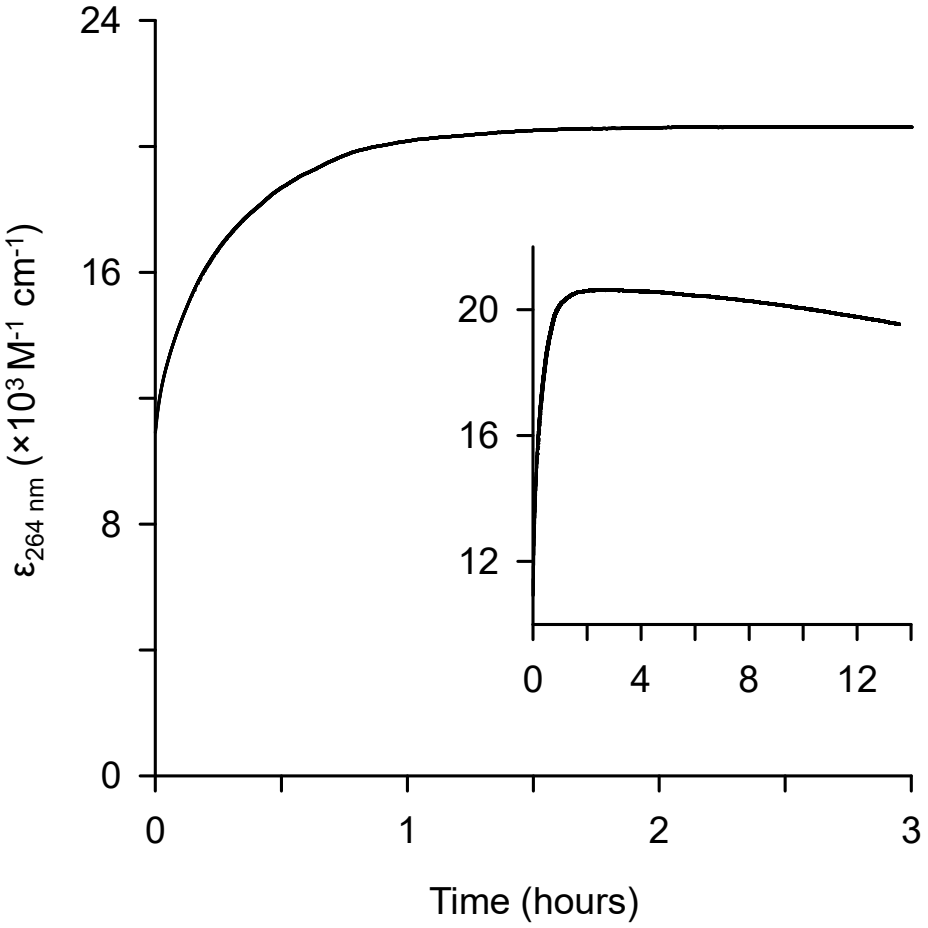

Figure 3.27 Time-course of Ni(II) binding to *Sty*Zur. Reaction initiated by manually mixing 3 equivalents of Ni(II) with 10.7 μM apo-Zur monomer. Ni(II) binding was monitored by increase in the Ni(II)-Zur spectral feature at 264 nm ($\varepsilon_{264\ nm}$). Inset shows absorbance change over 13 h.

Ni(II)-binding, a structurally distinct site with a tighter affinity could outcompete the initial site for the metal. A different set of ligands is likely to lead to altered spectral features upon Ni(II) binding resulting in changes for absorbance maxima or an extinction coefficient at a particular wavelength. These potentially different Ni(II) sites could have different affinities, however, the ability to constrain the initial site would be challenging as it does not appear stable for more than a few hours with a gradual decline in population of Ni(II). Therefore, all experiments consider only the state of Ni(II)-Zur after these changes have occurred. In the stoichiometry experiments (Section 3.8.1), the protein was left for ≥ 2 h before measuring the absorption spectra and this timescale was used for the affinity determination experiments (Section 3.8.3). The time-course experiment revealed a small decrease (~ 5%) in $A_{264\ nm}$ between 4 and 14 h (Figure 3.27). The cause of this was not investigated further but possibilities include protein precipitation, further slow conformational changes, or a slow intrusion of O_2 into the cuvette resulting in some cysteine oxidation.

3.8.3 Zur binds Ni(II) with picomolar affinity but displays negative cooperativity

The Ni(II) affinity of Zur was determined by competition with FluoZin-3. Ni(II) was titrated to three different concentrations of Zur monomer in competition with FluoZin-3 and generated affinities as K_{1a} 3.60×10^{-10} M, K_{1b} 7.60×10^{-9} M, $K_{1c\text{-}d}$ 1.13×10^{-8} M, and $K_{1e\text{-}f}$ 8.80×10^{-8} M (Table 3.2). The start and end points for each experiment differed slightly which indicated different starting concentrations of FluoZin-3. These concentrations (1 μM expected) were too small to quantify by UV/visible spectroscopy so were estimated during fitting by adjusting the DynaFit model. The calculated concentrations from the fits were all within 5% of the expected concentration. The Zur Ni(II) titration data was noisy compared to the other sensors and this may have reflected the complex timescale of Ni(II)-binding (Section 3.8.2) despite the effort to use a consistent time point for each measurement. The limits for determination of K_{1a} suggested that the observed affinity was in the measurable range (Figure 3.28b), but more data points would have increased the confidence in this value. The fitted values for K_{1b} (Figure 3.28c) and K_{1c} (Figure 3.28d) were within the limits of the assay, but $K_{1e\text{-}f}$ approached the lower limit (Figure 3.28e). As with other non-Ni(II) sensors, the best model for Ni(II) binding to Zur allowed K_{1a} and K_{1b} to vary, indicating negative cooperativity (20-fold).

The Ni(II) affinity of Zur was further investigated using mag-fura-2 which could provide a better fit for $K_{1e\text{-}f}$. Three data sets were fit simultaneously (Figure 3.29a) and generated affinities as K_{1a} 8.90×10^{-10} M, K_{1b} 8.30×10^{-9} M, $K_{c\text{-}d}$ 1.24×10^{-8} M, and $K_{1e\text{-}f}$ 6.10×10^{-8} M (Table 3.2), using the same model as the FluoZin-3 experiment. As with FluoZin-3, the

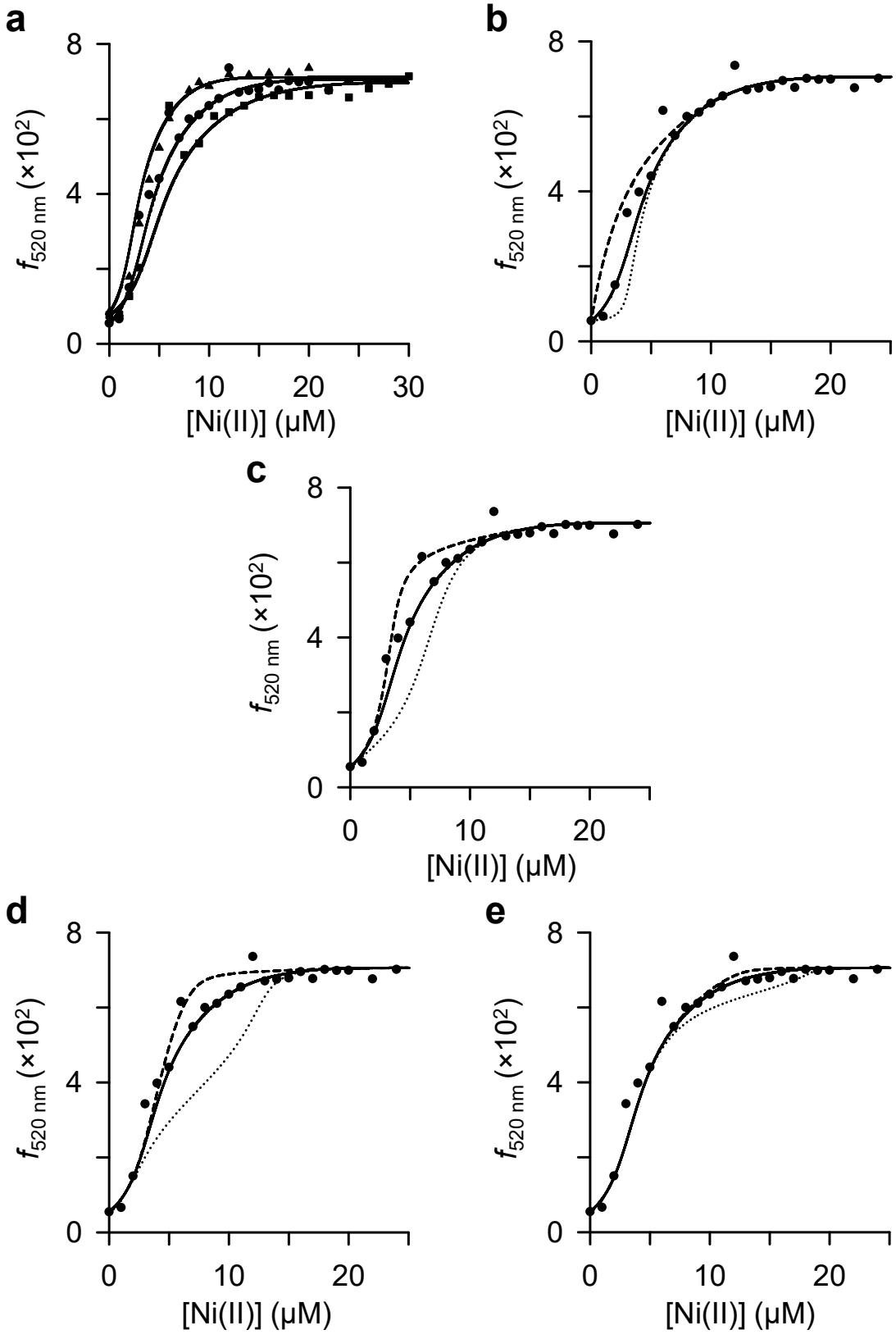

Figure 3.28 Determination of *Sty*Zur Ni(II) affinity by competition with FluoZin-3. (a) Ni(II) titration to three Zur monomer concentrations, 4 μM (▲), 6 μM (●), and 8 μM (■), in competition with 1 μM FluoZin-3. The plotted data correspond to FluoZin-3 emission ($f_{520\,nm}$). Solid lines indicate best simultaneous fit to all three data sets. The K_1 values and 95% confidence interval from the fit are listed in Table 3.2. **(b)** Modelled fits for 6 μM Zur titration using K_{1a} 10-fold tighter (dotted line) or 10-fold weaker (dashed line) to show the limits of the assay. **(c)** Same as (b) except with limits for K_{1b}. **(d)** Same as (b) except with limits for $K_{1c\text{-}d}$. **(e)** Same as (b) except with limits for $K_{1e\text{-}f}$.

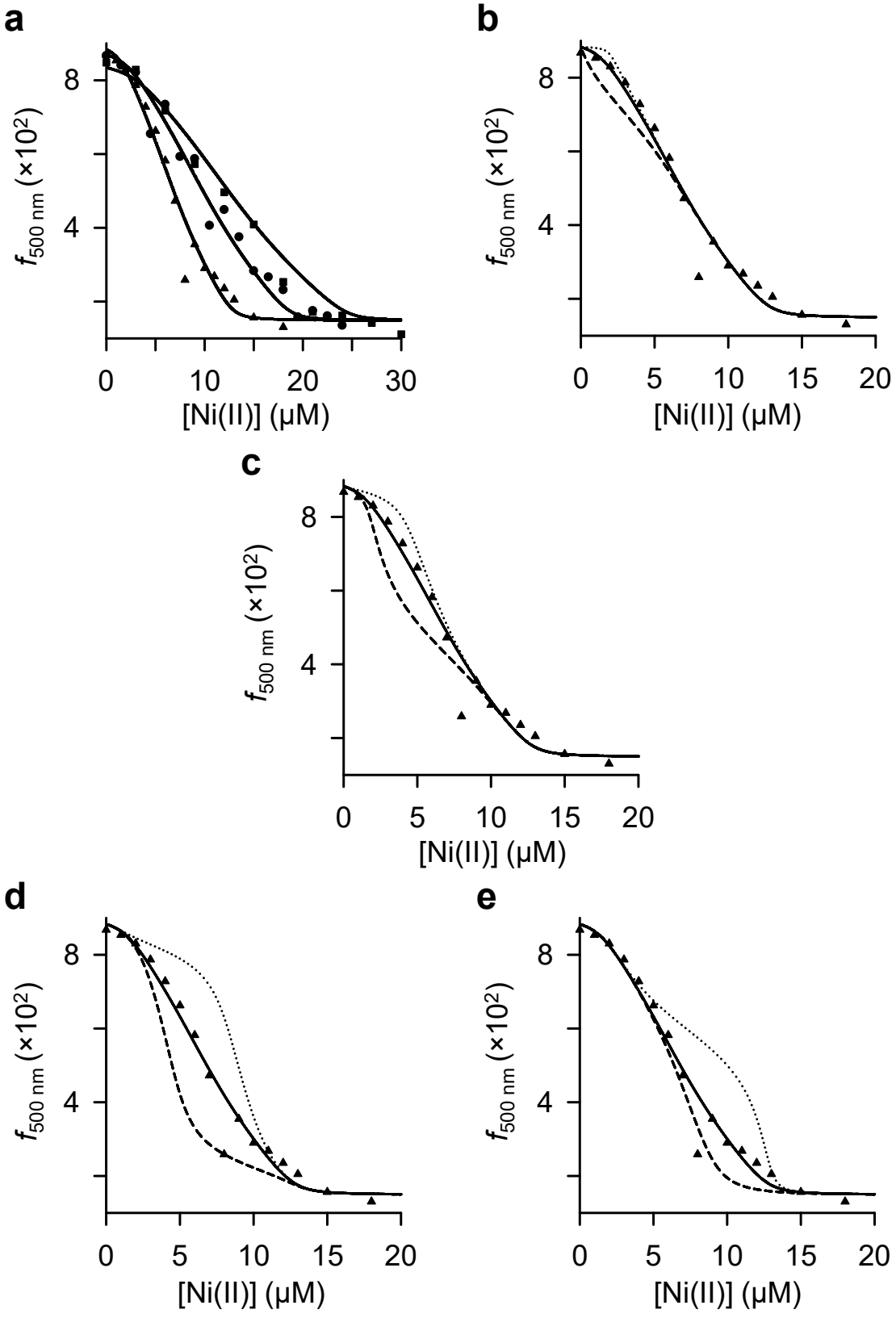

Figure 3.29 Determination of *Sty*Zur Ni(II) affinity by competition with mag-fura-2. (a) Ni(II) titration to three Zur monomer concentrations, 4 μM (▲), 6 μM (●), and 8 μM (■), in competition with 1 μM mag-fura-2. The plotted data correspond to mag-fura-2 emission ($f_{500\ nm}$). The solid line indicates best fit to the data set. The K_1 values and 95% confidence interval from the fit are listed in Table 3.2. **(b)** Modelled fits for 4 μM Zur titration using K_{1a} 10-fold tighter (dotted line) or 10-fold weaker (dashed line) to show the limits of the assay. **(c)** Same as (b) except with limits for K_{1b}. **(d)** Same as (b) except with limits for $K_{1c\text{-}d}$. **(e)** Same as (b) except with limits for $K_{1e\text{-}f}$.

concentration of mag-fura-2 appeared to differ in each experiment and therefore this value was allowed to vary in DynaFit, producing concentrations within 6% of that expected (1 μM). The 10-fold tighter and weaker limits indicated that K_{1a} was at the lower limit (Figure 3.29b), but affinities for K_{1b} (Figure 3.29c), $K_{c\text{-}d}$ (Figure 3.29d), and $K_{1e\text{-}f}$ (Figure 3.29e) were all in range for mag-fura-2 to determine accurate values. Although $K_{1e\text{-}f}$ appeared to be at the limit of the FluoZin-3 experiment, the affinity determined with mag-fura-2 indicates that both experiments are in reasonable agreement (~ 1.4-fold difference in $K_{1e\text{-}f}$). The data points again appear noisy, as seen with FluoZin-3 data.

A third competition experiment was carried out using bicine as a competitor, following the Ni(II)-dependent feature, $A_{264\ nm}$. As well as corroborating previous results, one objective of this titration was to see if following Zn(II)-Zur formation reduced the noise seen when monitoring competitor fluorescence. Ni(II) was titrated into three concentrations of Zur monomer in competition with bicine (Figure 3.30a) and were simultaneously fit to generate affinities as K_{1a} 5.70×10^{-12} M, K_{1b} 5.00×10^{-9} M, $K_{1c\text{-}d}$ 2.20×10^{-8} M, and $K_{1e\text{-}f}$ 7.70×10^{-8} M (Table 3.2). The 10-fold tighter and weaker limits for K_{1a} (Figure 3.30b) clearly demonstrated that bicine was an unsuitable competitor for this binding event. Similarly, K_{1b} was very close to the lower limit (Figure 3.30c). $K_{1c\text{-}d}$ (Figure 3.30d) and $K_{1e\text{-}f}$ (Figure 3.30e) were within the limits of the assay and both values are consistent with previous competitor data ($K_{1c\text{-}d}$ and $K_{1e\text{-}f}$ are 1.9-fold weaker and 1.1-fold tighter than FluoZin-3 affinities, respectively). Using bicine did not result in noisy data points, seen previously with the fluorescent probes, suggesting the competitors resulted in the inconsistent signal. Of note, bicine is structurally distinct compared to mag-fura-2 and FluoZin-3.

3.9 Comparing the Ni(II) affinities of the *Salmonella* regulators

3.9.1 Comparing the Ni(II)-affinity of *Sty*NikR with previous data

The Ni(II) affinity of *Sty*NikR has previously been determined at pH 7.0, indicating an average affinity of $2.5 \pm 0.4 \times 10^{-12}$ M (Osman et al., 2018). In this example, the average affinity corresponds to the concentration of Ni(II) required to achieve 50% Ni(II)-binding to the tetramer. The equivalent average affinity at pH 7.5 can be determined (Section 2.10.4) which gives a value of 2.95×10^{-13} M. This value could also be obtained directly from the titration data by modelling NikR as a monomer with a single Ni(II)-binding site. However, this approach would obscure possible cooperativity between sites in oligomeric proteins, which was repeatedly observed for non-cognate sensors. The K_1 value at pH 7.5 is an order

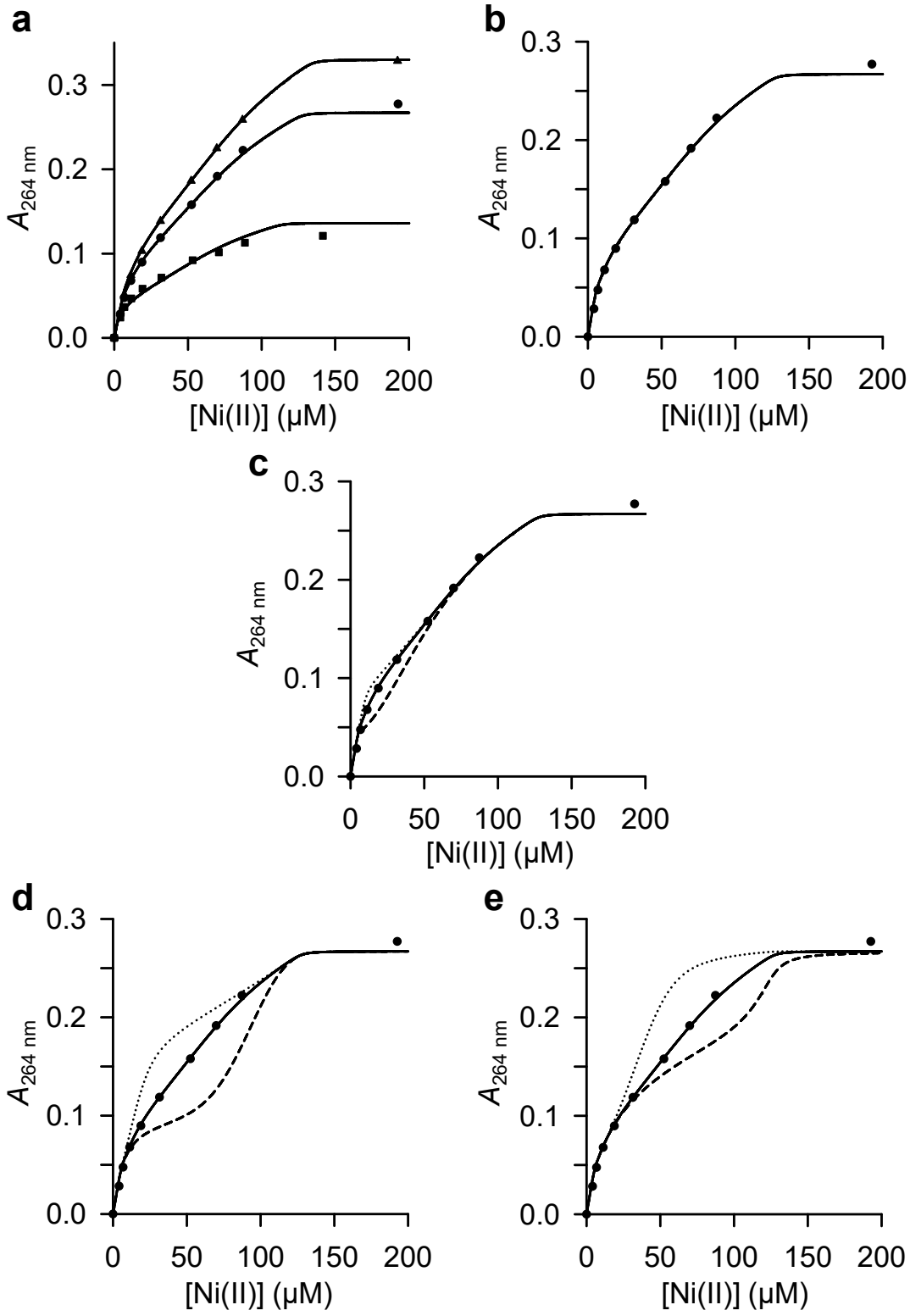

Figure 3.30 Determination of *Sty*Zur Ni(II) affinity by competition with bicine. (a) Ni(II) titration to three Zur monomer concentrations; 12.6 μM (▲) and 96.6 μM bicine; 10.2 μM (●) and 97.0 μM bicine; 5.2 μM (■) and 98.5 μM bicine. The plotted data correspond to the $A_{264\ nm}$ feature of Ni(II)-Zur. The solid line indicates best fit to the data set. The K_1 values and 95% confidence interval from the fit are listed in Table 3.2. **(b)** Modelled fits for 10.2 μM Zur titration using K_{1a} 10-fold tighter (dotted line) or 10-fold weaker (dashed line) to show the limits of the assay. **(c)** Same as (b) except with limits for K_{1b}. **(d)** Same as (b) except with limits for $K_{1c\text{-}d}$. **(e)** Same as (b) except with limits for $K_{1e\text{-}f}$.

of magnitude tighter than that at pH 7.0, consistent with a requirement to deprotonate residues that either directly coordinate Ni(II) or are involved in protein conformational changes in response to Ni(II)-binding.

Average K_1 values have been determined for all the sensors and are important for modelling DNA occupancy, discussed in Chapter 5.

3.9.2 Discussion of the *Sty*RcnR Ni(II)-binding model and cellular implications

Different preparations of RcnR led to different Ni(II)-binding models for this protein (Section 3.3.3). The "$K_{1a\text{-}c} + K_{1d}$" model was assumed to be physiologically irrelevant with the assumption that a small proportion of RcnR was effectively not in its native form (the < 10% oxidised thiol containing subunits) during the experiments leading to that model. However, there is still the possibility that extreme negative cooperativity occurs when loading the final Ni(II) site of RcnR, which cannot be ruled out from the affinity experiments. The Co(II) affinities for *Sty*RcnR have been reported (Osman et al., 2017) where negative cooperativity was observed for loading the final two sites after the first set (i.e. $K_{1a}/K_{1b} < K_{1c}/K_{1d}$, dissociation constants). Therefore, it is conceivable that cooperativity may be functional for Ni(II)-loading of the protein as well. The conclusion from the Co(II)-RcnR data was that only the first two sites are required for an allosteric DNA response. Since Ni(II)-RcnR cooperativity occurs after half the protein is loaded, the Co(II)-RcnR model suggests allostery would already have been achieved meaning the effect of negative cooperativity would likely be physiologically irrelevant.

The previously determined Ni(II) affinity for RcnR was six orders of magnitude weaker than NikR (and also weaker than the tightest sites of non-cognate sensors). Zn(II) homeostasis is controlled by two sensors (ZntR and Zur) and the affinities for these sensors differ allowing responses to follow in series (Outten and O'Halloran, 2001, Osman et al., 2017). However, the difference in affinity was only an order of magnitude, therefore, not on the same scale as between NikR and RcnR, which would appear to be non-physiological. However, the Ni(II) affinity of RcnR determined here (Section 3.3.2) is much closer to that of NikR (16-fold different) suggesting these two proteins could function in series, like ZntR and Zur (see Chapter 5).

3.9.3 Cognate versus non-cognate sensors

Determining the affinities for NikR and RcnR proved relatively straightforward which was likely due to "normal" behaviour with respect to Ni(II) binding. Determining the affinities of the non-cognate sensors was more challenging due to the lack of any previous data with

these sensors. Therefore, affinity values or models for Ni(II) binding were not wholly available to guide the initial experiments with each non-cognate sensor. The Ni(II) affinity of *B. subtilis* MntR has been previously estimated, using mag-fura-2, as $2.1 \pm 0.1 \times 10^{-6}$ M (Golynskiy et al., 2006). This value, however, was determined in a different buffer (10 mM HEPES pH 7.2, 100 mM KCl) and with a different model (assumed 1:1 Ni(II):MntR monomer stoichiometry) which could explain how the affinity was four orders of magnitude different compared to the tightest site determined here.

Interestingly, Ni(II) binding to CueR, ZntR, and Zur demonstrated a stoichiometry greater than that seen with their cognate metals (Sections 1.3.7 and 1.3.10). The results of the stoichiometry experiments for all non-cognate sensors necessitated the use of more complex fitting models, and was perhaps not unexpected as these sensors would not normally bind and respond to Ni(II) in the cell. Therefore, coordination geometries different from the cognate metal could result in conformational changes that distort symmetry related sites, thereby generating negative cooperativity (seen with MntR, ZntR, and Zur). Surprisingly, Fur demonstrated positive cooperativity for the first two binding events which suggested the protein structure can rearrange into a favourable conformation for one additional Ni(II) ion binding. The two regulatory sites within Fur use residues from the hinge loop region to coordinate metal ions (Section 1.3.7), therefore, it seems plausible the first Ni(II) binding event orders the ligands of the second site such that Ni(II) binding is favourable compared to when unstructured. Unexpectedly, the opposite effect is apparent for Zur even though the regulatory sites are analogous to Fur (Section 1.3.7).

The physiological significance of this cooperativity by Fur, combined with the anomalously high affinity for the first Ni(II) binding events (compared to non-cognate sensors), is unclear though there is one study proposing a Ni(II) and Fe(II) responsive protein that could be important in maintaining iron homeostasis under nickel stress (Wang et al., 2011), however, this is unlikely to be the case in *Salmonella*. The iron-responsive sensor DtxR from *Corynebacterium diphtheriae* appears to have a Ni(II) affinity comparable to Fe(II) (D'Aquino et al., 2005) but not four to five orders of magnitude tighter, as is the case with *Sty*Fur (Fe(II) affinity = $5.3 \pm 0.7 \times 10^{-7}$ M (Osman et al., 2018)). In *H. pylori*, there appears to be an interesting link between iron and nickel metabolism with overlap of gene regulation by Fur and NikR, however, this does not appear to be driven by multi-metal regulation of the sensors (i.e. nickel is not activating Fur, nor iron activating NikR) (Contreras et al., 2003, Bury-Moné et al., 2004, Delany et al., 2005) but is likely due to the role of both these metals in acid tolerance for this bacteria. Indeed, there appears to be two forms of the urease enzyme in the related *Helicobacter mustelae* which incorporate either nickel or iron as the metal co-

factor depending on the availability of the metals (Stoof et al., 2008), similar to *S. coelicolor* which expresses one of two forms of superoxide dismutase that require either nickel or iron (Chung et al., 1999a, Chung et al., 1999b). Given the first Fur binding event had the next tightest Ni(II) affinity after RcnR, this protein appears most susceptible to mis-metalation, which interestingly coincides with other reports that link Ni(II) toxicity with iron metabolism (Macomber and Hausinger, 2011). The allosteric effect of Ni(II) binding to Fur (and the other sensors) with respect to DNA affinity could indicate the consequences surrounding mis-metalation and is pursued in Chapter 4.

It is important to note that the oligomeric state of each non-cognate sensors has not been determined in the presence of Ni(II). Fur, which is generally considered a dimer in the cell, has been shown to form a tetramer (dimer of dimers) (Agriesti et al., 2014, Pérard et al., 2018). Even if affinity values for additional oligomerisation events were known, the presence of Ni(II) could facilitate favourable formation of these structures, meaning a different apparent oligomerisation constant. The Ni(II) stoichiometry for CueR was unusual being three ions per dimer, though this stoichiometry has been seen for *B. subtilis* MntR when binding non-cognate Co(II) (McGuire et al., 2013). It could be that the dimeric protein does have a pocket in which Ni(II) can bind which is not symmetrically replicated. Alternatively, dimer-dimer interactions could generate the interface to allow an additional Ni(II) to bind (Section 3.6.2).

Using different probes generated slightly different affinity values for non-cognate sensors, possibly owing to a degree of error which was not replicated across each experiment. Additionally, the method for detecting Ni(II) binding to the protein was determined either directly (through Ni(II)-dependent features specific for the sensor involved) or indirectly (through features associated with Ni(II)-bound to the competitor) which adds more variation to the data collected. Following Ni(II)-sensor features directly was generally avoided with CueR and ZntR due to the relative lack of linear features, however, these methods were used to consolidate fluorescent-chelant-determined affinities and indicated values were essentially indifferent. The affinity values determined for each sensor using different competitors were generally very consistent (sometimes even when at the limits of the assay) and was reassuring evidence that affinity determination by competition is accurate and reliable, assuming concentrations and affinities are known and that the affinity to be measured is tested with a competitor in the correct range (i.e. not too tight and not too weak in comparison).

3.9.4 An affinity-threshold for non-cognate sensors?

Figure 3.31 combines the affinities determined for all the sensors, with each competitor tested. This figure shows what appears to be an affinity-threshold for non-cognate sensors, with the exception of Fur. The tightest sites for the other sensors do not exceed 1×10^{-10} M which is two orders of magnitude weaker than RcnR, the weaker of the two cognate Ni(II) sensors (Fur is anomalous with a Ni(II) affinity comparable to RcnR for its tightest site). This suggest that for non-cognate sensors to bind Ni(II), they would depend on the metal concentration exceeding the set-point (Section 1.3.1) at which NikR and RcnR respond, indicating Ni(II) could be close to saturating the capacity of the buffer, likely leading to highly toxic conditions within the cell (Section 1.1.1). Simulations which predict these events are discussed in Chapter 5.

These results suggest the cell has overcome the potential hazard associated with Ni(II) mis-metalation through not only evolving metal-sensors which function appropriately for their physiological role, but also to reduce their thermodynamic competitiveness for potentially contaminating metal species (discussed in Chapter 6). Fur aside, the threshold at which the other sensors appear to be restrained suggests there could be a certain cellular pressure which ensures this threshold is not breached. The assumption would be that a threshold affinity would apply to this set of sensors for any given physiological metal, but the actual threshold itself would likely be set at a different thermodynamic value, based on the competitiveness of each metal (i.e. following the Irving-Williams series).

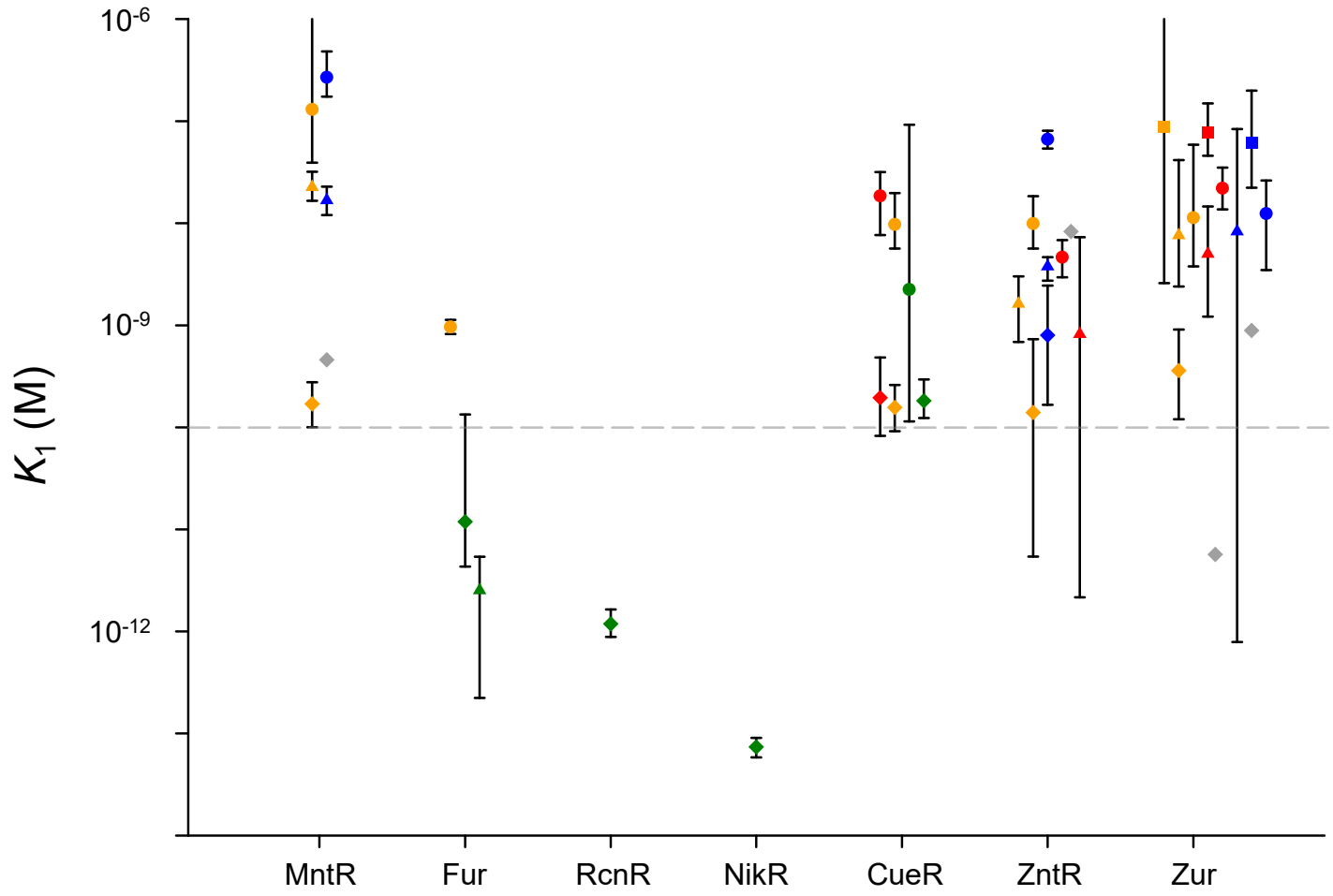

Figure 3.31 Comparison of all determined Ni(II) affinities for the seven *Salmonella* sensors. Competitors are indicated by different coloured symbols (EGTA, green; FluoZin-3, orange; mag-fura-2, blue; and bicine, red). Shapes represent individual stepwise affinities (K_{1a}, ♦; K_{1b}, ▲; $K_{1c\text{-}d}$, ●; and $K_{1e\text{-}f}$, ■). Grey symbols represent limit K_1 values which were out of range for the given competitor. Error bars show the 95% confidence intervals determined by Monte-Carlo simulations using DynaFit.

Table 3.1 UV/visible spectral features for Ni(II)-loaded sensors (pH 7.5).

Sensor	Wavelength (nm)	Ni(II) Binding Extinction Coefficient (M^{-1} cm^{-1})
NikR	463	~ 260
	302	7,020
	262	5,300
	243	6,290
RcnR	326	~ 400
	286	1,500
	280	1,540
MntR	n.a.	n.a.
Fur	n.a.	n.a.
CueR	410[a]	1,750
	340[a]	6,600
	303	10,000
	297[a]	10,100
	247[a]	13,000
ZntR	410[a]	1,790
	333[a]	9,300
	319[a]	10,000
	297[a]	12,300
	262[a]	9,900
	245[a]	14,100
Zur	*340*[b]	*2,060*
	290	9,040
	264	19,700

[a]Nonlinear peak indicating extinction coefficient at saturation.

[b]Extinction coefficient at saturation but unsure of peak linearity.

Table 3.2 Stepwise Ni(II)-binding affinities for the *Salmonella* sensors determined by competition assay.

Sensor	Ni(II) ions per multimer	Competitor			
		EGTA K_1 (M)	FluoZin-3 K_1 (M)	Mag-Fura-2 K_1 (M)	Bicine K_1 (M)
NikR$_4$	4	***a-d* = 7.38 × 10^{-14}** (5.83 – 9.06 × 10^{-14})[a]	n.d.	n.d.	n.d.
RcnR$_4$	4	***a-d* = 1.18 × 10^{-12}** (0.88 – 1.64 × 10^{-12})	n.d.	n.d.	n.d.
MntR$_2$	4	n.d.	***a* = 1.70 × 10^{-10}** (1.01 – 2.77 × 10^{-10}) ***b* = 2.26 × 10^{-8}** (1.66 – 3.20 × 10^{-8}) ***c-d* = *1.30 × 10^{-7}*** [b] *(3.92 × 10^{-8} – 1.30 × 10^{-1})*	***a* = *4.60 × 10^{-10}*** [b] *(4.61 × 10^{-16} – 2.88 × 10^{-9})* ***b* = 1.68 × 10^{-8}** (1.20 – 2.28 × 10^{-8}) ***c-d* = 2.68 × 10^{-7}** (1.74 – 4.82 × 10^{-7})	n.d.
Fur$_2$	4	***a* = 1.19 × 10^{-11}** (0.04 – 1.34 × 10^{-10}) ***b* = 2.52 × 10^{-12}** (0.22 – 5.40 × 10^{-12}) **c-d = n.d.**	***a-b* = *8.00 × 10^{-12}*** [b] *(8.78 × 10^{-12} – 3.24 × 10^{-5})* ***c-d* = 9.60 × 10^{-10}** (0.82 – 1.13 × 10^{-9})	n.d.	n.d.
CueR$_2$	3	***a-b* = *1.82 × 10^{-10}*** [c] *(1.24 – 2.95 × 10^{-10})* ***c* = *2.24 × 10^{-9}*** [c] *(0.01 – 9.24 × 10^{-8})*	***a-b* = 1.57 × 10^{-10}** (0.92 – 2.61 × 10^{-10}) **c = 9.70 × 10^{-9}** (0.57 – 1.98 × 10^{-8})	n.d.	***a-b* = *1.95 × 10^{-10}*** [c] *(0.83 – 4.83 × 10^{-10})* ***c* = *1.85 × 10^{-8}*** [c] *(0.77 – 3.17 × 10^{-8})*
ZntR$_2$	4	n.d.	***a* = 1.40 × 10^{-10}** (0.05 – 7.31 × 10^{-10}) ***b* = 1.62 × 10^{-9}** (0.69 – 3.02 × 10^{-9}) ***c-d* = 9.90 × 10^{-9}** (0.56 – 1.84 × 10^{-8})	***a* = *8.00 × 10^{-10}*** [c] *(0.17 – 2.45 × 10^{-9})* ***b* = *3.76 × 10^{-9}*** [c] *(2.73 – 4.66 × 10^{-9})* ***c-d* = *6.65 × 10^{-8}*** [c] *(5.40 – 8.08 × 10^{-8})*	***a* = *8.30 × 10^{-9}*** [c] *(5.09 × 10^{-10} – 4.03)* ***b* = *8.20 × 10^{-10}*** [c] *(2.16 × 10^{-12} – 7.30 × 10^{-9})* ***c-d* = *4.63 × 10^{-9}*** [c] *(2.96 – 6.83 × 10^{-9})*

Zur$_2$	6	n.d.	***a* = 3.60 × 10^{-10}** (1.20 – 9.10 × 10^{-10}) ***b* = 7.60 × 10^{-9}** (0.24 – 4.17 × 10^{-8}) ***c-d* = 1.13 × 10^{-8}** (0.38 – 5.88 × 10^{-8}) ***e-f* = *8.80 × 10^{-8}*** [b] *(2.59 × 10^{-9} – 8.74 × 10^{-2})*	***a* = *8.90 × 10^{-10}*** [b] *(8.85 × 10^{-16} – 2.80 × 10^{-5})* ***b* = 8.30 × 10^{-9}** (7.87 × 10^{-13} – 8.37 × 10^{-8}) ***c-d* = 1.24 × 10^{-8}** (0.35 – 2.62 × 10^{-8}) ***e-f* = 6.10 × 10^{-8}** (0.22 – 2.00 × 10^{-7})	***a* = *5.70 × 10^{-12}*** [b] *(1.14 × 10^{-15} – 1.31 × 10^{-9})* ***b* = 5.00 × 10^{-9}** (0.12 – 1.46 × 10^{-8}) ***c-d* = 2.20 × 10^{-8}** (1.37 – 3.51 × 10^{-8}) ***e-f* = 7.70 × 10^{-8}** (0.46 – 1.49 × 10^{-7})

[a]95% confidence interval for each calculated affinity.

[b]Beyond the limit of the assay.

[c]Determined from a single data set.

Chapter 4: The effect of Ni(II) on the DNA affinity of *Salmonella* sensors

4.1 Introduction

4.1.1 Background information

Metallosensors exhibit metal-dependent changes in DNA affinity. These effects are allosteric because the metal- and DNA-binding interfaces of each sensor are distinct, and the metal ion does not mediate direct interactions between protein and DNA. Sensors have been intensively studied to understand the structural basis for metal control of DNA-binding as well as the selectivity of this response. It is clear that metal coordination geometry plays a key role in determining metal specific responses (Section 1.3.2). Additionally, evidence suggests a single ligand within the correct coordination geometry is responsible for communicating metal-site occupancy to the DNA-binding interface (Eicken et al., 2003). Homologues of the *Salmonella* sensors have been studied to understand the mechanisms of metal selective responses in these different structural families (Section 1.3).

While there is a physical basis for distinguishing between the cognate metal and some non-cognate metals, the lack of a physiological response cannot be explained by *in vitro* data for other non-cognate metals. *In vitro* studies do suggest non-cognate metals induce transcriptional responses for some sensors though this is not commonly observed *in vivo* (Althaus et al., 1999, Que and Helmann, 2000, Changela et al., 2003, Mills and Marletta, 2005, Iwig et al., 2008, Foster et al., 2014a). Therefore, cellular factors may also control metal-specific responses. Studying the effect of Ni(II) on the DNA affinities of the *Salmonella* sensors will provide broader insight into the relative contributions of physical versus physiological contributions to metal selectivity.

While the cellular set of sensors were shown to bind Ni(II) in Chapter 3, the allosteric effect this metal has on non-cognate sensors is mostly unknown. The lack of non-cognate *in vivo* responses have been suggested to be a result of the buffered concentrations of metals maintained below the concentration required to populate weaker-binding non-cognate sensors, determined by the set-points from cognate sensors (Osman et al., 2017). By using conditions where the cellular metal concentration could exceed the capacity of the buffer, transcriptional responses due to mis-metalation have been observed for both Zn(II) and

Co(II) in *Salmonella* (Osman et al., 2017). These observations were predicted through understanding the thermodynamic cycle between metal- and DNA-binding of the sensors.

The DNA-affinities for each sensor in the presence and absence of Ni(II) have been determined here in order to complete the thermodynamic cycle described in Figure 1.2 (along with K_1 determined in Chapter 3) so that cellular predictions of operator occupancy can be made (Chapter 5). The ratio of the DNA affinities in the absence and presence of Ni(II) yields a coupling free energy (ΔG_C), the magnitude of which reports on the ability of Ni(II) to alter DNA affinity and these values are compared with the ΔG_C values for the sensors and their cognate metal.

4.1.2 Overview of the experimental approach

DNA affinities were measured by FA for both the apo and Ni(II)-bound forms of each *Salmonella* sensor (Section 2.9.3). The FA experiments were carried out in an identical buffer (Buffer N) that matches intracellular pH and cation/anion concentration (Epstein and Schultz, 1965). Apo-sensor DNA affinities used Buffer N containing 1 mM EDTA to prevent adventitious binding of trace contaminating metals (if present). Further experimental details are described in Section 2.9.3. Metal-free affinity values (K_3; Figure 1.2) have been determined previously for *Salmonella* sensors under slightly different conditions (pH 7.0, 5 mM EDTA). The parallel K_4 value refers to the affinity calculated for 1:1 Ni(II)-loaded sensor (i.e. one Ni(II) per monomeric subunit), however, when non-cognate sensors bind Ni(II) with greater than 1:1 stoichiometry then K_4', K_4'', and K_4''' are used to specify 1:1, 2:1, and 3:1 Ni(II)-loaded sensors, respectively.

The calculated affinities are shown in Table 4.1, which also shows the 95% confidence intervals determined by Monte-Carlo simulations. Model curves using 10-fold tighter and 10-fold weaker affinity values were used to identify the limits of the assay under the given experimental condition. The fitting models accounted for the extent of Ni(II) binding to each sensor (Section 2.10.2), a necessary correction for a subset of the sensors at lower protein concentrations.

4.2 NikR

4.2.1 Determination of the Ni(II)-NikR binding stoichiometry and K_4 affinity for *nixA*-Pro

The binding stoichiometry of Ni(II)-NikR and *nixA*-Pro was determined by direct addition of protein to a high concentration (100 nM) of HEX-labelled DNA (Section 2.9.1). The Δr_{obs} reached a plateau at 1:1 NikR tetramer to DNA (Figure 4.1a), as previously reported (Osman et al., 2018).

The DNA affinity (K_4) was determined by titrating Ni(II)-NikR to a limiting concentration (10 nM) of *nixA*-Pro. Fitting all four replicate data sets simultaneously to a 1:1 binding model (Figure 4.1b) generated a K_4 of 9.83×10^{-9} M (Table 4.1). The same experiment was also carried out at pH 7.0 and returned a very similar value of $9.5 \pm 0.8 \times 10^{-9}$ M (Osman et al., 2018) suggesting that pH affected DNA affinity to a lesser extent than Ni(II) affinity (Section 3.9.1), consistent with minimal protein-DNA contacts of side chains with a pK_a in the neutral range (Schreiter et al., 2006). The 10-fold tighter and weaker simulated curves for K_4 (Figure 4.1b) showed that the data fit within the limits of the assay and that the DNA concentration was not too high based on the determined K_4 value. NikR was fully saturated with Ni(II) over the entire protein concentration range.

The observed Δr_{obs} with 10 nM *nixA*-Pro (Figure 4.1b) was greater (~ 20%) than with 100 nM *nixA*-Pro (Figure 4.1a). The data for excess DNA did begin to increase in Δr_{obs} after the DNA was saturated and could suggest higher order complex association with *nixA*-Pro. This effect could be exacerbated using limited concentrations of DNA (since there will be a much greater excess of protein over DNA) and could result in the increase in Δr_{obs} compared to excess DNA. Nonetheless, the data from Figure 4.1b could be fit to a fixed response determined from Figure 4.1a with a negligible effect on K_4.

4.2.2 Determination of the NikR K_3 affinity for *nixA*-Pro

The K_3 affinity was determined by titrating apo-NikR to 10 nM *nixA*-Pro. Little binding was observed until > 1 μM protein had been added (Figure 4.1c), consistent with the requirement of Ni(II) for high affinity DNA binding. The total Δr_{obs} seen with Ni(II)-NikR (Figure 4.1a-b) was not observed due to the limiting constraint of the apo-NikR stock solution concentration. Four replicate data sets were fit simultaneously (Figure 4.1c) and generated a K_3 of 2.59×10^{-5} M (Table 4.1), with Δr_{obs} fixed to the Ni(II)-NikR response (Section 4.2.1). This value was well within the 10-fold limits of the assay (Figure 4.1c), with the assumption that Δr_{obs} is similar to Ni(II)-NikR. The same experiment was carried out at pH 7.0 and

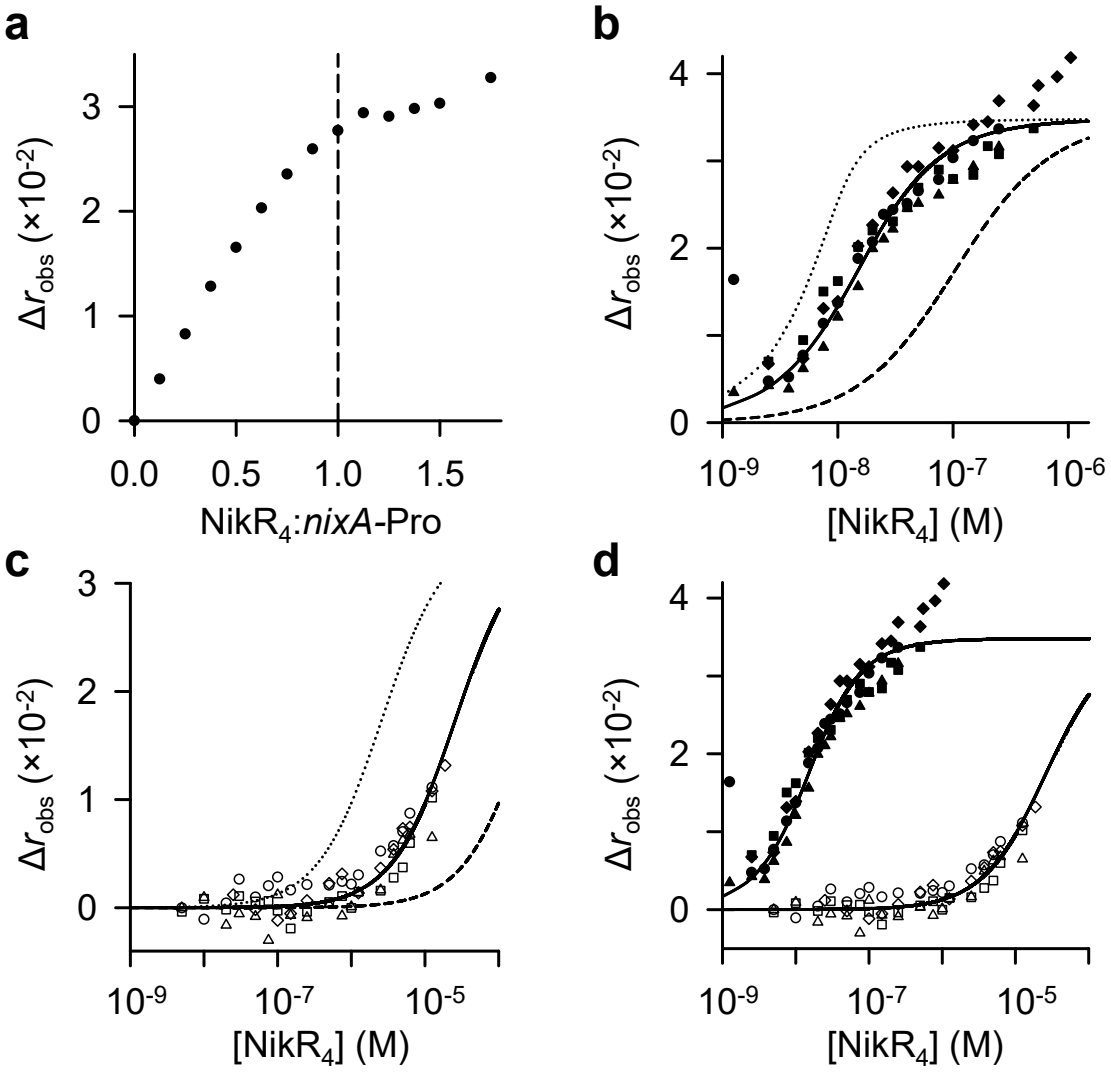

Figure 4.1 Determination of the *Sty*NikR DNA affinities for *nixA*-Pro by FA. (a) Ni(II)-NikR binding stoichiometry for *nixA*-Pro determined by titration to 100 nM HEX-labelled *nixA*-Pro. NikR was loaded with 0.95 equivalents of Ni(II) along with a small concentration of L-histidine (< 20 μM in a 50 μM stock of NikR monomer). The experiment without L-histidine showed the same result. **(b)** Ni(II)-NikR (0.95:1) titrated to 10 nM *nixA*-Pro (n=4) to determine the DNA affinity (K_4). The solid line indicates the best simultaneous fit to all data sets. Modelled fits are shown for the titration using K_4 10-fold tighter (dotted line) or 10-fold weaker (dashed line) to show the limits of the assay. **(c)** Same as (b) except data for apo-NikR (K_3; n=4). **(d)** Combined data for Ni(II)-NikR (solid symbols) and apo-NikR (empty symbols) showing the line of best fit for both sets.

returned a similar value ($1.1 \pm 0.1 \times 10^{-5}$ M), again suggesting a minimal effect of pH (in this range) on DNA binding (Osman et al., 2018).

It is important to note that an accurate upper baseline determination is critical to determine K_3 with high confidence since K_3 reflects 50% DNA-binding, therefore, an endpoint or a significant proportion of the titration curve is needed to properly fit this value.

4.2.3 Calculation of the coupling free energy (ΔG_C) for binding to *nixA*-Pro

The difference between K_3 and K_4 for *nixA*-Pro can be seen in Figure 4.1d. This difference can be quantified as ΔG_C for DNA binding (Section 2.9.4). For NikR with *nixA*-Pro, ΔG_C was -4.8 ± 0.2 kcal mol^{-1} (Table 4.1), representing a negative value as expected because of the role of Ni(II) as a co-repressor molecule. The ΔG_C value at pH 7.0 (-4.2 ± 0.1 kcal mol^{-1}) was less negative (Osman et al., 2018). The difference between the two ΔG_C values reflected the slightly tighter K_4 and slightly weaker K_3 values at pH 7.5, compared to pH 7.0. However, better determined K_3 values would be required before concluding that this difference was significant.

4.2.4 Determination of the Ni(II)-NikR K_4 affinity for *nikA*-Pro

*Sty*NikR binds a second operator site within the *Salmonella* genome; the *nikA* promoter (Section 1.3.9). Determination of K_4 for NikR with *nikA*-Pro required a modified approach because a small Δr_{obs} (< 0.01) resulted in very noisy data when protein was added. Instead, a competition experiment was developed whereby Ni(II)-NikR was titrated to a mixture of 10 nM HEX-labelled *nixA*-Pro and 50 nM unlabelled *nikA*-Pro (*nikA*-u). Here, *nikA*-u acted as a competitor to shift the binding curve for *nixA*-Pro. Three replicate data sets were fit simultaneously (Figure 4.2) and generated a K_4 of 4.26×10^{-9} M for *nikA*-u (Table 4.1), fitting within the 10-fold limits of the assay. The *nixA* and *nikA* operator sequences differ by a single base substitution within one half of the inverted repeat (Section 1.3.9) and this resulted in a 2-fold difference in K_4. At these tight affinities, this difference was not expected to affect the promoter response (see Section 5.4.1).

The poor Δr_{obs} for HEX-labelled *nikA*-Pro meant that determination of K_3 was not feasible due to the large quantities of DNA and protein that would be required. Therefore, ΔG_C was estimated for *nikA*-Pro by using K_3 for *nixA*-Pro, and generated a value of -5.2 ± 0.1 kcal mol^{-1} (Table 4.1).

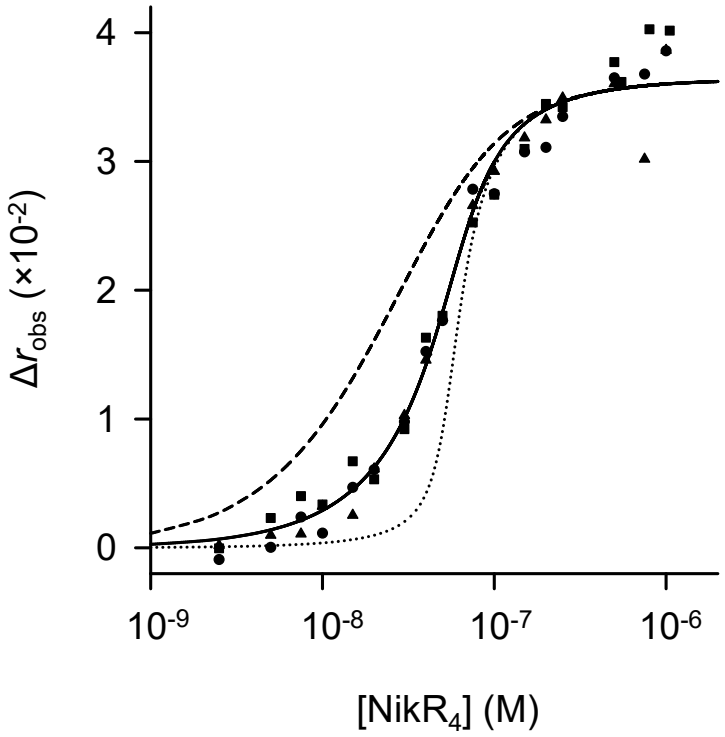

Figure 4.2 Determination of the *Sty*NikR DNA affinity (K_4) for *nikA*-Pro by FA. Ni(II)-NikR (0.95:1) titrated to 10 nM HEX-labelled *nixA*-Pro in the presence of 50 nM *nikA*-u (n=3). The solid line indicates the best simultaneous fit to all data sets. Modelled fits are shown for the titration using K_4 10-fold tighter (dotted line) or 10-fold weaker (dashed line) to show the limits of the assay.

4.3 RcnR

4.3.1 Determination of the RcnR K_3 affinity for *rcnRA*-Pro

The stoichiometry of *Sty*RcnR binding to *rcnRA*-Pro (2:1 with no cooperativity) has been determined (Osman et al., 2016). For this work, an initial determination of Δr_{obs} was carried out with apo-RcnR titrated to 10 nM *rcnRA*-Pro in Buffer J (Buffer N except pH 7.0). The data (Figure 4.3) showed the Δr_{obs} was very similar to that previously described (Osman et al., 2016). Therefore, the response fitted to this data was used for subsequent RcnR FA experiments when an endpoint needed to be fixed for data fitting. The K_3 value determined here was tighter than the published affinity, possibly due to a lower EDTA concentration, which could have affected affinity by competing for DNA binding, but this was not investigated further.

The apo-RcnR affinity for *rcnRA*-Pro in Buffer N was determined from fitting three replicate data sets simultaneously (Figure 4.4a), and generated a K_3 of 1.77×10^{-7} M (Table 4.1). The data showed additional binding events, necessitating a fixed Δr_{obs} value (Figure 4.3) to determine K_3. The data fit within the 10-fold limits of the assay (Figure 4.4a). The previously reported K_3 value for this DNA sequence was $1.5 \pm 0.8 \times 10^{-7}$ M (pH 7.0) and closely matches the value determined here (Osman et al., 2016).

4.3.2 Determination of the Ni(II)-RcnR K_4 affinity for *rcnRA*-Pro

The K_4 affinity was determined by titrating Ni(II)-RcnR to 10 nM *rcnRA*-Pro. Three replicate data sets were fit simultaneously (Figure 4.4b), using the fixed Δr_{obs} value (Figure 4.3), and generated a K_4 of 3.11×10^{-6} M (Table 4.1). The majority of the titration was complete (~ 65%) based on the fixed response and the data fit within the 10-fold limits of the assay (Figure 4.4b). Under the assay conditions, ≥ 97% of the RcnR was fully metalated at all concentrations.

The K_4 value for Ni(II)-RcnR binding to *rcnRA*-Pro calculated here is 5-fold tighter than K_4 for Co(II)-RcnR ($\geq 1.5 \pm 0.2 \times 10^{-5}$ M, pH 7.0), but only ~ 2-fold tighter than the reported Ni(II)-RcnR K_4 ($\geq 5.9 \pm 1.3 \times 10^{-6}$ M, pH 7.0) (Osman et al., 2016). The different K_4 values for Ni(II)- and Co(II)-bound proteins are not surprising because different ligand sets appear important for coordinating the different metals (Iwig et al., 2008, Carr et al., 2017), which could affect the allosteric response of the protein to each metal.

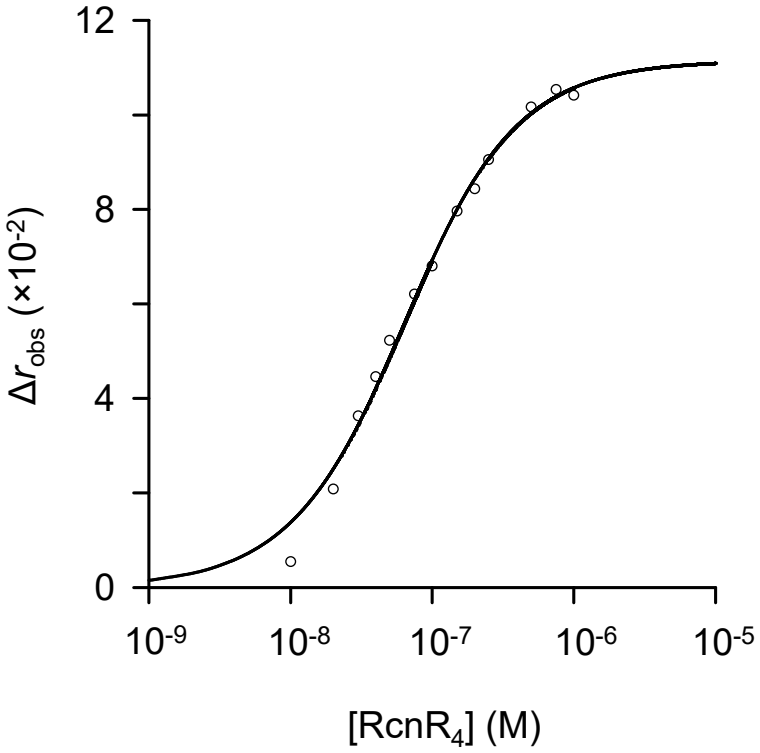

Figure 4.3 Determination of the *Sty*RcnR DNA binding response for *rcnRA*-Pro by FA. Apo-RcnR titrated to 10 nM HEX-labelled *rcnRA*-Pro (n=1) in Buffer J. The solid line indicates the best fit for this data set.

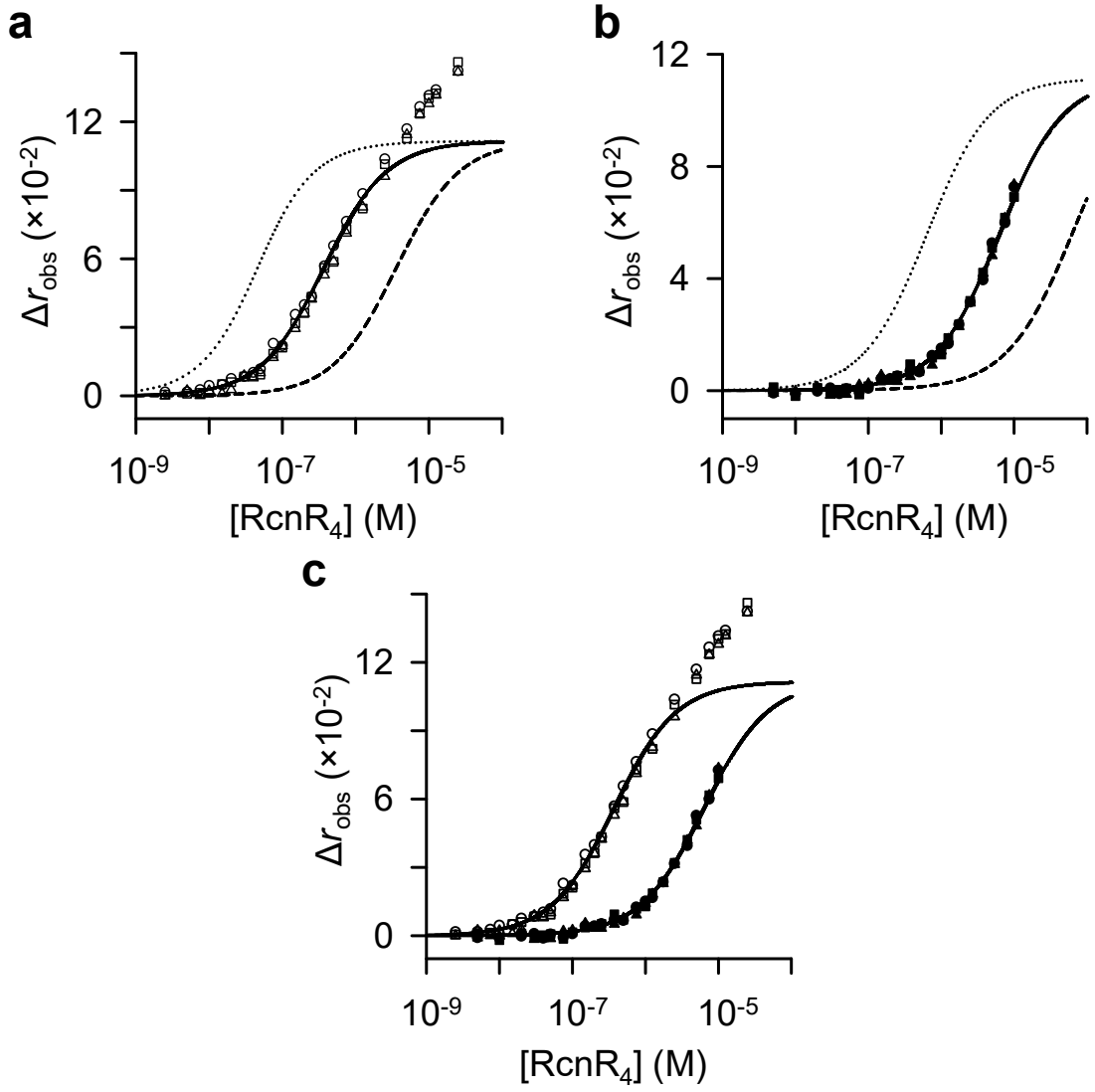

Figure 4.4 Determination of the *Sty*RcnR DNA affinities for *rcnRA*-Pro by FA. (a) Apo-RcnR titrated to 10 nM HEX-labelled *rcnRA*-Pro (n=3) to determine the DNA affinity (K_3). The solid line indicates the best simultaneous fit to all data sets. Modelled fits are shown for the titration using K_3 10-fold tighter (dotted line) or 10-fold weaker (dashed line) to show the limits of the assay. **(b)** Same as (a) except data for 1:1 Ni(II)-RcnR (K_4; n=3). **(c)** Combined data for apo-RcnR (empty symbols) and Ni(II)-RcnR (solid symbols) showing the line of best fit for both sets.

4.3.3 Calculation of the coupling free energy (ΔG_C) for binding to *rcnRA*-Pro

The K_3 and K_4 data were plotted for visual comparison (Figure 4.4c). K_3 was tighter than K_4, as expected for a metal-dependent de-repressor. Therefore, a positive ΔG_C of +1.7 ± 0.1 kcal mol^{-1} was observed (Table 4.1). The ΔG_C value for Ni(II)-RcnR (pH 7.0) was ≥ +2.2 ± 0.2 kcal mol^{-1} (Osman et al., 2016), indicating a greater difference between K_3 and K_4 at pH 7.0 compared to pH 7.5, though these values are very similar when accounting for the standard error. For comparison, at pH 7.0 the ΔG_C for Co(II)-RcnR is ≥ +2.7 ± 0.2 kcal mol^{-1}, consistent with the greater effect of Co(II) on K_4 (Osman et al., 2016).

4.4 MntR

4.4.1 Determination of the Ni(II)-MntR binding stoichiometry for *mntS*-Pro

The stoichiometry of Ni(II)-MntR for *mntS*-Pro was determined with 2:1 Ni(II)-MntR added to 1 μM *mntS*-Pro. The data (Figure 4.5a) demonstrated additional binding events as observed previously for Mn(II)-bound and apo-MntR (Osman et al., 2018). The initial linear phase from this experiment was extrapolated to a 1:1 ratio of MntR dimer:*mntS*-Pro to define the predicted Δr_{obs} in the absence of additional binding events, even though nonlinearity was apparent from 0.75:1 protein to DNA.

4.4.2 Determination of the Ni(II)-MntR K_4' affinity for *mntS*-Pro

The affinity (K_4') of 1:1 Ni(II)-MntR was determined by titration to 10 nM *mntS*-Pro. Six replicate data sets were fit simultaneously (Figure 4.5b) and generated $K_4' \geq 1.12 \times 10^{-8}$ M (Table 4.1). Because additional binding events were observed, the data was fit with the 1:1 Δr_{obs} determined above (Section 4.4.1), fitting only data points below this value (≤ 50 nM dimer). The data generally fit within the 10-fold tighter and weaker limits of the assay (Figure 4.5b). The lower baseline was allowed to vary in the DynaFit model (see Section 7.4) to account for the Δr_{obs} values below zero. Because of the impact of additional binding events on the shape of the curve before reaching the fixed Δr_{obs}, the affinity of 1:1 Ni(II)-MntR was considered a lower limit. The fit allowed for the presence of apo-MntR over the full range of protein concentrations.

4.4.3 Determination of the Ni(II)-MntR K_4'' affinity for *mntS*-Pro

The affinity (K_4'') of 2:1 Ni(II)-MntR was determined by titration to 10 nM *mntS*-Pro. Four replicate date sets were fit simultaneously (Figure 4.5c) and generated $K_4'' \geq 1.19 \times 10^{-9}$ M

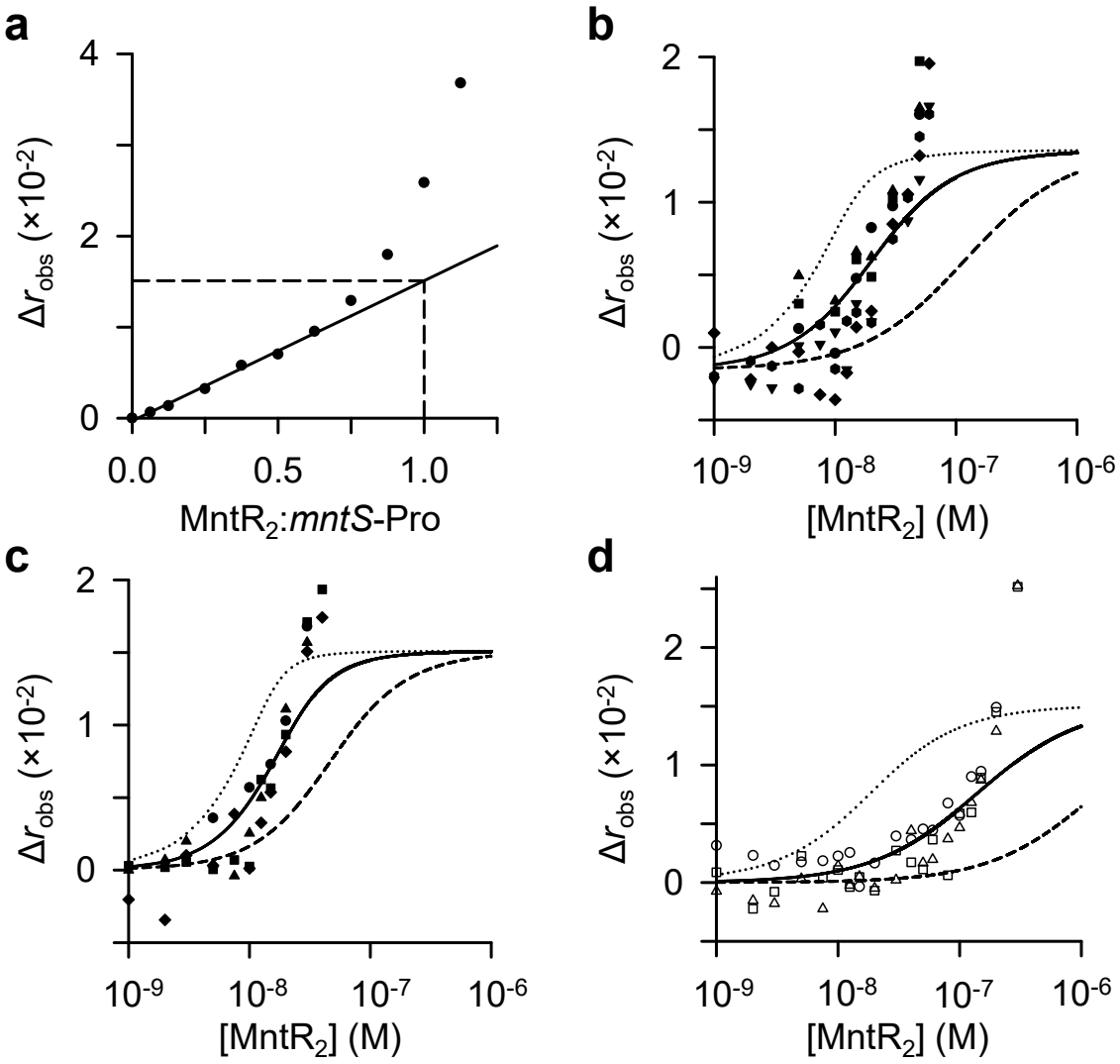

Figure 4.5 Determination of the *Sty*MntR DNA affinities for *mntS*-Pro by FA. (a) Ni(II)-MntR (2:1) binding stoichiometry for *mntS*-Pro determined by titration to 1 μM HEX-labelled *mntS*-Pro. The solid line represents a linear regression from the first seven data points. The dashed lines indicate what the expected Δr_{obs} would be for a 1:1 binding model. **(b)** 1:1 Ni(II):MntR titrated to 10 nM *mntS*-Pro (n=6) to determine the DNA affinity (K_4'). The solid line indicates the best simultaneous fit to all data sets. Modelled fits are shown for the titration using K_4' 10-fold tighter (dotted line) or 10-fold weaker (dashed line) to show the limits of the assay. **(c)** Same as (b) except data for 2:1 Ni(II)-MntR (K_4''; n=4). **(d)** Same as (b) except data for apo-MntR (K_3; n=3).

(Table 4.1). Additional binding events meant the data was fixed to the 1:1 Δr_{obs} determined above (Section 4.4.1), fitting only data points below this response (≤ 50 nM dimer). The data fit within the 10-fold tighter and weaker limits (Figure 4.5c) and no baseline offset was required. The fit allowed for the presence of apo-MntR over the full range of protein concentrations.

K_4'' appeared tighter than K_4' and tighter still than the reported value of 5×10^{-9} M for Mn(II)-MntR determined at pH 7.0 (Osman et al., 2018). This indicates Ni(II) could elicit a similar allosteric response to Mn(II) for DNA binding, but this is interpreted cautiously due to the additional binding events limiting the determined affinity values. Previously determined Ni(II)-MntR (*B. subtilis*) DNA affinities have been reported as $2.3 \pm 0.3 \times 10^{-6}$ M (for *mntH*) and $5.1 \pm 0.4 \times 10^{-7}$ M (for *mntA*), though conditions used were different to those here, where the salt concentration was higher (500 mM) and Ni(II) was added in great excess of the protein (Lieser et al., 2003, Golynskiy et al., 2005).

4.4.4 Determination of the MntR K_3 affinity for *mntS*-Pro

The K_3 affinity of MntR was determined by titration of apo-protein to 10 nM *mntS*-Pro. Three replicate data sets were fit simultaneously (Figure 4.5d) and generated $K_3 \geq 1.33 \times 10^{-7}$ M (Table 4.1). Additional binding events were observed meaning the data was fixed to the 1:1 Δr_{obs} (Section 4.4.1), fitting only the data points below this response (≤ 200 nM dimer). The data fell within the 10-fold tighter and weaker limits of the assay (Figure 4.5d). Again, the affinity value was considered a lower limit because additional binding events were still present. The K_3 value measured here was marginally weaker than that measured at pH 7.0 ($8.6 \pm 1.7 \times 10^{-8}$ M (Osman et al., 2018)), although the difficulty in determining the final Δr_{obs} complicated an accurate determination of any differences.

4.4.5 Calculation of the coupling free energy (ΔG_C) for binding to *mntS*-Pro

The combined data sets for 1:1 Ni(II)-loaded and apo-MntR (Figure 4.6a) highlight the offset fit for K_4' required to best fit the data (Section 4.4.2). ΔG_C of -1.4 ± 0.2 kcal mol^{-1} (Table 4.1) was calculated from the limits of K_3 and K_4', however, this value could vary due to the uncertain effects of additional binding events on the determination of K_3 and K_4' (also applicable for 2:1 ΔG_C, see below). The negative ΔG_C suggested that MntR still behaved as a co-repressor where Ni(II) binding to the protein had a positive effect regarding DNA affinity. The ΔG_C reported in the literature for Mn(II)-MntR with *mntS*-Pro is -1.7 ± 0.1 kcal mol^{-1} (Osman et al., 2018). This value is similar to the one determined here for Ni(II)-MntR, however the Mn(II)-determined ΔG_C value could be more negative because the Mn(II)-

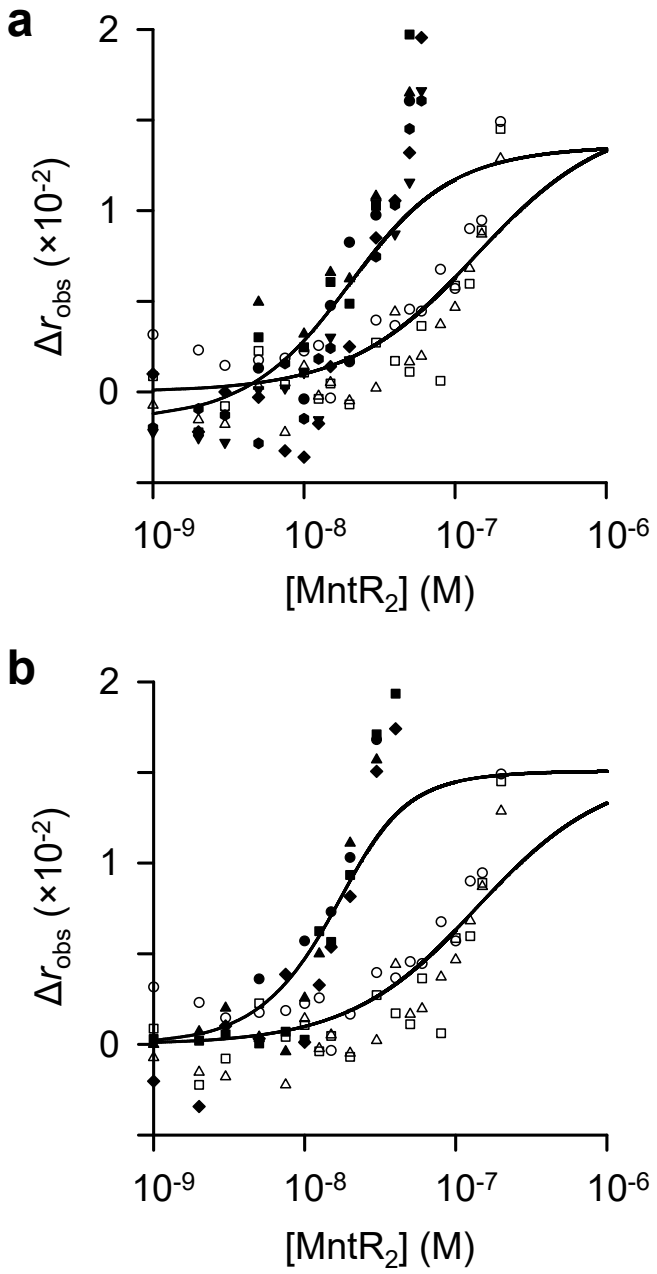

Figure 4.6 Comparison of Ni(II)-loaded and apo-MntR binding to *mntS*-Pro. (a) Combined data for 1:1 Ni(II)-MntR (solid symbols) and apo-MntR (empty symbols) showing the line of best fit for both sets. **(b)** Same as (a) except data for 2:1 Ni(II)-MntR (solid symbols) and apo-MntR (empty symbols).

MntR K_4 affinity was close to the lower limit of the assay and determination of the K_3 is limited by the additional binding events. Since the determined affinities are limit values, it is difficult to compare the ΔG_C values with the cognate metal.

The data for 2:1 Ni(II)-MntR can also be compared with apo-protein (Figure 4.6b). ΔG_C calculated for the limits of K_3 and K_4'' was -2.5 ± 0.3 kcal mol^{-1} (Table 4.1) and represents a much greater free energy change compared to 1:1 Ni(II)-MntR (and Mn(II)-MntR). Though, again, it is difficult to interpret the ΔG_C values since determined affinities only represent limits due to additional binding events.

4.5 Fur

4.5.1 Determination of the Ni(II)-Fur K_4' affinity for *fur-box*

*Sty*Fur binds to the *fur-box* with 2:1 stoichiometry (dimers per DNA) (Osman et al., 2018). The affinity (K_4') of 1:1 Ni(II)-Fur was determined by titration to 10 nM *fur-box*. Three replicate data sets were fit simultaneously (Figure 4.7a) and generated equivalent affinities for each dimer binding event, $K_{4a\text{-}b}'$ 1.28 × 10^{-5} M (Table 4.1). The titration did not approach an obvious endpoint and therefore Δr_{obs} was fixed to the value determined for K_4'' (see Section 4.5.2). The lack of data points up to this endpoint meant the presence of positive cooperativity could not be determined. The data fit within the 10-fold tighter and weaker limits of the assay (Figure 4.7a). As with MntR, there were data points with $\Delta r_{obs} < 0$, but when an offset for the lower baseline was included in the DynaFit model there was little effect on the $K_{4a\text{-}b}'$ affinity value so this correction was not used. Simulations indicated that the protein was fully metalated across the range of Fur concentrations used in this titration.

4.5.2 Determination of the Ni(II)-Fur K_4'' affinity for *fur-box*

The affinity (K_4'') of 2:1 Ni(II)-Fur was determined by titration to 10 nM *fur-box*. Four replicate data sets were fit simultaneously (Figure 4.7b-c) and generated affinities of K_{4a}'' 3.70 × 10^{-6} M and K_{4b}'' 7.50 × 10^{-7} M (Table 4.1). In this case, positive cooperativity (~ 5-fold) was observed between the two dimer binding events. Both K_4'' values fit within the 10-fold tighter and weaker limits of the assay (Figure 4.7b-c). The reported Fe(II)-Fur affinity for *fur-box* was 5.6 ± 2.1 × 10^{-8} M (pH 7.0) and was fit without cooperativity. This affinity is an order of magnitude tighter than the tightest binding event seen with Ni(II)-Fur which indicates the conformational changes associated with Fe(II) binding are different to Ni(II)

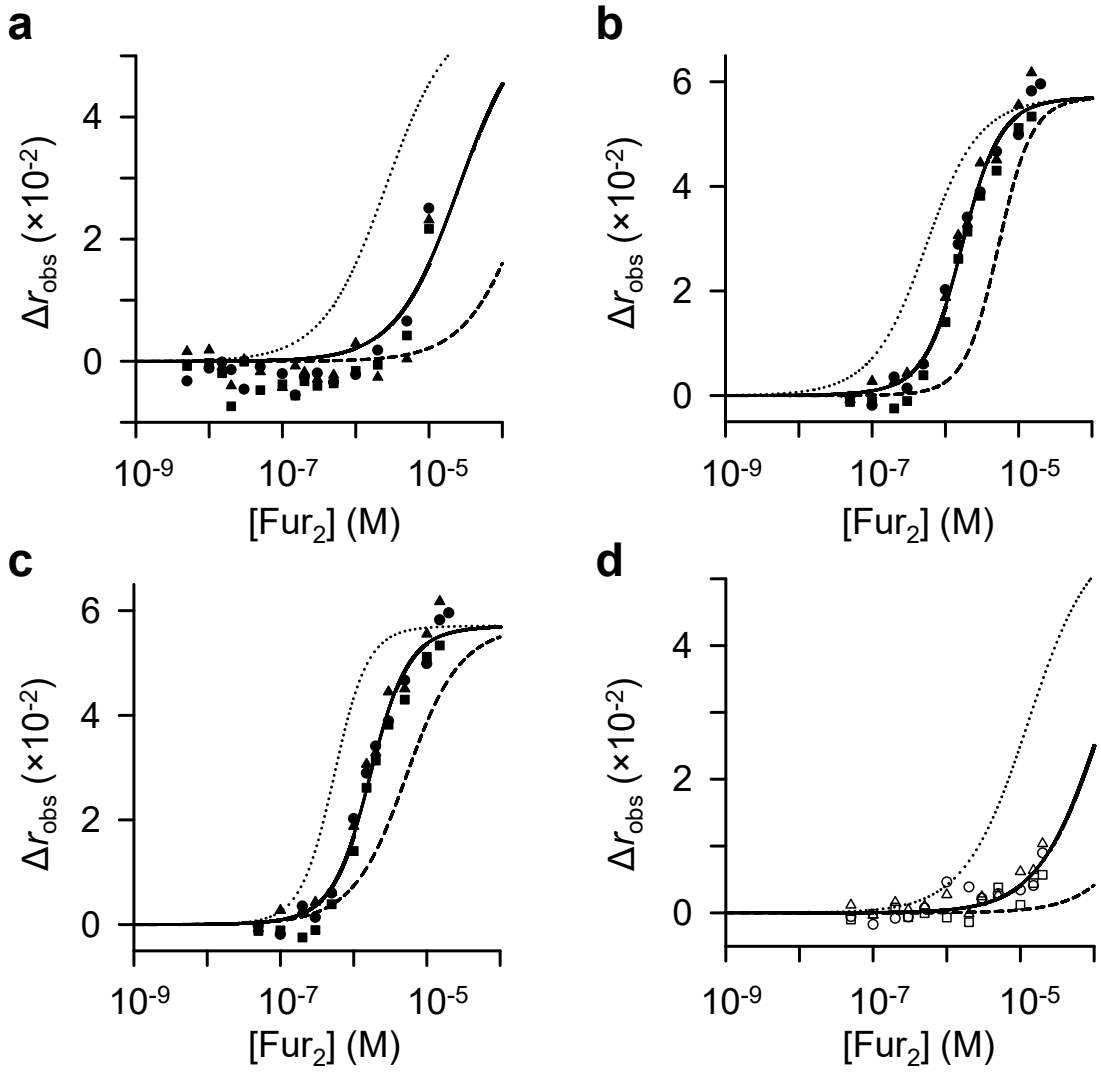

Figure 4.7 Determination of the *Sty*Fur DNA affinities for *fur-box* by FA. (a) Ni(II)-Fur (1:1) titrated to 10 nM HEX-labelled *fur-box* (n=3) to determine the DNA affinity (K_4'). The solid line indicates the best simultaneous fit to all data sets. Modelled fits are shown for the titration using $K_{4a\text{-}b}'$ 10-fold tighter (dotted line) or 10-fold weaker (dashed line) to show the limits of the assay. **(b)** Same as (a) except data for 2:1 Ni(II)-Fur (K_4''; n=3), indicating the limits for K_{4a}''. **(c)** Same as (b) except with limits for K_{4b}''. **(d)** Same as (a) except data for apo-Fur (K_3; n=3), indicating limits for $K_{3a\text{-}b}$.

(and probably other divalent metal ions), resulting in a more favourable allosteric response. The fit allowed for the presence of apo-Fur over the full range of protein concentrations.

4.5.3 Determination of the Fur K_3 affinity for *fur-box*

The affinity (K_3) of Fur was determined by titration of apo-protein to 10 nM *fur-box*. Three replicate data sets were fit simultaneously (Figure 4.7d) using a binding model without cooperativity ($K_{3a} = K_{3b}$) and generated a $K_{3a\text{-}b}$ of 6.38×10^{-5} M (Table 4.1), using Δr_{obs} from K_4'' (Section 4.5.2). Cooperativity was not used to fit the data because 15% of the titration curve was observed (limited by the concentration of the Fur protein stock), therefore, insufficient data was obtained to detect cooperative binding events. The data fit within the 10-fold tighter and weaker limits of the assay (Figure 4.7d). The affinity of apo-Fur for *fur-box* determined at pH 7.0 was $2.4 \pm 0.6 \times 10^{-5}$ M, also fit without cooperativity (Osman et al., 2018), using a similar portion of the titration curve. The similarity between values is reasonable given the modest amount of data available for each fit.

4.5.4 Calculation of the coupling free energy (ΔG_C) for binding to *fur-box*

The combined data sets for 1:1 Ni(II)-loaded and apo-Fur (Figure 4.8a) highlight the minimal difference between the two affinities. ΔG_C calculated for K_3 and K_4' was $\leq$ -1.0 ± 0.2 kcal mol^{-1} (Table 4.1). This suggested loading of the first two Ni(II) sites of the dimer does not correspond to an effective allosteric response.

The combined data sets for 2:1 Ni(II)-loaded and apo-Fur (Figure 4.8b) indicated a positive effect of Ni(II) on the DNA affinity of Fur, consistent for a co-repressor system. Consequently, ΔG_C calculated for K_3 and K_4'' was $\leq$ -2.0 ± 0.2 kcal mol^{-1} (Table 4.1). The value reported for Fe(II)-Fur (pH 7.0) was -3.6 ± 0.2 kcal mol^{-1} (Osman et al., 2018), as expected for the cognate metal which should have a greater allosteric effect on Fur.

4.5.5 Discussion and interpretation of the Fur DNA affinities for *fur-box*

The data indicated that Ni(II) can activate *Sty*Fur for DNA binding but less effectively than Fe(II). Interestingly, the Δr_{obs} from the FA experiments differ quite significantly between the two metalated forms. The Δr_{obs} seen here suggested a maximal change of ~ 0.057, approximately 40% greater than the response for Fe(II)-binding (~ 0.04 for 10 nM *fur-box* and ~ 0.045 for 1 µM *fur-box* (Osman et al., 2018)). This difference suggested distinct protein-DNA complexes with different tumbling times, with Ni(II)-Fur on DNA predicted to be larger due to the greater anisotropy change. This larger size could be due to formation of higher order species, such as a Ni(II)-Fur tetramer (Section 3.9.3). This would also yield

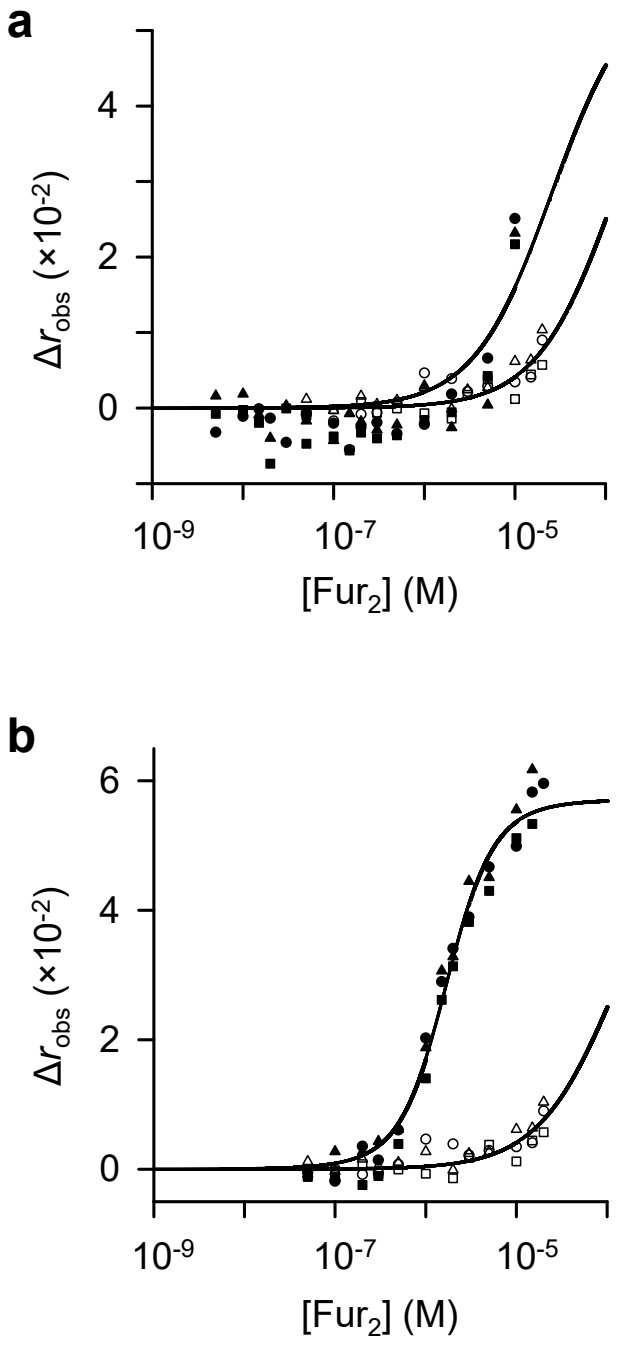

Figure 4.8 Comparison of Ni(II)-loaded and apo-Fur binding to *fur-box*. (a) Combined data for 1:1 Ni(II)-Fur (solid symbols) and apo-Fur (empty symbols). **(b)** Same as (a) except data for 2:1 Ni(II)-Fur (solid symbols) and apo-Fur (empty symbols).

a cooperative binding curve. Without information of Ni(II)-Fur oligomerisation (on or off DNA), it is not possible to generate an alternative model.

4.6 CueR

4.6.1 Determination of the Ni(II)-CueR binding stoichiometry with *copA*-Pro

The stoichiometry of *Sty*CueR binding to *copA*-Pro was determined using 1:1 Ni(II)-loaded protein. For the *Salmonella* protein, both apo- and Cu(I)-CueR bind to *copA*-Pro with a stoichiometry of two dimers per DNA (Osman et al., 2018), contrary to the 1:1 stoichiometry for the *E. coli* protein (Philips et al., 2015), though ternary complexes have been observed for MerR-family regulators (Chen et al., 2015). Ni(II)-CueR was titrated to 700 nM *copA*-Pro (Figure 4.9a) with an observed inflexion point at 2:1 dimers per *copA*-Pro. Additional binding events were also apparent, as has been reported for Cu(I)-CueR (Osman et al., 2018). From this result, the Δr_{obs} at the 2:1 inflexion point was used to fix the response in Ni(II)-CueR experiments. The Δr_{obs} for apo-CueR binding has been shown to differ to that for Cu(I)-CueR (Osman et al., 2018). Because the MerR-family regulators bind DNA with two different conformations (Figure 1.10), depending on whether the molecular signal is present, a difference in Δr_{obs} is not unexpected as the tumbling of two differently shaped molecules should be distinct.

4.6.2 Determination of the Ni(II)-CueR K_4 affinity for *copA*-Pro

The affinity (K_4) of 1:1 Ni(II)-CueR was determined by titration to 10 nM *copA*-Pro. Three replicate data sets were fit simultaneously (Figure 4.9b-c) to a binding model that allowed cooperativity between dimer binding events ($K_{4a} \neq K_{4b}$) and generated affinities of K_{4a} 5.50 $\times 10^{-8}$ M and K_{4b} 4.90 $\times 10^{-8}$ M (Table 4.1). Only data points with Δr_{obs} less than the response associated with a 2:1 binding stoichiometry (Section 4.6.1) were included in the fit. The data were within the 10-fold tighter and weaker limits of the assay (Figure 4.9b-c). The fit suggested only slight positive cooperativity (K_{4b} ~ 1.5-fold tighter than K_{4a}), however, the data did not fit well to an identical sites model. In contrast, Cu(I)-CueR showed greater positive cooperativity for binding to *copA*-Pro (K_{4a} 3.8 ± 1.8 $\times 10^{-7}$ M and K_{4b} 3.9 ± 1.7 $\times 10^{-8}$ M, pH 7.0 (Osman et al., 2018)). Interestingly, the K_{4a} values showed that the first Ni(II)-CueR dimer binds more favourably than the first Cu(I)-CueR dimer. The fit here allowed for the presence of apo-CueR over the full range of protein concentrations.

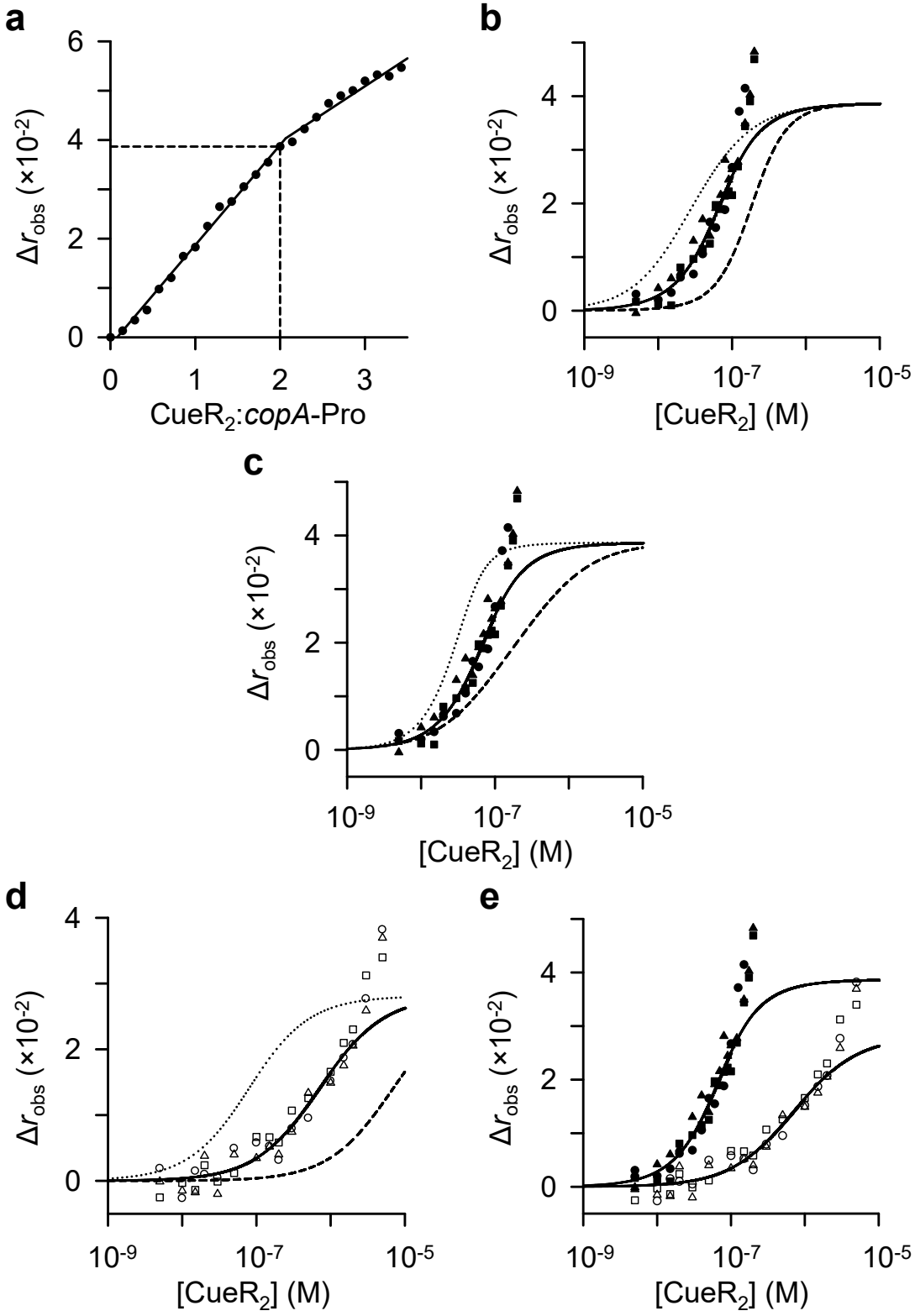

Figure 4.9 Determination of the *Sty*CueR DNA affinities for *copA*-Pro by FA. (a) Ni(II)-CueR (1:1) binding stoichiometry for *copA*-Pro determined by titration to 700 nM HEX-labelled *copA*-Pro. The solid line represents a linear regression from the data points up to a 2:1 ratio. The dashed lines indicate the Δr_{obs} for a 2:1 stoichiometry. **(b)** Ni(II)-CueR (1:1) titrated to 10 nM *copA*-Pro (n=3) to determine the DNA affinity (K_4). The solid line indicates the best simultaneous fit to all data sets. Modelled fits are shown for the titration using K_{4a} 10-fold tighter (dotted line) or 10-fold weaker (dashed line) to show the limits of the assay. **(c)** Same as (b) except with limits for K_{4b}. **(d)** Same as (b) except data for apo-CueR (K_3; n=3), indicating limits for $K_{3a\text{-}b}$. **(e)** Combined data for 1:1 Ni(II)-CueR (solid symbols) and apo-CueR (empty symbols) showing the line of best fit for both sets.

4.6.3 Determination of the CueR K_3 affinity for *copA*-Pro

The affinity (K_3) of CueR was determined by titration of apo-protein to 10 nM *copA*-Pro. Three replicate data sets were fit simultaneously (Figure 4.9d) to an equivalent sites model ($K_{3a} = K_{3b}$) and generated a $K_{3a\text{-}b}$ of 3.47×10^{-7} M (Table 4.1). There was an obvious inflexion point in the data ($\Delta r_{obs} \sim 0.02$) and therefore only data points below this Δr_{obs} were included in the fit (≤ 2 μM dimer). The Δr_{obs} fit to this data was similar to that reported for apo-CueR at pH 7.0 (Osman et al., 2018). The data fit within the 10-fold tighter and weaker limits of the assay (Figure 4.9d). The $K_{3a\text{-}b}$ values for CueR determined here differ from the reported values (K_{3a} $3.2 \pm 1.2 \times 10^{-8}$ M and K_{3b} $1.0 \pm 0.4 \times 10^{-6}$ M) which showed strong negative cooperativity (Osman et al., 2018). Differences in experimental conditions are likely a contributing factor (pH 7.5 with 1 mM EDTA was used here, in contrast to pH 7.0 with 5 mM EDTA previously, with otherwise identical salt concentrations in both experiments). Comparing these buffers, 1 mM EDTA may not have been sufficient to chelate trace Cu(I) in the buffer and the affinity of Cu(I)-CueR for *copA*-Pro is weaker than that of apo-CueR. Conversely, 5 mM EDTA could stabilise the apo-CueR:DNA complex, and pH may also influence this stability.

4.6.4 Calculation of the coupling free energy (ΔG_C) for binding to *copA*-Pro

There was a clear difference between affinities for apo and 1:1 Ni(II)-CueR (Figure 4.9e). This equated to ΔG_C -1.1 ± 0.3 kcal mol^{-1} (Table 4.1), similar to the action of a co-repressor system (e.g. NikR) where the metal binding increases DNA affinity of the sensor. In contrast, the ΔG_C for Cu(I)-CueR was $+1.4 \pm 0.4$ kcal mol^{-1} (Osman et al., 2018), indicating the opposite effect due to metal binding. The relatively small ΔG_C values are unsurprising since both protein forms (i.e. apo and holo) have a high affinity for DNA where promoter conformation rather than operator occupancy controls gene expression (Section 1.3.10).

4.6.5 Discussion and interpretation of the CueR and *copA*-Pro FA data

As seen for Ni(II)-Fur (Section 4.5.5), the Δr_{obs} for Ni(II)-CueR differed to that reported for the cognate metal. For CueR, the Ni(II)-bound protein demonstrated a Δr_{obs} of ~ 0.039 for a 2:1 stoichiometry, whereas Δr_{obs} was only ~ 0.015 for Cu(I)-CueR (less than that for apo-CueR) (Osman et al., 2018). The Δr_{obs} values differ more than 2-fold and it is unclear how the incorporation of a different metal could cause this difference. It could be possible that Ni(II)-CueR favours formation of tetrameric complexes which would have a greater mass (and therefore change in anisotropy) though this would have meant a stoichiometry of 4:1 (for two dimer of dimers binding to the DNA). Alternatively, it could be that a single Ni(II)-

facilitated CueR tetramer is able to associate with the DNA in which case the 2:1 stoichiometry would still hold but then that would mean the single tetramer would be expected to have a greater Δr_{obs} than two dimers (equivalent masses).

4.7 ZntR

4.7.1 Determination of the ZntR K_3 affinity for *zntA*-Pro

*Sty*ZntR binds to *zntA*-Pro with 1:1 stoichiometry (dimers per DNA) (Osman et al., 2018). The affinity (K_3) of ZntR was determined by titration of apo-protein to 10 nM *zntA*-Pro. Four replicate data sets were fit simultaneously (Figure 4.10a) and generated a K_3 of 5.60×10^{-8} M (Table 4.1). The endpoint for this titration was well-defined, although additional binding events appeared at higher concentrations of added protein, therefore, these data points were omitted from the fit. The data fit within the 10-fold tighter and weaker limits of the assay (Figure 4.10a). The affinity determined here was ~ 2-fold tighter than that in the literature ($1.1 \pm 0.4 \times 10^{-7}$ M, pH 7.0 (Osman et al., 2018)), with the differences in the buffer as for CueR (Section 4.6.3). A second important consideration is that apparent additional binding events at higher ZntR concentrations could affect the final Δr_{obs} observed in the two experiments, with potential impact on the determination of K_3.

4.7.2 Determination of the Ni(II)-ZntR K_4' affinity for *zntA*-Pro

The affinity (K_4') of 1:1 Ni(II)-ZntR was determined by titration to 10 nM *zntA*-Pro. Three replicate data sets were fit simultaneously (Figure 4.10b) using the same model as for K_3 (Section 4.7.1), and generated a K_4' of 3.12×10^{-7} M (Table 4.1). Additional binding events were observed, therefore, only data below the Δr_{obs} seen for apo-ZntR (Section 4.7.1) were fit (≤ 2 μM dimer). The data points used in the fit were within the 10-fold tighter and weaker limits of the assay (Figure 4.10b). Noisy data points were present at concentrations before DNA binding was observed, possibly due to low-level protein precipitation. The K_4 value for Zn(II)-ZntR (pH 7.0) is $7.8 \pm 1.3 \times 10^{-7}$ M (Osman et al., 2018), 2.5-fold weaker than that for K_4' with Ni(II). The fit here allowed for the presence of apo-ZntR over the full range of protein concentrations.

4.7.3 Determination of the Ni(II)-ZntR K_4'' affinity for *zntA*-Pro

The affinity (K_4'') of Ni(II)-ZntR for *zntA*-Pro was also investigated, however, the titration protocol required modification because 2:1 Ni(II)-ZntR stocks precipitated before they could be used. Therefore, to populate all Ni(II) sites, ZntR was loaded 1:1 with Ni(II) and titrated

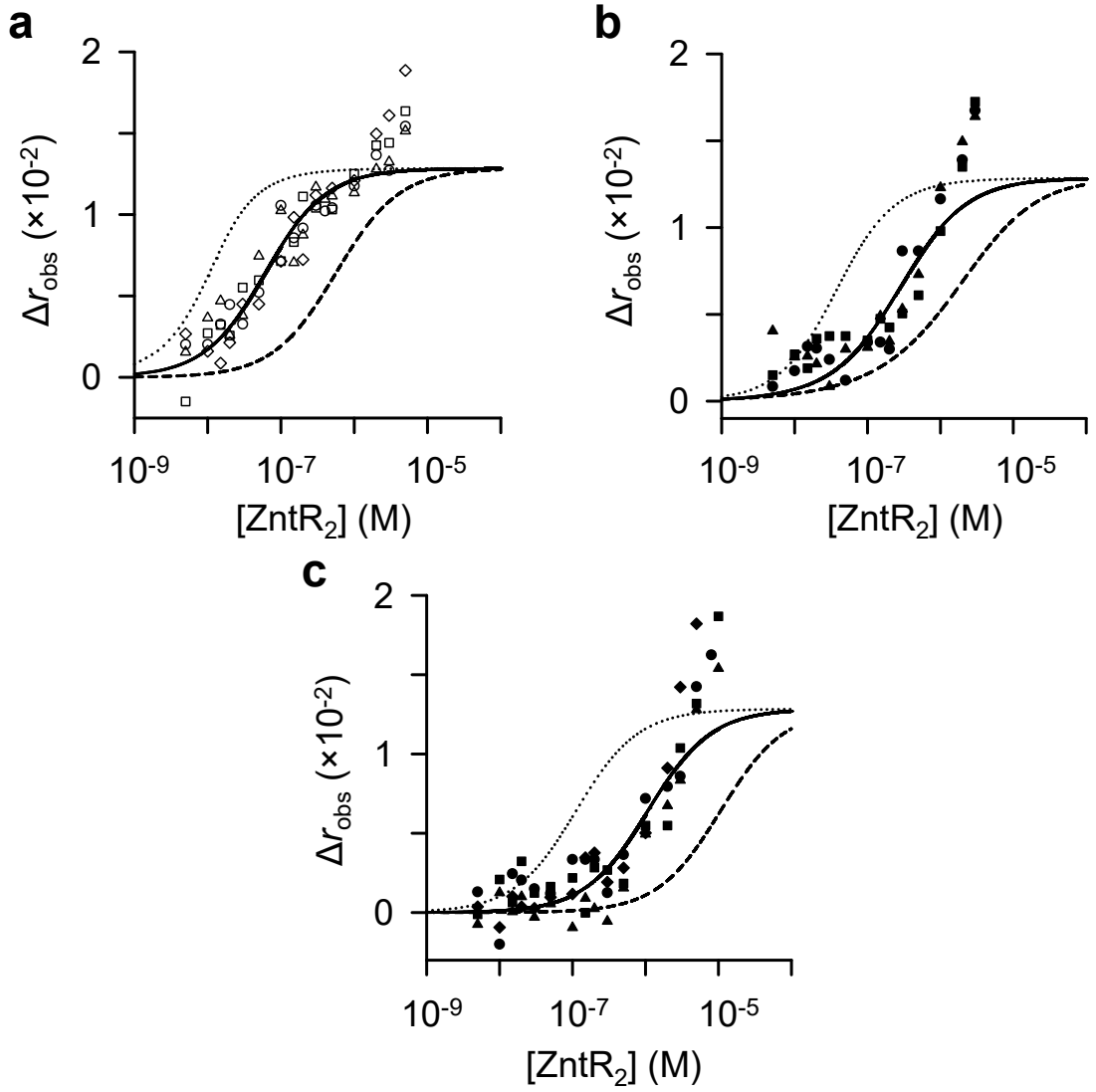

Figure 4.10 Determination of the *Sty*ZntR DNA affinities for *zntA*-Pro by FA. (a) Apo-ZntR titrated to 10 nM HEX-labelled *zntA*-Pro (n=4) to determine the DNA affinity (K_3). The solid line indicates the best simultaneous fit to all data sets. Modelled fits are shown for the titration using K_3 10-fold tighter (dotted line) or 10-fold weaker (dashed line) to show the limits of the assay. **(b)** Same as (a) except data for 1:1 Ni(II)-ZntR (K_4'; n=3). **(c)** Same as (a) except data for 2:1 Ni(II)-ZntR (K_4''; n=4).

to 10 nM *zntA*-Pro in Buffer N containing 5 μM $NiCl_2$. Four replicate data sets were fit simultaneously (Figure 4.10c) and generated a K_4'' of 1.07×10^{-6} M (Table 4.1), fixed to the response for apo-ZntR (Section 4.7.1). The fitted data points were within the 10-fold tighter and weaker limits of the assay (Figure 4.10c). Again, noisy data points were observed at lower protein concentrations, as seen with 1:1 Ni(II)-ZntR (Section 4.7.2). The K_4'' value was an order of magnitude weaker than K_4' and supports the negative effect of Ni(II) on DNA binding by ZntR. Under these conditions, ZntR was fully loaded with Ni(II) over the full range of protein concentrations.

4.7.4 Calculation of the coupling free energy (ΔG_C) for binding to *zntA*-Pro

The difference between affinities for apo and 1:1 Ni(II)-ZntR (Figure 4.11a) resulted in a ΔG_C value of +1.0 ± 0.2 kcal mol^{-1} (Table 4.1). The ΔG_C here was similar to the reported value for Zn(II)-ZntR (+1.2 ± 0.2 kcal mol^{-1}, pH 7.0 (Osman et al., 2018)), though this does not mean Ni(II) elicits the same conformational changes associated with Zn(II) binding. The difference between apo and 2:1 Ni(II)-ZntR affinities (Figure 4.11b) resulted in a ΔG_C value of +1.8 ± 0.3 kcal mol^{-1} (Table 4.1), consistent with the weaker binding of 2:1 Ni(II)-ZntR.

4.8 Zur

4.8.1 Determination of the Ni(II)-Zur K_4' affinity for *znuA*-Pro

Salmonella Zn(II)-Zur has a 2:1 binding stoichiometry (dimers per DNA) with *znuA*-Pro (Osman et al., 2017). The affinity (K_4') of Ni(II)-Zur was determined by titration to 10 nM *znuA*-Pro. Five replicate data sets were fit simultaneously (Figure 4.12a) to an equivalent sites model ($K_{4a}' = K_{4b}'$) and generated a $K_{4a\text{-}b}'$ of 1.67×10^{-8} M (Table 4.1). The endpoint of the titration was poorly defined, therefore, Δr_{obs} was fixed to the value determined for K_4''' (see Section 4.8.2). Nevertheless, the data fit within the 10-fold limits of the assay (Figure 4.12a). A possible explanation for the poor endpoint was that slow exchange kinetics between available Ni(II) sites in Zur (Section 3.8.2) meant that different Ni(II)-Zur species, with potentially different DNA affinities, were present in the assay. Alternatively, Zur could form tetramers and if these species have a weak DNA affinity then loss of active dimers could cause the decrease in Δr_{obs}. The fit here allowed for the presence of apo-Zur over the full range of protein concentrations.

Positive cooperativity has been determined for *E. coli* Zur binding to DNA (Gilston et al., 2014), though, like Ni(II)-Zur, no cooperativity was detected for *Salmonella* Zn(II)-Zur (pH

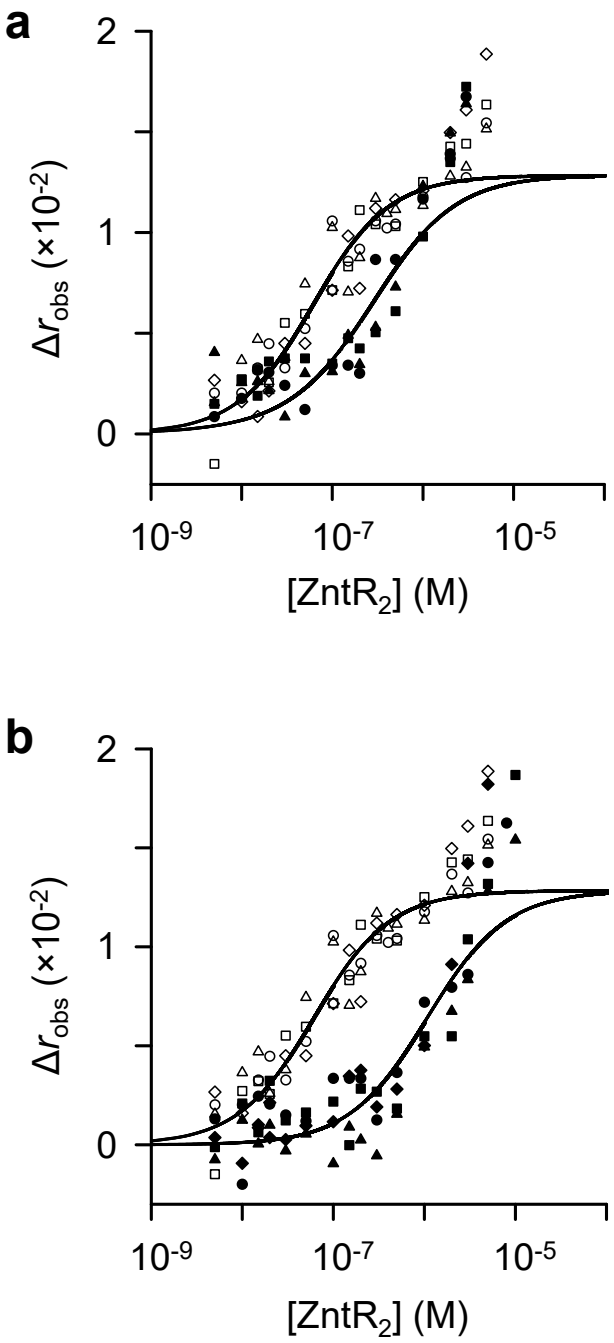

Figure 4.11 Comparison of Ni(II)-loaded and apo-ZntR binding to *zntA*-Pro. (a) Combined data for 1:1 Ni(II)-ZntR (solid symbols) and apo-ZntR (empty symbols) showing the line of best fit for both sets. **(b)** Same as (a) except data for 2:1 Ni(II)-ZntR (solid symbols) and apo-ZntR (empty symbols).

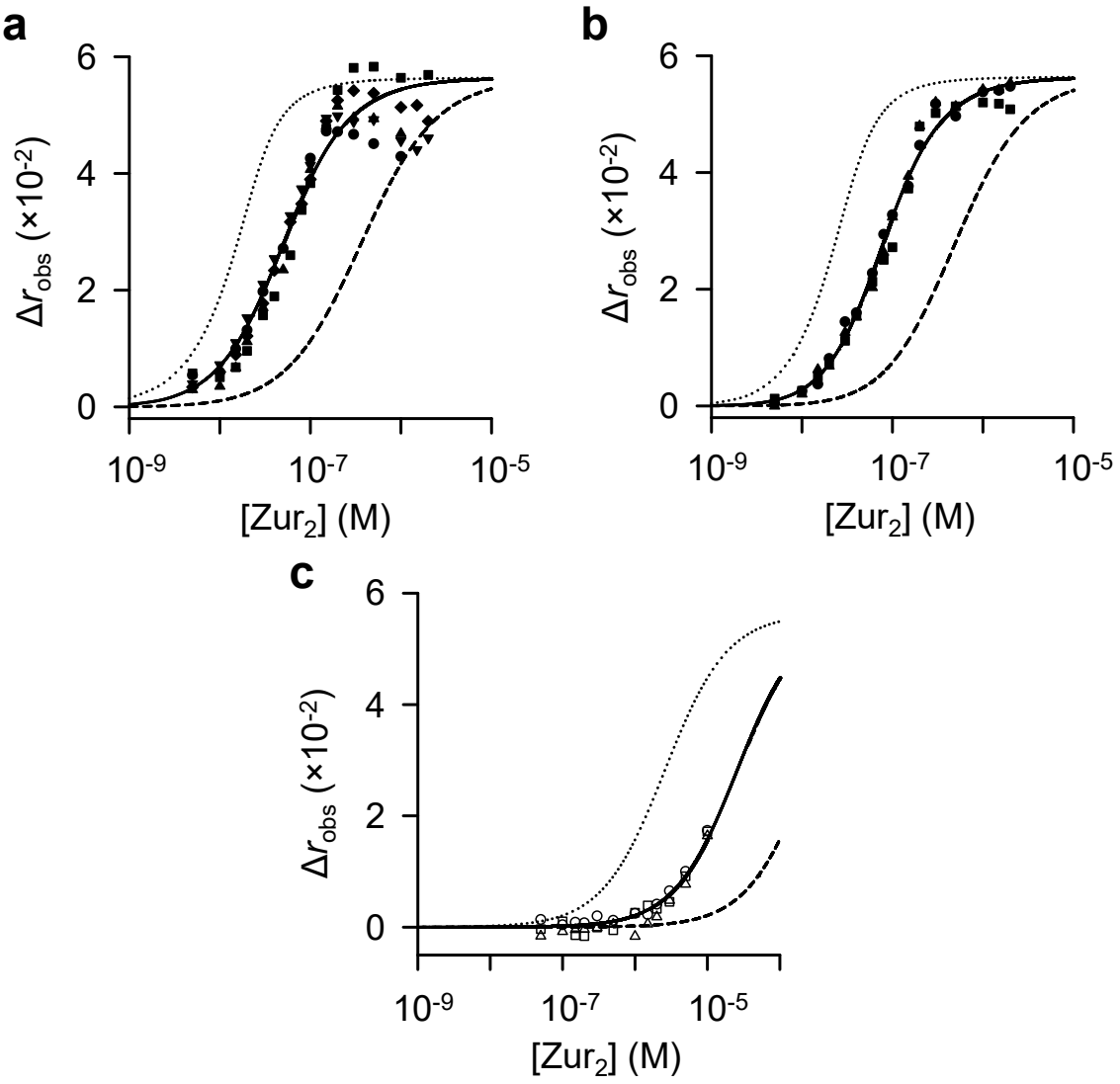

Figure 4.12 Determination of the *Sty*Zur DNA affinities for *znuA*-Pro by FA. (a) Ni(II)-Zur (1:1) titrated to 10 nM HEX-labelled *znuA*-Pro (n=5) to determine the DNA affinity (K_4'). The solid line indicates the best simultaneous fit to all data sets. Modelled fits are shown for the titration using K_4' 10-fold tighter (dotted line) or 10-fold weaker (dashed line) to show the limits of the assay. **(b)** Same as (a) except data for 3:1 Ni(II)-Zur (K_4'''; n=3). **(c)** Same as (a) except data for apo-Zur (K_3; n=3).

7.0) where the affinity was reported as 4.1 ± 1.0 × 10^{-8} M (for Zur dimer loaded with two Zn(II) ions) or 5.4 ± 1.8 × 10^{-8} M (for Zur dimer loaded with four Zn(II) ions) (Osman et al., 2017). The $K_{4a\text{-}b}'$ value for Ni(II)-Zur was tighter than both reported affinities for Zn(II)-Zur. The Co(II)-Zur affinity for DNA (3.1 ± 0.3 × 10^{-8} M (Osman et al., 2017)) was also shown to be tighter than that of Zn(II)-Zur which suggests non-cognate divalent metal ions are capable of allosterically activating the protein.

4.8.2 Determination of the Ni(II)-Zur K_4''' affinity for *znuA*-Pro

The affinity (K_4''') of Ni(II)-Zur was determined by titration to 10 nM *znuA*-Pro. Three replicate data sets were fit simultaneously (Figure 4.12b) to an equivalent sites model ($K_{4a}''' = K_{4b}'''$) and generated a $K_{4a\text{-}b}'''$ of 1.99 × 10^{-8} M (Table 4.1). Interestingly, the endpoint of this titration was well-defined, unlike for 1:1 Ni(II)-loaded Zur, consistent with the possibility that different Ni(II)-loaded Zur species impact the noise seen when using sub-stoichiometric Ni(II) (Section 4.8.1). Again, the data was able to fit to a simpler non-cooperative model, within the 10-fold limits of the assay (Figure 4.12b). Increasing the Ni(II) content of Zur weakened the DNA affinity slightly, as seen for Zn(II) (Section 4.8.1), which appears counterintuitive if it has an actual physiological purpose, unless different effects are apparent for different target sites. The fit here allowed for the presence of apo-Zur over the full range of protein concentrations.

4.8.3 Determination of the Zur K_3 affinity for *znuA*-Pro

The affinity (K_3) of Zur was determined by titration of apo-protein to 10 nM *znuA*-Pro. Three replicate data sets were fit simultaneously (Figure 4.12c) to an equivalent sites model ($K_{3a} = K_{3b}$) and generated $K_{3a\text{-}b} \geq 1.29 \times 10^{-5}$ M (Table 4.1), fixing Δr_{obs} to that from K_4''' (Section 4.8.2) due to not approaching an endpoint at the concentrations tested in the titration. The data fit within the 10-fold tighter and weaker limits of the assay (Figure 4.12c). The reported K_3 for *Sty*Zur (pH 7.0) was ≥ 2.7 ± 0.4 × 10^{-5} M (Osman et al., 2017) which is ~ 2-fold weaker than the limit determined here. As mentioned previously (Section 4.6.3), differences in the buffer could account for this, particularly as preliminary data collected in this work using buffer without EDTA indicated that Zur could bind *znuA*-Pro with tight affinity in the absence of added metal, likely due to binding trace metal in the Chelex-treated buffer.

4.8.4 Calculation of the coupling free energy (ΔG_C) for binding to *znuA*-Pro

There was a clear difference between affinities for apo and 1:1 Ni(II)-Zur (Figure 4.13a). This equated to $\Delta G_C \leq$ -4.0 ± 0.2 kcal mol^{-1} (Table 4.1), which was very similar to the reported value of ≤ -3.9 ± 0.2 kcal mol^{-1} for 2:1 Zn(II)-Zur (Osman et al., 2017), suggesting

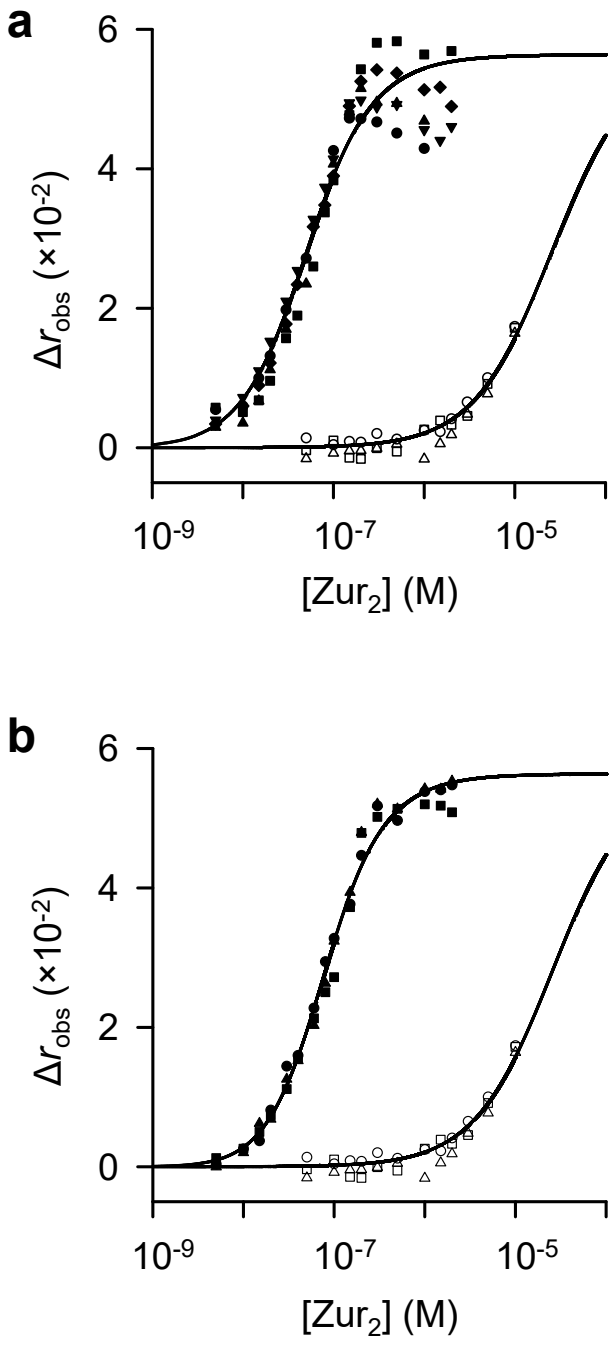

Figure 4.13 Comparison of Ni(II)-loaded and apo-Zur binding to *znuA*-Pro. (a) Combined data for 1:1 Ni(II)-Zur (solid symbols) and apo-Zur (empty symbols) showing the line of best fit for both sets. **(b)** Same as (a) except data for 3:1 Ni(II)-Zur (solid symbols) and apo-Zur (empty symbols).

Ni(II) is capable of allosterically activating Zur. The apo and 3:1 Ni(II)-Zur affinities also differed substantially (Figure 4.13b), resulting in a $\Delta G_C \leq -3.6 \pm 0.4$ kcal mol^{-1} (Table 4.1). The difference in ΔG_C for 1:1 and 3:1 Ni(II)-Zur was ~ 0.4 kcal mol^{-1} whereas the difference between 1:1 and 2:1 Zn(II)-Zur was ~ 0.2 kcal mol^{-1} (Osman et al., 2017). These differences suggest binding additional Ni(II) was more detrimental than binding additional Zn(II), however, the number of additionally bound ions differ in the above examples (four additional Ni(II) ions per dimer but only two additional Zn(II) ions).

4.9 Comparing the effect of Ni(II)-binding on DNA affinities for the sensors

4.9.1 The response of non-cognate co-repressor sensors to Ni(II)

The co-repressor proteins where Ni(II) is not the cognate metal (MntR, Fur, and Zur) still maintain the mode of action associated with a co-repressor, as indicated by ΔG_C (Table 4.1), though, in the majority of cases (not 1:1 Ni(II)-Zur), the coupling free energy was smaller than that produced with cognate metals. This suggests that different divalent metals will have different resulting conformational changes at an equivalent binding site (assuming all metals preferentially bind to the same site) which is likely driven by the preferred coordination geometry for the given metal. In the case of *B. subtilis* MntR, Mn(II) binding reduced the flexibility of the protein to fix the active DNA binding conformation (Golynskiy et al., 2005, Golynskiy et al., 2007, McGuire et al., 2013). Non-cognate metals were shown to bind to *Bs*MntR with different coordination geometries which meant the structures were more flexible than Mn(II)-MntR. Some stabilisation of the structure was shown for non-cognate metals which suggests Ni(II)-MntR could be more active for DNA binding than the fully flexible apo-MntR, resulting in a negative ΔG_C, though not as great as for Mn(II)-MntR. Similar stabilisation by cognate metal binding has been suggested for *E. coli* Zur (Gilston et al., 2014) and *M. gryphiswaldense* Fur (Deng et al., 2015) so it is conceivable that non-cognate metals could add some stability to these proteins too.

4.9.2 The effect of Ni(II) on DNA binding by non-cognate MerR family regulators

CueR and ZntR demonstrated opposite responses to Ni(II)-binding regarding DNA affinity. Ni(II)-CueR showed a tighter DNA affinity compared to the apo-protein whereas the DNA affinity of Ni(II)-ZntR was weaker than that for apo-ZntR. Cu(I) binds to CueR in a linear geometry, coordinated by two cysteines (Changela et al., 2003), and it could be possible for Ni(II) to bind the same site in a planar geometry (likely recruiting additional ligands) which

could stabilise a DNA-bound form. Interestingly, however, the Cu(I)-bound form of CueR appears to have a weaker DNA affinity than apo-CueR (by one order of magnitude (Osman et al., 2018)) which suggests that although divalent ions (Me(II)) have not been shown to alter gene expression *in vitro* or *in vivo* (Stoyanov et al., 2001, Changela et al., 2003), it could be possible that the Me(II)-bound forms, with different coordination geometries, could have differing effects on absolute DNA affinity. Zn(II) is proposed to bind ZntR with tetrahedral geometry (Changela et al., 2003) which is less favoured by Ni(II) so would likely be coordinated in a different geometry resulting in different structural conformations of ZntR that could inevitably reduce the proteins affinity for DNA. With MerR regulators, the DNA-bound holo-protein form is required for activating transcription, though the apo-protein is generally also DNA-bound but unable to distort the DNA to recruit RNA polymerase (Section 1.3.10). Therefore, DNA occupancy is not the driving force for mis-metalated regulation but instead whether non-cognate Ni(II) binding can result in appropriate conformational changes for activation of transcription and this appears not to be possible (as mentioned above for CueR).

4.9.3 The importance of Ni(II) affinities K_1 and K_2 for DNA binding

The K_4 DNA affinities of the non-Ni(II) sensors have been determined using sub-stoichiometric Ni(II) concentrations. Although average K_1 affinities were included in the fits (Section 2.10.2), the effect of K_2 has not been investigated. Stepwise K_2 values, where K_2 is described as the Ni(II) affinity for a sensor bound to DNA (Figure 1.2), cannot be easily measured *in vitro*, and were therefore unavailable for use in the fitting models. Average affinities for K_2 can be calculated (Table 5.2) since K_1, K_3, and K_4 have been determined for the thermodynamic cycle. Sensors with a negative ΔG_C (MntR, Fur, CueR, and Zur) will have a tighter K_2 value than K_1 where the ratio between K_3 and K_4 is the same as between K_1 and K_2. This could mean that once a sub-stoichiometric Ni(II)-associated sensor has bound to DNA, the empty Ni(II) sites may have a greater affinity for the metal than when the protein was off DNA. If this were the case, these sites would become more competitive for Ni(II) compared to the population of sensor off DNA and drive the Ni(II) to DNA-bound protein, ending up with a population of fully Ni(II)-loaded DNA-bound sensor and metal-free sensor off DNA. Since there could be multiple variations of the sub-stoichiometric Ni(II)-loaded sensors, where the DNA affinity of the differently populated species is unknown, the effect that K_2 could have on observed affinity for DNA is difficult to predict. In the case of 1:1 Ni(II)-Zur, the data shows large variability in the end point for the titration (Figure 4.12a) but for the equivalent experiment with 3:1 Ni(II)-Zur (fully loaded) there is no such variability (Figure 4.12b) which could be a result of K_2 affinities adding increased

complexity to the model for 1:1 Ni(II)-Zur (K_2 is largely redundant with 3:1 Ni(II)-Zur as there is sufficient Ni(II) to populate all sites within the protein).

4.9.4 The apparent allosteric effect of Fur as a result of Ni(II) binding compared to K_1

In Section 3.5.2, the Fur dimer was shown to have two Ni(II) sites with affinities similar to RcnR. The remaining two Ni(II) sites in the dimer were orders of magnitude weaker, therefore, it was possible to fully load the tighter sites of Fur without populating the weaker sites (assuming no effect from K_2). Interestingly, the allosteric effect associated with the population of the tight Ni(II) sites in Fur was small. Loading the weaker Ni(II) sites resulted in a greater allosteric effect on DNA binding. However, it was shown that loading the tighter Fur sites resulted in quenching of tyrosine fluorescence (the same as happens with Fe(II)), whereas, the weaker sites had no such effect (Section 3.5.1). Since the effect on fluorescence is the same for both high-affinity Ni(II)- and Fe(II)-binding, it suggests that Ni(II) could bind in a similar environment to Fe(II) and could result in a similar allosteric effect, therefore, it is peculiar that the Ni(II) sites which do not cause quenching of the tyrosine fluorescence result in a more effective allosteric response, but indicates geometry could be crucial at this first binding site (presumed to be site 1 at the interface of the DNA-binding and dimerisation domains; Section 1.3.7). Nevertheless, the data suggests that although Fur can bind Ni(II) tightly, the risk of mis-metalated-activation at Fur promoters remains low because the allosterically effective sites have substantially lower affinity for Ni(II). This draws on the conclusion from Chapter 3 that demonstrated an apparent Ni(II) affinity (K_1) threshold at 1×10^{-10} M for the non-Ni(II) sensors. Fur was the only exception to this threshold but the DNA binding experiments suggest that the threshold stands for all sensors when considering allosterically effective Ni(II) sites (the weaker Fur sites are weaker than 1×10^{-10} M).

4.9.5 The potential for non-specific effects of Ni(II)-binding on DNA affinity

For almost all cases of non-Ni(II) sensors, the ΔG_C was less than for their cognate metal. While binding to Ni(II) does result in a coupling free energy change, this may no longer be specific for the target site associated with the sensor in question. To test this, 2:1 Ni(II)-Fur and apo-Fur were titrated to 10 nM *zntA*-Pro in separate experiments (Figure 4.14) to determine if there is any effect on ΔG_C. To generate a binding model, it was assumed that one Fur dimer bound per DNA in the absence of the *fur-box* motif and that the total Δr_{obs} would be equivalent to that of one Fur dimer binding to *fur-box* (i.e. half the total response seen in Section 4.5.2). The data was normalised to fractional DNA occupancy for comparison with Fur binding to *fur-box*. ΔG_C for binding to a non-specific DNA fragment

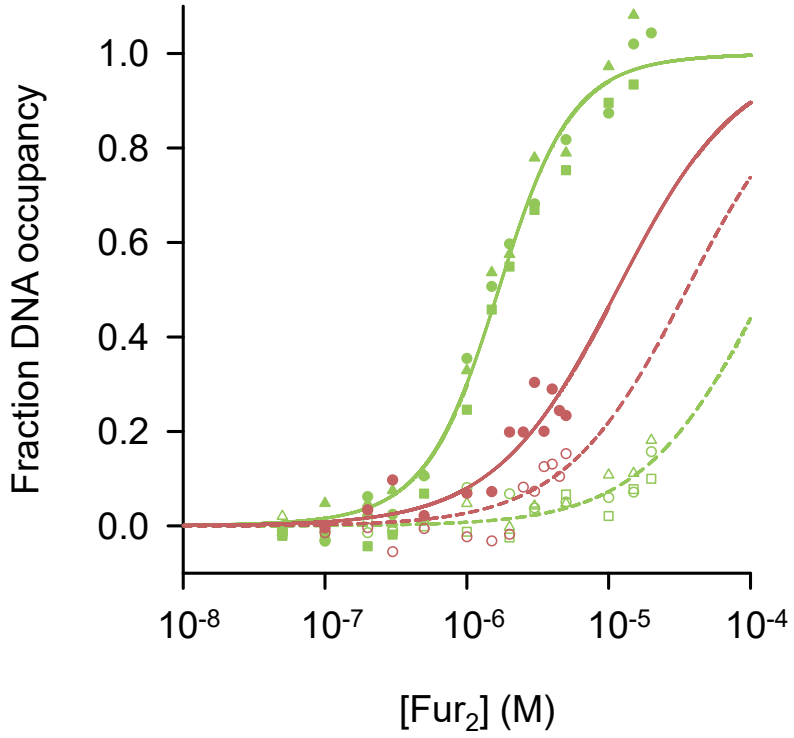

Figure 4.14 Determination of coupling free energy for non-specific DNA binding by Ni(II)-Fur. Normalised FA data for *Sty*Fur binding to *fur-box* (green) and *zntA*-Pro (red) as either 2:1 Ni(II)-Fur (solid symbols) or apo-Fur (empty symbols). Best fit lines to Ni(II)-Fur (solid) and apo-Fur (dashed) data sets are shown.

was estimated as -0.7 kcal mol^{-1} (from one replicate of holo and apo experiments). This demonstrates that while Ni(II) can increase the DNA affinity of Fur non-specifically, it is not to the same extent as achieved for binding to the specific target site.

4.9.6 Concluding remarks

The determination of a complete set of DNA affinities for Ni(II)-substituted sensors provides considerable insight into the allosteric activation of these proteins, and the potential for mis-metalation effects on DNA occupancy. Mis-metalation may be detrimental in two ways; through causing mal-responses of genes that play no role in maintaining a healthy concentration of the metal occupying the protein, and by inactivating the protein to sense and control the homeostasis of their cognate metal (essentially the non-cognate metal acts as a competitive inhibitor). Through using the affinity values determined here (K_3 and K_4), in conjunction with those determined in Chapter 3 (K_1), the extent of mal-responses by non-cognate sensors can be simulated (Chapter 5).

Table 4.1 Stepwise DNA-binding affinities of apo and Ni(II)-loaded *Salmonella* sensors.

Sensor	Multimers per DNA	Apo K_3 (M)	1:1 Ni(II) K_4' (M)	2:1 Ni(II) K_4'' (M)	3:1 Ni(II) K_4''' (M)	ΔG_C (kcal mol^{-1})[a]
NikR$_4$	1	**2.59×10^{-5}** (*nixA*) ($2.16 – 3.25 \times 10^{-5}$)[b]	**9.83×10^{-9}** (*nixA*) ($0.69 – 1.45 \times 10^{-8}$) **$4.26 \times 10^{-9}$** (*nikA*) ($3.05 – 6.89 \times 10^{-9}$)	n.d.	n.d.	-4.8 ± 0.2 (*nixA*) -5.2 ± 0.1 (*nikA*)[c]
RcnR$_4$	2	**1.77×10^{-7}** ($1.31 – 2.44 \times 10^{-7}$)	**3.11×10^{-6}** ($2.97 – 3.26 \times 10^{-6}$)	n.d.	n.d.	+1.7 ± 0.1
MntR$_2$	1	**≥ 1.33×10^{-7}** ($0.88 – 2.15 \times 10^{-7}$)	**≥ 1.12×10^{-8}** ($0.25 – 3.84 \times 10^{-8}$)	**≥ 1.19×10^{-9}** ($0.69 – 5.56 \times 10^{-9}$)	n.d.	-1.4 ± 0.2 -2.5 ± 0.3 *(2:1)*
Fur$_2$	2	***a-b*** **≥ 6.38×10^{-5}** ($0.47 – 1.01 \times 10^{-4}$)	***a-b*** **≥ 1.28×10^{-5}** ($0.77 – 3.25 \times 10^{-5}$)	***a*** **= 3.70×10^{-6}** ($1.54 \times 10^{-6} – 6.45 \times 10^{-3}$) **b = 7.50×10^{-7}** ($4.13 \times 10^{-10} – 2.40 \times 10^{-6}$)	n.d.	≤ -1.0 ± 0.2 ≤ -2.0 ± 0.2 *(2:1)*[d]
CueR$_2$	2	***a-b*** **= 3.47×10^{-7}** ($1.80 – 6.26 \times 10^{-7}$)	***a*** **= 5.50×10^{-8}** ($0.27 – 2.00 \times 10^{-7}$) ***b*** **= 4.90×10^{-8}** ($0.13 – 1.13 \times 10^{-7}$)	n.d.	n.d.	-1.1 ± 0.3[d]
ZntR$_2$	1	**5.60×10^{-8}** ($3.20 – 8.59 \times 10^{-8}$)	**3.12×10^{-7}** ($1.77 – 6.71 \times 10^{-7}$)	**1.07×10^{-6}** ($0.67 – 1.81 \times 10^{-6}$)	n.d.	+1.0 ± 0.2 +1.8 ± 0.3 *(2:1)*
Zur$_2$	2	***a-b*** **≥ 1.29×10^{-5}** ($1.09 – 1.60 \times 10^{-5}$)	***a-b*** **= 1.67×10^{-8}** ($1.30 – 2.06 \times 10^{-8}$)	n.d.	***a-b*** **= 1.99×10^{-8}** ($1.64 – 2.36 \times 10^{-8}$)	≤ -4.0 ± 0.2 ≤ -3.6 ± 0.4 *(3:1)*

[a]Calculated from 1:1 Ni(II)-sensor and apo-sensor affinities unless indicated (2:1 or 3:1).

[b]95% confidence interval for each calculated affinity.

[c]Calculated using K_3 determined for *nixA*.

[d]Calculated using the first DNA-binding event (K_{4a}).

Chapter 5: *In silico* simulations to model cellular Ni(II)-binding and DNA occupancy for the set of *Salmonella* sensors

5.1 Introduction

Thermodynamic affinity constants (K_1, K_2, K_3, and K_4; Figure 1.2), along with protein copy number and DNA site abundance, can be used to model cellular promoter occupancy and predict transcriptional responses for metallosensor-regulated genes, including the effect of metal ion buffering (Osman et al., 2017). The *in vitro* affinity values (Chapter 3 and Chapter 4) have been determined (or can be deduced in the case of K_2) for the *Salmonella* set of metal sensors with respect to Ni(II) to gain insight into metal sensing specificity within the cell. The data (Chapter 3) indicates that all of the sensors, including those which have not evolved to respond to Ni(II), can bind the metal with high affinity, presenting themselves as possible targets for Ni(II) mis-metalation. Additionally, Ni(II) was shown to elicit allosteric changes for each protein by altering DNA affinity compared to apo-protein (Chapter 4). This suggests that mis-metalation of sensors by Ni(II) could affect promoter occupancy and therefore affect transcription, along with ensuing translation, of other metal-regulating systems if Ni(II) were bound to the non-cognate sensors.

Modelling the fraction of Ni(II) bound to each sensor and the DNA occupancy for target sites has been conducted to predict how a cellular metalloregulatory network would respond to increased intracellular Ni(II) concentrations. Included in the modelling is a simple intracellular small molecule buffer, L-histidine, which is required for Ni(II) import via NikABCDE (Chivers et al., 2012) and appears to be significant for metal sensing (Foster et al., 2017), although, the intracellular buffer is likely more complex, involving other small molecules e.g. glutathione (Latinwo et al., 1998, Helbig et al., 2008). The cellular concentrations of L-histidine in *E. coli* vary with nutrient availability, demonstrating a range from 60 µM (grown on acetate) to 200 µM (grown on glycerol) (Bennett et al., 2009). L-histidine, at these physiological concentrations, was included in models to simulate the possible impact this molecule alone (out of the potentially diverse intracellular buffer) could have. These results suggest that metal buffering ensures metal-specific transcriptional responses are observed in response to elevated metal levels, before a threshold amount is

exceeded. These simulations can also be used to assess the physiological importance of previously published *in vitro* affinity measurements, for example, the NikR low-affinity Ni(II) binding site. More broadly, this work provides a strategy for understanding the thresholds for mis-metalation by any metal.

5.2 Ni(II)-binding to the *Salmonella* sensors

5.2.1 Ni(II)- and DNA-binding properties of each sensor

The stepwise affinity values for Ni(II)- and DNA-binding for the *Salmonella* set of sensors (Chapter 3 and Chapter 4) are listed in Table 5.1. The K_1 values were selected from the competition experiments for one chelator which showed the best fits for all Ni(II) sites. For non-cognate sensors, K_4 was determined using different Ni(II)-loaded forms of the protein where the Ni(II)-sensor ratio that elicited a detectable allosteric response was selected for use in simulations of DNA occupancy in the cell. The K_4 affinities used for MntR, CueR, ZntR, and Zur were from the 1:1 Ni(II)-loaded protein, whereas, the 2:1 Ni(II)-loaded protein was used for Fur (Section 4.9.4). Therefore, the number of allosteric sites requiring Ni(II) for DNA binding of the non-cognate sensors were two per dimer for MntR, CueR, ZntR, and Zur but four per dimer for Fur (i.e. fully loaded).

The number of allosteric sites required for DNA binding of the cognate sensors cannot be easily determined experimentally due to the effect of DNA on Ni(II) affinity (K_2). For example, when adding sub-stoichiometric Ni(II)-NikR to the DNA duplex, an intermediate value of K_4 for this species will result in enhanced Ni(II) affinity (K_2) compared to the non-DNA-bound protein (K_1). Based on published results for RcnR with Co(II) (Osman et al., 2015, Osman et al., 2017) and preliminary experiments using NikR with sub-stoichiometric amounts of Ni(II) combined with analysis of the NikR-DNA structure (Schreiter et al., 2006), two sites per tetramer were considered the requirement for allostery for both sensors.

5.2.2 Cellular concentrations of *Salmonella* sensors

The cellular copy number of each *Salmonella* sensor (Table 5.2) has been determined elsewhere (Osman et al., 2018). Protein abundances were determined individually by mass spectrometry for each sensor using cells grown in metal-limiting media (P_0) and media supplemented with the appropriate cognate metal (P_1). The values for P_0 and P_1 delineate the physiological range for sensor copy number and are important when considering the ability of each protein to bind metal, and the subsequent effect on DNA occupancy. The ratio

Table 5.1 Stepwise affinity values for Ni(II)- and DNA-binding by the *Salmonella* sensors.

Sensor	K_1 (M)	K_3 (M)	K_4 (M)[a]
NikR[b]	*a*-*d* = 7.38×10^{-14}	2.59×10^{-5}	9.83×10^{-9}
RcnR	*a*-*d* = 1.18×10^{-12}	1.77×10^{-7}	3.11×10^{-6}
MntR	*a* = 1.70×10^{-10} *b* = 2.26×10^{-8} *c*-*d* = 1.30×10^{-7} [c]	≥ 1.33×10^{-7}	≥ 1.12×10^{-8}
Fur	*a* = 1.19×10^{-11} *b* = 2.52×10^{-12} *c*-*d* = 9.60×10^{-10}	*a*-*b* ≥ 6.38×10^{-5}	*a* = 3.70×10^{-6} *b* = 7.50×10^{-7}
CueR	*a*-*b* = 1.57×10^{-10} *c* = 9.70×10^{-9}	*a*-*b* = 3.47×10^{-7}	*a* = 5.50×10^{-8} *b* = 4.90×10^{-8}
ZntR	*a* = 1.40×10^{-10} *b* = 1.62×10^{-9} *c*-*d* = 9.90×10^{-9}	5.60×10^{-8}	3.12×10^{-7}
Zur	*a* = 3.60×10^{-10} *b* = 7.60×10^{-9} *c*-*d* = 1.13×10^{-8} *e*-*f* = 8.80×10^{-8} [c]	*a*-*b* ≥ 1.29×10^{-5}	*a*-*b* = 1.67×10^{-8}

[a]Using the Ni(II)-sensor stoichiometry that elicits an allosteric response.
[b]K_3 and K_4 calculated using *nixA*-Pro.
[c]Limit values.

Table 5.2 Parameters required to simulate DNA occupancy of the *Salmonella* sensors in response to Ni(II).

Sensor (# allosteric sites)	Abundance (assemblies per cell)[a]	K_1 (M)[b]	K_2 (M)[c]	K_3 (M)	K_4 (M)[d]	DNA Target Site Number[a]
NikR[e] (2 sites)	68.3 ± 4.1 81.1 ± 3.7 (+ Ni(II))	1.48×10^{-13}	*5.62×10^{-17}*	2.59×10^{-5}	9.83×10^{-9}	2
RcnR (2 sites)	22.3 ± 2.4 94.9 ± 17.2 (+ Co(II))	2.37×10^{-12}	*4.16×10^{-11}*	1.77×10^{-7}	3.11×10^{-6}	1
MntR (2 sites)	18.5 ± 2.4 20.0 ± 4.8 (+ Mn(II))	1.96×10^{-9}	*1.65×10^{-10}*	1.33×10^{-7}	1.12×10^{-8}	4
Fur (4 sites)	201.1 ± 7.9 546.5 ± 120.5 (+ Fe(II))	5.76×10^{-11}	*7.52×10^{-13}*	1.28×10^{-4} [f]	1.67×10^{-6} [f]	37
CueR (2 sites)	24.4 ± 11.2 41.2 ± 10.0 (+ Cu(I))	3.14×10^{-10}	*2.35×10^{-11}*	6.94×10^{-7} [f]	5.19×10^{-8} [f]	3
ZntR (2 sites)	33.6 ± 14.5 30.0 ± 3.6 (+ Zn(II))	4.76×10^{-10}	*2.65×10^{-9}*	5.60×10^{-8}	3.12×10^{-7}	1
Zur (2 sites)	21.2 ± 7.0 35.7 ± 2.6 (+ Zn(II))	1.65×10^{-9}	*2.14×10^{-12}*	2.58×10^{-5} [f]	3.34×10^{-8} [f]	4

[a]Values determined from Osman et al., 2017 and Osman et al., 2018.

[b]Average affinity for allosterically required Ni(II) sites

[c]Calculated value using the thermodynamic cycle (Figure 1.2) and the experimentally determined K_1, K_3, and K_4.

[d]Reported for the Ni(II)-sensor stoichiometry that elicits an allosteric response.

[e]K_3 and K_4 calculated using *nixA*-Pro.

[f]Average binding constant calculated from the stepwise values (Table 5.1).

of P_1 to P_0 differs depending upon the functional role of the sensor and whether its expression is autoregulated.

The cellular concentrations of these sensors are essential for simulating DNA occupancy. However, the effect of Ni(II) on the sensor copy number is only known for NikR. Ni(II) is likely to affect RcnR copy number in a manner similar to Co(II) because of autoregulation, therefore, the P_1 concentration determined for Co(II) has been used for Ni(II) simulations. It must be noted that in this work, the K_4 affinity for RcnR with Ni(II) was determined to be tighter than for Co(II) (Section 4.3.2). Since RcnR is autoregulatory (Iwig and Chivers, 2009), its abundance is directly linked to DNA occupancy and may be lower when Ni(II) is present. This effect has been simulated to determine its potential significance (Section 5.3.2). For the non-cognate sensors it is assumed that the copy number is not changed by Ni(II) so P_0 values are used in all cases (unless specified).

5.2.3 Simulations predict Ni(II) occupancy is sensitive to a physiological buffer

The fraction of total Ni(II) bound to the *Salmonella* sensors was simulated using stepwise K_1 affinities from Table 5.1 with the P_1 (cognate sensors) and P_0 (non-cognate sensors) abundances (Table 5.2) converted to protein concentration (Section 2.10.5). Figure 5.1 shows the simulated data for Ni(II) binding to the total number of sites for each protein alone or in the presence of 60 μM and 200 μM L-histidine (see Section 5.1). Protein concentration, as expected, is a key variable when considering the fraction of Ni(II)-bound to a sensor (Figure 5.1a), since the lower concentration sensors (MntR, CueR, ZntR, and Zur) become fully Ni(II)-bound in the absence of L-histidine at lower concentrations of Ni(II) compared to NikR, RcnR (P_1), and Fur. However, when the physiological buffer (L-histidine) is introduced as a competing molecule, absolute affinities become more important (Figure 5.1b-c). L-histidine shifts the curves for MntR, CueR, ZntR, and Zur so that a higher total Ni(II) concentration is required to fully saturate the proteins. In contrast, NikR and RcnR are largely unaffected, indicating that L-histidine is not an especially effective competitor for the cognate sensors at these physiological concentrations of protein and small molecule, thus ensuring correct metalation of the cognate sensors. The tightest sites of Fur (K_{1a} and K_{1b}) are similar to NikR and RcnR in that L-histidine does not impact much on the concentration of Ni(II) required to fill them, but since the concentration of Fur is that much greater than for the cognate sensors, a greater concentration of Ni(II) is required to achieve a similar metal-bound fraction.

While mis-metalation is a potential problem for the cell, more important is the knowledge of the fraction of Ni(II) bound to the allosterically effective sites (Section 5.2.1). Simulations

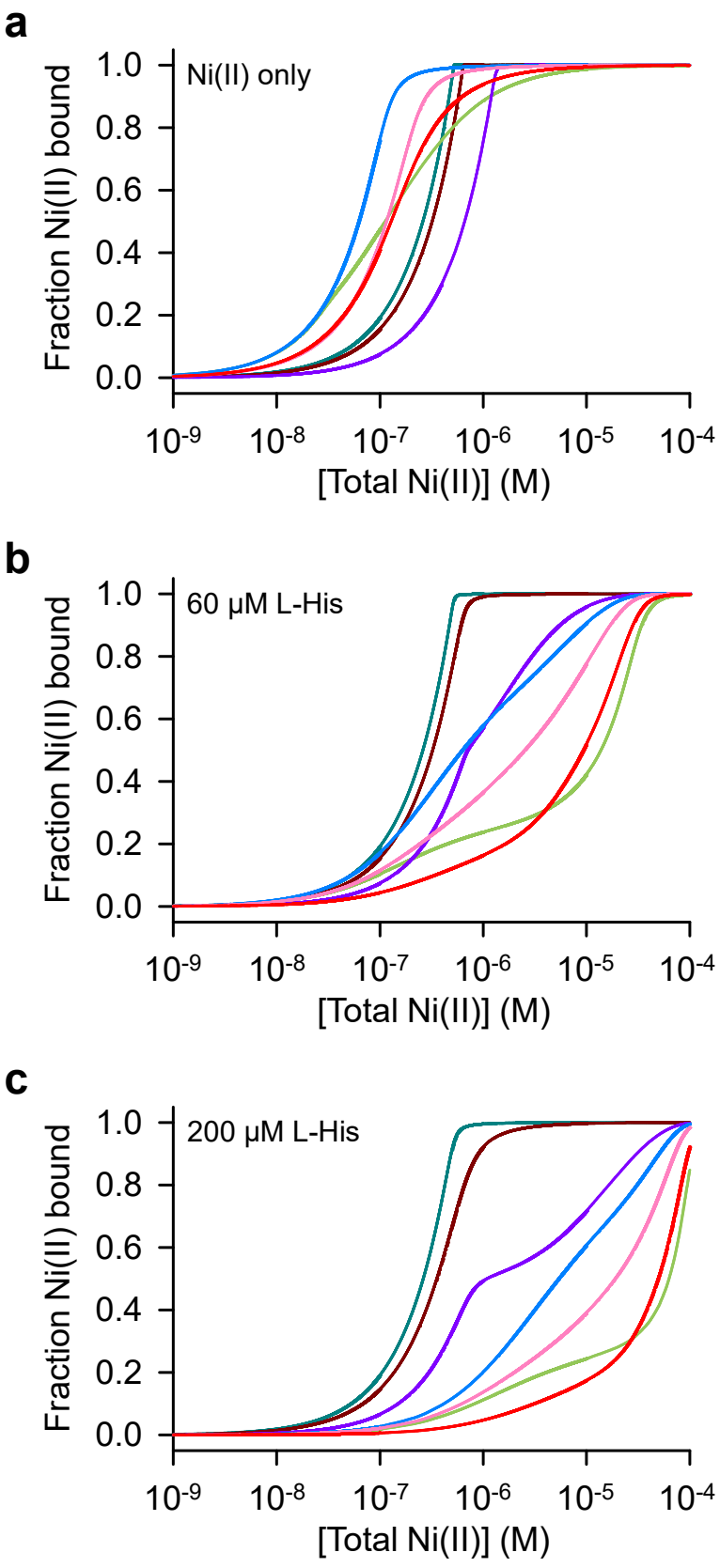

Figure 5.1 Simulation of fraction Ni(II) bound to each sensor for all sites in the absence or presence of L-histidine. Ni(II) titrations simulated for NikR (turquoise), RcnR (maroon), MntR (green), Fur (purple), CueR (blue), ZntR (pink), and Zur (red). **(a)** No L-histidine. **(b)** 60 μM L-histidine. **(c)** 200 μM L-histidine. P_1 protein concentrations were used for NikR and RcnR, and P_0 values for MntR, Fur, CueR, ZntR, and Zur.

for Ni(II) occupancy of these sites (Figure 5.2) showed the same general trend as described above for the total number of sites, though the lack of weaker metal sites results in the non-cognate sensors appearing more competitive in the absence of L-histidine (except for Fur which requires all sites to be occupied and is therefore unchanged). As before, L-histidine buffers Ni(II) so that the total Ni(II) concentration required for full occupancy of the allosteric sites of the non-cognate sensors is greatly increased, in line with that for Fur. Using CueR as an example, the concentration of Ni(II) required to achieve 50% Ni(II)-bound protein was ~ 41 nM with no L-histidine (Figure 5.2a), and subsequently increased to ~ 270 nM and ~ 2.3 μM when in the presence of 60 μM (Figure 5.2b) and 200 μM L-histidine (Figure 5.2c), respectively. The NikR and RcnR curves shift towards lower total Ni(II) concentrations since fewer sites must be filled (compared to the total site model in Figure 5.1), increasing the gap between them and the non-cognate sensors. In 200 μM L-histidine, NikR and RcnR can reach 100% and 90% Ni(II)-bound, respectively, at a total Ni(II) concentration where Fur is ~ 27% bound and the other sensors are < 15% bound. This result suggests that it will be challenging for a non-cognate sensor to respond to Ni(II) under physiological conditions because of limited Ni(II) binding.

5.2.4 The effect of changing protein concentration on Ni(II)-loading

The protein concentrations used in Section 5.2.3 were fixed to either P_1 (cognate sensors) or P_0 (non-cognate sensors). To understand how sensor concentration affects the fraction of Ni(II) bound, the simulations were repeated for P_0 concentrations of NikR and RcnR, and P_1 concentrations of MntR, Fur, CueR, ZntR, and Zur (Figure 5.3). The NikR traces for P_1 and P_0 differ slightly, with the P_1 concentration requiring more Ni(II) for complete occupancy where both traces are essentially unmoved when comparing the data for no L-histidine to 60 μM and 200 μM L-histidine. The P_1 and P_0 concentrations for RcnR are substantially different such that P_0 requires much less Ni(II) to load the protein compared to both NikR and P_1 RcnR. Interestingly for RcnR, the difference between the total Ni(II) concentration required to bind 50% of the protein at P_0 compared to P_1 decreases in 200 μM L-histidine (3.3-fold difference) compared to Ni(II) only (4.3-fold difference) and 60 μM L-histidine (4.5-fold difference), which were both very similar. This indicates that even though the Ni(II) affinity of RcnR is much tighter than that of L-histidine, this small molecule may still compete with the protein under certain physiological conditions.

Like RcnR, Fur demonstrates a large change in abundance between P_0 and P_1, therefore, the simulated data for the fraction of Ni(II) bound to the protein at these concentrations are noticeably different (Figure 5.4). As L-histidine increases, the initial phase of the curve

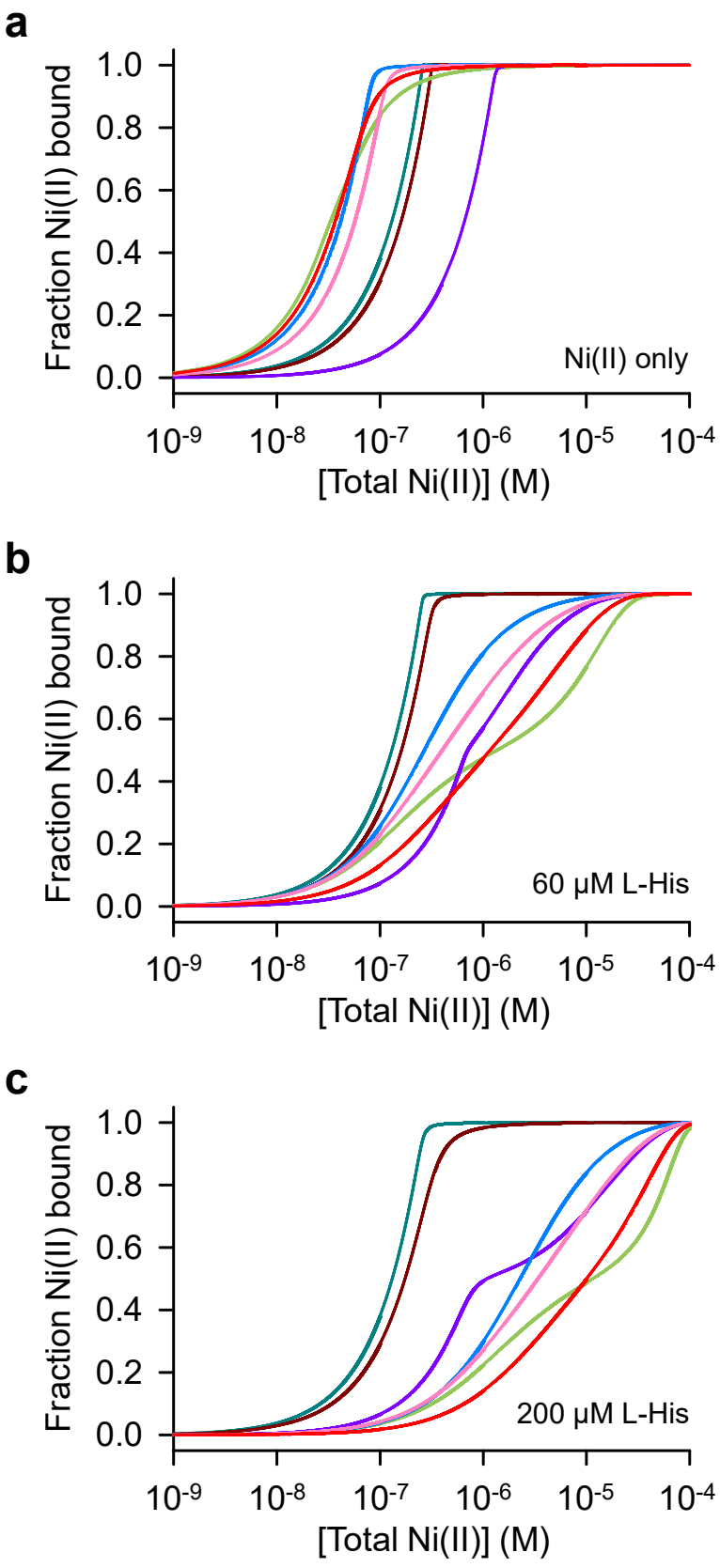

Figure 5.2 Simulation of fraction Ni(II) bound to each sensor for the allosterically active sites in the absence or presence of L-histidine. Ni(II) titrations simulated for NikR (turquoise), RcnR (maroon), MntR (green), Fur (purple), CueR (blue), ZntR (pink), and Zur (red). **(a)** No L-histidine. **(b)** 60 µM L-histidine. **(c)** 200 µM L-histidine. P_1 protein concentrations were used for NikR and RcnR, and P_0 values for MntR, Fur, CueR, ZntR, and Zur.

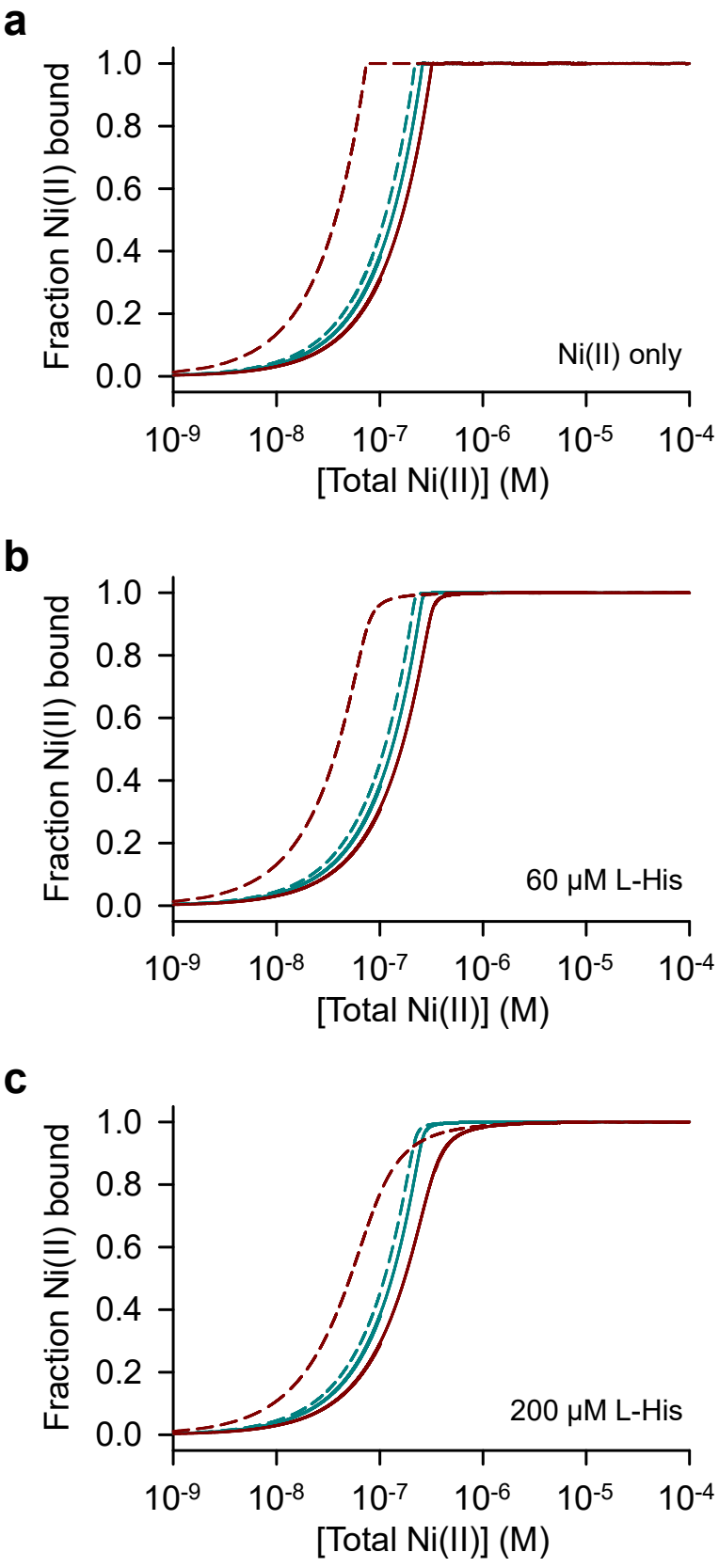

Figure 5.3 Simulation of the effect of cognate sensor concentration on fraction Ni(II) bound to allosteric sites. Ni(II) titrations simulated for NikR (turquoise) and RcnR (maroon) using P_1 (solid line) and P_0 (dashed line). **(a)** No L-histidine. **(b)** 60 µM L-histidine. **(c)** 200 µM L-histidine.

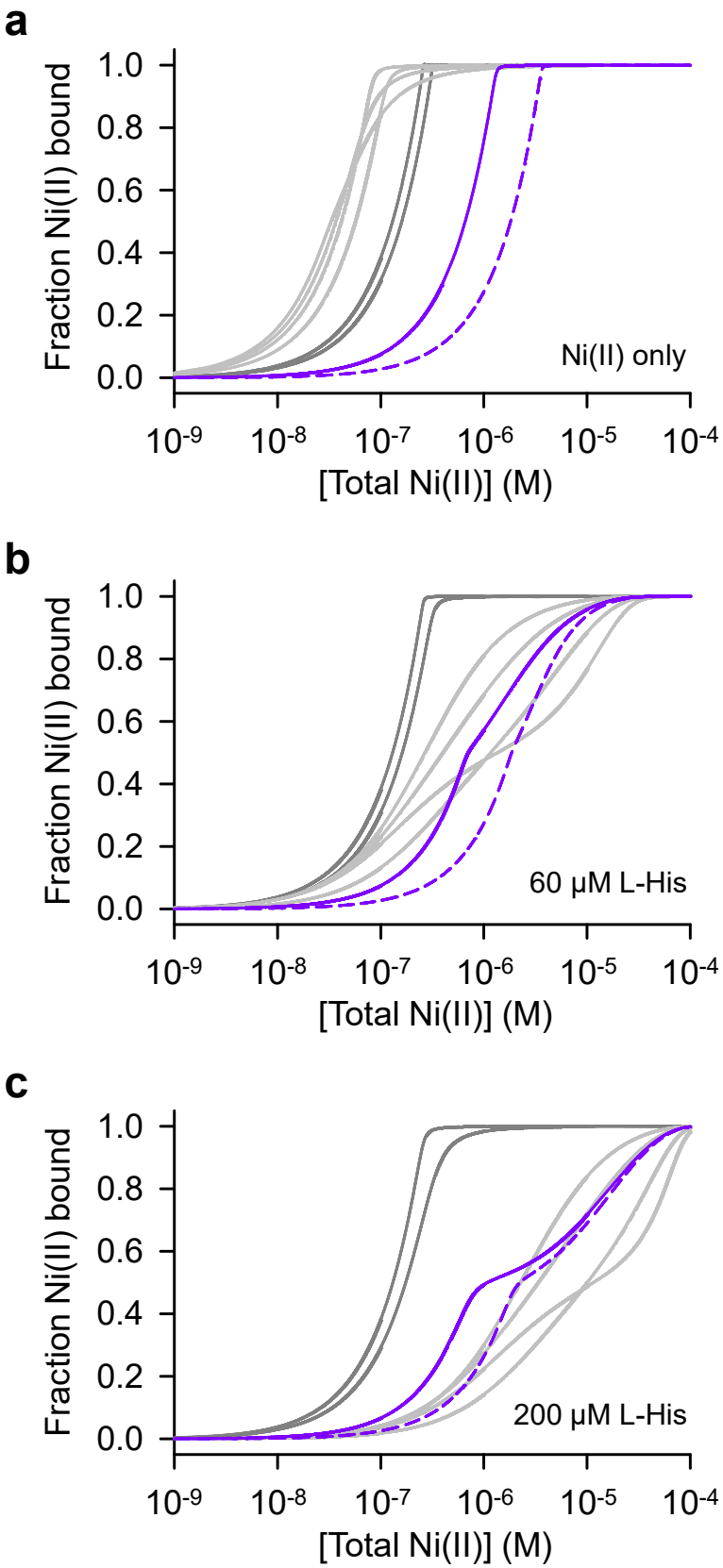

Figure 5.4 Simulation of the effect of Fur on fraction Ni(II) bound to allosteric sites. Ni(II) titration simulated for Fur (purple) using P_1 (solid line) and P_0 (dashed line). Cognate sensors (dark grey) and other non-cognate sensors (light grey) are shown, as in Figure 5.2. **(a)** No L-histidine. **(b)** 60 µM L-histidine. **(c)** 200 µM L-histidine.

remains separate owing to the difference in concentration, however, the latter phase converges to the point where it overlaps for P_0 and P_1. This suggests that Ni(II)-loading to the weaker Fur sites is concentration independent and that they are almost ineffective at competing with L-histidine.

For MntR, CueR, ZntR, and Zur, the difference between P_0 and P_1 is relatively small. These small differences can be seen in the fraction of Ni(II) bound to the proteins when L-histidine is not present, but when L-histidine is included in the simulation, the loading curves superimpose in most cases (Figure 5.5). To test whether the two traces converging was due to a small range in sensor concentration, the 200 μM L-histidine simulations were run again but this time with concentrations of 10-fold higher and 10-fold lower than P_0 (i.e. a 100-fold change in abundance; Figure 5.6a-d). The CueR and ZntR traces indicated a small difference with the new concentration range, whereas MntR and Zur were again essentially the same. The CueR and ZntR Ni(II) affinities are slightly tighter than for MntR and Zur, therefore, it appears that Ni(II) affinity is important for observing a concentration dependent shift for Ni(II)-bound non-cognate sensors. To test this, the 200 μM L-histidine simulations were repeated but with K_{1a} affinities 10-fold tighter for MntR, CueR, ZntR, and Zur, and also included 10-fold changes in protein concentration (Figure 5.6e-h). These simulations demonstrate that tighter affinities are required to allow a concentration dependent shift in the fraction of Ni(II) bound. This supports the observation that competition with L-histidine distinguishes cognate from non-cognate metal sensors.

5.3 Linking Ni(II)-bound sensors to DNA occupancy

5.3.1 Input values for DNA occupancy simulations

While it was possible to simulate Ni(II) occupancy of the sensors using stepwise K_1 values for Ni(II)-binding, the models required to simulate both Ni(II)-binding and DNA-binding to determine DNA occupancy using intermediate values were too complex. Average affinity constants were therefore calculated for K_1, K_2, K_3, and K_4 (Section 2.10.4) to describe 50% Ni(II) occupancy or 50% DNA occupancy (Table 5.2). The NikR K_4 value was for binding the *nixA* promoter and was used for all simulations, unless mentioned. Also required are the number of promoter targets within the *Salmonella* genome for each sensor. These have been previously determined (Osman et al., 2018) and are listed in Table 5.2 prior to conversion into a concentration value that can be used in the simulations (Section 2.10.5).

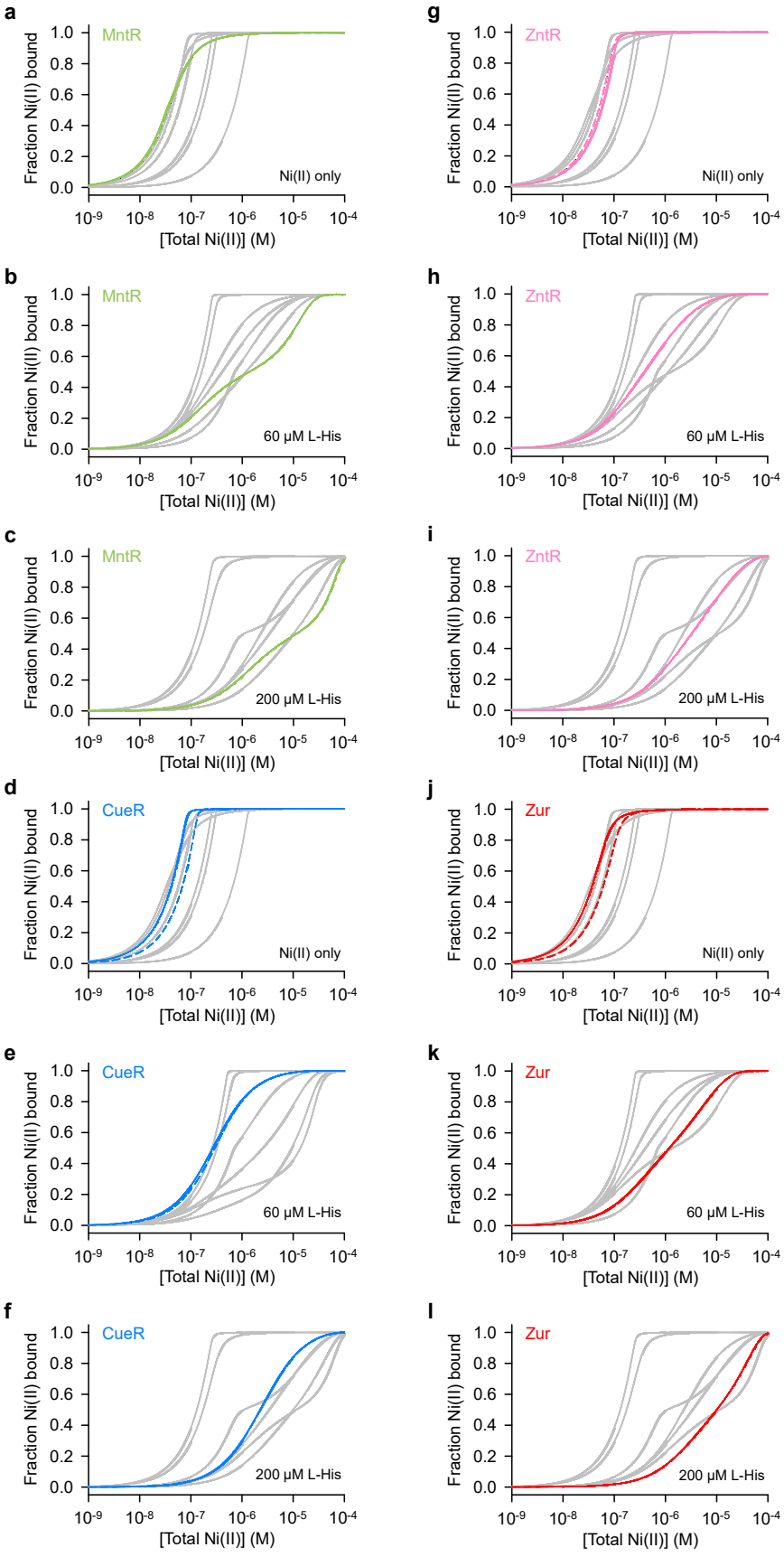

Figure 5.5 Simulation of the effect of non-cognate sensor concentration on fraction Ni(II) bound to allosteric sites. Ni(II) titration simulated for MntR **(a-c)**, CueR **(d-f)**, ZntR **(g-i)**, and Zur **(j-l)** (coloured) using P_1 (solid line) and P_0 (dashed line). Other sensors (grey) are shown for comparison, as in Figure 5.2. Panels **(a**, **d**, **g**, **j)**, no L-histidine; **(b**, **e**, **h**, **k)**, 60 µM L-histidine; and **(c**, **f**, **i**, **l)**, 200 µM L-histidine.

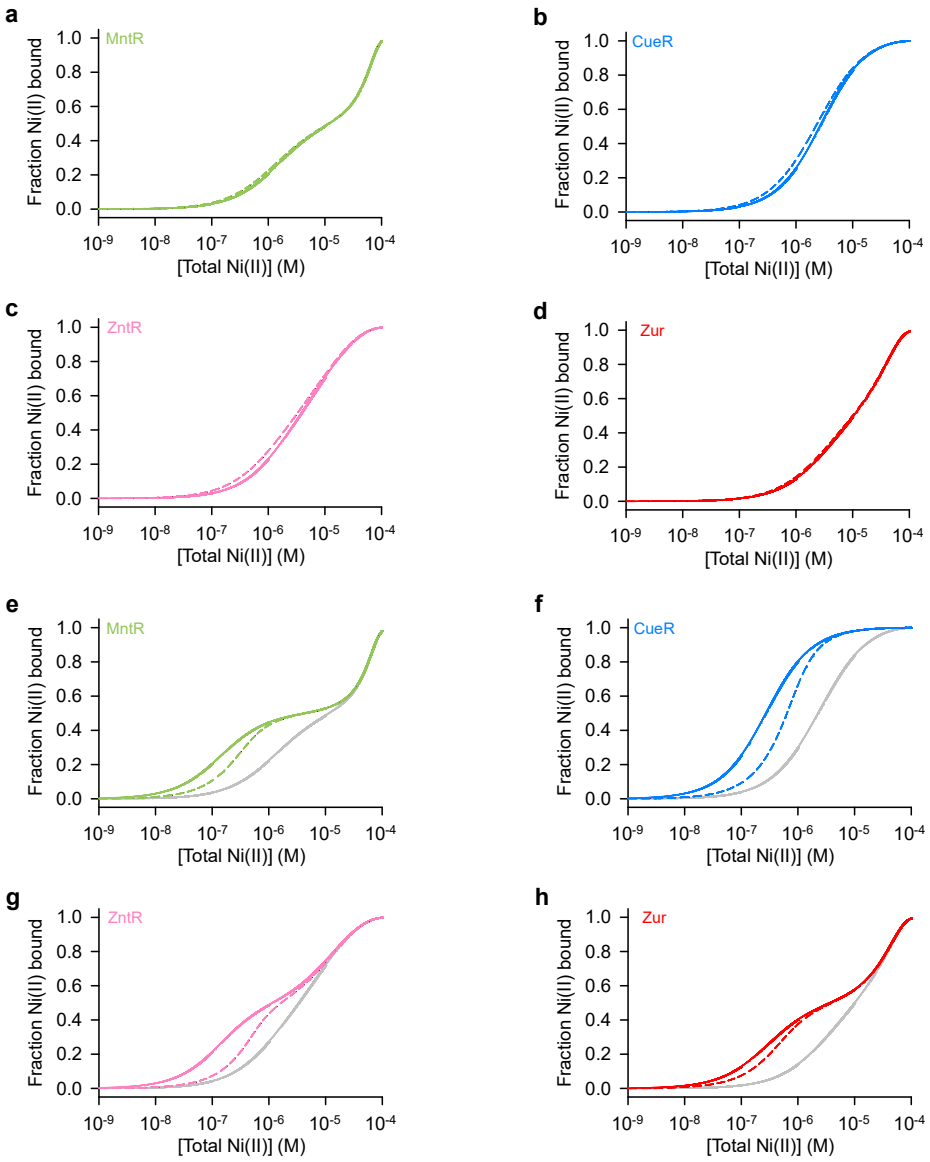

Figure 5.6 Simulation of the effect of 10-fold changes in protein concentration or metal affinity on fraction Ni(II) bound to allosteric sites. Ni(II) titrations simulated in the presence of 200 μM L-histidine. **(a)** MntR with P_0 10-fold higher (solid line) and 10-fold lower (dashed). **(b)** Same as (a) except for CueR. **(c)** Same as (a) except for ZntR. **(d)** Same as (a) except for Zur. **(e)** MntR at P_0 (grey line), or at P_0 with K_{1a} 10-fold tighter (coloured solid line), and at P_0 10-fold higher with K_{1a} 10-fold tighter (dashed line). **(f)** Same as (e) except for CueR. **(g)** Same as (e) except for ZntR. **(h)** Same as (e) except for Zur.

5.3.2 DNA occupancy of the sensors as a function of buffered Ni(II) concentrations (Model 1)

Sensor DNA occupancy can be described by the thermodynamic model shown in Figure 1.2. This simple model can be expanded to include a metal-buffering system where associative ligand exchange is responsible for metal transfer between systems components, as opposed to dissociative exchange involving a "free" hydrated metal intermediate (Osman et al., 2017, Osman et al., 2018). Therefore, the buffered metal concentration can effectively be maintained lower than one free metal ion per cell (equivalent to 2×10^{-9} M for the *Salmonella* cytosol). Using the average affinity values (Table 5.2), the concentrations determined for *Salmonella* sensors, and the concentrations of DNA targets (Section 5.3.1), total DNA sites occupancy was modelled through equations combining all the necessary thermodynamic values (Section 2.10.7). Additionally, a series of equations have been derived which link sensor promoter occupancy to the change in sensor abundance from P_0 to P_1 in a linear relationship (Osman et al., 2018) which is used where required (described in the text).

The absolute fractional occupancy of the total number of target sites for each sensor was determined (Figure 5.7). NikR is the first to respond to Ni(II), increasing from effectively no occupancy of DNA to > 90% over the range tested. RcnR initially has a low DNA occupancy (~ 17%) compared to that for the maximum occupancy seen by NikR (see Section 5.3.3), and decreases further with increasing Ni(II) due to the opposite mode of action for de-repressor proteins. Model curves are also shown to distinguish between two and four site allosteric activation models of NikR and RcnR, and demonstrate a small change in buffered Ni(II) required for a response. Due to the limits determined for the DNA affinities of MntR (Section 4.4), the protein occupies DNA (18%) at low concentrations of Ni(II) before increasing occupancy to almost 70% with higher buffered Ni(II) concentrations. The other two co-repressor proteins, Fur and Zur, reach occupancies of 16% and 49%, respectively, at high concentrations of Ni(II). The activator proteins, CueR and ZntR, are modelled where DNA occupancy is considered for the metal-bound protein and not the apo-protein (Section 2.10.7). CueR reaches an occupancy of 42% whereas ZntR only reaches 15% at high Ni(II).

The absolute DNA occupancies for each sensor can be normalised to the maximal occupancy seen with Ni(II), allowing a more direct comparison of the concentration dependence of the Ni(II) responses (Figure 5.8). Interestingly, this data predicts that NikR would achieve maximal response at the concentration of Ni(II) for which RcnR begins to respond, an observation which has been reported *in vivo* by *lacZ* reporter assay (Iwig et al., 2006). This demonstrates an elegant mechanism by which cells only begin upregulating export machinery when importer synthesis is maximally repressed and can no longer impact the

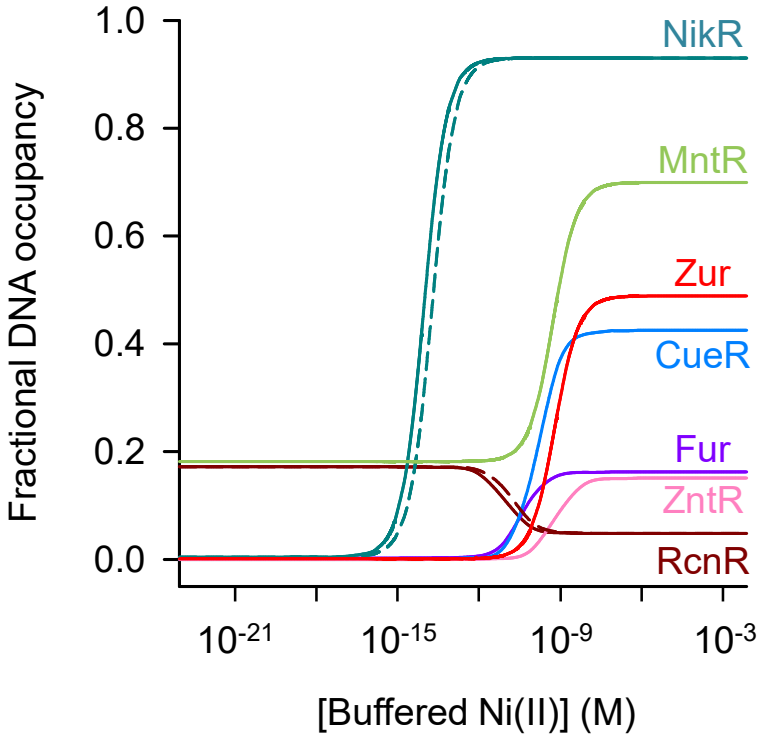

Figure 5.7 Simulation of the Ni(II)-dependent fractional DNA occupancy over all promoter sites for each *Salmonella* sensor (Model 1). Predicted occupancy based on averaged affinities (Table 5.2) for allosterically effective sites (solid lines). Cognate sensors – NikR (turquoise) and RcnR (maroon) – simulated the change from P_0 to P_1. Non-cognate sensors – MntR (green), Fur (purple), CueR (blue), ZntR (pink), and Zur (red) – used P_0 values. NikR and RcnR were also simulated when all four Ni(II) sites (per tetramer) are required to allosterically activate the protein (dashed lines).

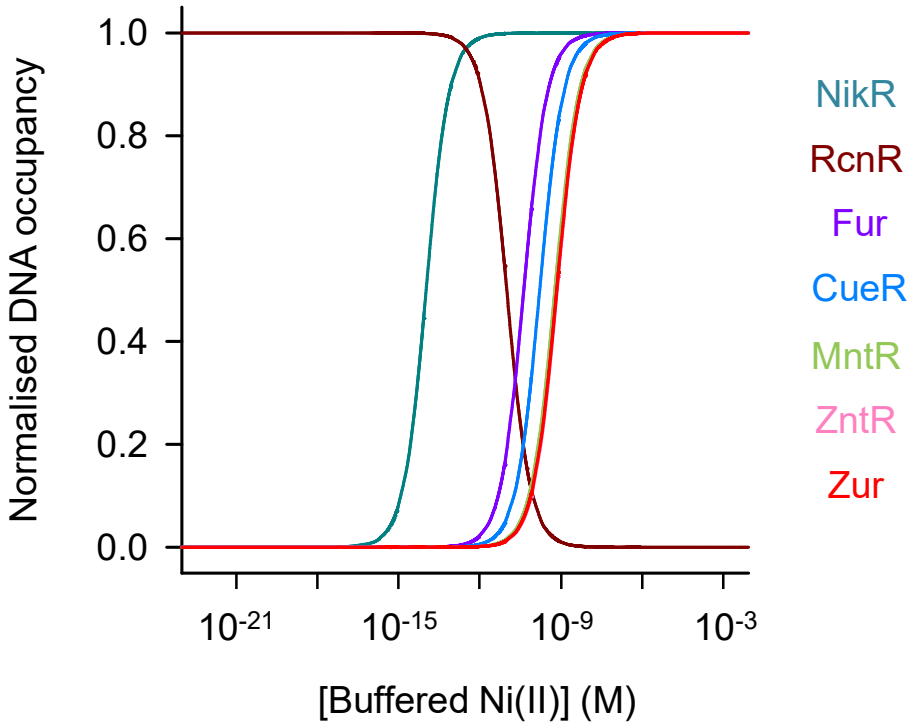

Figure 5.8 Normalised DNA occupancy over all promoter sites for each *Salmonella* sensor (Model 1). Determined from data in Figure 5.7 for NikR (turquoise), RcnR (maroon), MntR (green), Fur (purple), CueR (blue), ZntR (pink), and Zur (red). The list to the right (top to bottom) shows the order of 50% occupancy from lowest to highest [Ni(II)].

intracellular concentration of Ni(II). While RcnR is the next sensor to respond to increasing Ni(II) after NikR, fully expressed P_{rcnRA} is not achieved before all the other sensors begin to respond to Ni(II). The non-cognate sensors are all approaching, or are greater than, 90% maximal occupancy of DNA at the Ni(II) concentration required to cause full de-repression by RcnR. The extended responsive range by RcnR is a result of hysteresis due to increasing protein concentration (Osman et al., 2018) and could add further insight into the *lacZ* reporter assay data (conditions approaching maximally de-repressed P_{rcnRA} cause cell death (Iwig et al., 2006)) since mis-metalation could induce mal-responses by regulators, along with inactivating essential enzymes (e.g. FbaA – Chapter 6).

The concentration of Ni(II) required to produce 50% of the maximal DNA occupancy for all sensors is closely linked to K_1 (Figure 5.9a). Fur follows this trend even though the concentration of protein and DNA target sites are much greater than for the other sensors, indicating that protein concentrations are controlled appropriately for the number of targets within the cell. Extending this calculation to include the buffered Ni(II) concentration required for 20%, 50%, and 80% of the maximal response by all sensors suggests a threshold Ni(II) concentration ($\sim 2 \times 10^{-11}$ M) separating the cognate and non-cognate sensor responses (Figure 5.9b). This data shows an alternative representation for the overlap of responses by the sensors (compared to Figure 5.8), indicating that at approximately 50% of the RcnR response, Fur would be ~ 20% responsive, and at 80% of the RcnR response, Fur would be ~ 50% responsive and CueR would be ~ 20% responsive.

The normalised DNA occupancy for each sensor determined as a function of K_1 alone (Section 2.10.7) indicates that all the non-cognate sensor responses are closely approximated by this method, whereas both cognate sensors are not (Figure 5.10). This is consistent with reports that have previously demonstrated the close approximation of a response by K_1 for some sensors with their cognate metal (but not NikR) (Osman et al., 2018).

From the absolute DNA occupancies (Figure 5.7), it is clear that, not unexpectedly, the majority of non-cognate sensors demonstrate smaller responses compared to NikR. These DNA occupancies were therefore compared to the occupancies for each sensor with their cognate metals (using Co(II) for RcnR), using reported affinity values (Osman et al., 2018) and protein concentration ranging from P_0 to P_1 (Figure 5.11) in the responses to Ni(II), though the assumption is that non-cognate metals would not, in most cases, impact the sensor concentration of a cell the same as the cognate metal, unless dual metal stress was apparent. Comparing the traces for Co(II)- and Ni(II)-bound RcnR revealed differing start and end points for occupancy. The start points differ due to the slightly different K_3 affinities determined under different conditions (Section 4.3.1). The different end points reflect the

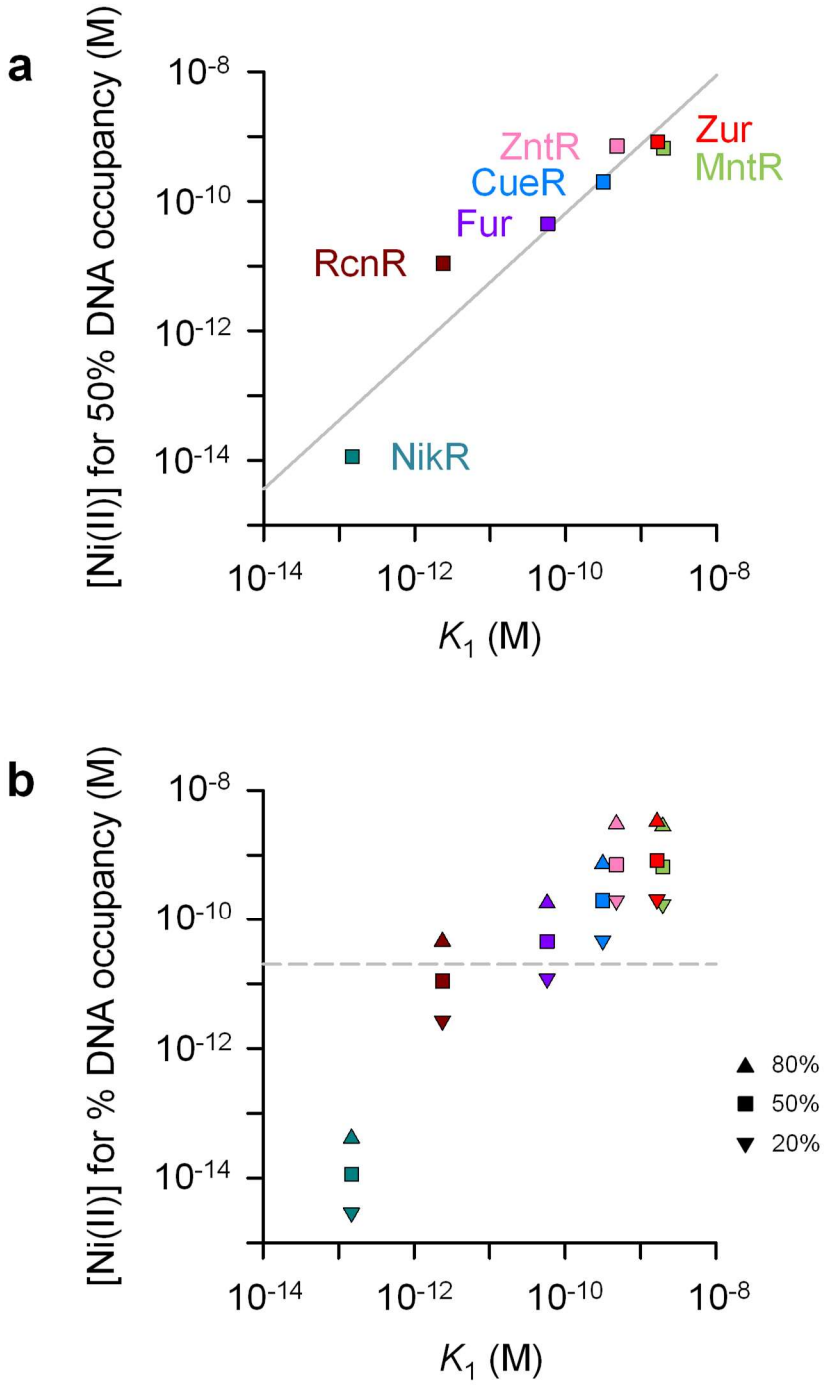

Figure 5.9 The relationship between average Ni(II) affinity (K_1) and DNA occupancy for each *Salmonella* sensor. Values are derived from Table 5.2 (K_1) and Figure 5.8 (DNA occupancy). **(a)** K_1 and Ni(II) required for 50% occupancy. The solid line represents a best fit ($y = 2.9041x^{1.0647}$; $R^2 = 0.90$) to the data. **(b)** K_1 and Ni(II) required to achieve 20% (▼), 50% (■), and 80% (▲) of the maximal occupancy for each sensor. The dashed line (grey) indicates an arbitrary threshold between the 50% occupancies of the weakest cognate sensor (RcnR) and the tightest non-cognate sensor (Fur).

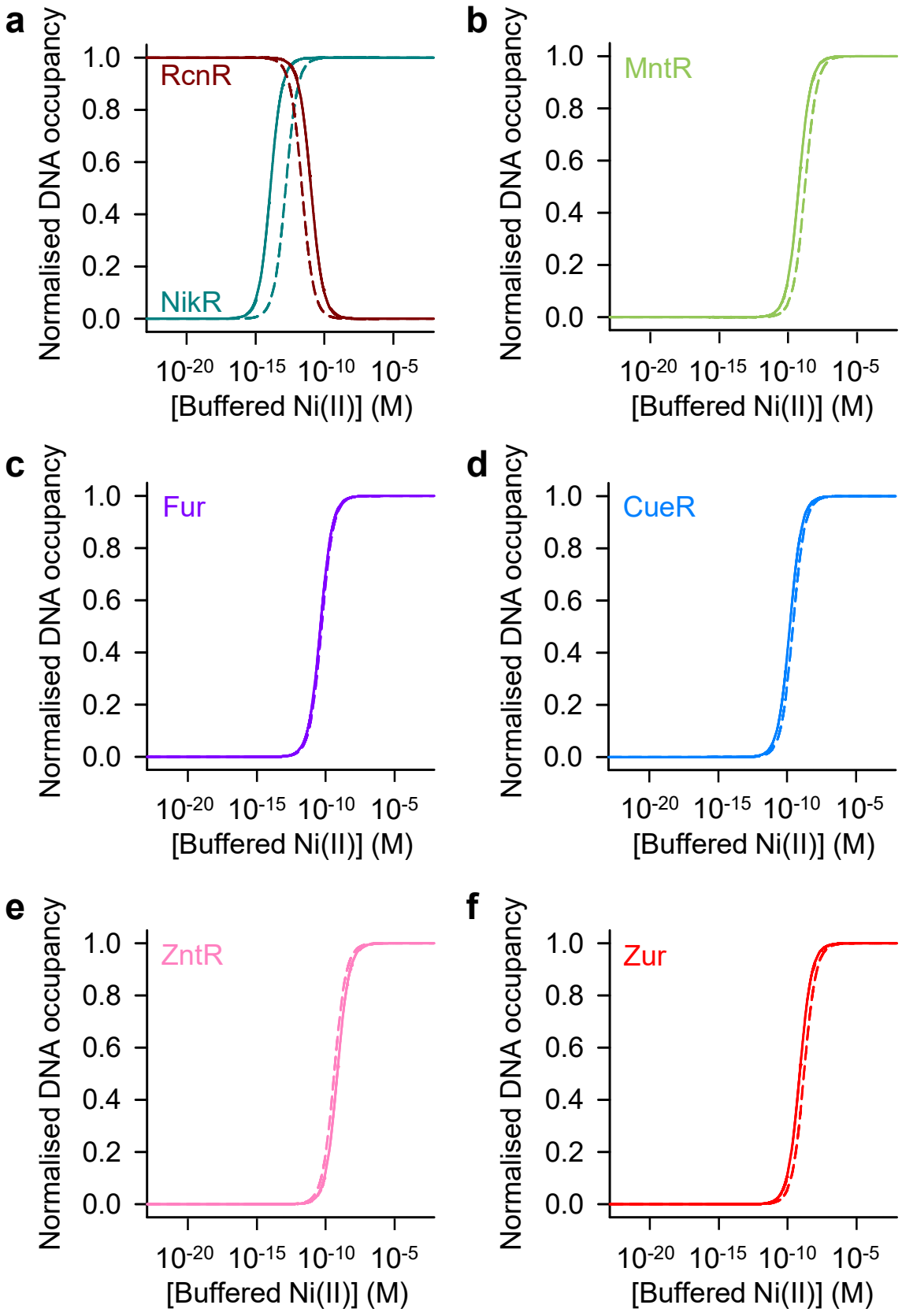

Figure 5.10 Simulation of DNA occupancy using only the Ni(II) affinity (K_1) of each sensor. Normalised occupancies (solid line; Figure 5.8) using all available parameters compared to occupancy predicted from K_1 alone (dashed line). **(a)** NikR (turquoise) and RcnR (maroon). **(b)** MntR. **(c)** Fur. **(d)** CueR. **(e)** ZntR. **(f)** Zur. Normalised occupancies calculated allowing concentrations for NikR and RcnR to change from P_0 to P_1, but fixing the other sensors to P_0.

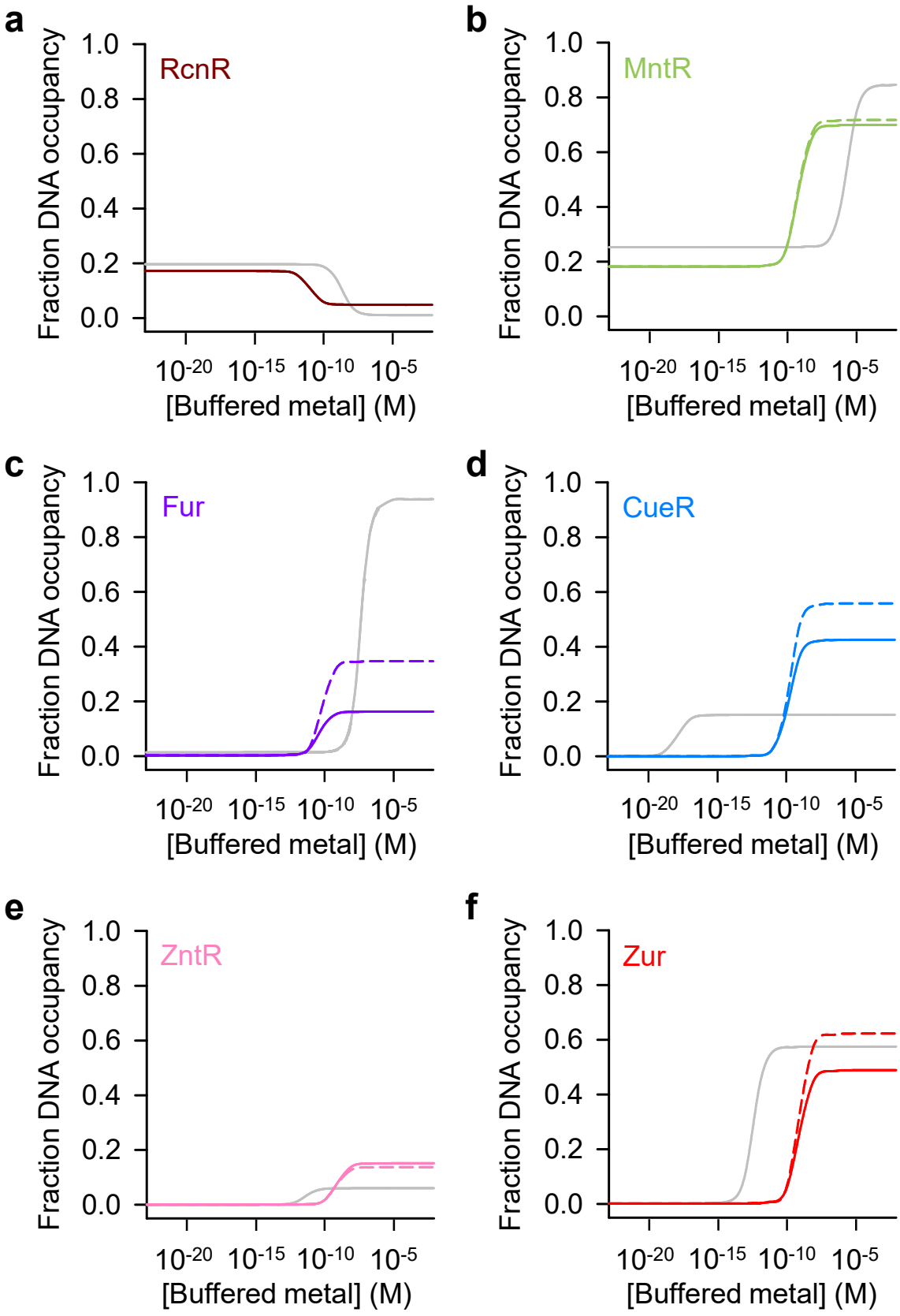

Figure 5.11 Simulation of fractional DNA occupancies for each sensor with Ni(II) in comparison to its cognate metal (Model 1). Ni(II) responses are shown in colour and cognate metal responses in grey. Unless mentioned, simulations with Ni(II) are shown for sensor concentration fixed at P_0 (solid line) or changing from P_0 to P_1 (dashed line). Simulations with cognate metal change from P_0 to P_1. **(a)** RcnR with Co(II) (grey) and Ni(II) (maroon) allowing protein concentration to change between P_0 and P_1 for both. **(b)** MntR with Mn(II) and Ni(II). **(c)** Fur with Fe(II) and Ni(II). **(d)** CueR with Cu(I) and Ni(II). **(e)** ZntR with Zn(II) and Ni(II). **(f)** Zur with Zn(II) and Ni(II).

efficacy of Co(II) on de-repression by RcnR (Section 4.3.2). The P_0 and P_1 concentrations used for Ni(II)-RcnR simulations were those determined with Co(II), however, this simulation suggests the concentration of the protein is likely to differ depending on the metal sensed by RcnR. Moreover, it has been shown that *rcnA* expression is lower in response to Ni(II) than Co(II) in *Salmonella* (Osman et al., 2018), which could be the result of different K_4 affinities. To test the effect of a smaller change in copy number from P_0 to P_1 (implied by the increased occupancy on DNA for Ni(II)-RcnR), the DNA occupancy of RcnR has been simulated using a P_1 value that corresponds to 70% of the P_0 to P_1 change seen with Co(II), since the change in occupancy shown for Ni(II)-RcnR is approximately 70% of that seen with Co(II)-RcnR. The reduced P_1 concentration results in increased de-repression of P_{rcnRA} by Ni(II)-RcnR (Figure 5.12a) since the association with DNA is concentration dependent which displays the importance of well-defined P_0 and P_1 values for accurate simulations. The normalised DNA occupancy suggests only a slightly lower concentration of buffered Ni(II) would result in half occupancy of the promoter at the altered P_1 concentration (Figure 5.12b).

The co-repressor (MntR, Fur, and Zur) occupancies with Ni(II) are all less than for their cognate metals (Figure 5.11). The starting point for Ni(II)-MntR and Mn(II)-MntR differ due to the slightly different limits for K_3 (this does not affect the end point). Allowing the protein concentration to vary between P_0 and P_1 does not dramatically change the curve for MntR (Figure 5.11b) but does significantly increase the occupancy by Fur (16% to 35%) and Zur (49% to 62%). Fe(II)-Fur results in almost full occupancy of DNA targets and therefore, even with the concentration change, Ni(II)-Fur would appear to only associate with one third of Fur targets (Figure 5.11c), but this is still a considerable problem given the size of the Fur regulon. When concentrations of Zur were allowed to vary, the occupancy of Ni(II)-Zur was found to be greater than for Zn(II)-Zur, due to the tighter K_4 (Section 4.8.1), though requiring a greater concentration of Ni(II) to induce the response compared to Zn(II) (Figure 5.11f). This is similar to the effect of Co(II) which was shown to induce a mal-response by Zur through shocking *Salmonella* with the metal (Osman et al., 2017). The responses of CueR and ZntR (Figure 5.11d-e) are difficult to interpret due to the mechanism of activation by these sensors (Section 1.3.10). DNA occupancy does not regulate gene expression; instead, the DNA-bound cognate metal-associated form induces activation of gene synthesis by distorting DNA. Non-cognate metal binding does not guarantee appropriate conformational changes to induce activation, therefore, monitoring Ni(II)-bound sensor occupancy of DNA in the simulations does not correspond to a transcriptional response. Indeed, CueR has evolved specificity for monovalent metal ions so the likelihood of a response to Ni(II) would

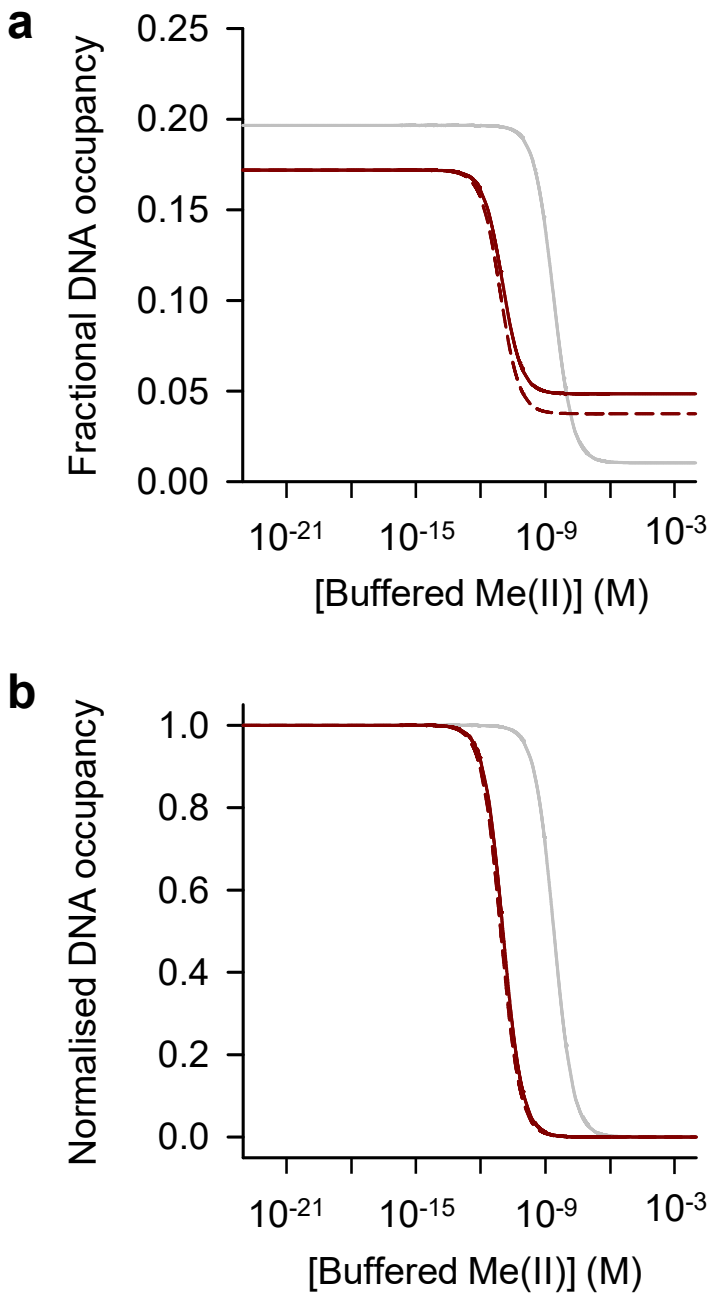

Figure 5.12 Simulation of protein concentration dependence of DNA occupancy (Model 1) by RcnR. (a) Fractional DNA occupancy of RcnR (solid line) with Ni(II) (maroon) and Co(II) (grey) using determined P_0 to P_1 concentration change observed experimentally for Co(II), and fractional DNA occupancy (dashed line) with Ni(II) using P_0 and a P_1 value that equates to 70% of the change determined for Co(II). **(b)** Normalised DNA occupancies from (a).

be low (Stoyanov et al., 2001, Stoyanov and Brown, 2003, Changela et al., 2003). Nevertheless, both CueR and ZntR appear to show greater fractional occupancy of DNA in response to Ni(II) binding compared to their cognate metals which is due to the Ni(II) K_4 values being tighter than for the reported cognate metal values (Osman et al., 2018). Using CueR as an example, this could indicate that Ni(II) binding results in alternative conformational changes compared to Cu(I) and although it increases the affinity of the protein for DNA, the specific allosteric changes required for DNA distortion may not occur.

An alternative (and potentially more appropriate) normalisation of the DNA occupancy data compares the responses of MntR, Fur, and Zur with Ni(II) to the responses with their cognate metals (Osman et al., 2018). Figure 5.13 shows the normalised occupancy data for NikR and RcnR, as seen in Figure 5.8, as well as the normalised data for MntR, Fur, and Zur with Ni(II) (fixed at P_0) where occupancy of 1 equates to the maximum absolute occupancy achieved with the cognate metal (seen in Figure 5.11). This indicates that MntR and Zur demonstrate a similar level of promoter occupancy when bound to Ni(II) as with their cognate metal, whereas Fur occupies substantially less targets than with Fe(II). The equivalent curves were not produced for CueR and ZntR due to the distinct mechanism for gene regulation.

5.3.3 Testing the contribution of Ni(II)- and DNA-affinities to DNA occupancy – alternative models for DNA occupancy as a function of buffered Ni(II)

The absolute occupancy of apo-RcnR for DNA was found to be relatively low as a consequence of the K_3 affinity which is not as tight as, for example, NikR K_4 (the active DNA binding form). The DNA binding affinity of *Ec*RcnR is enhanced through wrapping via non-specific contacts with extended regions of DNA (Section 1.3.8). The fragment used to determine K_3 and K_4 was too short to allow for DNA wrapping though it has been reported that increasing the length of DNA can result in a 4-fold increase in K_3 affinity (Iwig and Chivers, 2009). A 4-fold tighter K_3 affinity results in 45% DNA occupancy by RcnR at low Ni(II), compared to 17% originally (Figure 5.14a).

MntR DNA affinities were difficult to interpret due to additional binding events obscuring an accurate determination of K_3 and K_4 (Section 4.4). Therefore, only lower limits were defined for this protein meaning it is possible the DNA affinities could be weaker for both apo- and Ni(II)-MntR. The DNA occupancy for this protein using K_3 and K_4 values 10-fold weaker than the determined limits (concentrations fixed at P_0) indicates a DNA occupancy close to zero at low Ni(II), expected for a co-repressor, and only a slight increased response (up to ~ 20% occupancy) with higher Ni(II) (Figure 5.14b).

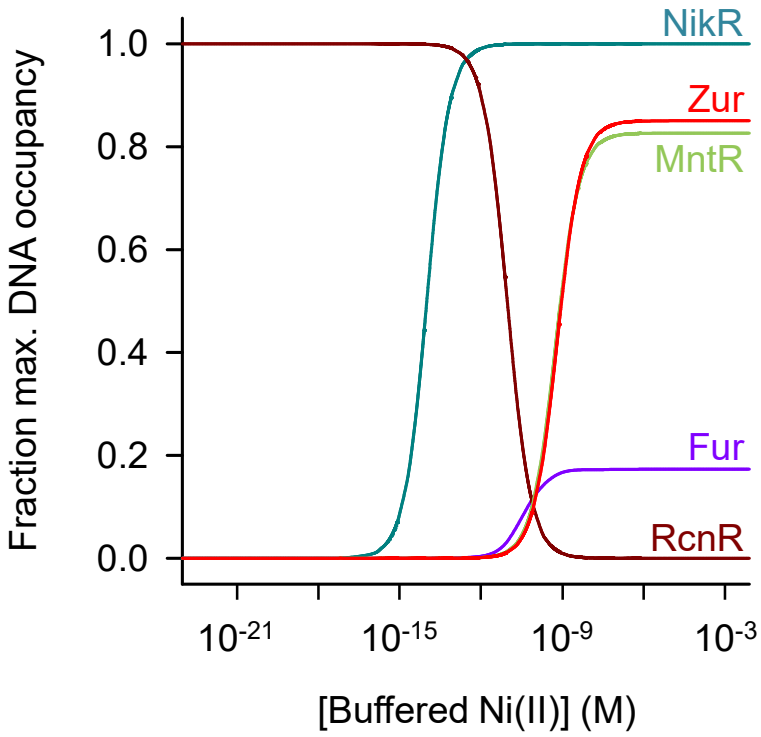

Figure 5.13 Simulation of fractional DNA occupancy for Ni(II)-bound sensors normalised to the maximum occupancy achieved with the cognate metal (Model 1). Occupancy determined for NikR, RcnR, MntR, Fur, and Zur, where Ni(II) is the cognate metal for NikR and RcnR. Ni(II)-sensor occupancy determined using concentrations that change from P_0 to P_1 for NikR and RcnR and fixed to P_0 for the other sensors. The cognate metal occupancies for the sensors were all collected allowing concentrations to change between P_0 and P_1.

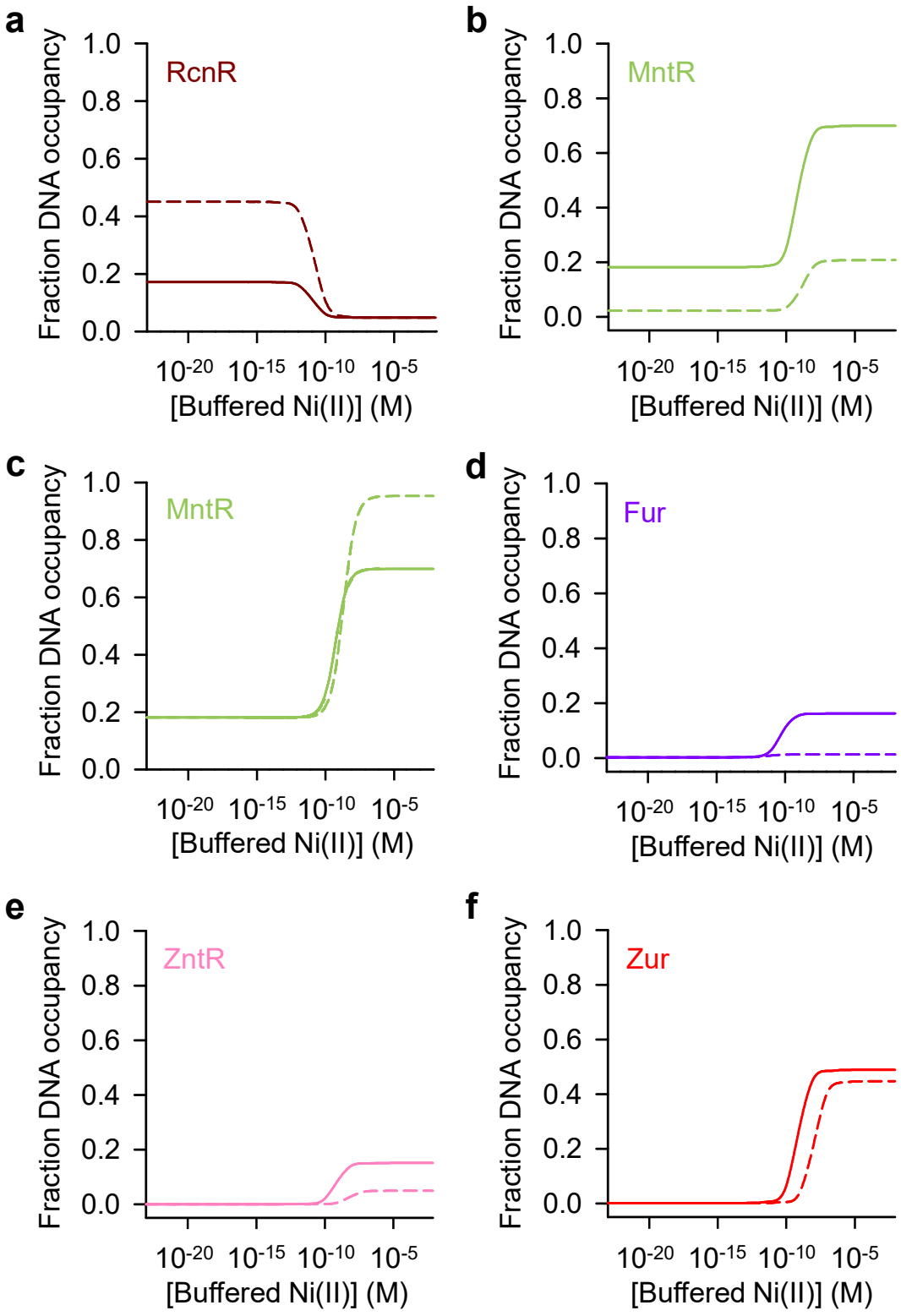

Figure 5.14 Simulations of Ni(II)-dependent fractional DNA occupancies (Model 1) using variation in Ni(II)- or DNA-affinity. (a) RcnR as in Figure 5.7 (solid line) and simulated with a 4-fold tighter K_3 to show the effects of DNA wrapping (dashed line). **(b)** MntR as in Figure 5.7 (solid line) and simulated with 10-fold weaker K_3 and K_4 (dashed line). **(c)** MntR as in Figure 5.7 (solid line) and simulated with affinity values (K_1, K_2, and K_4) adjusted for 2:1 Ni(II)-loaded protein (dashed line). **(d)** Fur as in Figure 5.7 (solid line) and simulated with affinity values adjusted for 1:1 Ni(II)-loaded protein (dashed line). **(e)** ZntR as in Figure 5.7 (solid line) and simulated with affinity values adjusted for 2:1 Ni(II)-loaded protein (dashed line). **(f)** Zur as in Figure 5.7 (solid line) and simulated with affinity values adjusted for 3:1 Ni(II)-loaded protein (dashed line). Concentrations were fixed at P_0 for sensors except RcnR which was allowed to vary between P_0 and P_1.

The K_4 DNA affinities have been determined for MntR, Fur, ZntR, and Zur using different ratios of Ni(II):sensor. Affinities were determined at 1:1 Ni(II):monomer for all sensors, but data for MntR, Fur, and ZntR were also collected at 2:1, and Zur at 3:1 (Table 4.1). Adjusting the K_1 (and K_2) affinity for the correct number of sites loaded allowed the DNA occupancy to be determined for the sensors with the K_4 values for different ratios of Ni(II) loading (Figure 5.14c-f). MntR when loaded with 2:1 Ni(II) demonstrated a tighter K_4 limit than 1:1, meaning the DNA occupancy was much greater (95%) at this ratio (Figure 5.14c). Ni(II) was considered allosterically effective for Fur at the 2:1 ratio and Figure 5.14d indicates that loading 1:1 results in a negligible change in the promoter occupancy due to the weak K_4 affinity, even though K_1 is tighter. ZntR and Zur were both considered allosterically effective at 1:1 Ni(II) and loading ZntR 2:1 shows a lesser fraction of metal-bound sensor on DNA due to the weaker K_4 affinity (Figure 5.14e). Zur demonstrates marginally lower occupancy at 3:1 Ni(II) and requires noticeably higher Ni(II) concentrations before a response appears (Figure 5.14f).

Modelling the DNA occupancy requires a single K_4 value which complicates the simulations for sensors that show cooperativity across multiple binding events per promoter (Fur and CueR). All models for these sensors have used average K_4 values (Section 2.10.4). In addition to the average K_4 value, Figure 5.15 shows the DNA occupancies for Fur and CueR using values that correspond to the K_{4a} or K_{4b} affinities (Table 5.1). Positive cooperativity is evident for both sensors and therefore the K_{4b} model shows the highest DNA occupancy, which is where the absolute occupancy would reach given a high enough concentration of Ni(II)-sensor to overcome the initial weaker DNA-binding. The positive cooperativity would be expected to result in a gradual rise in occupancy from the K_{4a} level to the K_{4b} level as Ni(II) increases, but this scenario cannot be simulated due to the consequential effects upon other thermodynamic values (i.e. K_2). Cooperativity was greatest with Fur suggesting it could occupy a greater proportion of its regulon (~ 30%) in response to Ni(II) than has been initially modelled (Figure 5.15a). The stepwise K_4 values of CueR are similar enough that little change is apparent in fractional DNA occupancy (Figure 5.15b), and this may have no effect at all if the DNA conformation is not altered.

5.3.4 The effect of L-histidine on DNA occupancy by the sensors (Model 2)

As for Ni(II) occupancy (Section 5.2.3), simulations for DNA occupancy can incorporate physiologically relevant buffering molecules (e.g. L-histidine). The fractional occupancy of the total number of target DNA sites for each sensor with differing concentrations of L-histidine has been determined (Figure 5.16). The occupancy ranges (start and end points) for

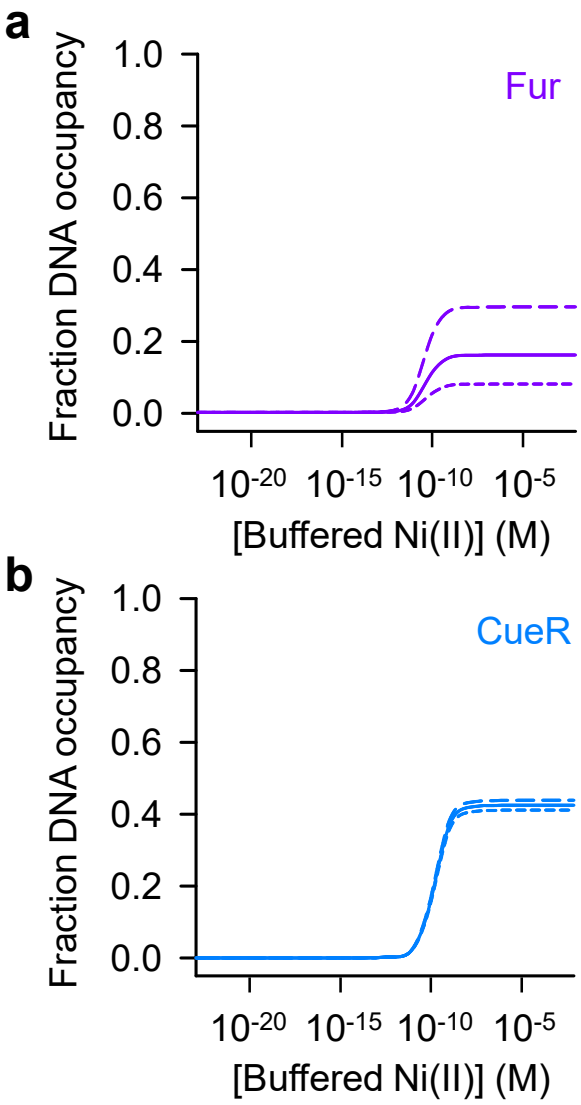

Figure 5.15 Simulation of fractional DNA occupancy (Model 1) for sensors that demonstrate cooperative DNA binding. (a) Fur using average K_4 (solid line), K_{4a} (short-dash line), and K_{4b} (long-dash line). **(b)** CueR using average K_4 (solid line), K_{4a} (short-dash line), and K_{4b} (long-dash line). Concentrations for both sensors were fixed to P_0.

each sensor are the same as those from Model 1 (Section 5.3.2) as expected through using the same K_3 and K_4 values (as well as the same concentrations). The inclusion of L-histidine in the model alters the appearance of the occupancy curves, shifting the responses of the weaker Ni(II)-binding non-cognate sensors (MntR, CueR, ZntR, and Zur) to a higher total Ni(II) concentration. The responses for the tighter Ni(II)-binding sensors (NikR, RcnR, and Fur) are shifted less, if at all, due to L-histidine. This indicates a simple model for a metal-buffered system can have relatively large consequences for maintaining the fidelity of metal-dependent transcriptional responses. Including additional small molecule ligands that could make up the intracellular buffer, along with L-histidine, would increase the buffering capacity, further ensuring the cognate sensor response to even higher Ni(II) levels.

Figure 5.17 shows the same data normalised to the maximum absolute fractional occupancy for each sensor. This reveals the effect of RcnR concentration on DNA occupancy and how hysteresis greatly increases the range of total Ni(II) concentration over which RcnR is responsive. Figure 5.17 also demonstrates more clearly the effect of L-histidine on the weak Ni(II)-binding non-cognate sensors. In the absence of L-histidine (Figure 5.17a), the normalised DNA occupancy by NikR is almost superimposed by that for RcnR (P_0), MntR, CueR, and Zur, with RcnR (P_1), ZntR, and Fur shifted to higher total Ni(II) concentrations. When 60 μM L-histidine is included (Figure 5.17b), the non-cognate sensor responses are shifted to a higher concentration of Ni(II) so that the cognate sensors are distinct in responding first. When NikR has undergone 90% of its total response at 60 μM L-histidine, CueR indicates 25% of its response, Fur 16%, and MntR, ZntR, and Zur < 10%. In contrast to Model 1 (Section 5.3.2), RcnR here becomes responsive during the concentration range in which NikR is also responsive, even at 200 μM L-histidine (Figure 5.17c). Additionally, at this concentration of L-histidine, Fur also begins to respond to Ni(II) reaching almost 20% maximal occupancy before NikR has undergone its full response. The differences for RcnR and Fur are due to the use of different *x*-axes in the graphs (see Section 5.4.1). The population of Ni(II)-CueR on DNA also increases (~ 10% of maximal response), though MntR, ZntR, and Zur remain essentially unresponsive (< 3%). All non-cognate sensors show DNA occupancy before both concentrations of RcnR (P_0 and P_1) have reached maximal de-repression of P_{rcnRA}, as seen in Section 5.3.2.

When comparing the concentration of Ni(II) required for 50% of the maximum occupancy of DNA for RcnR at concentrations of P_0 and P_1, the Ni(II) concentration range converges slightly at 200 μM L-histidine, emulating the result for Ni(II)-binding in Section 5.2.4.

A limitation with this model is that it does not account for change in protein concentration with promoter occupancy, which especially affects the ability to interpret the DNA

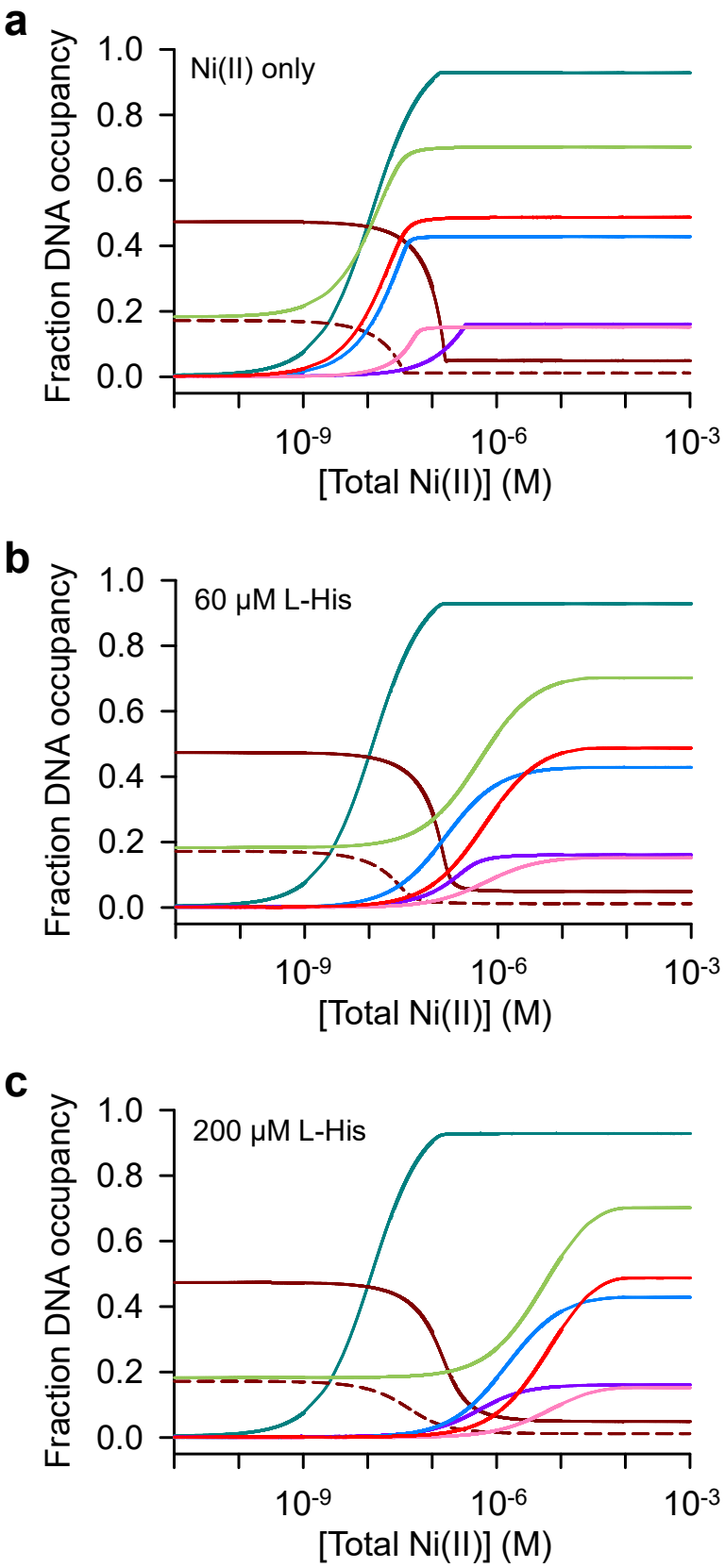

Figure 5.16 Simulation of fractional DNA occupancy for each sensor (Model 2). Simulation of DNA occupancy of sensors determined with Ni(II) titrated to NikR (turquoise), RcnR (maroon), MntR (green), Fur (purple), CueR (blue), ZntR (pink) and Zur (red). **(a)** No L-histidine. **(b)** 60 µM L-histidine. **(c)** 200 µM L-histidine. NikR and RcnR were modelled with P_1 concentrations (P_0 for RcnR indicated by dashed line) whereas MntR, Fur, CueR, ZntR and Zur were all modelled with P_0.

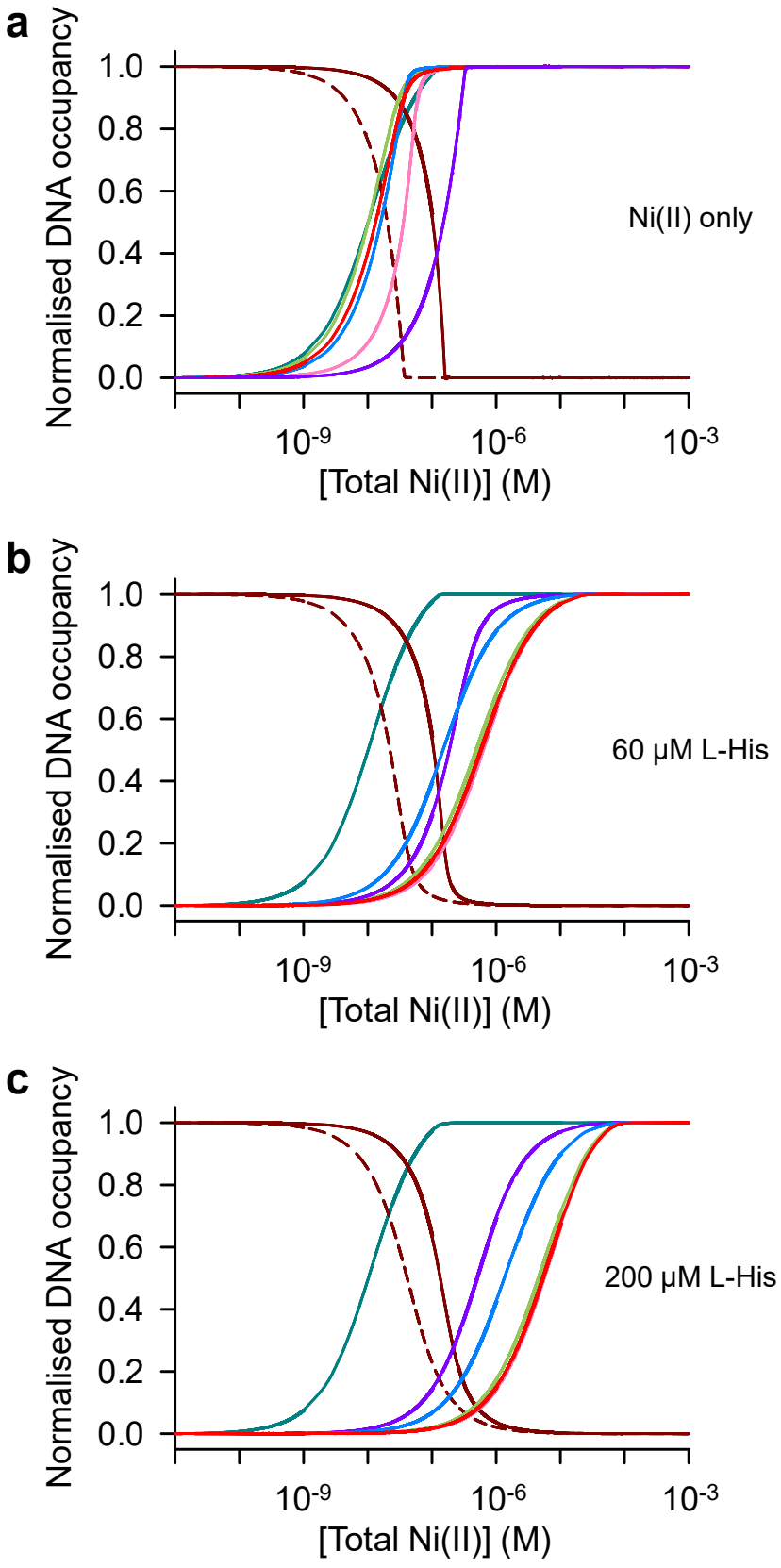

Figure 5.17 Normalised DNA occupancy for each sensor (Model 2). Data normalised using the maximal responses in Figure 5.16 for NikR (turquoise), RcnR (maroon), MntR (green), Fur (purple), CueR (blue), ZntR (pink) and Zur (red). **(a)** No L-histidine. **(b)** 60 µM L-histidine. **(c)** 200 µM L-histidine. NikR and RcnR were modelled with P_1 concentrations (P_0 for RcnR indicated by dashed line) whereas MntR, Fur, CueR, ZntR and Zur were all modelled with P_0.

occupancy by RcnR. P_0 concentrations were fixed for the non-cognate sensors, though allowing the Fur concentration to change between P_0 and P_1 would also have altered the occupancy for DNA as it too demonstrates hysteresis with Fe(II).

5.4 Discussion

5.4.1 Interpreting the simulated data

In the absence of a competing buffer molecule (L-histidine), the fraction of Ni(II) bound to each sensor and correspondingly the occupancy of DNA is favourable to the total concentration of allosteric Ni(II) sites for a protein since the Ni(II) affinities are tighter than the physiological concentrations of the sensors. With the inclusion of L-histidine, the Ni(II) affinities become much more influential and all curves but for NikR, RcnR, and Fur shift to higher Ni(II) concentrations for allosteric site loading and DNA occupancy. The high cellular concentration of Fur means that the protein cannot load the allosteric sites at the same concentrations of Ni(II) as NikR or RcnR and therefore remains with the other non-cognate sensors for Ni(II) loading and DNA occupancy at higher Ni(II) concentrations with L-histidine. It then becomes clear that K_1 provides a good measure for the order of responses by all sensors with 200 μM L-histidine (Figure 5.17). Additionally, K_1 alone provides a good representation for DNA occupancy of non-cognate sensors, though this is not the case for NikR and RcnR (Figure 5.10). The extreme K_1 affinities coupled with an effective allosteric response or a substantial change in protein concentration are possible reasons why K_1 alone does not predict these DNA occupancies. Nevertheless, K_1 could be used to estimate the half-maximal response of a sensor with any metal ion if the other parameters are unknown, though the absolute fractional occupancy of promoter sites would remain unknown.

Two methods have been used to simulate DNA occupancy for the sensors using buffered metal concentrations (Model 1) or total metal concentrations in the presence of a model buffer molecule, L-histidine (Model 2). Both techniques largely demonstrate the same outcomes where the major difference is the ability to model hysteresis. Data from Model 2 simulations at all L-histidine concentrations can be presented with an x-axis as buffered Ni(II) (the concentration of Ni(II) not bound to sensor or L-histidine – as in Model 1 simulations) which indicate occupancy curves with excellent agreement to Model 1 in all cases except RcnR (due to the inability to model hysteresis in Model 2).

The K_1 affinities determined in Chapter 3 demonstrate an obvious disparity between MntR, CueR, ZntR, and Zur compared to NikR and RcnR, with Fur the exception for non-cognate

sensors. This trend persists for DNA occupancy where MntR, ZntR, and Zur are all responsive at similar concentrations of Ni(II), though CueR, which has a tighter K_1, does respond to a slightly lower concentration of Ni(II). The effect of hysteresis with RcnR decreases the obvious distinction between the cognate sensor response and the non-cognate sensor mal-responses.

Both Model 1 and Model 2 predict the next non-cognate sensors poised to respond to Ni(II) after NikR and RcnR would be Fur and CueR. Fur poses the greater mal-responsive threat due to the mode of action of CueR (Section 4.9.2). The Ni(II)-Fur response appears to be initiated at a Ni(II) concentration where RcnR is also responsive and could mean that cells are able to tolerate some level of mis-metalation. The absolute occupancy of total Fur target sites with Ni(II) is much less than with Fe(II) (Figure 5.11c) but, due to the size of the Fur regulon, this occupancy (up to approximately one third of that seen with iron; Section 5.3.2) could still be significant. One possible physiological benefit of a transcriptional response by Ni(II)-Fur could be repression of iron import machinery. The absolute metal specificity for importer proteins cannot be guaranteed and, through reduction of metal membrane transporters, it could be possible to reduce the likelihood of non-specific metal import (see Chapter 6).

Salmonella NikR has two different target sites in the genome (Section 1.3.9) with differing K_4 values (Section 4.2). All above models have considered the two sites with equal affinity, determined for NikR bound to *nixA*, though binding to *nikA* demonstrated a tighter K_4 affinity. The fractional occupancy and normalised occupancy (using Model 1) has been simulated for the two sites using the NikR affinity determined at both promoters (Figure 5.18). This indicates that the 2-fold tighter K_4 (*nikA*) does alter the DNA occupancy by NikR, such that the set-point at which the protein responds changed from 1.04×10^{-14} M buffered Ni(II) to 4.64×10^{-15} M, a change of approximately 2-fold.

5.4.2 Cellular implications and applications

Each NikR tetramer contains four high-affinity Ni(II)-binding sites and two low-affinity Ni(II)-binding sites when bound to DNA (Section 1.3.9). Only the high-affinity sites have been considered so far in this study, however, studies showed that occupancy of the low-affinity site increased DNA affinity *in vitro* (from nanomolar to picomolar) (Chivers and Sauer, 2000, Bloom and Zamble, 2004). The physiological relevance of the low-affinity site has been questioned (Chivers and Sauer, 2002) and the most recent estimate for the Ni(II) affinity is $2.90 \pm 0.3 \times 10^{-8}$ M (Bloom and Zamble, 2004), a value five orders of magnitude weaker than that for the high-affinity site (Section 3.2.2). Ni(II) metalation of this site was

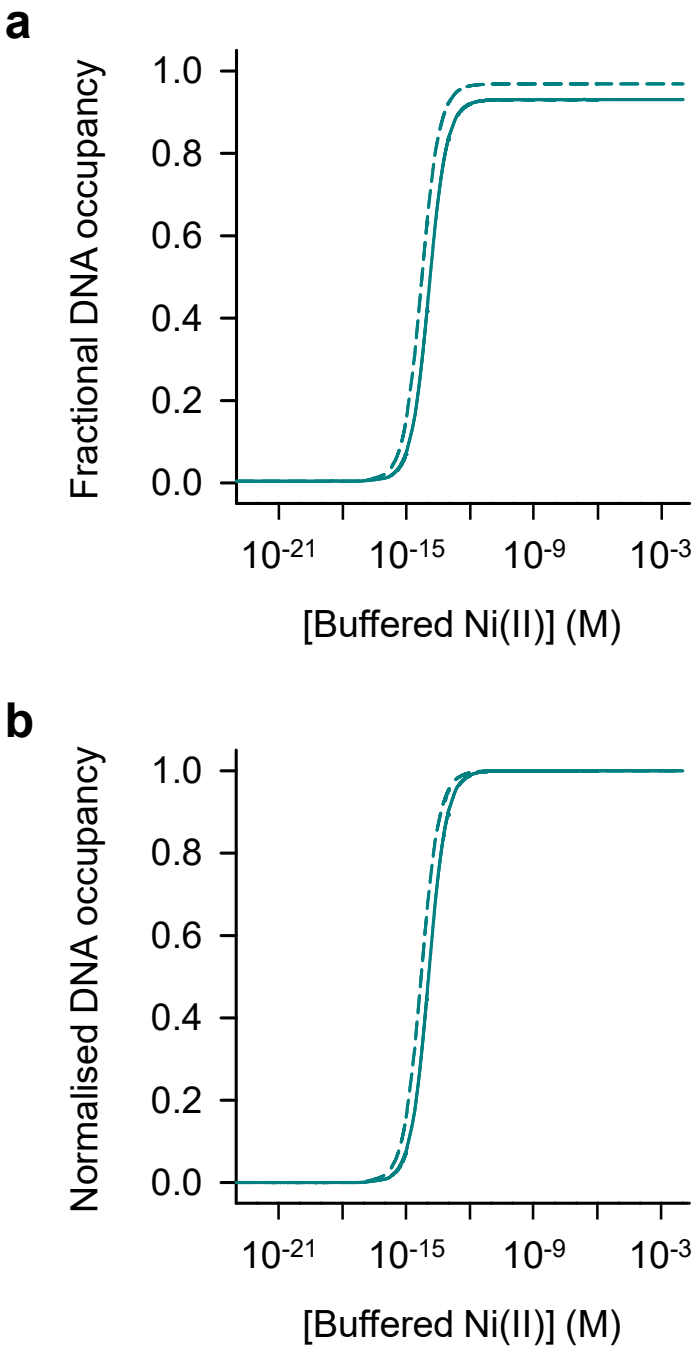

Figure 5.18 Simulation of NikR DNA occupancy for *nixA* versus *nikA* (Model 1). Simulations used K_4 values to calculate fractional occupancy for *nixA* (solid line) and *nikA* (dashed line). **(a)** Fractional DNA occupancy, **(b)** Normalised DNA occupancy.

simulated using the same model from Section 5.2.3 where the stepwise affinity for the low-affinity site was taken as 1.45×10^{-8} M (half the affinity described above for the total sites) and the concentration of the protein was fixed at 3.32×10^{-9} M, which is equivalent to the concentration of DNA target sites in the *Salmonella* cell (since the low-affinity site is only effective when the protein is bound to DNA). The fraction of Ni(II) bound to this site can be compared to the fraction of Ni(II) bound to the allosteric sites of the other sensors, in the presence of changing L-histidine concentrations (Figure 5.19). The low number of these sites means that loading initiates at lower total Ni(II) concentrations than the other sensors (Figure 5.19a). However, L-histidine effectively outcompetes the low-affinity site so that little Ni(II) is bound even at micromolar concentrations, where the non-cognate sensors demonstrate binding (Figure 5.19b-c). This suggests that although there appears to be an interesting link between loading this second Ni(II) binding site in NikR with an increase in DNA affinity, the inability for this site to be metalated under physiological conditions implies that it has no cellular function, unless additional cellular molecules stabilise this structure (Chivers and Sauer, 2002).

The models can be used to interrogate additional data from the literature, such as the previously reported Ni(II) affinity (K_1) of *E. coli* RcnR. The reported value was shown to be much weaker (four orders of magnitude) than the affinity determined in Chapter 3 (Section 3.3.2). Including this value in the determination of DNA occupancy by RcnR under physiological conditions with L-histidine (Model 2) is shown in Figure 5.20. This figure indicates that RcnR with the reported Ni(II) affinity is unable to compete with physiological concentrations of L-histidine where even the weaker Ni(II)-binding non-cognate sensors demonstrate a response before this version of the protein. The simulation therefore provides additional evidence that the reported value cannot be physiologically correct and is likely a consequence of the less rigorous experimental conditions (Section 3.3.3).

In principle, this model could be used to predict the ability of non-*Salmonella* Ni(II)-responsive sensors to function in this cytosol. These include NmtR, KmtR, Nur, and InrS. This would require having Ni(II) and DNA affinity parameters determined under the same conditions as used here. *Synechocystis* InrS parameters have been collected under similar buffer conditions to here (pH 7.0 rather than 7.5) (Foster et al., 2017). Therefore, the DNA occupancy of this sensor was simulated in the presence of 200 μM L-histidine and compared to the *Salmonella* sensors (Figure 5.21). InrS demonstrates a high fractional occupancy of DNA at low Ni(II) and drops to a lower occupancy at high Ni(II) (Figure 5.21a), consistent with its mode of action as a de-repressor (Foster et al., 2012). When considering the normalised occupancies of all the sensors, 50% DNA occupancy of InrS occurs at the same

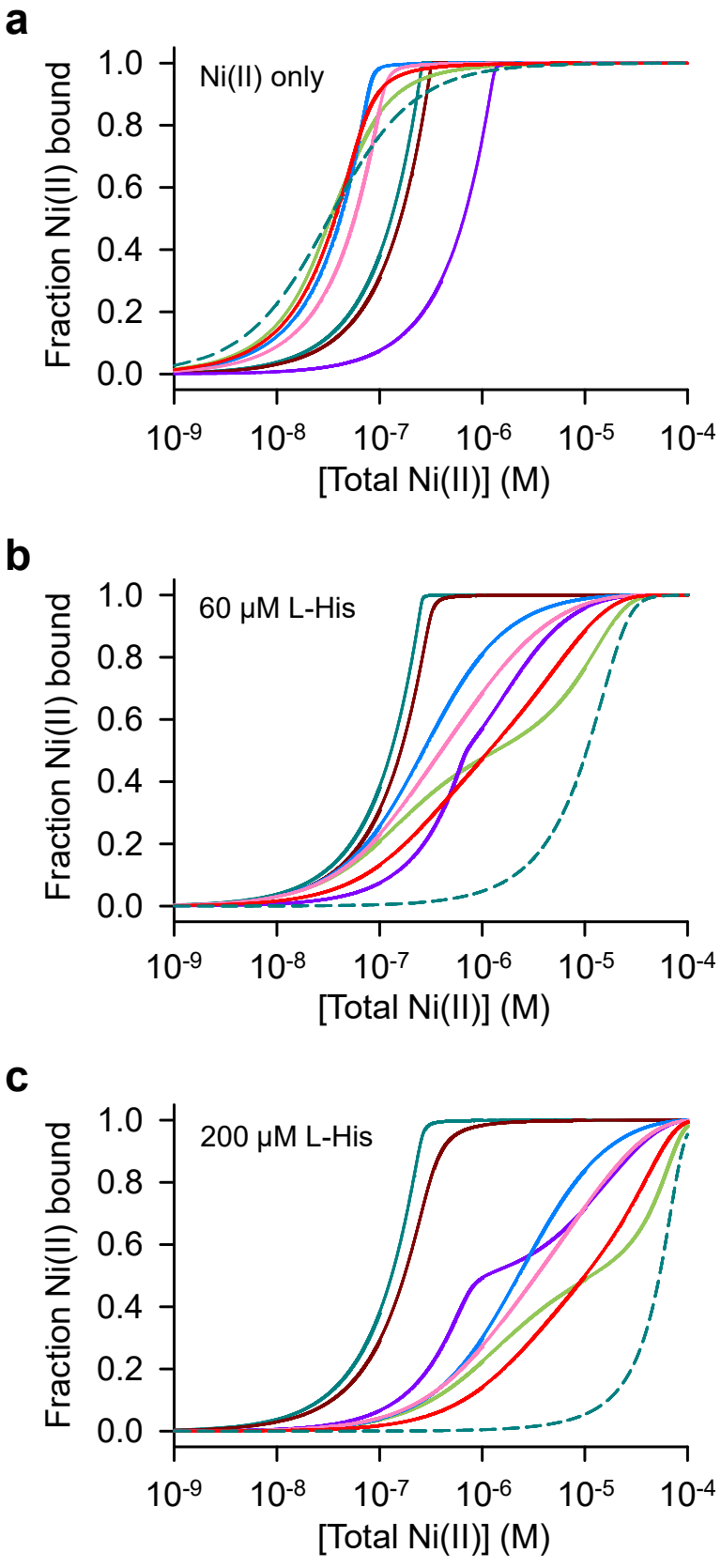

Figure 5.19 Simulation of fraction Ni(II) bound to low-affinity binding site (*Ec*NikR). Ni(II) occupancy simulated as in Figure 5.2 for allosterically effective sites of NikR (turquoise), RcnR (maroon), MntR (green), Fur (purple), CueR (blue), ZntR (pink), Zur (red), with addition of the NikR low-affinity site (dashed line). **(a)** No L-histidine. **(b)** 60 µM L-histidine. **(c)** 200 µM L-histidine. NikR and RcnR were modelled with P_1 concentrations (except the low-affinity site which was fixed at 3.32 nM – see text) whereas MntR, Fur, CueR, ZntR, and Zur were all modelled with P_0.

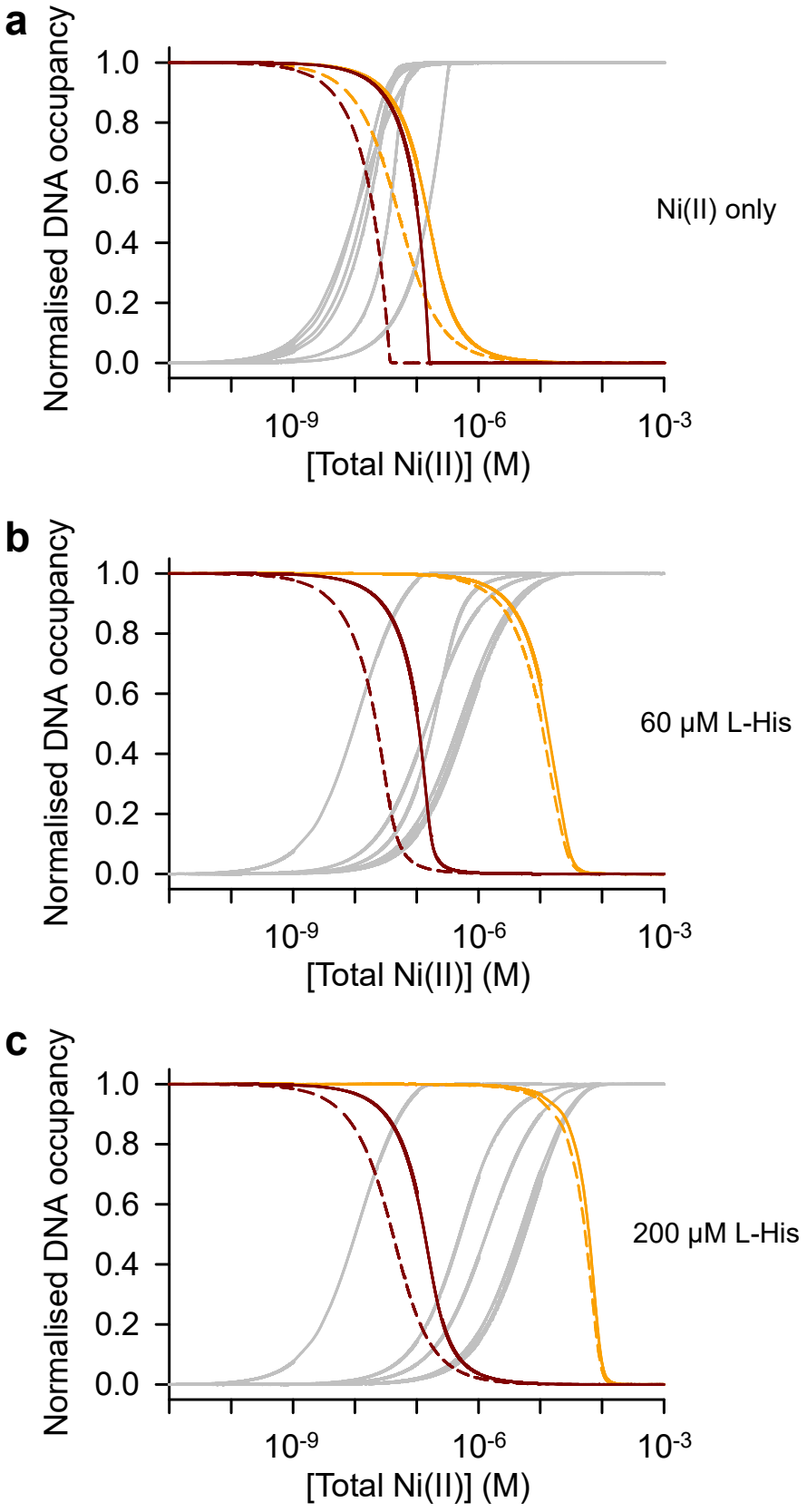

Figure 5.20 Comparison of normalised DNA occupancy for RcnR with published K_1 value (Model 2). DNA occupancy was simulated using K_1 determined in this work for *Sty*RcnR (maroon) with the published value for *Ec*RcnR (orange). RcnR simulations are shown for P_0 (dashed line) and P_1 (solid line). Other sensors (grey) shown for comparison, as in Figure 5.17. **(a)** No L-histidine. **(b)** 60 µM L-histidine. **(c)** 200 µM L-histidine.

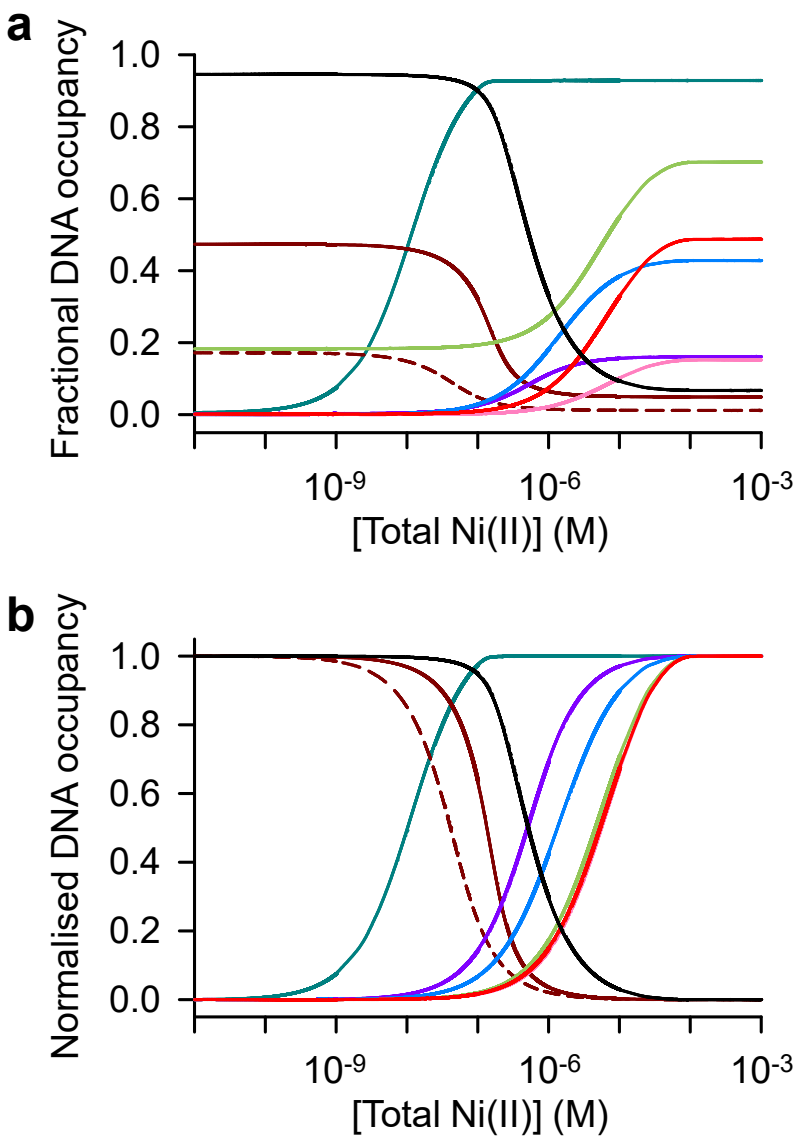

Figure 5.21 Comparison of DNA occupancy for *Synechocystis* InrS with *Salmonella* sensors (Model 2). DNA occupancy was simulated in the presence of 200 μM L-histidine for *Salmonella* sensors – NikR (turquoise), RcnR (maroon), MntR (green), Fur (purple), CueR (blue), ZntR (pink), Zur (red) – as in Figure 5.16c and Figure 5.17c, along with InrS using published parameters (black). **(a)** Fractional DNA occupancy. **(b)** Normalised DNA occupancy.

concentration of Ni(II) as for 50% DNA occupancy of Fur (Figure 5.21b), suggesting InrS would struggle to sense Ni(II) in the buffer since its set-point is shifted to a higher Ni(II) concentration than with the cognate sensors (NikR and RcnR). A possible reason for this shift maybe the pH-dependence of K_1, as observed for NikR (Section 3.9.1), weaker at pH 7.0 than 7.5. Additionally, the abundance of InrS has not been determined so the assumed abundance of 100 tetramers per cell was used in simulations (Foster et al., 2017). As is evident with RcnR, protein abundance impacts on the set-point for sensors, therefore, if InrS were present at a lower concentration it could be better tuned to the *Salmonella* buffered Ni(II) range. Tuning and verifying InrS copy number in a heterologous cell would be a significant challenge to experimentally test this prediction.

Chapter 6: General conclusions & future directions

6.1.1 Conclusions and discussion

Transition metals are essential to life due to their unique chemistry but also pose a toxic risk inside the cell. Organisms, including bacteria, have developed specialised metal-sensing transcriptional regulators which control the intracellular concentration of these metals in order to allow for the correct metalation of appropriate proteins and enzymes while reducing any toxic consequences (Giedroc and Arunkumar, 2007, Reyes-Caballero et al., 2011). Free (hydrated) metal ions can be toxic to cells due to Fenton reaction chemistry where free radical products cause extensive damage to a cell (Meneghini, 1997, Valko et al., 2005). Additionally these free metals could also bind to a range of cellular proteins and enzymes where allosteric inhibition or inactivation would disrupt the normal functioning of a cell (Macomber and Hausinger, 2011). Metals are usually buffered to concentrations much lower than that which would equate to a single free ion ($< 2 \times 10^{-9}$ M) and therefore a spike in extracellular metal concentration would be required to achieve intracellular concentrations to rise enough to reach the concentration equal to a free metal ion before an attempt to inhibit the increased level of metal has become effective by the sensors (Osman et al., 2017).

The possibility that metals still pose a toxic risk before free metal becomes available is a more intriguing prospect. The intracellular, polydisperse buffer is made up of a vast collection of small molecules (such as amino acids and glutathione) and organic acids which can coordinate transition metals based on the Irving-Williams series (Foster et al., 2014a). Recent studies suggest that the intracellular concentration of each metal is determined by this buffer for which metallosensors have evolved to detect changes in the capacity of the buffer to prevent saturation and limit depletion of the buffered metals (Foster et al., 2017, Osman et al., 2017, Osman et al., 2018). Rather than altering the concentration of metal within the cell, a weaker nickel binding mutant of the sensor InrS is unable to compete for this metal in the cytosolic buffer (Foster et al., 2017). The concentration to which a metal is buffered in the cell is predicted to be held in a tight range by the cognate metal sensor(s) (Osman et al., 2017). The Co(II) sensor RcnR responds to increased external concentrations of this metal, where the Zn(II) sensors Zur and ZntR do not display a response *in vivo* (Osman et al., 2017). However, if the Co(II) is added as a high concentration shock, initial transcriptional responses indicated that Zur and ZntR do respond to this metal, and the same

applies for RcnR responding to a Zn(II) shock, where the non-cognate sensors in each case have an estimated response that equates to an order of magnitude difference in buffered metal (Osman et al., 2017). These results suggest that while the buffered concentrations of metals are usually maintained in a tight range, if the metal transiently exceeds this range, other non-cognate sensors are capable of responding at marginally higher buffered concentrations, eliciting a mal-response.

This study determined the thermodynamic affinity constants with respect to Ni(II) for the set of *Salmonella* metallosensors to understand the cellular mechanisms for correct metal loading and possible consequences for mis-metalation. This is the first study in which a full set of metallosensors has been investigated for the response to a single metal, where previous work has considered mis-metalation for a select number of sensors only (Osman et al., 2017).

Through determining the Ni(II) affinities (K_1) of the sensors (Chapter 3), the affinity of RcnR was found to be three orders of magnitude tighter than the reported value (Iwig et al., 2008), likely a result of using fully anaerobic conditions to ensure reduction of the cysteine residue within the protein. This new evidence demonstrates the RcnR affinity is much closer to that of NikR, although still 16-fold weaker. This makes the coordinated regulation of Ni(II)-import and export similar to that of Zn(II) by the two sensors Zur and ZntR, which have different Zn(II) affinities in order to coordinate a metal response in series (Outten and O'Halloran, 2001, Osman et al., 2017). Simulations in Chapter 5 show that this indeed appears to be the case, where NikR reaches almost complete occupancy of DNA before RcnR begins to respond to the metal. This model predicts previous *in vivo* data collected for these proteins (Iwig et al., 2006) and demonstrates that export machinery is manufactured only when ceasing importer synthesis fails to resolve the issue of increased intracellular metal concentrations. It demonstrates the most efficient energetic model for a cell in order to limit the expression of complex operons until conditions are such that this must be enforced to allow survival.

Ni(II) binding affinities were also determined for the five non-cognate sensors of which three (MntR, ZntR, and Zur) demonstrated negative cooperativity when loading the first two metals to the oligomeric structure. This suggests that a non-cognate metal does not favourably load into proteins that have evolved to sense a different metal. It is likely that conformational changes associated with initial non-cognate metal binding generate weaker equivalent metal binding sites within the oligomer, with some crystal structures of non-cognate metal-bound sensors demonstrating altered coordination geometries at equivalent sites (Section 1.3.7). Consequently, non-cognate metal loading to metallosensors may be deterred by negative cooperativity since an increase in the concentration of buffered metal

would be required to fill the appropriate allosteric sites for a mal-response, allowing the cognate sensors further opportunity to actuate a more effective response. In order to test this prediction, the set of sensors would require analysis of their stepwise affinity constants for additional metals (e.g. Mn(II), Fe(II), Co(II), Cu(I), or Zn(II)). One consideration is the metal-specific flexibility of coordination geometries, for example, Ni(II) and Zn(II) are capable of forming four- or six-coordinate geometries, whereas Cu(I) typically favours two- or three-coordinate geometries, much lower than is favoured by other ions.

The first Ni(II) binding event was tight for the non-cognate sensors, indicating high picomolar values (with the exception of Fur). Although these affinities would ordinarily be considered tight, the cognate sensors (NikR and RcnR) have affinities in the high femtomolar to low picomolar range, therefore, the non-cognate values are between two- and four-orders of magnitude weaker. Fur was an exception since not only did this protein have the tightest initial Ni(II) affinity for the non-cognate sensors, it also demonstrated positive cooperativity for binding a second Ni(II) so that it had a comparable affinity to RcnR (Chapter 3). This therefore raised the possibility that Fur could be a candidate for mis-metalation where all the other non-cognate sensors appear limited by their Ni(II) affinities, held to a threshold value of 1×10^{-10} M.

The observation of a Ni(II) affinity threshold was unexpected since each non-cognate sensor has unique, albeit similar, metal binding regions within their protein structures. Therefore, it was assumed the affinity of a non-cognate metal would vary to a larger extent depending on whether a metal site was fortuitously favourable for binding Ni(II). Nevertheless, further experimentation would be required to uncover the reason behind this threshold and to determine whether a threshold, not necessarily at the same value, is apparent for non-cognate sensors with respect to other metals (e.g. Co(II)). One possibility is that since most metal binding sites contain similar residues, the intrinsic metal binding capabilities of these sites result in a basal Ni(II) affinity (abiding by the Irving-Williams series; Section 1.1.1) compared to sites which have evolved to incorporate this metal. A more intriguing possibility would be that this threshold has evolved for non-cognate sensors around the set-point of Ni(II)-sensors under normal conditions, preventing sensing of the wrong metals. It could be possible to gain insight into this by studying the Ni(II) affinities of metallosensors in an organism (e.g. *B. subtilis*) which does not contain a Ni(II)-specific sensor but contains homologous non-cognate sensors (MntR, Fur, and Zur) (Moore and Helmann, 2005). In the absence of a Ni(II) sensor, the same experiments would reveal a lack of an obvious threshold, a Ni(II) affinity threshold clustering around 1×10^{-10} M (as seen here), or possibly a different threshold value, maybe determined by the buffering capacity of the organism.

Mal-responsive transcriptional activity is only achievable if mis-metalation causes a change in DNA-binding affinity (or structural conformation, as for MerR regulators). One equivalent of Ni(II) elicited an allosteric response in the non-cognate co-repressor proteins, MntR, Fur, and Zur, however, the Fur response was shown to be much smaller than can be achieved with its cognate metal (Chapter 5), where this protein requires additional metal loading beyond its tightest Ni(II) sites (two equivalents) to observe a noticeable change in affinity. In this regard, the Fur protein abides by the threshold K_1 affinity of 1×10^{-10} M since the Ni(II) sites required for a more effective allosteric response possess an affinity weaker than this value (Chapter 3). MntR and Zur have a coupling free energy not too dissimilar from their cognate metals, therefore, they are simulated to show considerable occupancy of their promoter targets. Even the most effective allosteric conformation of Ni(II)-Fur does not equate to a substantial occupancy of the total number of targets within the Fur regulon. This suggests that while Fur has the affinity to compete for Ni(II), this metal does not potentiate allostery effectively. On the other hand, MntR and Zur are more favourably allosterically activated by Ni(II), though their affinities for this metal appear too weak to bind Ni(II) under non-toxic conditions.

The Fur regulon is extensive and although Ni(II)-Fur was only simulated to occupy a small portion of the total sites, this still equates to an estimated 10 genes which could be affected, based on the number of target sites published for Fur (Osman et al., 2018). Moreover, if site-specific Ni(II)-Fur affinity (K_4) increased compared to *fur-box* alone, the number of Fur-occupied promoters could be greater still. The consequential mal-responses could increase the energetic demand for the cell under conditions where the gene products are not useful and potentially deleterious for survival. This demonstrates a possible mechanism by which metals could be used as a bacteriocide to inhibit the growth of these organisms, where the first occurrences of metals being used in this way propagated the use of the term “nutritional immunity” (Weinberg, 1975). It was discovered that host organisms withhold certain metals (e.g. iron) from invading pathogens, and even intoxicate with other metals (e.g. copper/zinc), to disrupt the normal homeostatic mechanisms within the organism (Djoko et al., 2015). Alternatively, the mal-response could have some evolutionary benefit for the organism. Some importer systems may confer reduced specificity for metal ions, such as the magnesium channel CorA which has been shown to transport Ni(II) (and other metals) non-specifically (Hmiel et al., 1986, Snavely et al., 1991). It could be possible that some iron transporters (e.g. the anaerobically active FeoAB system (Kammler et al., 1993)) have reduced specificity, increasing the potential for Ni(II) to be transported instead. Therefore,

if Ni(II)-Fur were to reduce the synthesis of iron transporters, a potential benefit, used loosely, would be a decrease in the non-specific transport of surplus Ni(II) into the cytosol.

Three factors have been revealed for determining the specificity of a metallosensor; affinity, allostery, and access (Waldron et al., 2009, Foster et al., 2014a). While Fur has a high affinity for Ni(II) (Chapter 3), and would appear able to access the metal from a cytosolic buffer (Chapter 5), its pitfall for demonstrating specificity to Ni(II) resides in the proteins allosteric response, whereby the coupling free energy is much less than with NikR and for its cognate metal (Fe(II)) (Chapter 4). Thus, allostery might prevent the sensor from effectively causing a transcriptional mal-response *in vivo*, but there still may be toxic consequences as a result of non-cognate metal binding to the protein, for example, reducing the population of free-to-sense Fur dimers. Therefore, while these three factors can describe the correct sensor for a metal, as has been done for discriminating the Zn(II) sensor ZiaR from the equally tight Zn(II)-binding non-cognate sensor InrS (Foster et al., 2014b), it does not account for the negative impact that metal-binding alone would present when non-cognate sensors demonstrate two of the three specificity factors (affinity and access).

The simulated DNA occupancy data for activator proteins (CueR and ZntR) was less straightforward to analyse due to the alternative mechanism for gene synthesis. While promoter occupancy alone (regardless of the bound metal) is considered the important measure for co-repressor and de-repressor proteins, the unique mechanism by which cognate metal binding to CueR/ZntR results in distortion of DNA to facilitate RNA polymerase association means that predictions based on non-cognate binding have additional complexity (Philips et al., 2015, Osman et al., 2018). Simulations do suggest that CueR could be at risk of mis-metalation and a mal-response due to its affinity (the next tightest for non-cognate sensors after Fur) and relatively low cellular sensor concentration (Chapter 5). CueR detects metal ions in the +1 oxidation state and does not show a transcriptional response to +2 metals, such as Ni(II) or Zn(II) (Stoyanov et al., 2001, Changela et al., 2003). However, it may be possible to observe a response with short-term (~ 10 min) shock experiments (Osman et al., 2017) since previously the *copA* promoter response was monitored after two hours, potentially allowing cellular buffer adaptations to limit Ni(II) binding to CueR (Stoyanov et al., 2001). Co(II) shock causes a response by ZntR (Osman et al., 2017) which could suggest activator proteins are susceptible to a mal-response through non-cognate metal binding, however, ZntR may be more inclined to respond to a divalent metal since its cognate metal has an oxidation state of +2, unlike CueR. Nevertheless, the consequence of mis-metalation for CueR may be expanded beyond mal-responsive gene synthesis. If Ni(II) were able to populate a substantial portion of total cellular CueR then it could inhibit the normal

functioning of this protein. Additionally, the intracellular mechanism by which MerR regulator proteins behave has been studied to suggest that both the apo and holo forms of these proteins are competing for target sites, where binding and unbinding kinetics are important and are dependent on the condensed state of the chromosome and the effects of protein assisted dissociation or direct substitution from DNA (Joshi et al., 2012, Chen et al., 2015). This study predicts that MerR regulators are not simply bound to DNA where they sense the metal and alter the conformation of their DNA bound state. Instead, the much greater portion of non-DNA-bound sensors detect the buffered metal and then compete for the target sites (Chen et al., 2015). Ni(II) could disrupt this thermodynamic process for the cognate metal by acting as a competitive inhibitor with off-DNA protein. Furthermore, the DNA affinity of Ni(II)-CueR was tighter than that reported for Cu(I)-CueR and apo-CueR (Osman et al., 2018) which could suggest this conformation would have increased residency on the DNA target site, where removal by chromosome structure or protein-mediated dissociation could prove more challenging than with cognate-metal-protein complexes.

The role of affinity and allostery are easily interrogated through measurement of thermodynamic parameters (Chapters 3 and 4). Access to metal must also be considered when questioning the ability of a sensor to respond to a metal in the cell. The idea of an intracellular metal-binding polydisperse buffer is not new with increasing evidence demonstrating its presence and importance for normal cellular function (Waldron et al., 2009, Foster et al., 2014a, Ma et al., 2014, Foster et al., 2017, Osman et al., 2017). This buffer is capable of coordinating transition metals to ensure the absence of free ions, with helpful monitoring by appropriate sensor proteins (Outten and O'Halloran, 2001, Foster et al., 2017, Osman et al., 2017). A sensor must access the metal by associative ligand exchange with the buffer which is necessary on a physiological time scale (seconds to minutes), implying kinetics of loading would have a role in this system, and could also be important for unloading sensors in response to metal depletion (Waldron et al., 2009, Foster et al., 2014a, Foster et al., 2017, Osman et al., 2017). Preliminary experiments (data not shown) using manual mixing of Ni(II) with individual sensors monitored by UV/visible or fluorescence spectroscopy showed rapid loading of each sensor when Ni(II) was added directly, as might occur during an acute Ni(II) stress. The exception was Zur which was only partially loaded with rapid kinetics. MntR was not tested due to the lack of a direct spectroscopic probe. The addition of L-histidine slowed loading to the non-cognate sensors but had less effect on Fur and RcnR. These initial experiments suggested that only Fur is at risk of mis-metalation on rapid timescales in the presence of L-histidine, more likely if Ni(II) stress is sustained. This kinetics data, along with the thermodynamic simulations (Chapter

5), provide further evidence that the polydisperse buffer is a critical component for ensuring the fidelity of metal-specific transcriptional responses.

The use of L-histidine as a model physiological buffer (Chapter 5) motivated preliminary experiments using FA to determine the effects of L-histidine on K_4 for Ni(II)-loaded *Salmonella* sensors (except Zur, due to the time required to reach equilibrium with Ni(II)). As predicted, initial results (data not shown) indicated that non-cognate sensors showed decreased DNA affinity in the presence of L-histidine. However, unexpected, albeit small, effects were observed on K_4 for both NikR and RcnR. Based on the initial experiments, several factors must be considered when carrying out further experiments. First, the equilibration time used was the same as without L-histidine (Section 2.9.3). If L-histidine slows loading/unloading of Ni(II) from individual sensors (discussed above), then the equilibration time will need to be lengthened. More importantly, the experimental design may need to be altered, for example, carrying out FA using constant Ni(II) (i.e. a fixed Ni(II):L-histidine ratio), rather than titrating in Ni(II)-sensor. Again, equilibration time will be important. Simulated outcomes using different models will be useful in optimising experimental design. Finally, the experiment will need to control for the possibility that L-histidine can form stable complexes with one or more of the components at equilibrium, which would affect the interpretation of the data.

More complex buffer systems, as explored by the Robinson group previously (Foster et al., 2017), may be required to determine the critical components of metal buffering for different metals, but also to investigate how successful these buffers are at preventing mis-metalation. For example, the inclusion of other known metal buffering molecules (such as glutathione) could influence the effect of the buffer *in vitro*, or removing the presence of chloride and replacing with glutamate, which is the major anionic component of the cell (Bennett et al., 2009). Additionally, the components of the buffer can be increased when considering metallochaperones involved in metal loading pathways. Ni(II) is required in anaerobically growing *Salmonella* in order to synthesise [NiFe]-hydrogenase enzymes (Mulrooney and Hausinger, 2003, Rowe et al., 2005) where the key chaperones include HypA, HypB, and SlyD (Lutz et al., 1991, Zhang et al., 2005, Leach et al., 2007). These molecules could effectively increase the capacity of the buffer by acting as competitors and alter how the sensors respond. Interestingly, because of this pathway, the possibility of increased intracellular Ni(II) concentrations arise when cells in the stationary phase move to the lag phase of growth which typically coincides with the transfer from anaerobic growth to aerobic growth (Rolfe et al., 2012). Therefore, the need for Ni(II) and Ni(II)-containing enzymes (hydrogenase) is lost and it is assumed these proteins are degraded, releasing the bound

Ni(II) into the intracellular buffer (consistent with the observation of increased *rcnA* expression (Rolfe et al., 2012)). It was also shown that Fe(II) concentrations increased in the lag phase, which suggests the cell was preventing accumulation of both Ni(II) and Fe(II) simultaneously, possibly due to the interference of Ni(II) with Fe(II) homeostasis (Wang et al., 2011, Rolfe et al., 2012). Nevertheless, Ni(II) could exceed the capacity of the buffer under these conditions so that mis-metalation could occur eliciting mal-responses, most likely by Fur and potentially CueR based on the data collected in Chapter 5, and other potentially toxic consequences. Moreover, RNA sequencing data for *E. coli* exposed to excess Ni(II) in the exponential phase indicated iron import was downregulated and iron export was upregulated (Gault et al., 2016). *In vivo* studies demonstrated this response to Ni(II) was Fur-dependent and that cellular Fe(II) concentrations did not significantly change, suggesting Ni(II) could cause the mal-response of Fur, although the cells did not appear to accumulate Ni(II) after the exposure times tested (≥ 10 min) (Gault et al., 2016, Washington-Hughes et al., 2018).

While mis-metalation of metallosensors has been the focus of this work, there are studies of Ni(II) mis-metalation of other targets. A critical *E. coli* enzyme (FbaA) which reversibly converts fructose-1,6-bisphosphate to dihydroxyacetone phosphate and glyceraldehyde-3-phospohate within the glycolytic pathway is a primary target for Ni(II) mis-metalation and results in toxicity for cells grown with glucose as a carbon source (Section 1.4.2) (Marsh and Lebherz, 1992, Macomber et al., 2011). FbaA requires zinc for catalytic function in glycolysis but a second, non-catalytic, Zn(II) binding site appears to be the target for Ni(II) binding which results in allosteric inhibition of the enzyme (Macomber et al., 2011). Determining the Ni(II) affinity for this metal site of purified FbaA, along with determining the cellular FbaA level, would enable comparison of the free energy for Ni(II) binding with the set of sensors. It would also be possible to predict the Ni(II) occupancy of this enzyme at differing buffered concentration of Ni(II) so that intracellular conditions can be assumed based on the activity of FbaA.

6.1.2 Applications of the discoveries

In the search for a replacement of unsustainable fuels, biohydrogen (generated from Ni-containing enzymes) currently demonstrates huge potential owing to its sustainability and cleanliness in production (Maeda et al., 2008, Maeda et al., 2012, Ganesh et al., 2012, Gutekunst et al., 2018). Hydrogen is the most abundant element in the universe (Maeda et al., 2012), however, generating and storing H_2 has not proved an easy task. Hydrogen can be produced from molecules such as glycerol in thermal and electrolytic processes which

require a considerable amount of heat and energy (Vardar-Schara et al., 2008, Valliyappan et al., 2008, Ganesh et al., 2012). Current methods have been developed to utilise hydrogenase enzymes from bacteria which have evolved to grow anaerobically (and in some cases aerobically (Vargas et al., 2011)), fermenting compounds such as glucose, formate, and glycerol, producing hydrogen as a by-product (Maeda et al., 2012, Ganesh et al., 2012). Using microorganisms in the production of hydrogen (and other biofuels, e.g. ethanol) represents a much more energy efficient system (Maeda et al., 2008, Maeda et al., 2012, Gutekunst et al., 2018). The majority of hydrogenase enzymes which produce hydrogen are active under anaerobic conditions, therefore, producing this biofuel using whole-cell systems would appear most convenient, though research has investigated its production in cell-free systems too (Maeda et al., 2012). The pathways resulting in optimal hydrogen production have been engineered so that other enzymes and proteins which reduce or increase H_2 evolution efficiency have been repressed or overexpressed appropriately so that close to the maximum theoretical yield can be achieved in some cases (Ganesh et al., 2012). Hydrogenase 3 contains a NiFe core metal-site (Section 1.4.1) and is the main target for hydrogen production in engineered *E. coli* (Maeda et al., 2008, Maeda et al., 2012). One possible limitation for the modified bacteria is in the nickel supply and storage to ensure expressed hydrogenase enzymes can access Ni(II). The importance of nickel supplementation has been demonstrated (Daday et al., 1985, Axelsson and Lindblad, 2002, Ureta et al., 2005, Vargas et al., 2011), though simply increasing the available concentrations of Ni(II) may not necessarily overcome the limit since the bacteria will be fighting against the intracellular accumulation of toxic concentrations of this metal (Daday et al., 1985). Therefore, understanding the mechanisms for which Ni(II) is required in the cell, as well as the events leading to toxicity, means that further modification of cellular sensors can reduce the impact of mis-metalation while still allowing normal cellular functions to proceed and preventing the disruption of Ni(II) acquisition by the hydrogenase pathways, as well as overall growth of the culture.

Nutritional immunity (as described in Section 6.1.1) could revolutionise current antibiotic techniques in the fight against drug-resistant bacteria. Through understanding the set-points for mis-metalation and mal-responses by non-cognate sensors in a given cytosol, it may be possible to personalise metal-combination therapies to inhibit growth of certain bacteria. This could involve exposing the bacteria to high concentrations of a given sensor's cognate metal in conjunction with a non-cognate metal for which the sensor demonstrates susceptibility to mis-metalation, thereby overwhelming the internal homeostasis of metal concentrations by attacking the buffering mechanism of the cell which would usually prevent

accumulation of toxic metals. For example, since Fur appears to be the non-cognate sensor most susceptible to mis-metalation by Ni(II) in *Salmonella*, treating this bacteria with a combination of high Ni(II) and Fe(II) (the cognate metal of Fur) could disrupt metal homeostasis leading to toxicity. Alternative therapies could also prove effective, such as under-over-exposure of metals, whereby limiting exposure of one metal in combination with overexposure of another could disrupt metal homeostasis. For example, since Ni(II) mis-metalation of Fur could activate genes associated with decreased import and increased export of Fe(II), a combination of high Ni(II) and low Fe(II) could exacerbate the lack of Fe(II) through Ni(II) mimicking the presence of this essential metal. Further studies looking at the set-points of a full set of cytosolic sensors for other metals could indicate additional metal-combination therapies (e.g. Co(II) and Zn(II) (Osman et al., 2017)), which could differ depending on the organism-specific buffer to which the sensors are attuned.

Chapter 7: Appendices

7.1 Appendix 1

Determining the Ni(II) affinity of mag-fura-2

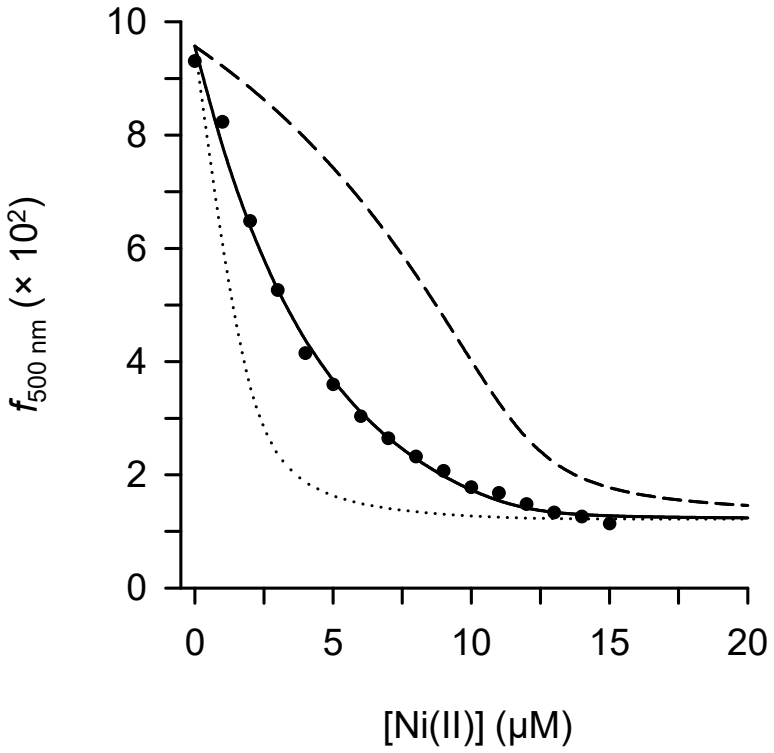

Figure 7.1 Ni(II)-affinity determination of mag-fura-2 using bicine as a competitor. Ni(II) was titrated to 2 μM mag-fura-2 in the presence of 10 μM bicine following Ni(II)-dependent quenching of the mag-fura-2 fluorescence emission ($f_{500\ nm}$; λ_{ex} = 366 nm). The data best fit with a K_d of 2.44 × 10^{-8} M (solid line), where 10-fold tighter (dotted line) or 10-fold weaker (dashed line) limits are also indicated.

7.2 Appendix 2

Model DynaFit script: Ni(II) binding affinity (K_1)

This script describes a general model for sequential Ni(II) binding events to a sensor in competition with a metal chelator. Multiple data sets are fit simultaneously, generating affinity constants most consistent with the model (see [mechanism] in script). As an example, a full set of experimental data is given for NikR in competition with EGTA. Red text indicates parameter values that will vary for competitor and/or sensor. *K* values are specified as dissociation constants so that DynaFit interprets these correctly for an equation describing an association reaction. Derivation of statistical coefficients was described in Section 2.10.3.

```
; M = Ni(II) ; C = competitor ; P = protein sensor (oligomer)

[task]
task = fit
data = equilibrium
confidence = monte-carlo                    ; to determine 95% confidence intervals (optional)

[mechanism]                                 ; all equilibria possible for chosen system
C  + M  <==> CM    :  K   dissociation      ; Ni(II) binding to the competitor (all 1:1 stoichiometry)
P  + M  <==> PM    :  K1a dissociation      ; first stepwise metal binding event to sensor
PM + M  <==> PM2   :  K1b dissociation      ; subsequent stepwise metal binding events vary with sensor
PM2 + M  <==> PM3  :  K1c dissociation      ; applicable to all sensors
PM3 + M  <==> PM4  :  K1d dissociation      ; applicable to all sensors except CueR
PM4 + M  <==> PM5  :  K1e dissociation      ; applicable to Zur only
PM5 + M  <==> PM6  :  K1f dissociation      ; applicable to Zur only


[constants] uM              ; units of µM for all subsequent inputs
K   = [input value]         ; input competitor Ni affinity
K1a = [input value]  ?      ; input estimated sensor affinity - "?" after any value to be optimised by DynaFit
K1b = [input value]  ?      ; input estimated value or linked to a previous K1 by statistical coefficient e.g. 2.67 * K1a
K1c = [input value]  ?      ; input estimated value or linked to a previous K1 by statistical coefficient e.g. 6 * K1a
K1d = [input value]  ?      ; input estimated value or linked to a previous K1 by statistical coefficient e.g. 16 * K1a
K1e = [input value]  ?      ; input estimated value or linked to a previous K1 by statistical coefficient e.g. 4 * K1a
K1f = [input value]  ?      ; input estimated value or linked to a previous K1 by statistical coefficient e.g. 4 * K1a

; note - use of statistical coefficients does not require "?"

[responses]          ; two examples shown - only one response mechanism can be presented in the model
; signal due to Ni binding to sensor - example assumes a linear response across the sites
PM  = 0.166 * PM6
PM2 = 0.333 * PM6
PM3 = 0.5   * PM6
PM4 = 0.666 * PM6
PM5 = 0.833 * PM6
PM6 = [input value]  ?      ; response estimated for the signal expected from µM protein or competitor

; alternative example for two possible competitor responses to metal binding
C = [input value]  ?        ; loss of spectral signal by the competitor with addition of metal (e.g. MF2)
CM = [input value]  ?       ; gain of spectral signal for the metal competitor (e.g. FZ3)

; note - only a response for C or CM can be used

[data]
```

```
variable M                  ; Ni concentrations
offset = [input value] ?    ; offset included if response does not begin or end at zero (optional)
plot logarithmic            ; plots the data using a logarithmic x-axis scale (optional)

; the following lines describe individual data sets used for the simultaneous fit
set NikRa   | concentration P = [input value],  C = [input value]      ; input concentrations for P (oligomer) and C (μM)
set NikRb   | concentration P = [input value],  C = [input value]      ; multiple sets of data can be fit together
set NikRc   | concentration P = [input value],  C = [input value]      ; can include "?" to fit these concentrations as well
; note - lower and upper limits can be placed on the values to be fit, e.g. (1 .. 5) after ?

[output]
directory ./ExampleData/Affinity      ; define the output directory

[set:NikRa]                           ; set must match the name given in the "data" section above
0               0                     ; input data as tab-delimited columns with x = [Ni] and y = response values
1.06967191      0.004628
1.782786516     0.008192
2.97131086      0.011613
4.952184767     0.019929
8.253641278     0.030355
13.7560688      0.041799
22.92678133     0.054016
38.21130221     0.060428
63.68550369     0.06485
106.1425061     0.066374
176.9041769     0.067144
294.8402948     0.064311
491.4004914     0.066051

[set:NikRb]
0               0
1.061845042     0.005289
1.769741737     0.009011
2.949569561     0.015948
4.915949268     0.025735
8.19324878      0.039168
13.65541463     0.054838
22.75902439     0.073827
37.93170732     0.085332
63.2195122      0.090824
105.3658537     0.094166
175.6097561     0.095761
292.6829268     0.094359
487.804878      0.09686

[set:NikRc]
0               0
1.055409617     0.006308
1.759016029     0.010707
2.931693382     0.017861
4.886155636     0.029387
8.143592727     0.045845
13.57265455     0.068411
22.62109091     0.091987
37.70181818     0.110675
62.83636364     0.118341
104.7272727     0.123583
174.5454545     0.125385
290.9090909     0.12517
484.8484848     0.125195

[end]
```

7.3 Appendix 3

Model DynaFit script: Apo-sensor DNA binding affinity (K_3)

This script describes a general model for DNA binding of an apo-sensor to its target DNA site. The oligomeric protein concentration is the variable and the change in anisotropy of the HEX-labelled DNA is the response. Multiple data sets are fit simultaneously, generating affinity constants most consistent with the model (see [mechanism] in script). As an example, a full set of experimental data has been included for determining K_3 for Zur binding to *znuA*-Pro. Red text indicates parameter values that will vary between sensors. *K* values are specified as dissociation constants so that DynaFit interprets these correctly for an equation describing an association reaction. Derivation of statistical coefficients was described in Section 2.10.3.

```
; P = protein sensor (oligomer) ; D = DNA

[task]
task = fit
data = equilibria
confidence = monte-carlo                ; to determine 95% confidence intervals (optional)

[mechanism]                             ; model for two binding events per DNA (remove second line if single event)
P + D   <==> P.D   :  K3a  dissociation
P + P.D <==> P2.D  :  K3b  dissociation          ; applicable to RcnR, Fur, CueR, and Zur

[constants] nM          ; all subsequent values to be input with units of nM
K3a = [input value] ?   ; input estimated affinity for first event
K3b = [input value] ?   ; input estimated value if cooperative or use statistical coefficient e.g. 4 * K3a

[responses]             ; change in anisotropy (Δr-obs) observed
P.D = 0.5 * P2.D        ; ratio for two binding events with linear response
P2.D = [input value] ?  ; input value for Δr-obs to be fit by DynaFit or fix the response (remove "?") if using pre-
                        determined response. "Input value" required for "P.D" complex in single event model

[data] nM
variable P              ; oligomeric protein concentration (e.g. Zur dimer)
offset = [input value] ?  ; offset if starting signal is non-zero (optional)
plot logarithmic        ; plots the data using a logarithmic x-axis scale (optional)

set   DNA1 | concentration D = [input value]    ; input DNA concentrations used
set   DNA2 | concentration D = [input value]    ; can fit multiple sets of data together
set   DNA3 | concentration D = [input value]

[output]
directory ./ExampleData/DNA             ; output destination

[set:DNA1]              ; set must match the name given in the "data" section above
0       0               ; input data as tab-delimited columns with x = [P] and y = response values
50      0.001366667
100     0.000416667
150     0.000866667
200     0.000766667
300     0.002016667
500     0.001216667
1000    0.002466667
1500    0.002266667
```

2000 0.004116667
3000 0.006516667
5000 0.010016667
10000 0.017366667

[set:DNA2]
0 0
50 -0.001583333
100 -0.000783333
150 -0.000433333
200 -0.000383333
300 -8.33333E-05
500 0.000516667
1000 -0.001633333
1500 0.000566667
2000 0.001866667
3000 0.004816667
5000 0.007716667
10000 0.016416667

[set:DNA3]
0 0
50 -0.00035
100 0.00105
150 -0.00145
200 -0.0016
300 -5E-05
500 -0.00055
1000 0.0026
1500 0.0039
2000 0.0033
3000 0.00455
5000 0.00915
10000 0.0172

[end]

7.4 Appendix 4

Model DynaFit script: Ni(II)-sensor DNA binding affinity (K_4)

This script describes a general model for DNA binding of a Ni(II)-loaded sensor to its target DNA site. The model calculates the amount of Ni(II)-bound protein using the average affinity (K_1) for the sensor thereby allowing for the presence of apo-sensor. Ni(II) was fixed to the concentration of protein added. The model allows for any contributions to the response of apo-sensor binding to DNA, based on K_3. The Ni(II)-loaded sensor concentration is the variable and the change in anisotropy of the HEX-labelled DNA is the response. Multiple data sets are fit simultaneously, generating affinity constants most consistent with the model (see [mechanism] in script). As an example, a full set of experimental data has been included for determining K_4'' values for 2:1 Ni(II)-Fur with *fur-box*. Red text indicates parameter values that will vary between sensors. *K* values are specified as dissociation constants so that DynaFit interprets these correctly for an equation describing an association reaction. Derivation of statistical coefficients was described in Section 2.10.3.

```
; P = protein sensor (oligomer) ; D = DNA

[task]
task = fit
data = equilibria
confidence = monte-carlo                ; to determine 95% confidence intervals (optional)

[mechanism]                             ; model for 2:1 sensor-DNA complex (remove K3b and K4b if single event)
P  + M   <==> PM    : K1  dissociation
P  + D   <==> P.D   : K3a  dissociation
P  + P.D <==> P2.D  : K3b  dissociation      ; applicable to RcnR, Fur, CueR, and Zur
PM + D   <==> PM.D  : K4a  dissociation
PM + PM.D <==> PM2.D : K4b  dissociation     ; applicable to RcnR, Fur, CueR, and Zur

[constants] nM          ; all subsequent values to be input with units of nM
K1 = [input value]      ; average K1 for the number of Ni(II)-loaded sites
K3a = [input value]     ; previously measured K3a affinity value
K3b = [input value]     ; previously measured K3b affinity value
K4a = [input value] ?   ; input estimated affinity for first event
K4b = [input value] ?   ; input estimated value if cooperative or use statistical coefficient e.g. 4 * K4a

[concentrations]
M = 1 * P               ; Ni(II) loaded to fill all applicable sites at each added sensor concentration

[responses]             ; change in anisotropy (Δr-obs) observed
P.D = 0.5 * PM2.D       ; assume same apo-sensor and Ni(II)-bound sensor responses; 1 * PM.D for single event
P2.D = 1 * PM2.D        ; assume same apo-sensor and Ni(II)-bound sensor responses (remove if single event)
PM.D = 0.5 * PM2.D      ; fractional coefficient for two binding events with linear response
PM2.D = [input value] ? ; input value for Δr-obs to be fit by DynaFit or fix the response (remove "?") if using pre-
                        determined response. "Input value" required for "PM.D" complex in single event model

[data] nM
variable P              ; oligomeric protein concentration
offset = [input value] ? ; offset if starting signal is non-zero (optional)
plot logarithmic        ; plots the data using a logarithmic x-axis scale (optional)

set   DNA1 | concentration D = [input value]    ; input DNA concentrations used
```

```
set   DNA2 | concentration D = [input value]      ; can fit multiple sets of data together
set   DNA3 | concentration D = [input value]

[output]
directory ./ExampleData/DNA                      ; output destination

[set:DNA1]                    ; set must match the name given in the "data" section above
0          0                  ; input data as tab-delimited columns with x = [P] and y = response values
50         -0.000166667
100        -0.001866667
200        0.003533333
300        0.001383333
500        0.006033333
1000       0.020233333
1500       0.028933333
2000       0.034083333
3000       0.038933333
5000       0.046683333
10000      0.049883333
15000      0.058233333
20000      0.059566667

[set:DNA2]
0          0
50         -0.000766667
100        0.002733333
200        0.002683333
300        0.004283333
500        0.006183333
1000       0.018783333
1500       0.030633333
2000       0.032833333
3000       0.044483333
5000       0.045083333
10000      0.055533333
15000      0.061733333

[set:DNA3]
0          0
50         -0.0012
100        -0.0011
200        -0.00245
300        -0.00105
500        0.0039
1000       0.01405
1500       0.02615
2000       0.03135
3000       0.0382
5000       0.043
10000      0.05115
15000      0.05335

[end]
```

7.5 Appendix 5

Model DynaFit script: Simulating the Ni(II) occupancy of sensors

This script describes a model for simulating the Ni(II) occupancy of a sensor under different conditions (e.g. in the presence of a model cellular competitor/buffer). This model used L-histidine as a competitor and its concentration can be varied. The simulation generates a normalised response for Ni(II) occupancy as a function of added Ni(II). The Ni(II)-specific affinity constants for L-histidine are listed in Section 2.10.6. Red text indicates parameter values that will vary for competitor and/or sensors. The same script was used to simulate 10-fold tighter and 10-fold weaker curves for fitted affinities of sensors (Chapter 3), but with the appropriate competitor K value and protein/competitor response, adjusting the appropriate K_n value by 10-fold tighter or weaker while maintaining the others at the calculated values. K values are specified as dissociation constants so that DynaFit interprets these correctly for an equation describing an association reaction. Derivation of statistical coefficients was described in Section 2.10.3.

```
; M = Ni(II) ; C = L-His/competitor ; P = protein sensor (oligomer)

[task]
task = simulate
data = equilibria

[mechanism]
C  + M  <==> CM    :  K dissociation      ; first L-His binding event
CM + C  <==> C2M   :  KK dissociation     ; second L-His binding event
P  + M  <==> PM    :  K1a dissociation    ; first protein metal binding event
PM + M  <==> PM2   :  K1b dissociation    ; number of subsequent binding events dependent on sensor
PM2 + M <==> PM3   :  K1c dissociation    ; applicable for all sensors
PM3 + M <==> PM4   :  K1d dissociation    ; applicable for all sensors but CueR
PM4 + M <==> PM5   :  K1e dissociation    ; applicable for Zur only
PM5 + M <==> PM6   :  K1f dissociation    ; applicable for Zur only

[constants] uM              ; units of µM for all subsequent inputs
; below example representative of Zur
K  = 0.64                  ; literature value
KK = 8.85                  ; literature value
K1a = [input value]        ; input fixed stepwise affinity constants for sensor
K1b = [input value]        ; use statistical coefficients where appropriate (see Section 7.2)
K1c = [input value]
K1d = [input value]
K1e = [input value]
K1f = [input value]

[concentrations]
P = [input value]          ; concentration of the oligomeric sensor
C = [input value]          ; L-His or competitor concentration (can be zero)

[responses]                ; protein response - equivalent to fitting model in Section 7.2
; below example representative for Zur
PM = 0.167 * PM6           ; number of binding events dependent on "mechanism" above for each sensor
PM2 = 0.333 * PM6
PM3 = 0.5 * PM6
PM4 = 0.667 * PM6
```

```
PM5 = 0.833 * PM6
PM6 = [input value]          ; define a total response value - absolute value irrelevant (typically used 100 for ease)
; response used to define the fully loaded species (e.g. [P]*PM6) so that unsaturated fractions can be calculated

[data] uM
variable  M                  ; Ni(II) concentration

; input the range of variable concentrations (A and B) and the stepwise increment (C), respectively
mesh from [input valueA] to [input valueB] step [input valueC]

directory ./simulations-output/          ; define the location of the simulated data
extension txt
file      sim1

[output]
directory ./ExampleDataNi/simfit         ; define the output directory

[end]
```

7.6 Appendix 6

Model DynaFit script: Simulating the DNA-occupancy of sensors at physiological concentrations (Model 2)

This script describes a model to simulate DNA occupancy under physiological conditions by a Ni(II)-loaded sensor using the thermodynamic cycle shown in Figure 1.2. The simulation generates a response based on the DNA-bound form for each sensor (except CueR and ZntR where only the metal-bound sensor on DNA generates a response). This occupancy is converted to a fractional occupancy based on the maximal possible occupancy (i.e. concentration of the DNA multiplied by the response). L-histidine can be included in the model, using the Ni(II) affinity constants listed in Section 2.10.6. *K* values are specified as dissociation constants so that DynaFit interprets these correctly for an equation describing an association reaction.

```
; M = Ni(II) ; C = L-His ; P = protein sensor (oligomer) ; D = DNA promoter

[task]
task = simulate
data = equilibria

[mechanism]                                  ; using average affinity values
C  + M  <==> CM     :  K dissociation        ; first L-His binding event
CM + C  <==> C2M    :  KK dissociation       ; second L-His binding event
P  + M  <==> PM     :  K1  dissociation      ; equilibria as in Figure 1.2
P.D + M <==> PM.D   :  K2 dissociation
P  + D  <==> P.D    :  K3 dissociation
PM + D  <==> PM.D   :  K4 dissociation


[constants] uM               ; units of µM for all subsequent inputs
K  = 0.64                    ; literature value
KK = 8.85                    ; literature value
K1 = [input value]           ; K1 value for sensor from Table 5.2
K2 = [input value]           ; K2 value for sensor from Table 5.2
K3 = [input value]           ; K3 value for sensor from Table 5.2
K4 = [input value]           ; K4 value for sensor from Table 5.2

[concentrations]
P = [input value]            ; insert physiological oligomeric protein concentration (e.g. P0)
C = [input value]            ; insert physiological concentration of L-His
D = [input value]            ; insert physiological concentration of DNA promoter targets (specific for each sensor)

[responses]                  ; response associated with altered gene expression
PM.D = [input value]         ; arbitrary response value (absolute value irrelevant) - applicable for all sensors
P.D  = [input value]         ; equivalent value as PM.D (note not applicable for CueR or ZntR)

[data] uM
variable  M                  ; Ni(II) concentration

; input the range of variable concentrations (A and B) and the stepwise increment (C), respectively
mesh from [input valueA] to [input valueB] step [input valueC]

directory ./simulations-output/          ; define the location of the simulated data
extension txt
file      sim1
```

```
[output]
directory ./ExampleDataDNA/simfit      ; define the output directory

[end]
```

References

Abed, N., Bickle, M., Mari, B., Schapira, M., Sanjuan-España, R., Robbe Sermesant, K., Moncorgé, O., Mouradian-Garcia, S., Barbry, P., Rudkin, B. B., Fauvarque, M. O., Michaud-Soret, I. and Colas, P. (2007) 'A comparative analysis of perturbations caused by a gene knock-out, a dominant negative allele, and a set of peptide aptamers', *Mol Cell Proteomics,* 6(12), pp. 2110-21.

Agriesti, F., Roncarati, D., Musiani, F., Del Campo, C., Iurlaro, M., Sparla, F., Ciurli, S., Danielli, A. and Scarlato, V. (2014) 'FeON-FeOFF: the Helicobacter pylori Fur regulator commutates iron-responsive transcription by discriminative readout of opposed DNA grooves', *Nucleic Acids Res,* 42(5), pp. 3138-51.

Ahmad, R., Brandsdal, B. O., Michaud-Soret, I. and Willassen, N. P. (2009) 'Ferric uptake regulator protein: binding free energy calculations and per-residue free energy decomposition', *Proteins,* 75(2), pp. 373-86.

Althaus, E. W., Outten, C. E., Olson, K. E., Cao, H. and O'Halloran, T. V. (1999) 'The ferric uptake regulation (Fur) repressor is a zinc metalloprotein', *Biochemistry,* 38(20), pp. 6559-69.

Andreini, C., Bertini, I., Cavallaro, G., Holliday, G. L. and Thornton, J. M. (2008) 'Metal ions in biological catalysis: from enzyme databases to general principles', *J Biol Inorg Chem,* 13(8), pp. 1205-18.

Andrews, S. C. (2010) 'The Ferritin-like superfamily: Evolution of the biological iron storeman from a rubrerythrin-like ancestor', *Biochim Biophys Acta,* 1800(8), pp. 691-705.

Archibald, F. S. and Fridovich, I. (1981) 'Manganese, superoxide dismutase, and oxygen tolerance in some lactic acid bacteria', *J Bacteriol,* 146(3), pp. 928-36.

Ausubel, F. M. (2002) *Short protocols in molecular biology: a compendium of methods from current protocols in molecular biology.*

Axelsson, R. and Lindblad, P. (2002) 'Transcriptional regulation of Nostoc hydrogenases: effects of oxygen, hydrogen, and nickel', *Appl Environ Microbiol,* 68(1), pp. 444-7.

Bagg, A. and Neilands, J. B. (1985) 'Mapping of a mutation affecting regulation of iron uptake systems in *Escherichia coli* K-12', *J Bacteriol,* 161(1), pp. 450-3.

Bagg, A. and Neilands, J. B. (1987) 'Ferric uptake regulation protein acts as a repressor, employing iron (II) as a cofactor to bind the operator of an iron transport operon in *Escherichia coli*', *Biochemistry,* 26(17), pp. 5471-7.

Baichoo, N. and Helmann, J. D. (2002) 'Recognition of DNA by Fur: a reinterpretation of the Fur box consensus sequence', *J Bacteriol,* 184(21), pp. 5826-32.

Balbontín, R., Villagra, N., Pardos de la Gándara, M., Mora, G., Figueroa-Bossi, N. and Bossi, L. (2016) 'Expression of IroN, the salmochelin siderophore receptor, requires mRNA activation by RyhB small RNA homologues', *Mol Microbiol,* 100(1), pp. 139-55.

Bauerfeind, P., Garner, R. M. and Mobley, L. T. (1996) 'Allelic exchange mutagenesis of *nixA* in *Helicobacter pylori* results in reduced nickel transport and urease activity', *Infect Immun,* 64(7), pp. 2877-80.

Beers, J., Glerum, D. M. and Tzagoloff, A. (1997) 'Purification, characterization, and localization of yeast Cox17p, a mitochondrial copper shuttle', *J Biol Chem,* 272(52), pp. 33191-6.

Benini, S., Rypniewski, W. R., Wilson, K. S., Miletti, S., Ciurli, S. and Mangani, S. (1999) 'A new proposal for urease mechanism based on the crystal structures of the native and inhibited enzyme from *Bacillus pasteurii*: why urea hydrolysis costs two nickels', *Structure,* 7(2), pp. 205-16.

Bennett, B. D., Kimball, E. H., Gao, M., Osterhout, R., Van Dien, S. J. and Rabinowitz, J. D. (2009) 'Absolute metabolite concentrations and implied enzyme active site occupancy in *Escherichia coli*', *Nat Chem Biol,* 5(8), pp. 593-9.

Bertani, G. (1951) 'Studies on lysogenesis. I. The mode of phage liberation by lysogenic *Escherichia coli*', *J Bacteriol,* 62(3), pp. 293-300.

Blériot, C., Effantin, G., Lagarde, F., Mandrand-Berthelot, M. A. and Rodrigue, A. (2011) 'RcnB is a periplasmic protein essential for maintaining intracellular Ni and Co concentrations in *Escherichia coli*', *J Bacteriol,* 193(15), pp. 3785-93.

Blokesch, M. and Böck, A. (2002) 'Maturation of [NiFe]-hydrogenases in *Escherichia coli*: the HypC cycle', *J Mol Biol,* 324(2), pp. 287-96.

Bloom, S. L. and Zamble, D. B. (2004) 'Metal-selective DNA-binding response of *Escherichia coli* NikR', *Biochemistry,* 43(31), pp. 10029-38.

Böck, A. and Neidhardt, F. C. (1966) 'Properties of a Mutant of *Escherichia coli* with a Temperature-sensitive Fructose-1,6-Diphosphate Aldolase', *J Bacteriol,* 92(2), pp. 470-6.

Boer, J. L., Mulrooney, S. B. and Hausinger, R. P. (2014) 'Nickel-dependent metalloenzymes', *Arch Biochem Biophys,* 544, pp. 142-52.

Boyd, J., Oza, M. N. and Murphy, J. R. (1990) 'Molecular cloning and DNA sequence analysis of a diphtheria tox iron-dependent regulatory element (dtxR) from *Corynebacterium diphtheriae*', *Proc Natl Acad Sci U S A,* 87(15), pp. 5968-72.

Bradford, M. M. (1976) 'A rapid and sensitive method for the quantitation of microgram quantities of protein utilizing the principle of protein-dye binding', *Anal Biochem,* 72, pp. 248-54.

Bradley, M. J., Chivers, P. T. and Baker, N. A. (2008) 'Molecular dynamics simulation of the *Escherichia coli* NikR protein: equilibrium conformational fluctuations reveal interdomain allosteric communication pathways', *J Mol Biol,* 378(5), pp. 1155-73.

Brocklehurst, K. R., Hobman, J. L., Lawley, B., Blank, L., Marshall, S. J., Brown, N. L. and Morby, A. P. (1999) 'ZntR is a Zn(II)-responsive MerR-like transcriptional regulator of zntA in *Escherichia coli*', *Mol Microbiol,* 31(3), pp. 893-902.

Bury-Moné, S., Thiberge, J. M., Contreras, M., Maitournam, A., Labigne, A. and De Reuse, H. (2004) 'Responsiveness to acidity via metal ion regulators mediates virulence in the gastric pathogen *Helicobacter pylori*', *Mol Microbiol,* 53(2), pp. 623-38.

Butcher, J., Sarvan, S., Brunzelle, J. S., Couture, J. F. and Stintzi, A. (2012) 'Structure and regulon of *Campylobacter jejuni* ferric uptake regulator Fur define apo-Fur regulation', *Proc Natl Acad Sci U S A,* 109(25), pp. 10047-52.

Campoy, S., Jara, M., Busquets, N., Pérez De Rozas, A. M., Badiola, I. and Barbé, J. (2002) 'Role of the high-affinity zinc uptake *znuABC* system in *Salmonella enterica* serovar typhimurium virulence', *Infect Immun,* 70(8), pp. 4721-5.

Carr, C. E., Musiani, F., Huang, H. T., Chivers, P. T., Ciurli, S. and Maroney, M. J. (2017) 'Glutamate Ligation in the Ni(II)- and Co(II)-Responsive *Escherichia coli* Transcriptional Regulator, RcnR', *Inorg Chem,* 56(11), pp. 6459-6476.

Cavet, J. S., Meng, W., Pennella, M. A., Appelhoff, R. J., Giedroc, D. P. and Robinson, N. J. (2002) 'A nickel-cobalt-sensing ArsR-SmtB family repressor. Contributions of cytosol and effector binding sites to metal selectivity', *J Biol Chem,* 277(41), pp. 38441-8.

Chang, F. M., Coyne, H. J., Cubillas, C., Vinuesa, P., Fang, X., Ma, Z., Ma, D., Helmann, J. D., García-de los Santos, A., Wang, Y. X., Dann, C. E. and Giedroc, D. P. (2014) 'Cu(I)-mediated allosteric switching in a copper-sensing operon repressor (CsoR)', *J Biol Chem,* 289(27), pp. 19204-17.

Changela, A., Chen, K., Xue, Y., Holschen, J., Outten, C. E., O'Halloran, T. V. and Mondragón, A. (2003) 'Molecular basis of metal-ion selectivity and zeptomolar sensitivity by CueR', *Science,* 301(5638), pp. 1383-7.

Checa, S. K., Espariz, M., Audero, M. E., Botta, P. E., Spinelli, S. V. and Soncini, F. C. (2007) 'Bacterial sensing of and resistance to gold salts', *Mol Microbiol,* 63(5), pp. 1307-18.

Chen, K., Yuldasheva, S., Penner-Hahn, J. E. and O'Halloran, T. V. (2003) 'An atypical linear Cu(I)-S2 center constitutes the high-affinity metal-sensing site in the CueR metalloregulatory protein', *J Am Chem Soc,* 125(40), pp. 12088-9.

Chen, T. Y., Santiago, A. G., Jung, W., Krzemiński, Ł., Yang, F., Martell, D. J., Helmann, J. D. and Chen, P. (2015) 'Concentration- and chromosome-organization-dependent regulator unbinding from DNA for transcription regulation in living cells', *Nat Commun,* 6, pp. 7445.

Chivers, P. T., Benanti, E. L., Heil-Chapdelaine, V., Iwig, J. S. and Rowe, J. L. (2012) 'Identification of Ni-(L-His)$_2$ as a substrate for NikABCDE-dependent nickel uptake in *Escherichia coli*', *Metallomics,* 4(10), pp. 1043-50.

Chivers, P. T. and Sauer, R. T. (1999) 'NikR is a ribbon-helix-helix DNA-binding protein', *Protein Sci,* 8(11), pp. 2494-500.

Chivers, P. T. and Sauer, R. T. (2000) 'Regulation of high affinity nickel uptake in bacteria. Ni2+-Dependent interaction of NikR with wild-type and mutant operator sites', *J Biol Chem,* 275(26), pp. 19735-41.

Chivers, P. T. and Sauer, R. T. (2002) 'NikR repressor: high-affinity nickel binding to the C-terminal domain regulates binding to operator DNA', *Chem Biol,* 9(10), pp. 1141-8.

Choudhury, S. B., Lee, J. W., Davidson, G., Yim, Y. I., Bose, K., Sharma, M. L., Kang, S. O., Cabelli, D. E. and Maroney, M. J. (1999) 'Examination of the nickel site structure and reaction mechanism in *Streptomyces seoulensis* superoxide dismutase', *Biochemistry,* 38(12), pp. 3744-52.

Chumanov, R. S. and Burgess, R. R. (2011) 'Artifact-inducing enrichment of ethylenediaminetetraacetic acid and ethyleneglycoltetraacetic acid on anion exchange resins', *Anal Biochem,* 412(1), pp. 34-9.

Chung, C. T., Niemela, S. L. and Miller, R. H. (1989) 'One-step preparation of competent *Escherichia coli*: transformation and storage of bacterial cells in the same solution', *Proc Natl Acad Sci U S A,* 86(7), pp. 2172-5.

Chung, H. J., Choi, J. H., Kim, E. J., Cho, Y. H. and Roe, J. H. (1999a) 'Negative regulation of the gene for Fe-containing superoxide dismutase by an Ni-responsive factor in *Streptomyces coelicolor*', *J Bacteriol,* 181(23), pp. 7381-4.

Chung, H. J., Kim, E. J., Suh, B., Choi, J. H. and Roe, J. H. (1999b) 'Duplicate genes for Fe-containing superoxide dismutase in *Streptomyces coelicolor* A3(2)', *Gene,* 231(1-2), pp. 87-93.

Chung, K. C. and Zamble, D. B. (2011) 'The *Escherichia coli* metal-binding chaperone SlyD interacts with the large subunit of [NiFe]-hydrogenase 3', *FEBS Lett,* 585(2), pp. 291-4.

Clugston, S. L., Barnard, J. F., Kinach, R., Miedema, D., Ruman, R., Daub, E. and Honek, J. F. (1998) 'Overproduction and characterization of a dimeric non-zinc glyoxalase I from *Escherichia coli*: evidence for optimal activation by nickel ions', *Biochemistry,* 37(24), pp. 8754-63.

Collier, H. B. (1973) 'Letter: A note on the molar absorptivity of reduced Ellman's reagent, 3-carboxylato-4-nitrothiophenolate', *Anal Biochem,* 56(1), pp. 310-1.

Contreras, M., Thiberge, J. M., Mandrand-Berthelot, M. A. and Labigne, A. (2003) 'Characterization of the roles of NikR, a nickel-responsive pleiotropic autoregulator of *Helicobacter pylori*', *Mol Microbiol,* 49(4), pp. 947-63.

Crammer, J. L. and Neuberger, A. (1943) 'The state of tyrosine in egg albumin and in insulin as determined by spectrophotometric titration', *Biochem J,* 37(2), pp. 302-10.

Crichton, R. R. and Declercq, J. P. (2010) 'X-ray structures of ferritins and related proteins', *Biochim Biophys Acta,* 1800(8), pp. 706-18.

Cubillas, C., Vinuesa, P., Tabche, M. L. and García-de los Santos, A. (2013) 'Phylogenomic analysis of Cation Diffusion Facilitator proteins uncovers Ni2+/Co2+ transporters', *Metallomics,* 5(12), pp. 1634-43.

Cui, G. and Merz, K. M. (2008) 'The intrinsic dynamics and function of nickel-binding regulatory protein: insights from elastic network analysis', *Biophys J,* 94(10), pp. 3769-78.

Culotta, V. C., Klomp, L. W., Strain, J., Casareno, R. L., Krems, B. and Gitlin, J. D. (1997) 'The copper chaperone for superoxide dismutase', *J Biol Chem,* 272(38), pp. 23469-72.

D'Aquino, J. A., Tetenbaum-Novatt, J., White, A., Berkovitch, F. and Ringe, D. (2005) 'Mechanism of metal ion activation of the diphtheria toxin repressor DtxR', *Proc Natl Acad Sci U S A,* 102(51), pp. 18408-13.

Da Silva, J. F. and Williams, R. J. P. (2001) *The biological chemistry of the elements: the inorganic chemistry of life.* Oxford University Press.

Daday, A., Mackerras, A. H. and Smith, G. D. (1985) 'The effect of nickel on hydrogen metabolism and nitrogen fixation in the cyanobacterium *Anabaena cylindrica*', *Microbiology,* 131(2), pp. 231-238.

Davis, A. V. and O'Halloran, T. V. (2008) 'A place for thioether chemistry in cellular copper ion recognition and trafficking', *Nat Chem Biol,* 4(3), pp. 148-51.

de Lorenzo, V., Wee, S., Herrero, M. and Neilands, J. B. (1987) 'Operator sequences of the aerobactin operon of plasmid ColV-K30 binding the ferric uptake regulation (fur) repressor', *J Bacteriol,* 169(6), pp. 2624-30.

De Pina, K., Desjardin, V., Mandrand-Berthelot, M. A., Giordano, G. and Wu, L. F. (1999) 'Isolation and characterization of the nikR gene encoding a nickel-responsive regulator in *Escherichia coli*', *J Bacteriol,* 181(2), pp. 670-4.

de Pina, K., Navarro, C., McWalter, L., Boxer, D. H., Price, N. C., Kelly, S. M., Mandrand-Berthelot, M. A. and Wu, L. F. (1995) 'Purification and characterization of the periplasmic nickel-binding protein NikA of *Escherichia coli* K12', *Eur J Biochem,* 227(3), pp. 857-65.

Delany, I., Ieva, R., Soragni, A., Hilleringmann, M., Rappuoli, R. and Scarlato, V. (2005) '*In vitro* analysis of protein-operator interactions of the NikR and Fur metal-responsive regulators of coregulated genes in *Helicobacter pylori*', *J Bacteriol,* 187(22), pp. 7703-15.

Delany, I., Spohn, G., Rappuoli, R. and Scarlato, V. (2003) 'An anti-repression Fur operator upstream of the promoter is required for iron-mediated transcriptional autoregulation in *Helicobacter pylori*', *Mol Microbiol,* 50(4), pp. 1329-38.

Denby, K. J., Iwig, J., Bisson, C., Westwood, J., Rolfe, M. D., Sedelnikova, S. E., Higgins, K., Maroney, M. J., Baker, P. J., Chivers, P. T. and Green, J. (2016) 'The mechanism of a formaldehyde-sensing transcriptional regulator', *Sci Rep,* 6, pp. 38879.

Deng, Z., Wang, Q., Liu, Z., Zhang, M., Machado, A. C., Chiu, T. P., Feng, C., Zhang, Q., Yu, L., Qi, L., Zheng, J., Wang, X., Huo, X., Qi, X., Li, X., Wu, W., Rohs, R., Li, Y. and Chen, Z. (2015) 'Mechanistic insights into metal ion activation and operator recognition by the ferric uptake regulator', *Nat Commun,* 6, pp. 7642.

Dian, C., Vitale, S., Leonard, G. A., Bahlawane, C., Fauquant, C., Leduc, D., Muller, C., de Reuse, H., Michaud-Soret, I. and Terradot, L. (2011) 'The structure of the *Helicobacter pylori* ferric uptake regulator Fur reveals three functional metal binding sites', *Mol Microbiol,* 79(5), pp. 1260-75.

Dias, A. V. and Zamble, D. B. (2005) 'Protease digestion analysis of *Escherichia coli* NikR: evidence for conformational stabilization with Ni(II)', *J Biol Inorg Chem,* 10(6), pp. 605-12.

Djoko, K. Y., Ong, C. L., Walker, M. J. and McEwan, A. G. (2015) 'The Role of Copper and Zinc Toxicity in Innate Immune Defense against Bacterial Pathogens', *J Biol Chem,* 290(31), pp. 18954-61.

Dojindo (2013) *Metal Chelate Stability Constants*. Available at: https://www.dojindo.com/Images/Product%20Photo/Chelate_Table_of_Stability_Constants.pdf (Accessed: February 2017).

Douglas, C. D., Ngu, T. T., Kaluarachchi, H. and Zamble, D. B. (2013) 'Metal transfer within the *Escherichia coli* HypB-HypA complex of hydrogenase accessory proteins', *Biochemistry,* 52(35), pp. 6030-9.

Dudev, T. and Lim, C. (2014) 'Competition among metal ions for protein binding sites: determinants of metal ion selectivity in proteins', *Chem Rev,* 114(1), pp. 538-56.

Dwarakanath, S., Chaplin, A. K., Hough, M. A., Rigali, S., Vijgenboom, E. and Worrall, J. A. (2012) 'Response to copper stress in *Streptomyces lividans* extends beyond genes under direct control of a copper-sensitive operon repressor protein (CsoR)', *J Biol Chem,* 287(21), pp. 17833-47.

Eicken, C., Pennella, M. A., Chen, X., Koshlap, K. M., VanZile, M. L., Sacchettini, J. C. and Giedroc, D. P. (2003) 'A metal-ligand-mediated intersubunit allosteric switch in related SmtB/ArsR zinc sensor proteins', *J Mol Biol,* 333(4), pp. 683-95.

Ellman, G. L. (1959) 'Tissue sulfhydryl groups', *Arch Biochem Biophys,* 82(1), pp. 70-7.

Epstein, W. and Schultz, S. G. (1965) 'Cation Transport in *Escherichia coli*: V. Regulation of cation content', *J Gen Physiol,* 49(2), pp. 221-34.

Ernst, J. F., Bennett, R. L. and Rothfield, L. I. (1978) 'Constitutive expression of the iron-enterochelin and ferrichrome uptake systems in a mutant strain of *Salmonella typhimurium*', *J Bacteriol,* 135(3), pp. 928-34.

Escolar, L., Pérez-Martín, J. and de Lorenzo, V. (1999) 'Opening the iron box: transcriptional metalloregulation by the Fur protein', *J Bacteriol,* 181(20), pp. 6223-9.

Fenton, H. J. H. (1894) 'LXXIII.—Oxidation of tartaric acid in presence of iron', *Journal of the Chemical Society, Transactions,* 65, pp. 899-910.

Fillat, M. F. (2014) 'The FUR (ferric uptake regulator) superfamily: diversity and versatility of key transcriptional regulators', *Arch Biochem Biophys,* 546, pp. 41-52.

Finney, L. A. and O'Halloran, T. V. (2003) 'Transition metal speciation in the cell: insights from the chemistry of metal ion receptors', *Science,* 300(5621), pp. 931-6.

Ford, G. C., Harrison, P. M., Rice, D. W., Smith, J. M., Treffry, A., White, J. L. and Yariv, J. (1984) 'Ferritin: design and formation of an iron-storage molecule', *Philos Trans R Soc Lond B Biol Sci,* 304(1121), pp. 551-65.

Foster, A. W., Osman, D. and Robinson, N. J. (2014a) 'Metal preferences and metallation', *J Biol Chem,* 289(41), pp. 28095-103.

Foster, A. W., Patterson, C. J., Pernil, R., Hess, C. R. and Robinson, N. J. (2012) 'Cytosolic Ni(II) sensor in cyanobacterium: nickel detection follows nickel affinity across four families of metal sensors', *J Biol Chem,* 287(15), pp. 12142-51.

Foster, A. W., Pernil, R., Patterson, C. J. and Robinson, N. J. (2014b) 'Metal specificity of cyanobacterial nickel-responsive repressor InrS: cells maintain zinc and copper below the detection threshold for InrS', *Mol Microbiol,* 92(4), pp. 797-812.

Foster, A. W., Pernil, R., Patterson, C. J., Scott, A. J. P., Pålsson, L. O., Pal, R., Cummins, I., Chivers, P. T., Pohl, E. and Robinson, N. J. (2017) 'A tight tunable range for Ni(II) sensing and buffering in cells', *Nat Chem Biol,* 13(4), pp. 409-414.

Foster, T. J., Nakahara, H., Weiss, A. A. and Silver, S. (1979) 'Transposon A-generated mutations in the mercuric resistance genes of plasmid R100-1', *J Bacteriol,* 140(1), pp. 167-81.

Franke, S., Grass, G. and Nies, D. H. (2001) 'The product of the ybdE gene of the *Escherichia coli* chromosome is involved in detoxification of silver ions', *Microbiology,* 147(Pt 4), pp. 965-72.

Franke, S., Grass, G., Rensing, C. and Nies, D. H. (2003) 'Molecular analysis of the copper-transporting efflux system CusCFBA of *Escherichia coli*', *J Bacteriol,* 185(13), pp. 3804-12.

Fridovich, I. (1989) 'Superoxide dismutases. An adaptation to a paramagnetic gas', *J Biol Chem,* 264(14), pp. 7761-4.

Fulkerson, J. F. and Mobley, H. L. (2000) 'Membrane topology of the NixA nickel transporter of *Helicobacter pylori*: two nickel transport-specific motifs within transmembrane helices II and III', *J Bacteriol,* 182(6), pp. 1722-30.

Ganesh, I., Ravikumar, S. and Hong, S. H. (2012) 'Metabolically engineered *Escherichia coli* as a tool for the production of bioenergy and biochemicals from glycerol', *Biotechnology and bioprocess engineering,* 17(4), pp. 671-678.

Gault, M., Effantin, G. and Rodrigue, A. (2016) 'Ni exposure impacts the pool of free Fe and modifies DNA supercoiling via metal-induced oxidative stress in *Escherichia coli* K-12', *Free Radic Biol Med,* 97, pp. 351-361.

Giedroc, D. P. and Arunkumar, A. I. (2007) 'Metal sensor proteins: nature's metalloregulated allosteric switches', *Dalton Trans,* (29), pp. 3107-20.

Gilston, B. A., Wang, S., Marcus, M. D., Canalizo-Hernández, M. A., Swindell, E. P., Xue, Y., Mondragón, A. and O'Halloran, T. V. (2014) 'Structural and mechanistic basis of zinc regulation across the *E. coli* Zur regulon', *PLoS Biol,* 12(11), pp. e1001987.

Golynskiy, M., Li, S., Woods, V. L. and Cohen, S. M. (2007) 'Conformational studies of the manganese transport regulator (MntR) from *Bacillus subtilis* using deuterium exchange mass spectrometry', *J Biol Inorg Chem,* 12(5), pp. 699-709.

Golynskiy, M. V., Davis, T. C., Helmann, J. D. and Cohen, S. M. (2005) 'Metal-induced structural organization and stabilization of the metalloregulatory protein MntR', *Biochemistry,* 44(9), pp. 3380-9.

Golynskiy, M. V., Gunderson, W. A., Hendrich, M. P. and Cohen, S. M. (2006) 'Metal binding studies and EPR spectroscopy of the manganese transport regulator MntR', *Biochemistry,* 45(51), pp. 15359-72.

González-Guerrero, M. and Argüello, J. M. (2008) 'Mechanism of Cu+-transporting ATPases: soluble Cu+ chaperones directly transfer Cu+ to transmembrane transport sites', *Proc Natl Acad Sci U S A,* 105(16), pp. 5992-7.

Gonzalez de Peredo, A., Saint-Pierre, C., Adrait, A., Jacquamet, L., Latour, J. M., Michaud-Soret, I. and Forest, E. (1999) 'Identification of the two zinc-bound cysteines in the ferric uptake regulation protein from *Escherichia coli*: chemical modification and mass spectrometry analysis', *Biochemistry,* 38(26), pp. 8582-9.

Grant, G. A. (2006) 'The ACT domain: a small molecule binding domain and its role as a common regulatory element', *J Biol Chem,* 281(45), pp. 33825-9.

Grass, G., Otto, M., Fricke, B., Haney, C. J., Rensing, C., Nies, D. H. and Munkelt, D. (2005) 'FieF (YiiP) from *Escherichia coli* mediates decreased cellular accumulation of iron and relieves iron stress', *Arch Microbiol,* 183(1), pp. 9-18.

Gu, M. and Imlay, J. A. (2013) 'Superoxide poisons mononuclear iron enzymes by causing mismetallation', *Mol Microbiol,* 89(1), pp. 123-34.

Guan, G., Pinochet-Barros, A., Gaballa, A., Patel, S. J., Argüello, J. M. and Helmann, J. D. (2015) 'PfeT, a P1B4 -type ATPase, effluxes ferrous iron and protects *Bacillus subtilis* against iron intoxication', *Mol Microbiol,* 98(4), pp. 787-803.

Guerra, A. J. and Giedroc, D. P. (2012) 'Metal site occupancy and allosteric switching in bacterial metal sensor proteins', *Arch Biochem Biophys,* 519(2), pp. 210-22.

Gutekunst, K., Hoffmann, D., Westernströer, U., Schulz, R., Garbe-Schönberg, D. and Appel, J. (2018) 'In-vivo turnover frequency of the cyanobacterial NiFe-hydrogenase during photohydrogen production outperforms in-vitro systems', *Sci Rep,* 8(1), pp. 6083.

Ha, N. C., Oh, S. T., Sung, J. Y., Cha, K. A., Lee, M. H. and Oh, B. H. (2001) 'Supramolecular assembly and acid resistance of *Helicobacter pylori* urease', *Nat Struct Biol,* 8(6), pp. 505-9.

Hall, D. R., Leonard, G. A., Reed, C. D., Watt, C. I., Berry, A. and Hunter, W. N. (1999) 'The crystal structure of *Escherichia coli* class II fructose-1, 6-bisphosphate aldolase in complex with phosphoglycolohydroxamate reveals details of mechanism and specificity', *J Mol Biol,* 287(2), pp. 383-94.

Hall, H. K. and Foster, J. W. (1996) 'The role of fur in the acid tolerance response of *Salmonella typhimurium* is physiologically and genetically separable from its role in iron acquisition', *J Bacteriol,* 178(19), pp. 5683-91.

Hantke, K. (1981) 'Regulation of ferric iron transport in *Escherichia coli* K12: isolation of a constitutive mutant', *Mol Gen Genet,* 182(2), pp. 288-92.

Hantke, K. (2001) 'Iron and metal regulation in bacteria', *Curr Opin Microbiol,* 4(2), pp. 172-7.

Harber, F. and Weiss, J. (1934) 'The catalytic decomposition of hydrogen peroxide by iron salts', *Proc. R. Soc. Lond. A,* 147(861), pp. 332-351.

Haritha, A., Sagar, K. P., Tiwari, A., Kiranmayi, P., Rodrigue, A., Mohan, P. M. and Singh, S. S. (2009) 'MrdH, a novel metal resistance determinant of *Pseudomonas putida* KT2440, is flanked by metal-inducible mobile genetic elements', *J Bacteriol,* 191(19), pp. 5976-87.

He, M. M., Clugston, S. L., Honek, J. F. and Matthews, B. W. (2000) 'Determination of the structure of *Escherichia coli* glyoxalase I suggests a structural basis for differential metal activation', *Biochemistry,* 39(30), pp. 8719-27.

Healy, W. B., Cheng, S. C. and McElroy, W. D. (1955) 'Metal toxicity and iron deficiency effects on enzymes in *Neurospora*', *Arch Biochem Biophys,* 54(1), pp. 206-14.

Helbig, K., Bleuel, C., Krauss, G. J. and Nies, D. H. (2008) 'Glutathione and transition-metal homeostasis in *Escherichia coli*', *J Bacteriol,* 190(15), pp. 5431-8.

Herring, C. D. and Blattner, F. R. (2004) 'Global transcriptional effects of a suppressor tRNA and the inactivation of the regulator frmR', *J Bacteriol,* 186(20), pp. 6714-20.

Higgins, C. F. (1992) 'ABC transporters: from microorganisms to man', *Annu Rev Cell Biol,* 8, pp. 67-113.

Higgins, K. A., Chivers, P. T. and Maroney, M. J. (2012) 'Role of the N-terminus in determining metal-specific responses in the *E. coli* Ni- and Co-responsive metalloregulator, RcnR', *J Am Chem Soc,* 134(16), pp. 7081-93.

Hmiel, S. P., Snavely, M. D., Miller, C. G. and Maguire, M. E. (1986) 'Magnesium transport in *Salmonella typhimurium*: characterization of magnesium influx and cloning of a transport gene', *J Bacteriol,* 168(3), pp. 1444-50.

Hodgkin, D. G., Pickworth, J., Robertson, J. H., Trueblood, K. N., Prosen, R. J. and White, J. G. (1955) 'The crystal structure of the hexacarboxylic acid derived from B12 and the molecular structure of the vitamin', *Nature,* 176(4477), pp. 325-8.

Huang, H.-T., Bobst, C. E., Iwig, J. S., Chivers, P. T., Kaltashov, I. A. and Maroney, M. J. (2018) 'Co (II) and Ni (II) binding of the *Escherichia coli* transcriptional repressor RcnR orders its N terminus, alters helix dynamics, and reduces DNA affinity', *Journal of Biological Chemistry,* 293(1), pp. 324-332.

Huckle, J. W., Morby, A. P., Turner, J. S. and Robinson, N. J. (1993) 'Isolation of a prokaryotic metallothionein locus and analysis of transcriptional control by trace metal ions', *Mol Microbiol,* 7(2), pp. 177-87.

Ibáñez, M. M., Checa, S. K. and Soncini, F. C. (2015) 'A single serine residue determines selectivity to monovalent metal ions in metalloregulators of the MerR family', *J Bacteriol,* 197(9), pp. 1606-13.

Ikeda, J. S., Janakiraman, A., Kehres, D. G., Maguire, M. E. and Slauch, J. M. (2005) 'Transcriptional regulation of *sitABCD* of *Salmonella enterica* serovar Typhimurium by MntR and Fur', *J Bacteriol,* 187(3), pp. 912-22.

Inoue, Y. and Kimura, A. (1995) 'Methylglyoxal and regulation of its metabolism in microorganisms', *Adv Microb Physiol,* 37, pp. 177-227.

Irving, H. and Williams, R. J. P. (1953) '637. The stability of transition-metal complexes', *Journal of the Chemical Society (Resumed),* (0), pp. 3192-3210.

Iwig, J. S. and Chivers, P. T. (2009) 'DNA recognition and wrapping by *Escherichia coli* RcnR', *J Mol Biol,* 393(2), pp. 514-26.

Iwig, J. S., Leitch, S., Herbst, R. W., Maroney, M. J. and Chivers, P. T. (2008) 'Ni(II) and Co(II) sensing by *Escherichia coli* RcnR', *J Am Chem Soc,* 130(24), pp. 7592-606.

Iwig, J. S., Rowe, J. L. and Chivers, P. T. (2006) 'Nickel homeostasis in *Escherichia coli* - the rcnR-rcnA efflux pathway and its linkage to NikR function', *Mol Microbiol,* 62(1), pp. 252-62.

Jabri, E., Carr, M. B., Hausinger, R. P. and Karplus, P. A. (1995) 'The crystal structure of urease from *Klebsiella aerogenes*', *Science,* 268(5213), pp. 998-1004.

Joshi, C. P., Panda, D., Martell, D. J., Andoy, N. M., Chen, T. Y., Gaballa, A., Helmann, J. D. and Chen, P. (2012) 'Direct substitution and assisted dissociation pathways for turning off transcription by a MerR-family metalloregulator', *Proc Natl Acad Sci U S A,* 109(38), pp. 15121-6.

Kalliri, E., Grzyska, P. K. and Hausinger, R. P. (2005) 'Kinetic and spectroscopic investigation of CoII, NiII, and N-oxalylglycine inhibition of the FeII/alpha-ketoglutarate dioxygenase, TauD', *Biochem Biophys Res Commun,* 338(1), pp. 191-7.

Kammler, M., Schön, C. and Hantke, K. (1993) 'Characterization of the ferrous iron uptake system of *Escherichia coli*', *J Bacteriol,* 175(19), pp. 6212-9.

Kasprzak, K. S. and Hernandez, L. (1989) 'Enhancement of hydroxylation and deglycosylation of 2'-deoxyguanosine by carcinogenic nickel compounds', *Cancer Res,* 49(21), pp. 5964-8.

Kasprzak, K. S., Sunderman, F. W. and Salnikow, K. (2003) 'Nickel carcinogenesis', *Mutat Res,* 533(1-2), pp. 67-97.

Kawanishi, S., Inoue, S. and Yamamoto, K. (1989) 'Site-specific DNA damage induced by nickel(II) ion in the presence of hydrogen peroxide', *Carcinogenesis,* 10(12), pp. 2231-5.

Kehrer, J. P. (2000) 'The Haber-Weiss reaction and mechanisms of toxicity', *Toxicology,* 149(1), pp. 43-50.

Kehres, D. G., Janakiraman, A., Slauch, J. M. and Maguire, M. E. (2002a) 'Regulation of *Salmonella enterica* serovar Typhimurium *mntH* transcription by H(2)O(2), Fe(2+), and Mn(2+)', *J Bacteriol,* 184(12), pp. 3151-8.

Kehres, D. G., Janakiraman, A., Slauch, J. M. and Maguire, M. E. (2002b) 'SitABCD is the alkaline Mn(2+) transporter of *Salmonella enterica* serovar Typhimurium', *J Bacteriol,* 184(12), pp. 3159-66.

Kehres, D. G., Zaharik, M. L., Finlay, B. B. and Maguire, M. E. (2000) 'The NRAMP proteins of *Salmonella typhimurium* and *Escherichia coli* are selective manganese transporters involved in the response to reactive oxygen', *Mol Microbiol,* 36(5), pp. 1085-100.

Khan, S., Brocklehurst, K. R., Jones, G. W. and Morby, A. P. (2002) 'The functional analysis of directed amino-acid alterations in ZntR from *Escherichia coli*', *Biochem Biophys Res Commun,* 299(3), pp. 438-45.

Kidd, S. P., Djoko, K. Y., Ng, J., Argente, M. P., Jennings, M. P. and McEwan, A. G. (2011) 'A novel nickel responsive MerR-like regulator, NimR, from *Haemophilus influenzae*', *Metallomics,* 3(10), pp. 1009-18.

Kiley, P. J. and Beinert, H. (1998) 'Oxygen sensing by the global regulator, FNR: the role of the iron-sulfur cluster', *FEMS Microbiol Rev,* 22(5), pp. 341-52.

Kim, E. H., Nies, D. H., McEvoy, M. M. and Rensing, C. (2011) 'Switch or funnel: how RND-type transport systems control periplasmic metal homeostasis', *J Bacteriol,* 193(10), pp. 2381-7.

Klein, J. S. and Lewinson, O. (2011) 'Bacterial ATP-driven transporters of transition metals: physiological roles, mechanisms of action, and roles in bacterial virulence', *Metallomics,* 3(11), pp. 1098-108.

Kliegman, J. I., Griner, S. L., Helmann, J. D., Brennan, R. G. and Glasfeld, A. (2006) 'Structural basis for the metal-selective activation of the manganese transport regulator of *Bacillus subtilis*', *Biochemistry,* 45(11), pp. 3493-505.

Kolaj-Robin, O., Russell, D., Hayes, K. A., Pembroke, J. T. and Soulimane, T. (2015) 'Cation Diffusion Facilitator family: Structure and function', *FEBS Lett,* 589(12), pp. 1283-95.

Krecisz, S., Jones, M. D. and Zamble, D. B. (2012) 'Nonspecific interactions between *Escherichia coli* NikR and DNA are critical for nickel-activated DNA binding', *Biochemistry,* 51(40), pp. 7873-9.

Kuzmic, P. (1996) 'Program DYNAFIT for the analysis of enzyme kinetic data: application to HIV proteinase', *Anal Biochem,* 237(2), pp. 260-73.

Laemmli, U. K. (1970) 'Cleavage of structural proteins during the assembly of the head of bacteriophage T4', *Nature,* 227(5259), pp. 680-5.

Latinwo, L. M., Donald, C., Ikediobi, C. and Silver, S. (1998) 'Effects of intracellular glutathione on sensitivity of *Escherichia coli* to mercury and arsenite', *Biochem Biophys Res Commun,* 242(1), pp. 67-70.

Lavrrar, J. L. and McIntosh, M. A. (2003) 'Architecture of a fur binding site: a comparative analysis', *J Bacteriol,* 185(7), pp. 2194-202.

Leach, M. R., Zhang, J. W. and Zamble, D. B. (2007) 'The role of complex formation between the *Escherichia coli* hydrogenase accessory factors HypB and SlyD', *J Biol Chem,* 282(22), pp. 16177-86.

Lebrette, H., Brochier-Armanet, C., Zambelli, B., de Reuse, H., Borezée-Durant, E., Ciurli, S. and Cavazza, C. (2014) 'Promiscuous nickel import in human pathogens: structure, thermodynamics, and evolution of extracytoplasmic nickel-binding proteins', *Structure,* 22(10), pp. 1421-32.

Lee, M. H., Pankratz, H. S., Wang, S., Scott, R. A., Finnegan, M. G., Johnson, M. K., Ippolito, J. A., Christianson, D. W. and Hausinger, R. P. (1993) 'Purification and characterization of *Klebsiella aerogenes* UreE protein: a nickel-binding protein that functions in urease metallocenter assembly', *Protein Sci,* 2(6), pp. 1042-52.

Lee, S. W., Glickmann, E. and Cooksey, D. A. (2001) 'Chromosomal locus for cadmium resistance in *Pseudomonas putida* consisting of a cadmium-transporting ATPase and a MerR family response regulator', *Appl Environ Microbiol,* 67(4), pp. 1437-44.

Leitch, S., Bradley, M. J., Rowe, J. L., Chivers, P. T. and Maroney, M. J. (2007) 'Nickel-specific response in the transcriptional regulator, *Escherichia coli* NikR', *J Am Chem Soc,* 129(16), pp. 5085-95.

Lieser, S. A., Davis, T. C., Helmann, J. D. and Cohen, S. M. (2003) 'DNA-binding and oligomerization studies of the manganese(II) metalloregulatory protein MntR from *Bacillus subtilis*', *Biochemistry,* 42(43), pp. 12634-42.

Lin, S. J., Pufahl, R. A., Dancis, A., O'Halloran, T. V. and Culotta, V. C. (1997) 'A role for the *Saccharomyces cerevisiae* ATX1 gene in copper trafficking and iron transport', *J Biol Chem,* 272(14), pp. 9215-20.

Lippard, S. J. and Berg, J. M. (1994) *Principles of bioinorganic chemistry.* University Science Books.

Liu, T., Ramesh, A., Ma, Z., Ward, S. K., Zhang, L., George, G. N., Talaat, A. M., Sacchettini, J. C. and Giedroc, D. P. (2007) 'CsoR is a novel *Mycobacterium tuberculosis* copper-sensing transcriptional regulator', *Nat Chem Biol,* 3(1), pp. 60-8.

Lloyd, D. R. and Phillips, D. H. (1999) 'Oxidative DNA damage mediated by copper(II), iron(II) and nickel(II) fenton reactions: evidence for site-specific mechanisms in the formation of double-strand breaks, 8-hydroxydeoxyguanosine and putative intrastrand cross-links', *Mutat Res,* 424(1-2), pp. 23-36.

Louwrier, A. and Knowles, C. J. (1996) 'The purification and characterization of a novel D (−)-specific carbamoylase enzyme from an *Agrobacterium sp*', *Enzyme and microbial technology,* 19(8), pp. 562-571.

Lucarelli, D., Russo, S., Garman, E., Milano, A., Meyer-Klaucke, W. and Pohl, E. (2007) 'Crystal structure and function of the zinc uptake regulator FurB from *Mycobacterium tuberculosis*', *J Biol Chem,* 282(13), pp. 9914-22.

Lutz, S., Jacobi, A., Schlensog, V., Böhm, R., Sawers, G. and Böck, A. (1991) 'Molecular characterization of an operon (hyp) necessary for the activity of the three hydrogenase isoenzymes in *Escherichia coli*', *Mol Microbiol,* 5(1), pp. 123-35.

Ma, Z., Chandrangsu, P., Helmann, T. C., Romsang, A., Gaballa, A. and Helmann, J. D. (2014) 'Bacillithiol is a major buffer of the labile zinc pool in *Bacillus subtilis*', *Mol Microbiol,* 94(4), pp. 756-70.

Macomber, L., Elsey, S. P. and Hausinger, R. P. (2011) 'Fructose-1,6-bisphosphate aldolase (class II) is the primary site of nickel toxicity in *Escherichia coli*', *Mol Microbiol,* 82(5), pp. 1291-300.

Macomber, L. and Hausinger, R. P. (2011) 'Mechanisms of nickel toxicity in microorganisms', *Metallomics,* 3(11), pp. 1153-62.

Maeda, T., Sanchez-Torres, V. and Wood, T. K. (2008) 'Metabolic engineering to enhance bacterial hydrogen production', *Microb Biotechnol,* 1(1), pp. 30-9.

Maeda, T., Sanchez-Torres, V. and Wood, T. K. (2012) 'Hydrogen production by recombinant *Escherichia coli* strains', *Microb Biotechnol,* 5(2), pp. 214-25.

Makui, H., Roig, E., Cole, S. T., Helmann, J. D., Gros, P. and Cellier, M. F. (2000) 'Identification of the *Escherichia coli* K-12 Nramp orthologue (MntH) as a selective divalent metal ion transporter', *Mol Microbiol,* 35(5), pp. 1065-78.

Maret, W. (2010) 'Metalloproteomics, metalloproteomes, and the annotation of metalloproteins', *Metallomics,* 2(2), pp. 117-25.

Marsh, J. J. and Lebherz, H. G. (1992) 'Fructose-bisphosphate aldolases: an evolutionary history', *Trends Biochem Sci,* 17(3), pp. 110-3.

Martell, A. E. and Smith, R. M. (1974) *Critical stability constants.* Springer.

McCall, K. A. and Fierke, C. A. (2004) 'Probing determinants of the metal ion selectivity in carbonic anhydrase using mutagenesis', *Biochemistry,* 43(13), pp. 3979-86.

McCord, J. M. and Day, E. D. (1978) 'Superoxide-dependent production of hydroxyl radical catalyzed by iron-EDTA complex', *FEBS Lett,* 86(1), pp. 139-42.

McCord, J. M. and Fridovich, I. (1988) 'Superoxide dismutase: the first twenty years (1968-1988)', *Free Radic Biol Med,* 5(5-6), pp. 363-9.

McCord, J. M., Keele, B. B. and Fridovich, I. (1971) 'An enzyme-based theory of obligate anaerobiosis: the physiological function of superoxide dismutase', *Proc Natl Acad Sci U S A,* 68(5), pp. 1024-7.

McGuire, A. M., Cuthbert, B. J., Ma, Z., Grauer-Gray, K. D., Brunjes Brophy, M., Spear, K. A., Soonsanga, S., Kliegman, J. I., Griner, S. L., Helmann, J. D. and Glasfeld, A. (2013) 'Roles of the A and C sites in the manganese-specific activation of MntR', *Biochemistry,* 52(4), pp. 701-13.

Meneghini, R. (1997) 'Iron homeostasis, oxidative stress, and DNA damage', *Free Radic Biol Med,* 23(5), pp. 783-92.

Merchant, A. T. and Spatafora, G. A. (2014) 'A role for the DtxR family of metalloregulators in gram-positive pathogenesis', *Mol Oral Microbiol,* 29(1), pp. 1-10.

Miller, A. F. (2012) 'Superoxide dismutases: ancient enzymes and new insights', *FEBS Lett,* 586(5), pp. 585-95.

Mills, S. A. and Marletta, M. A. (2005) 'Metal binding characteristics and role of iron oxidation in the ferric uptake regulator from *Escherichia coli*', *Biochemistry,* 44(41), pp. 13553-9.

Minot, G. R. and Murphy, W. P. (1926) 'Treatment of pernicious anemia by a special diet', *Journal of the American Medical Association,* 87(7), pp. 470-476.

Mobley, H. L., Garner, R. M. and Bauerfeind, P. (1995a) '*Helicobacter pylori* nickel-transport gene nixA: synthesis of catalytically active urease in *Escherichia coli* independent of growth conditions', *Mol Microbiol,* 16(1), pp. 97-109.

Mobley, H. L., Island, M. D. and Hausinger, R. P. (1995b) 'Molecular biology of microbial ureases', *Microbiol Rev,* 59(3), pp. 451-80.

Moore, C. M. and Helmann, J. D. (2005) 'Metal ion homeostasis in *Bacillus subtilis*', *Curr Opin Microbiol,* 8(2), pp. 188-95.

Moore, S. J. and Warren, M. J. (2012) 'The anaerobic biosynthesis of vitamin B12', *Biochem Soc Trans,* 40(3), pp. 581-6.

Mulrooney, S. B. and Hausinger, R. P. (2003) 'Nickel uptake and utilization by microorganisms', *FEMS Microbiol Rev,* 27(2-3), pp. 239-61.

Munkelt, D., Grass, G. and Nies, D. H. (2004) 'The chromosomally encoded cation diffusion facilitator proteins DmeF and FieF from *Wautersia metallidurans* CH34 are transporters of broad metal specificity', *J Bacteriol,* 186(23), pp. 8036-43.

Murakami, S., Nakashima, R., Yamashita, E. and Yamaguchi, A. (2002) 'Crystal structure of bacterial multidrug efflux transporter AcrB', *Nature,* 419(6907), pp. 587-93.

Nakai, T., Hasegawa, T., Yamashita, E., Yamamoto, M., Kumasaka, T., Ueki, T., Nanba, H., Ikenaka, Y., Takahashi, S., Sato, M. and Tsukihara, T. (2000) 'Crystal structure of N-carbamyl-D-amino acid amidohydrolase with a novel catalytic framework common to amidohydrolases', *Structure,* 8(7), pp. 729-37.

Navarro, C., Wu, L. F. and Mandrand-Berthelot, M. A. (1993) 'The *nik* operon of *Escherichia coli* encodes a periplasmic binding-protein-dependent transport system for nickel', *Mol Microbiol,* 9(6), pp. 1181-91.

Neilands, J. B. (1995) 'Siderophores: structure and function of microbial iron transport compounds', *J Biol Chem,* 270(45), pp. 26723-6.

Nevo, Y. and Nelson, N. (2006) 'The NRAMP family of metal-ion transporters', *Biochim Biophys Acta,* 1763(7), pp. 609-20.

Nies, D. H. (1995) 'The cobalt, zinc, and cadmium efflux system CzcABC from *Alcaligenes eutrophus* functions as a cation-proton antiporter in *Escherichia coli*', *J Bacteriol,* 177(10), pp. 2707-12.

Nies, D. H. (2003) 'Efflux-mediated heavy metal resistance in prokaryotes', *FEMS Microbiol Rev,* 27(2-3), pp. 313-39.

Nies, D. H. and Silver, S. (1995) 'Ion efflux systems involved in bacterial metal resistances', *J Ind Microbiol,* 14(2), pp. 186-99.

Noinaj, N., Guillier, M., Barnard, T. J. and Buchanan, S. K. (2010) 'TonB-dependent transporters: regulation, structure, and function', *Annu Rev Microbiol,* 64, pp. 43-60.

Nucifora, G., Chu, L., Misra, T. K. and Silver, S. (1989) 'Cadmium resistance from *Staphylococcus aureus* plasmid pI258 *cadA* gene results from a cadmium-efflux ATPase', *Proc Natl Acad Sci U S A,* 86(10), pp. 3544-8.

O'Halloran, T. and Walsh, C. (1987) 'Metalloregulatory DNA-binding protein encoded by the *merR* gene: isolation and characterization', *Science,* 235(4785), pp. 211-4.

O'Halloran, T. V. and Culotta, V. C. (2000) 'Metallochaperones, an intracellular shuttle service for metal ions', *J Biol Chem,* 275(33), pp. 25057-60.

O'Halloran, T. V., Frantz, B., Shin, M. K., Ralston, D. M. and Wright, J. G. (1989) 'The MerR heavy metal receptor mediates positive activation in a topologically novel transcription complex', *Cell,* 56(1), pp. 119-29.

Odermatt, A. and Solioz, M. (1995) 'Two trans-acting metalloregulatory proteins controlling expression of the copper-ATPases of *Enterococcus hirae*', *J Biol Chem,* 270(9), pp. 4349-54.

Odermatt, A., Suter, H., Krapf, R. and Solioz, M. (1993) 'Primary structure of two P-type ATPases involved in copper homeostasis in *Enterococcus hirae*', *J Biol Chem,* 268(17), pp. 12775-9.

Osman, D., Foster, A. W., Chen, J., Svedaite, K., Steed, J. W., Lurie-Luke, E., Huggins, T. G. and Robinson, N. J. (2017) 'Fine control of metal concentrations is necessary for cells to discern zinc from cobalt', *Nat Commun,* 8(1), pp. 1884.

Osman, D., Martini, M. A., Foster, A. W., Chen, J., Scott, A. J. P., Morton, R. J., Steed, J. W., Lurie-Luke, E., Huggins, T. G., Lawrence, A. D., Deery, E., Warren, M. J., Chivers, P. T. and Robinson, N. J. (2018) *In review*.

Osman, D., Patterson, C. J., Bailey, K., Fisher, K., Robinson, N. J., Rigby, S. E. and Cavet, J. S. (2013) 'The copper supply pathway to a *Salmonella* Cu,Zn-superoxide dismutase (SodCII) involves P(1B)-type ATPase copper efflux and periplasmic CueP', *Mol Microbiol,* 87(3), pp. 466-77.

Osman, D., Piergentili, C., Chen, J., Chakrabarti, B., Foster, A. W., Lurie-Luke, E., Huggins, T. G. and Robinson, N. J. (2015) 'Generating a Metal-responsive Transcriptional Regulator to Test What Confers Metal Sensing in Cells', *J Biol Chem,* 290(32), pp. 19806-22.

Osman, D., Piergentili, C., Chen, J., Sayer, L. N., Usón, I., Huggins, T. G., Robinson, N. J. and Pohl, E. (2016) 'The Effectors and Sensory Sites of Formaldehyde-responsive Regulator FrmR and Metal-sensing Variant', *J Biol Chem,* 291(37), pp. 19502-16.

Osman, D., Waldron, K. J., Denton, H., Taylor, C. M., Grant, A. J., Mastroeni, P., Robinson, N. J. and Cavet, J. S. (2010) 'Copper homeostasis in *Salmonella* is atypical and copper-CueP is a major periplasmic metal complex', *J Biol Chem,* 285(33), pp. 25259-68.

Outten, C. E. and O'Halloran, T. V. (2001) 'Femtomolar sensitivity of metalloregulatory proteins controlling zinc homeostasis', *Science,* 292(5526), pp. 2488-92.

Outten, F. W., Huffman, D. L., Hale, J. A. and O'Halloran, T. V. (2001) 'The independent *cue* and *cus* systems confer copper tolerance during aerobic and anaerobic growth in *Escherichia coli*', *J Biol Chem,* 276(33), pp. 30670-7.

Outten, F. W., Outten, C. E., Hale, J. and O'Halloran, T. V. (2000) 'Transcriptional activation of an *Escherichia coli* copper efflux regulon by the chromosomal MerR homologue, *cueR*', *J Biol Chem,* 275(40), pp. 31024-9.

Panina, E. M., Mironov, A. A. and Gelfand, M. S. (2003) 'Comparative genomics of bacterial zinc regulons: enhanced ion transport, pathogenesis, and rearrangement of ribosomal proteins', *Proc Natl Acad Sci U S A,* 100(17), pp. 9912-7.

Patzer, S. I. and Hantke, K. (1998) 'The ZnuABC high-affinity zinc uptake system and its regulator Zur in *Escherichia coli*', *Mol Microbiol,* 28(6), pp. 1199-210.

Patzer, S. I. and Hantke, K. (2001) 'Dual repression by Fe(2+)-Fur and Mn(2+)-MntR of the *mntH* gene, encoding an NRAMP-like Mn(2+) transporter in *Escherichia coli*', *J Bacteriol,* 183(16), pp. 4806-13.

Pecqueur, L., D'Autréaux, B., Dupuy, J., Nicolet, Y., Jacquamet, L., Brutscher, B., Michaud-Soret, I. and Bersch, B. (2006) 'Structural changes of *Escherichia coli* ferric uptake regulator during metal-dependent dimerization and activation explored by NMR and X-ray crystallography', *J Biol Chem,* 281(30), pp. 21286-95.

Pennella, M. A., Arunkumar, A. I. and Giedroc, D. P. (2006) 'Individual metal ligands play distinct functional roles in the zinc sensor *Staphylococcus aureus* CzrA', *J Mol Biol,* 356(5), pp. 1124-36.

Pennella, M. A., Shokes, J. E., Cosper, N. J., Scott, R. A. and Giedroc, D. P. (2003) 'Structural elements of metal selectivity in metal sensor proteins', *Proc Natl Acad Sci U S A,* 100(7), pp. 3713-8.

Pérard, J., Nader, S., Levert, M., Arnaud, L., Carpentier, P., Siebert, C., Blanquet, F., Cavazza, C., Renesto, P., Schneider, D., Maurin, M., Coves, J., Crouzy, S. and Michaud-Soret, I. (2018) 'Structural and functional studies of the metalloregulator Fur identify a promoter-binding mechanism and its role in *Francisella tularensis* virulence', *Communications Biology,* 1(1), pp. 93.

Philips, S. J., Canalizo-Hernandez, M., Yildirim, I., Schatz, G. C., Mondragón, A. and O'Halloran, T. V. (2015) 'TRANSCRIPTION. Allosteric transcriptional regulation via changes in the overall topology of the core promoter', *Science,* 349(6250), pp. 877-81.

Phillips, C. M., Schreiter, E. R., Guo, Y., Wang, S. C., Zamble, D. B. and Drennan, C. L. (2008) 'Structural basis of the metal specificity for nickel regulatory protein NikR', *Biochemistry,* 47(7), pp. 1938-46.

Phillips, S. A. and Thornalley, P. J. (1993) 'The formation of methylglyoxal from triose phosphates. Investigation using a specific assay for methylglyoxal', *Eur J Biochem,* 212(1), pp. 101-5.

Pohl, E., Haller, J. C., Mijovilovich, A., Meyer-Klaucke, W., Garman, E. and Vasil, M. L. (2003) 'Architecture of a protein central to iron homeostasis: crystal structure and spectroscopic analysis of the ferric uptake regulator', *Mol Microbiol,* 47(4), pp. 903-15.

Pufahl, R. A., Singer, C. P., Peariso, K. L., Lin, S. J., Schmidt, P. J., Fahrni, C. J., Culotta, V. C., Penner-Hahn, J. E. and O'Halloran, T. V. (1997) 'Metal ion chaperone function of the soluble Cu(I) receptor Atx1', *Science,* 278(5339), pp. 853-6.

Que, Q. and Helmann, J. D. (2000) 'Manganese homeostasis in *Bacillus subtilis* is regulated by MntR, a bifunctional regulator related to the diphtheria toxin repressor family of proteins', *Mol Microbiol,* 35(6), pp. 1454-68.

Randhawa, V. K., Zhou, F., Jin, X., Nalewajko, C. and Kushner, D. J. (2001) 'Role of oxidative stress and thiol antioxidant enzymes in nickel toxicity and resistance in strains of the green alga *Scenedesmus acutus f. alternans*', *Can J Microbiol,* 47(11), pp. 987-93.

Reissmann, S., Hochleitner, E., Wang, H., Paschos, A., Lottspeich, F., Glass, R. S. and Böck, A. (2003) 'Taming of a poison: biosynthesis of the NiFe-hydrogenase cyanide ligands', *Science,* 299(5609), pp. 1067-70.

Rensing, C., Mitra, B. and Rosen, B. P. (1997) 'The *zntA* gene of *Escherichia coli* encodes a Zn(II)-translocating P-type ATPase', *Proc Natl Acad Sci U S A,* 94(26), pp. 14326-31.

Reyes-Caballero, H., Campanello, G. C. and Giedroc, D. P. (2011) 'Metalloregulatory proteins: metal selectivity and allosteric switching', *Biophys Chem,* 156(2-3), pp. 103-14.

Rice, A. J., Park, A. and Pinkett, H. W. (2014) 'Diversity in ABC transporters: type I, II and III importers', *Crit Rev Biochem Mol Biol,* 49(5), pp. 426-37.

Riddles, P. W., Blakeley, R. L. and Zerner, B. (1983) 'Reassessment of Ellman's reagent', *Methods Enzymol,* 91, pp. 49-60.

Rivera, M. (2017) 'Bacterioferritin: Structure, Dynamics, and Protein-Protein Interactions at Play in Iron Storage and Mobilization', *Acc Chem Res,* 50(2), pp. 331-340.

Rodrigue, A., Effantin, G. and Mandrand-Berthelot, M. A. (2005) 'Identification of *rcnA* (*yohM*), a nickel and cobalt resistance gene in *Escherichia coli*', *J Bacteriol,* 187(8), pp. 2912-6.

Rodriguez, G. M. and Smith, I. (2006) 'Identification of an ABC transporter required for iron acquisition and virulence in *Mycobacterium tuberculosis*', *J Bacteriol,* 188(2), pp. 424-30.

Rolfe, M. D., Rice, C. J., Lucchini, S., Pin, C., Thompson, A., Cameron, A. D., Alston, M., Stringer, M. F., Betts, R. P., Baranyi, J., Peck, M. W. and Hinton, J. C. (2012) 'Lag phase is a distinct growth phase that prepares bacteria for exponential growth and involves transient metal accumulation', *J Bacteriol,* 194(3), pp. 686-701.

Rosch, J. W., Gao, G., Ridout, G., Wang, Y. D. and Tuomanen, E. I. (2009) 'Role of the manganese efflux system *mntE* for signalling and pathogenesis in *Streptococcus pneumoniae*', *Mol Microbiol,* 72(1), pp. 12-25.

Rosenzweig, A. C. (2002) 'Metallochaperones: bind and deliver', *Chem Biol,* 9(6), pp. 673-7.

Roth, J. R., Lawrence, J. G. and Bobik, T. A. (1996) 'Cobalamin (coenzyme B12): synthesis and biological significance', *Annu Rev Microbiol,* 50, pp. 137-81.

Roth, J. R., Lawrence, J. G., Rubenfield, M., Kieffer-Higgins, S. and Church, G. M. (1993) 'Characterization of the cobalamin (vitamin B12) biosynthetic genes of *Salmonella typhimurium*', *J Bacteriol,* 175(11), pp. 3303-16.

Rowe, J. L., Starnes, G. L. and Chivers, P. T. (2005) 'Complex transcriptional control links NikABCDE-dependent nickel transport with hydrogenase expression in *Escherichia coli*', *J Bacteriol,* 187(18), pp. 6317-23.

Rubino, J. T. and Franz, K. J. (2012) 'Coordination chemistry of copper proteins: how nature handles a toxic cargo for essential function', *J Inorg Biochem,* 107(1), pp. 129-43.

Saier, M. H., Tam, R., Reizer, A. and Reizer, J. (1994) 'Two novel families of bacterial membrane proteins concerned with nodulation, cell division and transport', *Mol Microbiol,* 11(5), pp. 841-7.

Sakamoto, K., Agari, Y., Agari, K., Kuramitsu, S. and Shinkai, A. (2010) 'Structural and functional characterization of the transcriptional repressor CsoR from *Thermus thermophilus* HB8', *Microbiology,* 156(Pt 7), pp. 1993-2005.

San Francisco, M. J., Hope, C. L., Owolabi, J. B., Tisa, L. S. and Rosen, B. P. (1990) 'Identification of the metalloregulatory element of the plasmid-encoded arsenical resistance operon', *Nucleic Acids Res,* 18(3), pp. 619-24.

Schreiter, E. R., Sintchak, M. D., Guo, Y., Chivers, P. T., Sauer, R. T. and Drennan, C. L. (2003) 'Crystal structure of the nickel-responsive transcription factor NikR', *Nat Struct Biol,* 10(10), pp. 794-9.

Schreiter, E. R., Wang, S. C., Zamble, D. B. and Drennan, C. L. (2006) 'NikR-operator complex structure and the mechanism of repressor activation by metal ions', *Proc Natl Acad Sci U S A,* 103(37), pp. 13676-81.

Sen, K. I., Sienkiewicz, A., Love, J. F., vanderSpek, J. C., Fajer, P. G. and Logan, T. M. (2006) 'Mn(II) binding by the anthracis repressor from *Bacillus anthracis*', *Biochemistry,* 45(13), pp. 4295-303.

Seo, S. W., Kim, D., Latif, H., O'Brien, E. J., Szubin, R. and Palsson, B. O. (2014) 'Deciphering Fur transcriptional regulatory network highlights its complex role beyond iron metabolism in *Escherichia coli*', *Nat Commun,* 5, pp. 4910.

Sheikh, M. A. and Taylor, G. L. (2009) 'Crystal structure of the *Vibrio cholerae* ferric uptake regulator (Fur) reveals insights into metal co-ordination', *Mol Microbiol,* 72(5), pp. 1208-20.

Shin, J. H., Jung, H. J., An, Y. J., Cho, Y. B., Cha, S. S. and Roe, J. H. (2011) 'Graded expression of zinc-responsive genes through two regulatory zinc-binding sites in Zur', *Proc Natl Acad Sci U S A,* 108(12), pp. 5045-50.

Snavely, M. D., Gravina, S. A., Cheung, T. T., Miller, C. G. and Maguire, M. E. (1991) 'Magnesium transport in *Salmonella typhimurium*. Regulation of *mgtA* and *mgtB* expression', *J Biol Chem,* 266(2), pp. 824-9.

Soriano, A. and Hausinger, R. P. (1999) 'GTP-dependent activation of urease apoprotein in complex with the UreD, UreF, and UreG accessory proteins', *Proc Natl Acad Sci U S A,* 96(20), pp. 11140-4.

Stoof, J., Breijer, S., Pot, R. G., van der Neut, D., Kuipers, E. J., Kusters, J. G. and van Vliet, A. H. (2008) 'Inverse nickel-responsive regulation of two urease enzymes in the gastric pathogen *Helicobacter mustelae*', *Environ Microbiol,* 10(10), pp. 2586-97.

Stoyanov, J. V. and Brown, N. L. (2003) 'The *Escherichia coli* copper-responsive *copA* promoter is activated by gold', *J Biol Chem,* 278(3), pp. 1407-10.

Stoyanov, J. V., Hobman, J. L. and Brown, N. L. (2001) 'CueR (YbbI) of *Escherichia coli* is a MerR family regulator controlling expression of the copper exporter CopA', *Mol Microbiol,* 39(2), pp. 502-11.

Studier, F. W. and Moffatt, B. A. (1986) 'Use of bacteriophage T7 RNA polymerase to direct selective high-level expression of cloned genes', *J Mol Biol,* 189(1), pp. 113-30.

Tainer, J. A., Getzoff, E. D., Beem, K. M., Richardson, J. S. and Richardson, D. C. (1982) 'Determination and analysis of the 2 A-structure of copper, zinc superoxide dismutase', *J Mol Biol,* 160(2), pp. 181-217.

Theil, E. C., Matzapetakis, M. and Liu, X. (2006) 'Ferritins: iron/oxygen biominerals in protein nanocages', *J Biol Inorg Chem,* 11(7), pp. 803-10.

Thornalley, P. J. (1998) 'Glutathione-dependent detoxification of alpha-oxoaldehydes by the glyoxalase system: involvement in disease mechanisms and antiproliferative activity of glyoxalase I inhibitors', *Chem Biol Interact,* 111-112, pp. 137-51.

Tottey, S., Rondet, S. A., Borrelly, G. P., Robinson, P. J., Rich, P. R. and Robinson, N. J. (2002) 'A copper metallochaperone for photosynthesis and respiration reveals metal-specific targets, interaction with an importer, and alternative sites for copper acquisition', *J Biol Chem,* 277(7), pp. 5490-7.

Touati, D., Jacques, M., Tardat, B., Bouchard, L. and Despied, S. (1995) 'Lethal oxidative damage and mutagenesis are generated by iron in delta fur mutants of *Escherichia coli*: protective role of superoxide dismutase', *J Bacteriol,* 177(9), pp. 2305-14.

Tseng, T. T., Gratwick, K. S., Kollman, J., Park, D., Nies, D. H., Goffeau, A. and Saier, M. H. (1999) 'The RND permease superfamily: an ancient, ubiquitous and diverse family that includes human disease and development proteins', *J Mol Microbiol Biotechnol,* 1(1), pp. 107-25.

Tsolis, R. M., Bäumler, A. J., Heffron, F. and Stojiljkovic, I. (1996) 'Contribution of TonB- and Feo-mediated iron uptake to growth of *Salmonella typhimurium* in the mouse', *Infect Immun,* 64(11), pp. 4549-56.

Ureta, A. C., Imperial, J., Ruiz-Argüeso, T. and Palacios, J. M. (2005) '*Rhizobium leguminosarum biovar viciae* symbiotic hydrogenase activity and processing are limited by the level of nickel in agricultural soils', *Appl Environ Microbiol,* 71(11), pp. 7603-6.

Valko, M., Morris, H. and Cronin, M. T. (2005) 'Metals, toxicity and oxidative stress', *Curr Med Chem,* 12(10), pp. 1161-208.

Valliyappan, T., Bakhshi, N. N. and Dalai, A. K. (2008) 'Pyrolysis of glycerol for the production of hydrogen or syn gas', *Bioresour Technol,* 99(10), pp. 4476-83.

Van Nostrand, J. D., Arthur, J. M., Kilpatrick, L. E., Neely, B. A., Bertsch, P. M. and Morris, P. J. (2008) 'Changes in protein expression in Burkholderia vietnamiensis PR1 301 at pH 5 and 7 with and without nickel', *Microbiology,* 154(Pt 12), pp. 3813-24.

VanZile, M. L., Cosper, N. J., Scott, R. A. and Giedroc, D. P. (2000) 'The zinc metalloregulatory protein *Synechococcus* PCC7942 SmtB binds a single zinc ion per monomer with high affinity in a tetrahedral coordination geometry', *Biochemistry,* 39(38), pp. 11818-29.

Vardar-Schara, G., Maeda, T. and Wood, T. K. (2008) 'Metabolically engineered bacteria for producing hydrogen via fermentation', *Microb Biotechnol,* 1(2), pp. 107-25.

Vargas, W. A., Weyman, P. D., Tong, Y., Smith, H. O. and Xu, Q. (2011) '[NiFe] hydrogenase from *Alteromonas macleodii* with unusual stability in the presence of oxygen and high temperature', *Appl Environ Microbiol,* 77(6), pp. 1990-8.

Vignais, P. M., Billoud, B. and Meyer, J. (2001) 'Classification and phylogeny of hydrogenases', *FEMS Microbiol Rev,* 25(4), pp. 455-501.

Vitale, S., Fauquant, C., Lascoux, D., Schauer, K., Saint-Pierre, C. and Michaud-Soret, I. (2009) 'A ZnS(4) structural zinc site in the *Helicobacter pylori* ferric uptake regulator', *Biochemistry,* 48(24), pp. 5582-91.

Waldron, K. J., Rutherford, J. C., Ford, D. and Robinson, N. J. (2009) 'Metalloproteins and metal sensing', *Nature,* 460(7257), pp. 823-30.

Wang, S., Wu, Y. and Outten, F. W. (2011) 'Fur and the novel regulator YqjI control transcription of the ferric reductase gene *yqjH* in *Escherichia coli*', *J Bacteriol,* 193(2), pp. 563-74.

Wang, S. C., Dias, A. V., Bloom, S. L. and Zamble, D. B. (2004) 'Selectivity of metal binding and metal-induced stability of *Escherichia coli* NikR', *Biochemistry,* 43(31), pp. 10018-28.

Wang, S. C., Li, Y., Ho, M., Bernal, M. E., Sydor, A. M., Kagzi, W. R. and Zamble, D. B. (2010a) 'The response of *Escherichia coli* NikR to nickel: a second nickel-binding site', *Biochemistry,* 49(31), pp. 6635-45.

Wang, S. C., Li, Y., Robinson, C. V. and Zamble, D. B. (2010b) 'Potassium is critical for the Ni(II)-responsive DNA-binding activity of *Escherichia coli* NikR', *J Am Chem Soc,* 132(5), pp. 1506-7.

Wang, W. C., Hsu, W. H., Chien, F. T. and Chen, C. Y. (2001) 'Crystal structure and site-directed mutagenesis studies of N-carbamoyl-D-amino-acid amidohydrolase from *Agrobacterium radiobacter* reveals a homotetramer and insight into a catalytic cleft', *J Mol Biol,* 306(2), pp. 251-61.

Warren, M. J., Raux, E., Schubert, H. L. and Escalante-Semerena, J. C. (2002) 'The biosynthesis of adenosylcobalamin (vitamin B12)', *Nat Prod Rep,* 19(4), pp. 390-412.

Washington-Hughes, C. L., Ford, G. T., Jones, A. D., McRae, K. and Outten, F. W. (2018) 'Nickel exposure reduces enterobactin production in *Escherichia coli*', *Microbiologyopen*, pp. e00691.

Waters, L. S., Sandoval, M. and Storz, G. (2011) 'The *Escherichia coli* MntR miniregulon includes genes encoding a small protein and an efflux pump required for manganese homeostasis', *J Bacteriol,* 193(21), pp. 5887-97.

Weeratunga, S. K., Gee, C. E., Lovell, S., Zeng, Y., Woodin, C. L. and Rivera, M. (2009) 'Binding of *Pseudomonas aeruginosa* apobacterioferritin-associated ferredoxin to bacterioferritin B promotes heme mediation of electron delivery and mobilization of core mineral iron', *Biochemistry,* 48(31), pp. 7420-31.

Weeratunga, S. K., Lovell, S., Yao, H., Battaile, K. P., Fischer, C. J., Gee, C. E. and Rivera, M. (2010) 'Structural studies of bacterioferritin B from *Pseudomonas aeruginosa* suggest a

gating mechanism for iron uptake via the ferroxidase center', *Biochemistry,* 49(6), pp. 1160-75.

Weinberg, E. D. (1975) 'Nutritional immunity. Host's attempt to withold iron from microbial invaders', *JAMA,* 231(1), pp. 39-41.

Wolfram, L. and Bauerfeind, P. (2002) 'Conserved low-affinity nickel-binding amino acids are essential for the function of the nickel permease NixA of *Helicobacter pylori*', *J Bacteriol,* 184(5), pp. 1438-43.

Wu, L. F., Mandrand-Berthelot, M. A., Waugh, R., Edmonds, C. J., Holt, S. E. and Boxer, D. H. (1989) 'Nickel deficiency gives rise to the defective hydrogenase phenotype of *hydC* and *fnr* mutants in *Escherichia coli*', *Mol Microbiol,* 3(12), pp. 1709-18.

Wuerges, J., Lee, J. W., Kang, S. O. and Djinovic Carugo, K. (2002) 'Crystallization of a nickel-containing superoxide dismutase and preliminary phase determination by MAD at the Ni K edge', *Acta Crystallogr D Biol Crystallogr,* 58(Pt 7), pp. 1220-3.

Xiao, Z. and Wedd, A. G. (2010) 'The challenges of determining metal-protein affinities', *Nat Prod Rep,* 27(5), pp. 768-89.

Xiong, A. and Jayaswal, R. K. (1998) 'Molecular characterization of a chromosomal determinant conferring resistance to zinc and cobalt ions in *Staphylococcus aureus*', *J Bacteriol,* 180(16), pp. 4024-9.

Yao, H., Wang, Y., Lovell, S., Kumar, R., Ruvinsky, A. M., Battaile, K. P., Vakser, I. A. and Rivera, M. (2012) 'The structure of the BfrB-Bfd complex reveals protein-protein interactions enabling iron release from bacterioferritin', *J Am Chem Soc,* 134(32), pp. 13470-81.

Youn, H. D., Kim, E. J., Roe, J. H., Hah, Y. C. and Kang, S. O. (1996) 'A novel nickel-containing superoxide dismutase from *Streptomyces spp*', *Biochem J,* 318 (Pt 3), pp. 889-96.

Zgurskaya, H. I. and Nikaido, H. (1999a) 'AcrA is a highly asymmetric protein capable of spanning the periplasm', *J Mol Biol,* 285(1), pp. 409-20.

Zgurskaya, H. I. and Nikaido, H. (1999b) 'Bypassing the periplasm: reconstitution of the AcrAB multidrug efflux pump of *Escherichia coli*', *Proc Natl Acad Sci U S A,* 96(13), pp. 7190-5.

Zhang, J. W., Butland, G., Greenblatt, J. F., Emili, A. and Zamble, D. B. (2005) 'A role for SlyD in the *Escherichia coli* hydrogenase biosynthetic pathway', *J Biol Chem,* 280(6), pp. 4360-6.

Zhang, Y., Akilesh, S. and Wilcox, D. E. (2000) 'Isothermal titration calorimetry measurements of Ni(II) and Cu(II) binding to His, GlyGlyHis, HisGlyHis, and bovine serum albumin: a critical evaluation', *Inorg Chem,* 39(14), pp. 3057-64.

Zhao, J., Bertoglio, B. A., Devinney, M. J., Dineley, K. E. and Kay, A. R. (2009) 'The interaction of biological and noxious transition metals with the zinc probes FluoZin-3 and Newport Green', *Anal Biochem,* 384(1), pp. 34-41.